Gold-Induced Atomic Wires on Terraced Silicon Surfaces:

Formation and Interactions of Silicon Spin Chains

Dissertation zur Erlangung des
naturwissenschaftlichen Doktorgrades
der Julius-Maximilians-Universität Würzburg

vorgelegt von
Julian Aulbach
aus Erlenbach am Main

Würzburg 2017

Eingereicht am: 09.11.2017
bei der Fakultät für Physik und Astronomie

1. Gutachter: Prof. Dr. Jörg Schäfer

2. Gutachter: Prof. Dr. Matthias Bode

3. Gutachter: Prof. Dr. Michael Horn-von Hoegen

der Dissertation

Vorsitzender:

1. Prüfer: Prof. Dr. Jörg Schäfer

2. Prüfer: Prof. Dr. Matthias Bode

3. Prüfer: Prof. Dr. Giorgio Sangiovanni

im Promotionskolloquium

Tag des Promotionskolloquiums: 12.10.2018

Doktorurkunde ausgehändigt am:

Abstract

Atomic nanowires formed by self-assembled growth on semiconducting surfaces represent a feasible physical realization of quasi-one-dimensional (1D) electron systems and can be used to study fascinating 1D quantum phenomena. The system in the focus of this thesis, Si(553)-Au, is generated by Au adsorption onto a stepped silicon surface. It features two different chain types, interspersed with each other: A Au chain on the terrace, and a honeycomb chain of graphitic silicon located at the step edge. The silicon atoms at the exposed edges of the latter are predicted to be spin-polarized and charge-ordered [1], leading to an ordered array of local magnetic moments referred to as “spin chains”.

The present thesis puts this spin chain proposal to an experimental test. A detailed scanning tunneling microscopy (STM) and scanning tunneling spectroscopy (STS) scrutiny reveals a distinct unoccupied density of states (DOS) feature localized at every third Si step-edge atom, which aligns perfectly with the density functional theory (DFT) prediction. This finding provides strong evidence for the formation of spin chains at the Si(553)-Au step edges, and simultaneously rules out the interpretation of previous studies which attributed the ×3 step-edge superstructure to a Peierls instability. To study the formation of spin chains in further detail, an additional member of the so-called Si(*hhk*)-Au family – Si(775)-Au – is analyzed. Based on DFT modeling (performed by S.C. Erwin, Naval Research Laboratory, USA) and detailed STM and STS experiments, a new structure model for this surface is developed, and the absence of spin chains at the Si(775)-Au step edges is demonstrated. The different step-edge charge distributions of all known Si(*hhk*)-Au surfaces are traced back to an electron transfer between the terrace and the step edge. Accordingly, an unintentional structure defect should create a localized spin at the Si(775)-Au step edge. This prediction is verified experimentally, and suggest that surface chemistry can be used to create and destroy Si spin chains.

Having clarified why spin chains form on some Si(*hhk*)-Au surfaces but not on others, various interaction effects of the Si(553)-Au spin chains are inspected. A collaborative analysis by spot profile analysis LEED (SPA-LEED) (M. Horn-von Hoegen group, University of Duisburg-Essen, Germany), DFT (S.C. Erwin), and STM reveals strong lateral coupling between adjacent spin chains, bearing interesting implications for their magnetic ordering. The centered geometry uncovered leads to magnetic frustration, and may stabilize a two-dimensional (2D) quantum spin liquid.

Moreover, a complex interplay between neighboring Au and Si chains is detected. Specifically, the interaction is found effectively “one-way”, i.e., the Si step edges respond to the Au chains but not vice versa. This unidirectional effect breaks the parity of the Si chains, and creates two different configurations of step edges with opposite directionality.

In addition to the static properties of the Si(553)-Au surface mentioned above, the occurrence of solitons in both wire types is witnessed in real space by means of high-resolution STM imaging. The solitons are found to interact with one another such that both move in a coupled fashion along the chains. Likewise, STM experiments as a function of the tunneling current suggest an excitation of solitons along the step edge by the STM tunneling

tip. Solitons are also found to play an essential role in the temperature-dependent behavior of the Si(553)-Au step edges. It is an accepted fact that the distinct ×3 superstructure of the Si(553)-Au step edges vanishes upon heating to room temperature (RT). As a first step in exploring this transition in detail over a large temperature range, a previously undetected, occupied electronic state associated with the localized step-edge spins is identified by means of angle-resolved photoemission spectroscopy (ARPES). A tracking of this state as a function of temperature reveals an order-disorder-type transition. Complementary STM experiments attribute the origin of this transition to local, thermally activated spin site hops, which correspond to soliton-anitsoliton pairs.

Finally, a manipulation of the Si(553)-Au atomic wire array is achieved by the stepwise adsorption of potassium atoms. This does not only increase the filling of the Au-induced surface bands culminating in a metal-insulator transition (MIT), but also modifies the Si step-edge charge distribution, as indicated by STM and ARPES experiments.

Zusammenfassung

Durch Selbstorganisation erzeugte atomare Nanodrähte auf Halbleiteroberflächen erlauben die experimentelle Realisierung quasi-eindimensionaler Elektronensysteme und ermöglichen so die Untersuchung faszinierender eindimensionaler Quantenphänomene. Das Nanodrahtsystem im Zentrum dieser Arbeit [Si(553)-Au] lässt sich durch Adsorption von Goldatomen auf eine gestufte Siliziumoberfläche herstellen. Es besteht aus zwei unterschiedlichen, alternierend angeordneten Kettenarten. Auf jeder Terrasse befindet sich eine Goldkette, während die Stufenkanten aus einer graphitartigen Honigwabenstruktur aus Silizium aufgebaut sind. Für die Stufenkantenatome der Siliziumhonigwabenkette wurde eine Ladungsordnung mit vollständiger Spin-Polarisation jedes dritten Stufenkantenatoms vorhergesagt [1]. Dies entspricht einer regelmäßigen Anordnung von lokalen magnetischen Momenten, die als "Spinketten" bezeichnet werden.

Die vorliegende Arbeit unterzieht diese theoretische Voraussage einem experimentellen Test. Mittels Rastertunnelmikroskopie (engl. scanning tunneling microscopy, STM) und Rastertunnelspektroskopie (engl. scanning tunneling spectroscopy, STS) wurde die lokale Zustandsdichte entlang der Stufenkante charakterisiert. Die experimentellen Befunde zeigen eine nahezu perfekte Übereinstimmung mit dem theoretisch vorhergesagten Spinketten-Szenario. Gleichzeitig konnte eine bis dato in der Literatur überwiegend favorisierte Peierls-Instabilität ausgeschlossen werden.

Um die Ausbildung von Spinketten auf goldinduzierten gestuften Siliziumoberflächen genauer zu verstehen, wurde ein weiteres Probensystem der sogenannten Si(*hhk*)-Au-Familie – Si(775)-Au – detailliert untersucht. Basierend auf Dichte-Funktional-Theorie Rechnungen (durchgeführt von S.C. Erwin, Naval Research Laboratory, USA) und STM/STS-Experimenten wurde ein neues Strukturmodell für diese Oberfläche entwickelt. Außerdem konnte die Abwesenheit von Spinketten an den Si(775)-Au-Stufenkanten nachgewiesen werden. Als Ursache für die variierende Ladungsanhäufung an den Stufenkanten der Si(*hhk*)-Au-Systeme konn-te ein Ladungsaustausch zwischen der Terrasse und der Stufenkante ausgemacht werden. Weiter wurde gezeigt, dass ein struktureller Defekt einen lokalisierten Spin an der Si(775)-Au-Stufenkante erzeugen kann. Dies untermauert das Bild des Ladungstransfers zwischen Terrasse und Stufenkante und legt außerdem nahe, Siliziumspinketten mit Hilfe von Oberflächenchemie zu modifizieren.

Neben der Etablierung des Spinketten-Szenarios wurden verschiedene Wechselwirkungseffekte der Si(553)-Au-Spinkette mit ihrer Umgebung untersucht. In Zusammenarbeit mit der Gruppen um Prof. M. Horn-von Hoegen (Universität Duisburg-Essen) und S.C. Erwin konnte eine starke laterale Kopplung zwischen benachbarten Spinketten festgestellt werden, welche interessante Konsequenzen für die magnetische Ordnung der lokalisierten Spins mit sich bringt. Die entdeckte zentrierte Dreiecksanordnung der Spins führt zu magnetischer Frustration und suggeriert die Ausbildung einer zweidimensionalen Spin-Flüssigkeit.

Des Weiteren konnte ein unerwartetes Wechselspiel zwischen benachbarten Gold- und Siliziumketten festgestellt werden. Es zeigte sich, dass die Goldketten auf die Siliziumketten einwirken, jedoch nicht umgekehrt. Diese lediglich in einer Richtung wirkende Beeinflussung

erzeugt einen Symmetriebruch entlang der Siliziumstufenkante, der dazu führt, dass zwei Arten von Stufenkanten mit unterschiedlicher Direktionalität auftreten.

Darüber hinaus konnte mit Hilfe hochaufgelöster STM-Aufnahmen die Existenz von Solitonen in beiden Kettenarten nachgewiesen werden. Dabei stellte sich heraus, dass die beiden Soliton-Typen miteinander wechselwirken und sich daher wider Erwarten nicht unabhängig sondern aneinander gekoppelt durch die Kettenstrukturen bewegen. Weiterhin suggerieren tunnelstromabhängige STM-Messungen, dass sich Solitonen in der Siliziumkette mit der Tunnelspitze des Rastertunnelmikroskops anregen lassen. Solitonen konnte außerdem eine wichtige Rolle im temperaturabhängigen Verhalten der Siliziumstufenkanten zugeschrieben werden. Es war bereits seit Längerem bekannt, dass die ausgeprägte ×3 Überstruktur, die sich bei tiefen Temperaturen entlang der Stufenkante beobachten lässt, bei Raumtemperatur verschwindet. Um diese Temperaturabhängigkeit genauer zu untersuchen, wurde ein neu entdeckter, elektronischer Zustand, der sich den an der Stufenkanten lokalisierten Spins zuordnen lässt, mittels winkelaufgelöster Photoelektronenspektroskopie temperaturabhängig analysiert. Dabei stellte sich heraus, dass es sich bei dem Phasenübergang um einen speziellen Ordnungs-Unordnungs-Übergang handelt. Mit Hilfe komplementärer STM-Messungen konnte ein thermisch aktivierter Platzwechsel der lokalisierten Elektronenspins (d.h. die Erzeugung von Soliton-Antisoliton-Paaren) für das temperaturabhängige Verhalten der Siliziumstufenkante verantwortlich gemacht werden.

Weiterhin konnte eine gezielte Manipulation des Si(553)-Au-Nanodrahtsystems durch sukzessive Dotierung mit Kaliumatomen realisiert werden. Dabei wurde ein Anstieg der Befüllung der goldinduzierten Oberflächenbänder, der letztendlich zu einem Metall-Isolator-Übergang führt, beobachtet. Außerdem deuten die experimentellen Befunde auf eine Modifizierung der Spinketten entlang der Stufenkante hin.

Contents

List of figures

List of acronyms

1D one-dimensional

2D two-dimensional

3D three-dimensional

AFM antiferromagnetic

AN Abukawa-Nishigaya

ARPES angle-resolved photoemission spectroscopy

BZ Brillouin zone

CDW charge density wave

DFT density functional theory

DOS density of states

EBH Erwin-Barke-Himpsel

EDC energy distribution curve

FM ferromagnetic

FWHM full-width at half maximum

PBE Perdew, Burke, and Ernzerhof

PES Photoelectron spectroscopy

GGA generalized gradient approximation

HSE Heyd-Scuseria-Ernzerhof

HCC honeycomb chain

KK Kwon-Kang

LDOS local density of states

LEED low energy electron diffraction

LDA local density approximation

LT low-temperature

LT-STM low-temperature STM

MIT metal-insulator transition

ML monolayer

PDOS partial density of states

PLD periodic lattice distortion

RT room temperature

SBZ surface Brillouin zone

QSL quantum spin liquid

SOC spin-orbit coupling

SPA-LEED spot profile analysis LEED

SP-STM spin-polarized scanning tunneling microscopy

STM scanning tunneling microscopy

STS scanning tunneling spectroscopy

SSH Su-Schrieffer-Heeger

SXRD surface x-ray diffraction

TLL Tomonaga-Luttinger liquid

UHV ultra-high vacuum

XMCD x-ray magnetic circular dichroism

1 Introduction

Physics of 1D Electron Systems – In 1D electron systems, cooperative interactions are expected to give rise to exotic quantum phenomena. This may seem counterintuitive, as it is a common approach in physics to simplify complex issues by reducing the dimensionality of the underlying system to 1D. For example, solid state physics textbooks commonly introduce the concept of band structure by placing electrons in a notional 1D lattice potential. Phonons, i.e., collective excitations of a crystal lattice, are typically introduced using a 1D chain of atoms. In these two cases, the spatial reduction is applied in order to simplify the problem. On the other hand, electron-electron and electron-phonon interactions are of much higher relevance in 1D than in higher dimensional systems due to less effective screening, which can give rise to complex quantum phenomena. As first analyzed by R. Peierls [2], the interaction between electrons and phonons in an initially metallic 1D chain of atoms can result in the formation of a charge density wave (CDW) accompanied by a periodic lattice distortion (PLD) and a band gap opening in the electronic structure at $T = 0\,\mathrm{K}$. In the case of a strongly interacting 1D electron system, the low energy properties can no longer be described as quasiparticles, i.e., Landau's Fermi liquid paradigm breaks down. Instead, the electrons show Tomonaga-Luttinger liquid (TLL) behavior [3]. With regard to topological physics, 1D architectures can realize a 1D topological insulator, hosting 0D topologically protected edge states also known as solitons [4, 5].

Quasi-1D Model Systems – However, strictly 1D electron systems remain a theoretical construct since they are impossible to realize experimentally. In contrast, real-world architectures are at least quasi-1D due to their embedding in a three-dimensional (3D) environment. On the one hand, the coupling to higher dimensions leads to a stabilization of a Peierls instability or, more generally, to long-range order above $T = 0\,\mathrm{K}$ [6, 7]. On the other hand, a 3D environment can reduce electron correlation effects such that Fermi liquid rather than TLL behavior is observed. One intensively studied group of model systems are anisotropic (and thus quasi-1D) bulk materials such as the Bechgaard salts [8] and molybdenum bronzes or oxides [9]. Yet an alternative class of setups to study 1D electron physics are self-assembled metal adatom chain reconstructions on semiconducting substrates, often referred to as nanowires [10, A8]. Aside from maximum lateral confinement, i.e., a wire width on the atomic scale, this approach offers a certain degree of tunability that can be realized, for example, using different substrate materials and orientations or by doping via adatom adsorption. Moreover, unintentional de-

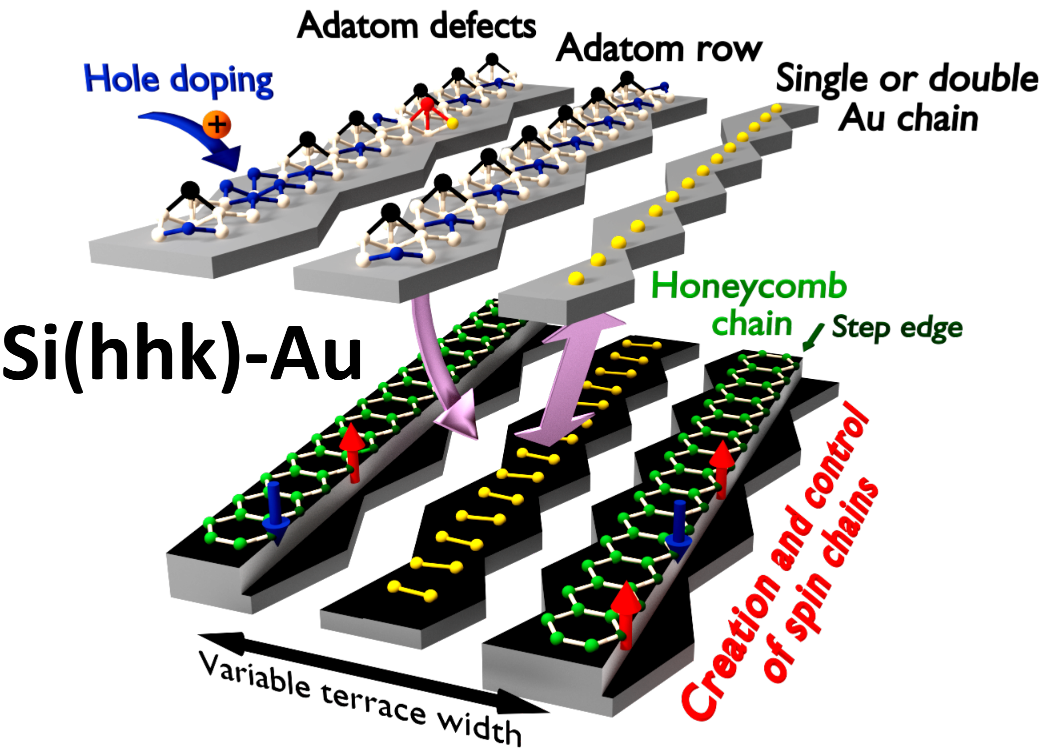

Figure 1.1: *Overview of the characteristic structural motifs of the Si(hhk)-Au surfaces that control the spin chain formation at the Si step edge. The crystallographic surface orientation and, hence, the terrace width leads to different Au chain variants (single or double strand), and determines the presence of an additional Si adatom row. From [A3].*

fects can terminate the nanowires, resulting in a finite wire length, which may give rise to modified physical properties. Another advantage of these kind of quasi-1D model systems is that they are well-suited for powerful surface science techniques like STM, STS, low energy electron diffraction (LEED), and ARPES. To mention a few selected prototype example systems hosting fascinating quantum phenomena: Atomic wires induced by adsorption of a submonolayer of gold on a Ge(001) surface have been claimed to exhibit signatures of a TLL [11], although these findings are controversially discussed at present [12, 13, A8]. Indium chains grown on a Si(111) template form a coupled double Peierls chain system [4, 14], which, in addition, features various types of interacting topological solitons [4, 15, 16].

Au Chains on Stepped Si(*hhk*) Substrates: An Atomic Toolbox – The quasi-1D model systems that will be analyzed in this thesis are created by the adsorption of a submonolayer of Au atoms on different stepped (high-index) Si substrates, which act as a template for self-assembled nanowire growth. At present, there are four established stable systems of this kind: Si(335)-Au, Si(557)-Au, Si(553)-Au and Si(775)-Au. These are collectively referred to as the Si(*hhk*)-Au family [17]. As will be demonstrated in this thesis, all members of the Si(*hhk*)-Au family are built by a small set of recurring structural motives (see Fig. 1.1). It is a common feature of all Si(*hhk*)-Au systems that their step edges are formed by a graphitic (sp^2-hybridized) Si honeycomb chain. The reconstruction of the terraces depends on the high-index substrate, and, thus, differs for each Si(*hhk*)-Au member. In particular, the Au chain located in the middle of the terrace can be either a single or a double strand. Systems with wider terraces may include a Si adatom row as well. Consequently, not only the inter-wire coupling, but also the bonding network and the electronic configuration can be altered (tuned) by using different Si(*hhk*) substrates. Unique to the Si(*hhk*)-Au surfaces (and not present in other quasi-1D surface reconstructions), local magnetic moments may form at the step edges of some Si(*hhk*)-Au members. Before returning to this topic in more detail, some Si(*hhk*)-Au findings from previous literature will be reviewed.

State of Si(*hhk*)-Au Research: A Brief Historic Summary – Au-stabilized vicinal Si surfaces became famous due to their band structure, which features a 1D character with a peculiar band splitting [Fig. 1.2(a)] that was initially mistaken as spin-charge separation in a TLL [18,19]. It was subsequently discovered that the split bands, which are characteristic for all members of the Si(*hhk*)-Au family [17] and were originally assigned as spinon and holon of a TLL, are in fact Rashba-type spin split bands [1,20–23]. In other words, the splitting arises from spin-orbit coupling of 1D free electron-like states in the inversion symmetry-breaking field of the surface, augmented by the heavy Au atoms. Additional experimental investigations found that the Si(*hhk*)-Au atomic chains display various superstructures with respect to the Si lattice constant along the steps. For Si(557)-Au and Si(553)-Au, a temperature dependence of the chain superstructures accompanied by a band gap opening was observed [Fig. 1.2(b)] and interpreted as a Peierls instability [24–27]. Before and after these studies, significant effort was put into the development of proper structural models [1,17,22,23,28–33] on the basis of which the Rashba-type spin splitting could be confirmed [1,22,23,34]. In addition, the explanation of the phase transitions as a (conventional) Peierls instability was called into question [1,20,34,35]. An alternative explanation was provided by a DFT study in 2010 [1], which predicts a charge ordering at the Si step edges (similar to an observation made recently at the edges of graphene [36]). Specifically, the dangling bond of every third Si step-edge atom is proposed to host one single electron, while the dangling bonds of the edge atoms in between are occupied by two electrons. This results in a periodic array of local magnetic moments referred to as "spin chains" [see Fig. 1.2(c)]. With regard to magnetic ordering, an antiferromagnetic coupling of the localized spins along the step edge is predicted [1], bearing fascinating spintronic applications like spin-based memory devices [37]. The spin chain proposal laid the groundwork for the primary studies and associated results achieved in the framework of this thesis and allowed for a fruitful collaboration with S.C. Erwin – one of the co-authors of Ref. [1]. For a more detailed summary of the Si(*hhk*)-Au research performed between the late 1990s and 2009, please refer to the excellent review article by Snijders and Weitering [10].

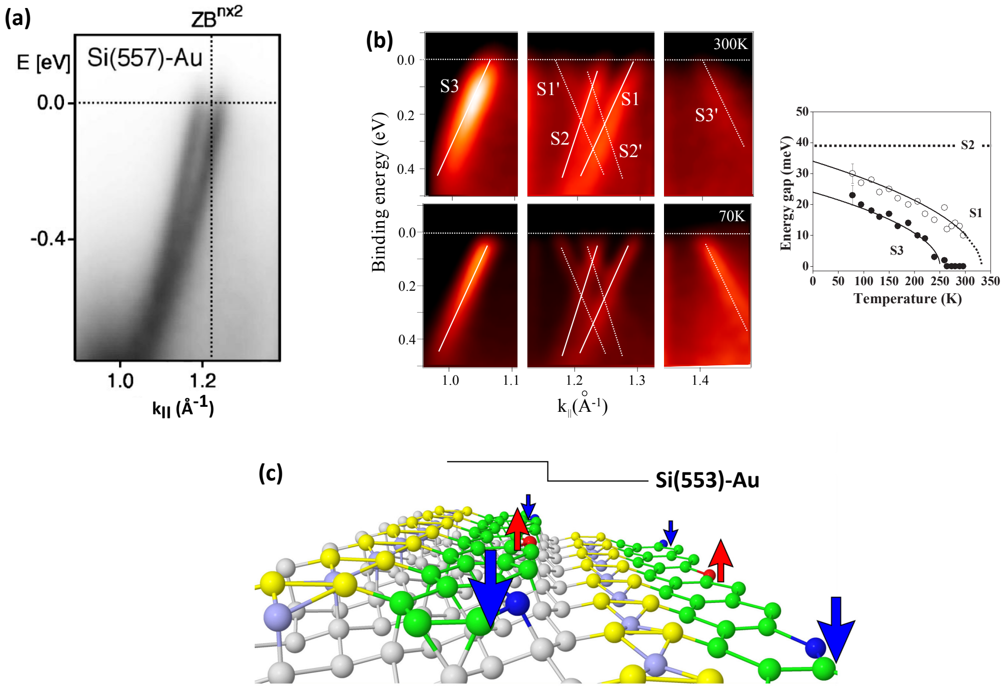

Figure 1.2: *(a) ARPES map of the Rashba-split, Au-induced surface band of the Si(557)-Au reconstruction initially mistaken for the spinon and holon branch of a TLL. Reprinted figure with permission from [19], Copyright 2001 by the American Physical Society. (b) Temperature dependence of the Au-induced Si(553)-Au surface bands measured by ARPES. The gap opening observed has been interpreted as a signature of a Peierls transition [25]. Reprinted figures with permission from [25], Copyright 2005 by the American Physical Society. (c) Structure model of the Si(553)-Au surface comprising a Au double strand (yellow) and a Si honeycomb chain at the step edge (green). Spin-polarized DFT calculations predict the formation of periodic local magnetic moments at the step edges which order antiferromagentically [1]. Reprinted by permission from Macmillan Publishers Ltd: Nature Communications [1], Copyright 2010.*

Solitons in Atomic Wires – When dealing with atomic wires hosting a higher order periodicity, one may expect the occurrence of (moving) domain walls, so-called solitons, separating the degenerate ground state phases of the 1D chain. However, their microscopic dimension in combination with their high mobility render the observation of solitons in real space a difficult task. Only recently, immobile solitons – so-called frozen solitons – have been observed on the CDW systems $NbSe_3$ [38] and In/Si(111) [15]. For the latter, deposition of a submonolayer of In atoms on a Si(111) substrate leads to atomically defined In chains, which form an array of two coupled Peierls chains separated by a row of Si substrate atoms (see Fig. 1.3) [4,14,39,40]. On this surface, various nonsolitonic phase defects [15,41] as well as topological solitons have been observed [15]. In particular, the unique setup of coupled double Peierls chains gives rise to chiral solitons, i.e., chiral topological edge states [4]. A recent experimental study also revealed an interaction of chiral and non-chiral solitons which switches the handedness of the chiral soliton [16]. This switching between different solitons opens the door for the realization of soliton-based logic devices (“solitonics”) [16]. For the system in the focus of this thesis,

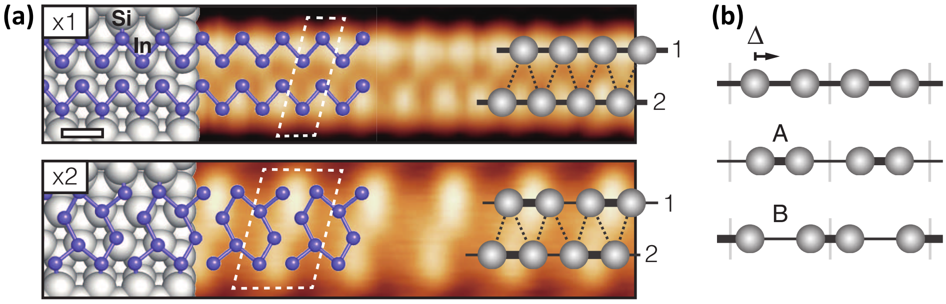

Figure 1.3: *(a) Structure models and STM images of the coupled Peierls chain system of In atoms on Si(111) above (top) and below (bottom) the Peierls transition temperature. (b) Schematic illustration of the two degenerate ground state phases A and B of a single Peierls chain. From [4]. Reprinted with permission from AAAS.*

initial observations of phase shifts at the Si step edge have been made [26,27]. In both reports noted, however, the domain walls were frozen for an unknown reason. Moreover, there is no reference to the occurrence of mobile solitons or the interactions of solitons on Si(hhk)-Au surfaces, which is one objective of the present thesis. Solitons may also be involved in the temperature-dependent change of the Si(553)-Au step edge pattern. Although previously attributed to a Peierls transition [25, 26], the findings of this thesis exclude such a scenario on the Si(553)-Au surface. Yet another explanation is provided by a theoretical study of Erwin and Snijders [42], and is based on the formation of dynamic soliton-antisoliton pairs as modeled by molecular dynamics and kinetic Monte Carlo simulations. An experimental verification of this proposal is outstanding.

Focus of this Thesis – One central issue of this thesis will be the formation of spin chains at the step edges of the Si(553)-Au surface as predicted theoretically in Ref. [1]. This DFT proposal will be put to an detailed experimental test. The methods of choice for this purpose are STM and STS, which combine local atomic resolution with spectroscopic access to both occupied and unoccupied electronic states. In particular, only the singly occupied and, therefore, spin-polarized Si atoms should exhibit an unoccupied state as a final state for tunneling into, providing an experimental fingerprint to evidence spin chain formation. The second chain type of the Si(553)-Au surface, the Au chain, is rather well understood and, thus, of secondary interest. Nevertheless, the two chain types are interspersed and, thus, may influence each other. As this issue has not yet to been examined, its clarification is another objective of this thesis. To further explore the step-edge spin chain formation, other members of the family of Au-stabilized, stepped Si surfaces will be analyzed. STM and STS experiments will not only characterize the intrinsic charge distribution of the Si(557)-Au and Si(775)-Au step edges, but also the influence of defects thereon. As it is impossible to determine an exact orbital occupancy by STM/STS experiments alone, theoretical modeling is required. This is realized by close collaboration with S.C. Erwin from the Naval Research Laboratory in

Washington, DC, USA. On the basis of DFT total energy calculations, new structure models can be developed. DFT-simulated STM images and electronic structure calculations allow for a detailed comparison with the experimental findings, which may provide evidence of the presence or absence of spin chains.

When dealing with uncompensated local spins, it is logical to also consider magnetic ordering. This will be addressed for Si(553)-Au using a combined STM, SPA-LEED, and DFT analysis of the lateral coupling between adjacent spin chains. In addition, the Si(553)-Au chains will be analyzed with respect to the occurrence of solitons in both chain types using the spatial and time resolution of an STM experiment. In 2013, an excitation of the Si step edge by the STM tunneling tip was reported [43, 44]. However, the nature of the excited state could not be determined unambiguously – a topic that will also be covered in this thesis. As mentioned above, the temperature dependence of the Si(553)-Au step edge pattern is not well understood. To tackle this issue experimentally, the low-temperature (LT) band structure will be analyzed and tracked as a function of temperature by means of ARPES. Temperature-dependent STM experiments complement the ARPES results. A further aspect of this thesis is the modification of the electronic structure, the step-edge charge distribution in particular, by doping. This will be realized by a stepwise deposition of electron-donating potassium atoms on the Si(553)-Au surface. In addition, the zoo of stepped quasi-1D model systems, which may be subject to spin chain formation, will be extended by changing the substrate material from Si to Ge.

Structure of this thesis – The thesis is organized as follows: First, the theoretical concepts of the Peierls instability and of solitons in solid state physics will be reviewed. Then, in Chapt. 3, the experimental and theoretical methods applied in the framework of this thesis will be introduced, providing the relevant background information needed to understand the experimental results obtained. Chapt. 4 will outline the preparation and characterization of various Si(*hhk*) substrates essential for proper atomic wire growth. The formation of spin chains in different Si(*hhk*)-Au systems will be analyzed in Chapt. 5. Chapt. 6 focuses exclusively on Si(553)-Au, and will address the possibility of a magnetic ordering of the localized spins as well as the interaction between Au and Si chains. In addition, the occurrence of solitons and their role regarding the excited step edge state observed in low-temperature STM (LT-STM) experiments as well as the temperature dependence of the step edge pattern will be discussed. Finally, the manipulation of the Si(553)-Au electronic structure by doping will be presented.

2 Theoretical Concepts of Quasi-1D Atomic Wires

As laid out in the introduction, atomic chain arrays, formed by self-assembled growth on semiconducting surfaces, offer the opportunity to study peculiar (quasi)-1D quantum phenomena. In turn, simplified model systems are, theoretically, utilized to address and predict the fundamental characteristics of these phenomena. Most relevant for the issues discussed in this thesis are the concept of a Peierls instability as well as that of solitons in solid state physics. Thus, the first part of this chapter will summarize the fundamental mechanism of a Peierls instability, comprising the experimental fingerprints as well as the limitations of the textbook Peierls scenario; both of which are essential for the interpretation of experimental data presented and are primarily based on [6]. In the second part, the concept of solitons in a 1D chain of atoms will be reviewed using the prototype example of polyacetylene. The section mainly follows [45] and will provide the theoretical background to discus the versatile role of solitons found on the Si(553)-Au wire array (Secs. 6.3, 6.4, 6.6).

2.1 Peierls Instability

The concept of a Peierls instability can be traced back to Rudolf Peierls' studies of a 1D chain of atoms equally spaced by a lattice constant a [2]. Each atom was supposed to provide one electron leading to a half-filled band [see Fig. 2.1(a)]. Peierls found that such a chain is subject to an instability resulting in a metal-insulator transition accompanied by a PLD [2]. In this so-called Peierls instability, the concept of Fermi surface nesting plays an essential role. The nesting vector $q = 2k_F$, spanned by the Fermi points $\pm k_F$, dictates the periodicity of the restructured lattice. As a consequence, the charge density $\rho(x)$ as well as the lattice are modulated with the same periodicity $2a$. In addition, a band gap opens at the zone boundary of the new unit cell [see Fig. 2.1(b)]. This scenario reduces the total energy of the system once the energy cost of the elastic lattice distortion is overcompensated by the electronic energy gain due to the energy lowering of the filled electron states [46]. In 1965, Walter Kohn demonstrated that Fermi surface nesting gives rise to a screening of phonons. This produces a so-called Kohn anomaly in the phonon dispersion [47]. At temperatures lower than the transition temperature T_{CDW}, the phonon at $q = 2k_F$ freezes out and the lattice manifests its new periodicity. Experimentally, a Peierls instability may thus be identified by a band gap opening accompanied by the formation of a new lattice periodicity as a function of temperature. The following will present the basic concept of Peierls' idea and finally stress the limitations of this simple model in real-world systems.

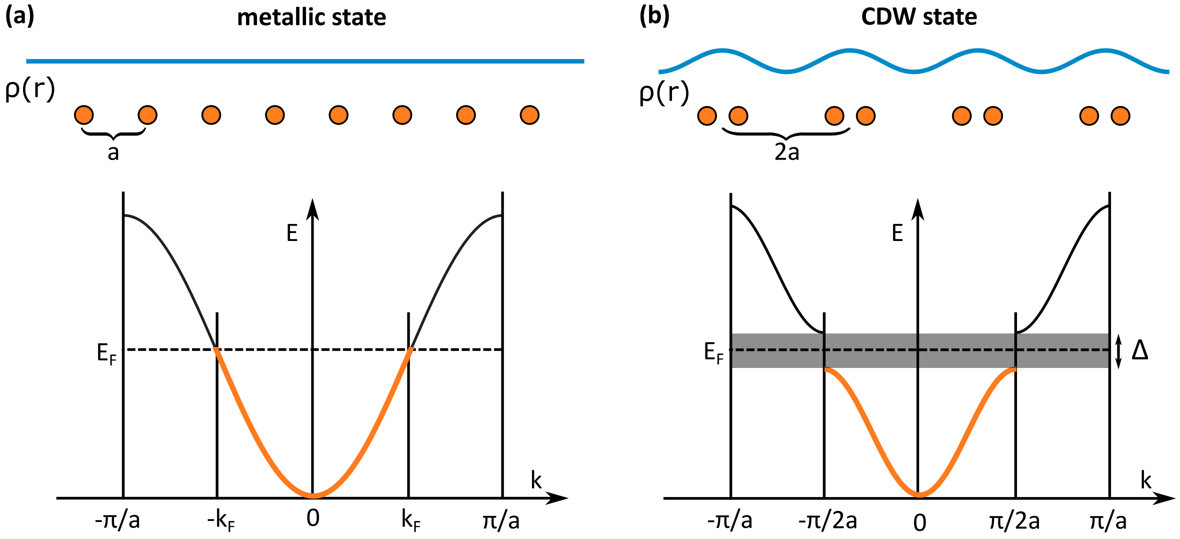

Figure 2.1: *Schematic of a Peierls transition. (a) Linear chain of atoms providing one electron each. The charge density $\rho(r)$ is constant and the band structure features a half-filled band. (b) For $T < T_{CDW}$ the chain is subject to a PLD which is accompanied by a band gap opening at the zone boundary of the new unit cell. Consequently, $\rho(r)$ is modulated with the periodicity of the distorted lattice. After [6].*

2.1.1 Electron-Phonon Interaction: Mean Field Approximation

The transition to a CDW ground state can be described quantitatively as a 1D free electron gas coupled to a chain of ions by electron-phonon coupling in the weak coupling limit [6]. Such electron-lattice systems can by modeled by a Fröhlich Hamiltonian written in second quantization [6, 48]:

$$\begin{aligned} H &= H_{el} + H_{ph} + H_{el-ph} \\ &= \sum_k E_k a_k^\dagger a_k + \sum_q \hbar\omega_q b_q^\dagger b_q + \frac{1}{\sqrt{N}} \sum_{k,q} g_q a_{k+q}^\dagger a_k (b_{-q}^\dagger + b_q), \end{aligned} \tag{2.1}$$

where $a_k^\dagger$ and a_k are creation and annihilation operators for the electronic Bloch state k with energy E_k. $b_q^\dagger$ and b_q denote creation and annihilation of a longitudinal phonon mode q with frequency ω_q. N is the number of ions in the linear chain and g_q represents the electron-phonon coupling. The following will present some results of this model according to Ref. [48]. For a detailed derivation within the framework of mean field theory refer to [6].

The static displacement u_q of a phonon q induces a potential

$$v_q = g_q u_q \sqrt{\frac{2Mw_q}{\hbar}}. \tag{2.2}$$

with M being the ionic mass and ω_q the frequency of the phonon mode q. On the one hand, the static displacement u_q results in a distortion energy of the lattice given by

$$\delta E_{lattice} = \frac{1}{2} M \omega_q^2 u_q^2. \tag{2.3}$$

On the other hand, the induced potential v_q leads to a total band energy gain, which, according to linear response theory (see e.g. Ref. [49]), is described by

$$\delta E_{band} = -|v_q|^2 \chi(q). \tag{2.4}$$

$\chi(q)$ is the static dielectric susceptibility also called the Lindhard response function [6], which describes the response of a free-electron gas to an external perturbation – in this case a phonon mode q. The pivotal role of $\chi(q)$ will be discussed in detail in the next section. If the electronic energy gain exceeds the energy penalty due to the lattice distortion, i.e., if $\delta E_{band} + \delta E_{lattice} < 0$, a CDW accompanied by a PLD will form. Applying Eqs. 2.3 and 2.4 leads to the following instability condition:

$$\frac{4g_q^2}{\hbar w_q} > \frac{1}{\chi(q)}. \tag{2.5}$$

Chan and Heine refined this condition by taking Coulomb (U_q) as well as exchange interactions (V_q) into account [50]:

$$\frac{4g_q^2}{\hbar w_q} - 2U_q + V_q \geq \frac{1}{\chi(q)} \tag{2.6}$$

with $\frac{4g_q^2}{\hbar w_q} > 2U_q > V_q > 0$. Based on Eq. 2.5 and 2.6 a CDW/PLD transition is supported by i) strong electron-phonon coupling (large g_q), ii) low phonon frequency ω_q resulting in a small distortion energy of the lattice, iii) weak Coulomb interaction U_q, iv) strong electron-electron exchange interaction (large V_q), and v) a large static dielectric susceptibility $\chi(q)$.

2.1.2 Response of a 1D Electron Gas: The Role of Fermi Surface Nesting

The static dielectric susceptibility $\chi(\vec{q})$ of a d-dimensional free-electron gas is given by [6]

$$\chi(\vec{q}) = \frac{1}{V} \sum_k \frac{f(E_k) - f(E_{k+q})}{E_k - E_{k+q}}. \tag{2.7}$$

Where $f(E_k)$ is the Fermi-Dirac distribution function for state k and V the volume of the system. Contrary to the 2D and 3D case, $\chi(q)_{1D}$ diverges at $q = 2k_F$ [see Fig. 2.2(a)]. The reason for this singularity is the special Fermi surface topology of a 1D electron gas. To understand this, a close inspection of Eq. 2.7 is helpful: A large $\chi(\vec{q})$ requires a large nominator $f(E_k) - f(E_{k+q})$, a small denominator $E_k - E_{k+q}$, and many states coupled by the same $\vec{q}$. Moreover, the summands in Eq. 2.7 only differ from zero if $E_k < E_F < E_{k+q}$ or $E_{k+q} < E_F < E_k$ [51]. Consequently, pairs of electronic states with one state just below and one state just above the Fermi level serve as the largest contributors in Eq. 2.7, suggesting the important role of the system's Fermi surface contour. A 1D electron gas fulfills these requirements in a perfect way: Its Fermi surface, composed by two parallel lines, provides many k-point pairs connected by the same $q = 2k_F$ [see Fig. 2.2(b)]. This situation is considered *perfect nesting* and raises a singularity in $\chi(\vec{q})$ so that every perturbation that supplies a wave vector $q = 2k_F$ will be perfectly screened (see Eq. 2.4). For the 2D case, nesting is significantly reduced as depicted in Fig. 2.2(b). The sinusoidal Fermi surface of a quasi-1D electron gas may, however, provide enough electron-hole pairs, which fulfill the nesting conditions [6, 46]. The impact of the dimensionality, in particular the role of Fermi surface nesting, will be elaborated upon later in this work while discussing the applicability of the simple Peierls picture to real-world systems.

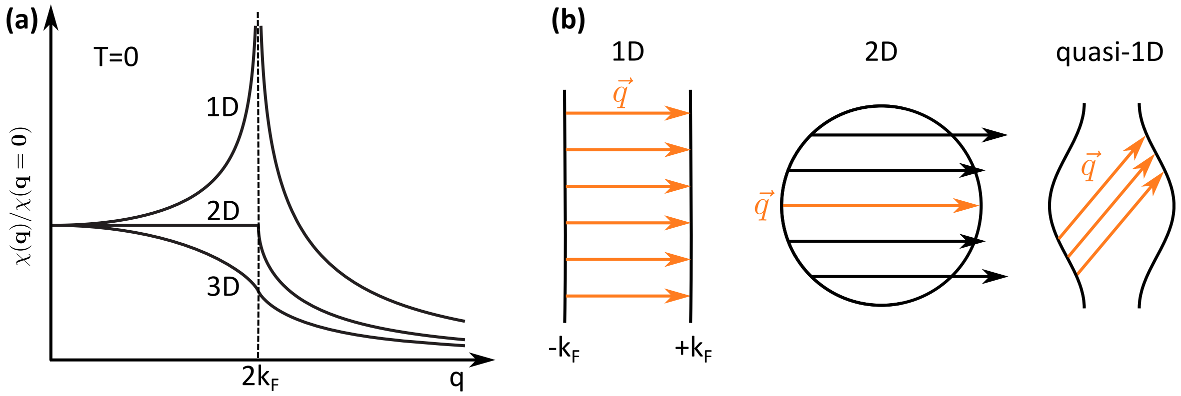

Figure 2.2: *(a) Static dielectric susceptibility for a 1D, 2D and 3D free electron gas. In 1D the static dielectric susceptibility diverges at the wave vector $q = 2k_F$. After [6]. (b) Fermi surface of 1D, 2D and quasi-1D free electron gas. Fermi surface nesting is indicated by the orange arrows which connect an empty and a filled state separated by $q = 2k_F$. After [6].*

2.1.3 The Kohn Anomaly and Temperature Dependence

The essential role of electron-phonon coupling suggests that not only the charge distribution but also the phonon dispersion will be modified. Assuming a half-filled cosine band $E(k) = -E_F \cos(ka)$ (ideal 1D case), results in the following temperature dependence of the static dielectric susceptibility at $q_0 = 2k_F$ [46,48]:

$$\chi(2k_F, T) = \frac{1}{2}n(E_F)\ln\left(\frac{2.28E_F}{k_BT}\right) \tag{2.8}$$

with $n(E_F)$ being the density of states at the Fermi level. If E_F/k_BT is large, $\chi(2k_F, T)$ diverges at low temperatures and leads to a strong renormalization of the phonon frequency ω_q, known as the Kohn anomaly:

$$\omega^2_{ren,q} = \omega^2_q\left(1 - \frac{4g^2_q}{\hbar\omega_q}\chi(q)\right). \tag{2.9}$$

As discussed above, $\chi(q)$ diverges for $q_0 = 2k_F$ and, thus, the softening of the phonon frequency will be most pronounced at this wave vector. Combining Eq. 2.9 and Eq. 2.8 reveals that ω_{ren,q_0} becomes zero at the finite transition temperature T_{CDW} if

$$k_BT_{CDW} = 2.28E_F \cdot e^{(-\frac{1}{\lambda})} \tag{2.10}$$

with λ being the dimensionless electron-phonon coupling constant $\lambda = \frac{2{g_0}^2n(E_F)}{\hbar\omega_0} = g'n(E_F)$. This complete softening of the phonon mode q_0 corresponds to a static, "frozen-in" lattice distortion at and below T_{CDW}. In addition, a band gap opens at the boundary of the new Brillouin zone (BZ), i.e. at $\pm k_F$. The gap size Δ given by

$$\Delta = u_{q_0}g_{q_0}\sqrt{\frac{2M\omega_{q_0}}{\hbar}} \tag{2.11}$$

depends on the displacement amplitude u_{q_0}, the electron-phonon coupling constant g_{q_0}, and the phonon frequency ω_{q_0} [46]. A close inspection of the total energy change $\delta E_{band} + \delta E_{lattice}$ leads to the Bardeen-Cooper-Schrieffer (BCS) relation between the zero-temperature energy gap and the transition temperature obtained by the mean field approach [6]:

$$2\Delta(0) = 3.52k_BT_{CDW}. \tag{2.12}$$

2.1.4 The Simple Peierls Picture in Real-World Systems

Although the model presented above yields many quantitative results, the simplicity of the model per se as well as the assumptions made during its derivation entail various limitations of the simple Peierls picture. These have to be considered when analyzing experimental results obtained from real-world systems.

I) **Thermal Fluctuations:**

In a strictly 1D system, thermal fluctuations suppress long range order preventing the development of a CDW ground state at finite temperatures [6,7]. In fact, the formation of a long range ordered ground state at a finite transition temperature T_{CDW} in the model presented above is an artifact of the mean field approximation, which ignores thermal fluctuations [6]. Therefore, a coupling to higher dimensions is actually essential to stabilize a CDW ground state in the presence of thermal fluctuations [6]. The resulting finite transition temperature, however, may then be significantly smaller than the mean field transition temperature [52].

II) **Deviations from Perfect Nesting:**

According to a seminal paper by Johannes and Mazin [53], even small deviations from perfect nesting significantly reduce the divergence of $\chi(\vec{q})$ at $2k_F$. In addition, the authors pointed out that the electronic energy gain δE_{band}, connected to the CDW transition, is in most cases achieved by lower lying filled states instead of states close to the Fermi level. Both findings contradict the important role of Fermi surface nesting implied by the basic Peierls model. Instead, their DFT studies prove that the CDW transitions observed in apparent prototypical Peierls systems like $NbSe_2$, $TaSe_2$, and $CeTe_3$ are structural transitions driven by the mutual interaction of the ionic lattice and the electronic system, i.e. by $\vec{q}$-dependent electron-phonon coupling [53]. Johannes and Mazin therefore concluded that "only a tiny fraction, if any, of the observed charge ordering phase transitions are true analogs of the Peierls instability" [53]. Instead, Ref. [54] suggests the following classification of CDWs:
Type 1: CDWs that have their origin in Fermi surface nesting. The lattice distortion is driven by the electronic perturbation and is a side effect.
Type 2: CDWs that are driven by electron-phonon coupling instead of Fermi surface nesting. The instability is caused by an interplay between the lattice and the electronic structure. There is a phonon mode q_0, which freezes out at T_{CDW}. Notably, a metal-insulator transition is not mandatory for such an instability [54]. Instead, the transition is driven by a strong $\vec{q}$-dependence of electron-phonon coupling constant as in the case of $NbSe_2$ [54, 55].
Type 3: CDWs that exhibit charge ordering with neither electron-phonon coupling nor Fermi surface nesting as the driving force.

III) **Role of Defects:**

Defects are an inevitable feature of real-world atomic wire systems. They can be caused by, for example, missing atoms in the surface reconstruction (see Sec. 5.9) or by adsorption of residual gas atoms (see Subsec. 5.2.2). The effects of impurities on the CDW formation comprises various aspects. Indeed, disorder in the lattice can blur the k-space distribution of the electronic states, which, in turn, attenuates the enhanced static dielectric susceptibility required for the instability [56]. As a consequence, the CDW transition will occur at lower temperatures as shown for $NbSe_3$ and TaS_3 [57–60].

Moreover, the potential of a charged impurity may destroy long range order [6]. Conversely, defects can act as nucleation centers [61] and locally stabilize the CDW ground state at $T > T_{CDW}$ [62]. A recent hyperscaling description revealed that a finite chain length, e.g., provided by a chain terminated by two defects, can induce a decay of the CDW amplitude [63]. In particular, the decay length τ of the CDW amplitude augments with increasing system size L. The CDW is fully developed if L is larger than the critical length L_C, which is a system-specific parameter [63].

2.2 Soliton Excitations

A soliton in general is a spatially localized wave (a solitary wave) which preserves its energy and shape when it moves [45]. It arises whenever nonlinear interactions and dispersion effects are precisely balanced. From a mathematical point of view, there are various completely integrable equations, which provide soliton solutions. Thus, it is not surprising that solitons can be found in many fields of physics. For example, it is reported that the first soliton was observed in the field of hydrodynamics in a water canal near Edinburgh in 1834, by John Scott Russel [64]. Today, solitons are utilized in optical fibers to transmit and store information [65] or in biology to describe the dynamics of proteins and DNA [45]. In solid state physics, the concept of solitons has been applied to analyze diverse phenomena such as ferroelectric domain walls, Bose-Einstein condensates, dislocations in crystals, and the charge transport in organic polymers [45]. The following section will take polyacetylene – a conducting polymer, but also a CDW system obeying the simple Peierls scenario – as a prototype example to introduce the basic properties of solitons in atomic wire arrays. This fundamental knowledge is of particular importance for the discussion in Secs. 6.3, 6.4, and 6.6. For a detailed overview of the physics of solitons in general see Ref. [45].

2.2.1 The Su-Schrieffer-Heeger Hamiltonian: Ground State Properties

The Su-Schrieffer-Heeger (SSH) model was originally developed to study the soliton formation in polyacetylene, the simplest conducting polymer. Polyacetylene is built by a chain of CH elements [see Fig. 2.3(a)]. Each carbon atom forms three σ-bonds and one π-bond. Since the π-electrons are delocalized along the chain, it can be considered an essentially (quasi)-1D system [66]. In addition, the π-band is half-filled, rendering polyacetlyene a prototypical Peierls system. Consequently, the polyacetylene ground state features insulating rather than metallic behavior and the lattice is subject to a PLD accompanied by a CDW as indicated by the alternating single and double bonds in Fig. 2.3(a). Such a dimerization can result in two distinct patterns, which are energetically degenerate and considered either A or B phase. The corresponding phases for a CDW with ×2 period are displayed in Fig. 2.3(b). In order to quantitatively analyze the physical properties of a such system, Su, Schrieffer, and Heeger

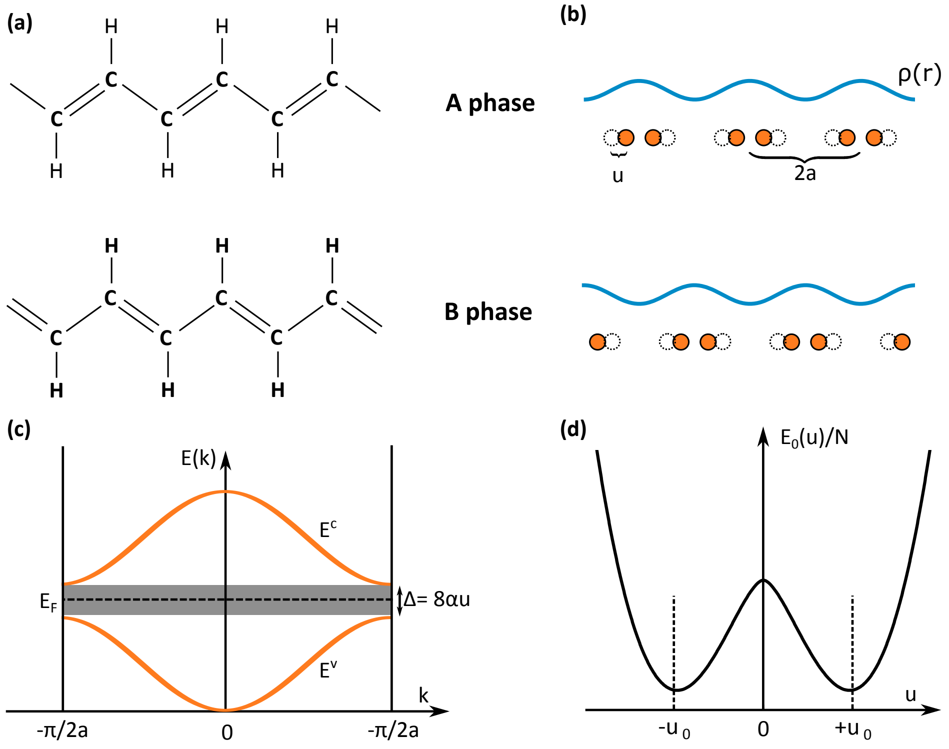

Figure 2.3: *(a) Two different phases (A and B) of trans-polyacetylene. (b) Two degenerate ground states of a CDW with ×2 periodicity. (c) Ground state electronic structure of the SSH model. The PLD results in a band gap at the new zone boundary $\pi/(2a)$. After [45]. (d) Ground state energy of the SSH model as a function of the displacement u from the equilibrium atom positions of the undimerized system according to Eq. 2.15. The characteristic double-well shape shows two minima at $u = \pm u_0$, which correspond to the two degenerate phases A ($+u_0$) and B ($-u_0$).*

proposed the following model Hamiltonian [67]:

$$\begin{aligned} H_{SSH} &= H_\sigma + H_\pi \\ &= \underbrace{\sum_n \frac{1}{2} K (u_{n+1} - u_n)^2}_{H_\sigma} + \underbrace{\sum_{n,s} t_{n+1,n} (c^\dagger_{n+1,s} c_{n,s} + c^\dagger_{n,s} c_{n+1,s})}_{H_\pi} . \end{aligned} \tag{2.13}$$

It consists of two parts, namely, H_σ, which describes the dynamics of the carbon atoms linked with σ-bonds, and H_π, which represents the π-electrons in this tight binding model [45,66]. Of note, the on-site energy E_0 has been chosen to be the origin of the energy axis, i.e. $E_0 = 0$, and a kinetic energy term has been omitted, assuming the ground state to be static [45]. In Eq. 2.13, K denotes the spring constant between the n-th and the $(n+1)$-th site and u_n is the displacement of the nth site from the undimerized equilibrium position. $c_{n,s}$ and $c^\dagger_{n,s}$ are the creation and annihilation operators of an electron on site n with spin $s = \pm 1/2$. $t_{n+1,n}$ is the nearest-neighbor hopping integral, which depends on the distance between adjacent sites: $t_{n+1,n} = t_0 - \alpha(u_{n+1} - u_n)$ with t_0 being the equilibrium hopping integral and α a positive constant. The following section will discuss the ground state properties of the SSH model. For a detailed derivation of the model refer to Refs. [67, 68].

The corresponding eigenvalues are $E_k^v = -\sqrt{4t_0^2\cos^2(ka) + 16\alpha^2u^2\sin^2(ka)}$ for the valance band and $E_k^c = -E_k^v$ for the conduction band. At the zone boundary, a gap opens with the size of $\Delta = 8\alpha u$ as illustrated in Fig. 2.3(c). The physical mechanism leading to the gapped, dimerized ground state is the Peierls scenario described in Sec. 2.1. The total energy $E_0(u)$ of the ground state is given by the energy cost of the σ-bond distortion and the sum of the occupied valance band energies E_k^v [68]:

$$\begin{aligned} E_0(u) &= 2KNu^2 + 2\sum_n E_k^v \\ &= 2KNu^2 - 2\sum_n \sqrt{4t_0^2\cos^2(ka) + 16\alpha^2u^2\sin^2(ka)} \end{aligned} \tag{2.14}$$

with N being the number of sites. For large N the sum turns into an integral. Introducing $z = 2\alpha u/t_0$ as well as the elliptic integral $E(1-z^2) = \int_0^{\pi/2}[1-(1-z^2)\sin^2(ka)]^{1/2}dk$ expanded around $z = 0$ leads to [68]

$$E_0(u) \cong N\left(\frac{Kt_0^2}{2\alpha^2}z^2 - \frac{4t_0}{\pi}\left[1 + \frac{1}{2}\left(\ln(\frac{4}{z}) - \frac{1}{2}\right)z^2\right]\right). \tag{2.15}$$

$E_0(u)/N$ is plotted in Fig. 2.3(d). Its double-well shape shows that the undimerized state ($z = 0$) is unstable. Instead, the ground state of the SSH model is dimerized. The total energy per site has minima for a displacement from the equilibrium position of $\pm u_0$. $+u_0$ and $-u_0$ correspond to the two degenerate phases A and B. Typical parameter values for polyacetylene are $u_0 \approx \pm 0.04$ Å [66].

2.2.2 Soliton Excitations of the SSH Model

Since the ground state of the SSH model is twofold-degenerate it provides nonlinear excitations, i.e. solitons, which manifest as moving domain walls separating the two phases A and B [66]. These excitations are topologically protected as shown in detail in Ref. [69]. In particular, such solitons are the zero-dimensional edge states, localized at the interface between the two topologically distinct phases A and B [69].

In order to gain quantitative information about the solitons, the following method is applied: First, an order parameter ϕ_n is defined, which is equal to $-u_0$ for the A phase and $+u_0$ for the B phase. Second, assume a long chain with $+u_0$ (A phase) for $n \to \infty$ and $-u_0$ (B phase) for $n \to -\infty$. Around the center of the system ($n_0 = 0$), a region is defined where the hopping is set to zero and replaced by a perturbation V. The Hamiltonian of such a system can be written as $H = H_0 + V$ where H_0 is the Hamiltonian of the respective perfectly dimerized A and B phases, with the hopping integral pinned to zero in the boundary region between A and B phase, i.e where the soliton is localized [68]. In order to minimize the total energy, a domain wall will form around n_0 separating the two phase A and B. Numerical calculations reveal that the soliton has the form

$$\phi_n \cong u_0 \tanh[(n - n_0)a/\xi] \tag{2.16}$$

and extends over several unit cells (width $\xi \approx 7a$ for typical polyacetylene parameters) [66,68]. The formation energy of a soliton is found to be $E_s = 0.42\,\text{eV}$, which is smaller than half of the single particle band gap ($\Delta = 1.4\,\text{eV}$) [68]. Thus, a soliton is the lowest lying excitation in polyacetlyene. Moreover, E_s varies only slightly between the lattice sites ($\approx 0.002\,\text{eV}$), implying that the solitons are *highly mobile* even at low temperatures [68]. The electronic spectrum in the presence of a soliton features a state at $E_0 = 0$, i.e. in the middle of the gap, considered a *mid-gap state* [68]. The mid-gap state is formed by states from the conduction as well as the valence band, each providing one-half of a state per spin [68]. As a consequence, the mid-gap state is occupied by one electron that has an unpaired spin. This quasi-particle is considered a neutral soliton (the total number of electrons is conserved) and features an *unusual spin-charge* relation of $(s, q) = (1/2, 0)$. Doping of one electron or one hole to the system leads to double or zero occupation of the mid-gap state, i.e. to charged solitons with $(s, q) = (0, \pm e)$. Notably, the formation of one single soliton would violate Kramer's theorem, which states that the total number of electrons determines the total spin of the system [68]. In particular, the spin of a system with an even number of electrons is an integer, while the spin of a system with an odd number of electrons has to be half an odd integer. Since the formation of a neutral soliton conserves the total number of electrons but has spin 1/2, a second soliton – an antisoliton – must compensate the 1/2 spin [68]. That is why solitons can only be *created in pairs.*

3 Methods for Surface Analysis

3.1 Scanning Tunneling Microscopy and Spectroscopy

In 1981, Gerd Binning and Heinrich Rohrer invented the STM, which was awarded with the Nobel price in physics only five years later [70]. Since then, STM has become one of the most powerful techniques in surface science. Its spatial resolution enables studying of the topography as well as of the local electronic properties of a surface on the atomic scale.

The following section will summarize the basic principles and theoretical concepts of STM and is primarily based on the books by R. Wiesendanger [71], C. Bai [72] and C. J. Chen [69]. In addition, this section will focus on issues relevant for the understanding and interpretation of the experimental results obtained by this method.

3.1.1 Fundamental Working Principles

Tunneling Effect – STM is based on the quantum mechanical tunneling effect. It implies that there is a finite probability that a particle – an electron, for example – can traverse a potential barrier even if its energy E is smaller than the barrier height V_0. This can not be understood in the framework of classical physics but requires a quantum mechanical description of the electron with both wave-like and particle-like properties (wave-particle duality). Assuming a one-dimensional rectangular potential barrier results in a probability P that the electron can "tunnel" through this barrier which is given by [71]

$$P \propto e^{-2\kappa d} \quad \text{with the decay rate of the wave function} \quad \kappa = \frac{\sqrt{2m(V_0 - E)}}{\hbar}. \tag{3.1}$$

m is the mass of the electron and d the width of the barrier. In a scanning tunneling microscope, one utilizes the tunneling effect by placing a metallic tip in close distance to the sample surface (typically 5-10 Å [73]). Consequently, electrons can tunnel between the tip and sample (wave functions overlap). Although the tunneling process in an STM experiment should actually be described by a three-dimensional tunneling barrier [71], one can infer some fundamental features of STM from the simplified 1D model introduced above. Since the tunneling probability depends exponentially on the barrier width, i.e. the tip-sample distance d, small changes in d lead to a tremendous change of the tunneling probability. For example, a

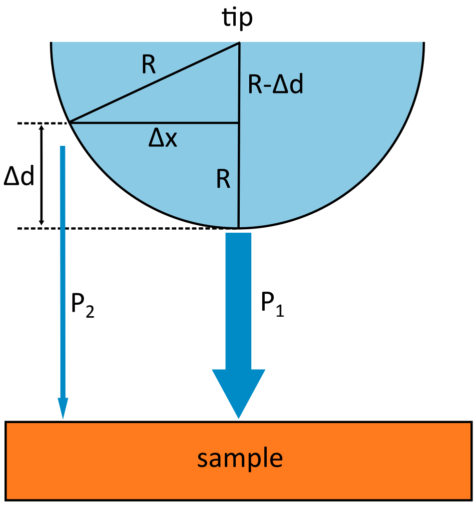

Figure 3.1: *Estimation of the lateral STM resolution limit according to Ref. [74]. The tunneling tip is modeled by a sphere with radius R, which is in close distance to the sample surface. The tunneling probability between tip and sample is highest at the position of the tip center, i.e., at the point of the tip closest to the surface. For points Δx away from the tip center, the tunneling probability decreases exponentially, which allows for a rough estimate of the lateral resolution limit of STM as described in more detail in the text.*

change by $\Delta d = d_2 - d_1 = 1\,\text{Å}$ results in a change of P by about one order of magnitude:

$$\frac{P_1}{P_2} = \frac{e^{-2\kappa d_1}}{e^{-2\kappa d_2}} = e^{2\kappa \Delta d} \approx 10. \tag{3.2}$$

For this approximate calculation, the barrier height V_0 was set to 5 eV, a typical value for the work function of a metal [69]. This does not only explain the high sensitivity of an STM in the vertical direction but also the atomic resolution in the lateral direction, which can be illustrated by a simple estimation inspired by Binning and Rohrer [74]: Assume a tip with an apex radius R which is in close vicinity to the sample surface (Fig. 3.1). The tip-sample distance at a point Δx away from the tip center is given by $\Delta x = \sqrt{R^2 - (R - \Delta d)^2} \approx \sqrt{2R \cdot \Delta d}$. The simple estimate based on this geometrical consideration reveals that the transmission probability is reduced by about one order of magnitude for $\Delta x = 4.5\,\text{Å}$ $(P_1 = e^{-2} \cdot P_2$ with $\kappa = 1\,\text{Å}^{-1}$, and $R = 10\,\text{Å})$. The diameter $2\Delta x = 9\,\text{Å}$ of such a tunneling probability cylinder is a reasonable estimate for the lateral resolution limit. However, lateral resolution achieved by today's STM apparatuses is significantly higher. This can only be explained by a more complex description of the tunneling process originally developed by Bardeen and finally applied by Tersoff and Hamann to the tunneling process in an STM setup.

Modes of Operation and Image Acquisition – The basic setup of an STM is shown in Fig. 3.2(a). A piezoelectric drive (z-piezo drive) approaches the tunneling tip in close distance (a few Å) to the sample surface. The bias U applied between the sample and tip leads to a net tunneling current that is first amplified and then detected by the control unit. When a certain set-point current is reached, the tip approach is stopped and the tip is scanned across the sample line by line. This inherently results in a fast scan direction along the lines [x direction in Fig. 3.2(a)] and a slow scan direction perpendicular to them [line feed direction and y direction in Fig. 3.2(a)]. A detailed understanding of this scanning procedure will be of particular importance to comprehend the STM images presented in Sec. 6.3. During the tip approach as well as during the scanning procedure, the elongation of the z-piezo is controlled by a feedback loop. The most common operation mode of an STM is the *constant current mode*, which is illustrated in Fig. 3.2(b).

Thereby, the tip-sample distance is permanently adjusted by the control unit via the z-piezo drive in order to keep the tunneling current constant while scanning the surface. The respective z-piezo elongation is detected at each point (pixel) and can be displayed as a false-color plot [see computer screen in Fig. 3.2(a) for an example constant current STM image]. As a consequence of this continuous readjustment, the scanned tip will follow the sample contour which may be determined by steps, depressions and protrusions [see A in Fig. 3.2(b)]. However, areas with different electronic properties may also influence the tunneling current and, thus, the elongation of the z-piezo [see light orange atoms at B in Fig. 3.2(b)]. In this case, the line profile corresponds to contours of constant DOS rather than to the topography of the surface. Therefore, constant current STM images always contain both structural and electronic properties. This will be important for the interpretation of the STM images shown in this thesis. All images presented in this document are taken in constant current mode.

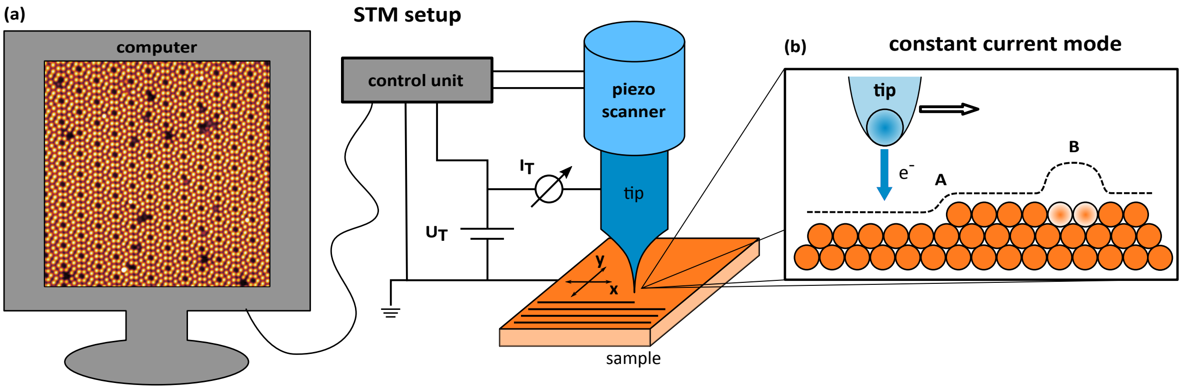

Figure 3.2: *Basic working principle of an STM. (a) STM setup: Piezo drives enable a tip movement in all the spatial directions. The tunneling bias U_T applied between tip and surface results in a net tunneling current I_T which is detected by the control unit. A feedback loop is utilized to control the displacement of the z-piezo, which is then recorded and displayed in a false color image on the computer screen. Computer screen: Constant current STM image of the Si(111)-(7×7) surface. (b) Constant current mode of operation. Following [74].*

3.1.2 Theoretical Description of the Tunneling Current

In 1961 – long before Binning and Rohrer built the first scanning tunneling microscope – Bardeen described the tunneling between two metals separated by a thin oxide film with a transfer Hamiltonian approach based on a time-dependent, perturbative treatment of the tunneling process [75]. Tersoff and Hamann applied this formalism to the tunneling process between a tip and a surface [76, 77]. Their description includes several simplifications such as a specific geometry and wave function of the tip. These result in some limitations to the model. For example, it cannot explain the $\approx 1\,\text{Å}$ resolution [69] achieved in some of the STM images presented in this thesis. This can only be understood in terms of a convolution between certain tip and sample electronic states as will be discussed at the end of this section. Nevertheless, the model of Tersoff and Hamann successfully captures the basic physics of the STM tunneling process and will thus be presented here following Refs. [76, 77] and the book of R. Wiesendanger [71]. Accordingly, the tunneling current for a sample bias voltage U is given by

$$I_T = \frac{2\pi e}{\hbar} \sum_{\mu,\nu} \left\{ \underbrace{f(E_\mu)[1 - f(E_\nu + eU)]}_{A} - \underbrace{f(E_\nu + eU)[1 - f(E_\mu)]}_{B} \right\} \cdot |M_{\mu\nu}|^2 \, \delta(E_\nu - E_\mu), \tag{3.3}$$

where $f(E)$ represents the Fermi function and, thus, term A (B) of Eq. 3.3 describes tunneling from the tip (sample) to the sample (tip). The delta function δ guarantees energy conservation, i.e only elastic tunneling is allowed. $M_{\mu\nu}$ is the tunneling matrix element between an unperturbed electronic state of the tip ψ_μ with energy E_μ and an unperturbed electronic state of the sample ψ_ν with energy E_ν. Assuming very low temperatures, i.e. the Fermi function to be a step function, as well as small bias values (U< k_BT) [78] leads to

$$I_T = \frac{2\pi}{\hbar} e^2 U \sum_{\mu,\nu} |M_{\mu\nu}|^2 \, \delta(E_\mu - E_F) \cdot \delta(E_\nu - E_F), \tag{3.4}$$

where E_F represents the Fermi energy. The crucial part of Eq. 3.4 is the tunneling matrix element $M_{\mu\nu}$, which according to Ref. [75] can be written as

$$M_{\mu\nu} = \frac{-\hbar^2}{2m} \int d\vec{S} \cdot \underbrace{(\psi_\mu^* \vec{\nabla} \psi_\nu - \psi_\nu^* \vec{\nabla} \psi_\mu)}. \tag{3.5}$$

The integral runs over any arbitrary surface that lies completely within the tunneling barrier region. The term in brackets is a quantum mechanical current density. Since the tip wave function is generally unknown, one needs to make an assumption in order to evaluate M. The simplest approach is a mathematical point source of current.

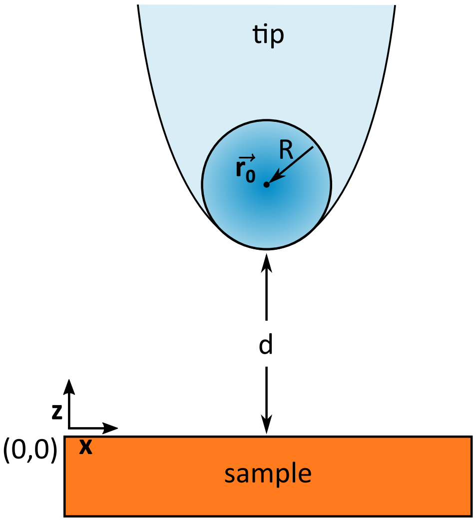

Figure 3.3: *Geometry of the tunneling model introduced by Tersoff and Hamann [77]. The tip is of arbitrary shape but has a spherical apex with radius R and s-orbital wave function. The center of the sphere is defined by $\vec{r_0}$ and d represents the distance between the tip and sample. After [77].*

Point Source Tip – Assuming the tunneling tip as a point probe represents an ideal STM experiment where the influence of the complex tip-sample system is neglected. For this case, the tunneling matrix element M is proportional to the amplitude of the sample wave function at the position $\vec{r_0}$ defined by the position of the tip [77]:

$$I_T \propto \sum_{\nu} |\psi_\nu(\vec{r_0})|^2 \, \delta(E_\nu - E_F) = n_s(E_F, \vec{r_0}). \tag{3.6}$$

Consequently, the tunneling current represents the DOS $n_s(E_F, \vec{r_0})$ of the sample at E_F and $\vec{r_0}$. A constant current STM image thus reflects the sample's local density of states (LDOS) rather than its atomic structure. This is key to understanding why the structural models developed in the framework of this thesis cannot solely be constructed on the basis of STM images, but also require DFT simulations (see Sec. 3.4 and Chapt. 5).

S-Wave Tip – A more realistic model was introduced by Tersoff and Hamann in 1985 in Ref. [77]. Here, the tip is assumed to be a locally spherical potential well with radius R. Its center is located at $\vec{r_0}$. d defines the distance between the tip and sample, as sketched in Fig. 3.3. Assuming an s-orbital wave function for the tip-apex, i.e. all the angular momentum of the tip wave function is neglected, the following expression for the tunneling current results [77]:

$$I_T \propto U \cdot n_t(E_F) \cdot e^{2\kappa R} \cdot \sum_{\nu} |\psi_\nu(\vec{r_0})|^2 \, \delta(E_\nu - E_F), \tag{3.7}$$

where $n_t(E_F)$ is the tip's DOS at the Fermi level. This agrees with the result for the point source tip. Indeed, the tunneling current remains proportional to the DOS of the sample at the position defined by the tip $[I_T \propto \sum_\nu |\psi_\nu(\vec{r_0})|^2 \, \delta(E_\nu - E_F) = n_s(E_F, \vec{r_0})]$. Moreover, the wave function decays exponentially in the z direction ($\psi_\nu \propto e^{-\kappa z}$). Thus,

$$|\psi_\nu(\vec{r_0})|^2 \propto e^{-2\kappa(d+R)} \tag{3.8}$$

and

$$I_T \propto e^{-2\kappa d}. \tag{3.9}$$

The tunneling current depends exponentially on the distance d between the tip and sample. In this sense, the Tersoff-Hamann approach leads to the same result as achieved for a 1D rectangular barrier in Subsec. 3.1.1.

However, the approach of a spherical tunneling tip with s-orbital character results in a lateral resolution limit of 6 Å [76, 79]. Although this value was first confirmed experimentally [76], today's STM experiments often exceed this limit (see e.g. [80–82] or Sec. 6.2). Apart from this, all STM data presented in this thesis have been recorded with commonly used tungsten (W) or platinum-iridium (PtIr) tunneling tips, which both have a 5d-state at the Fermi level [79]. In particular, calculations for a small pyramidal W cluster reveal a strongly localized d_z^2-state near the Fermi level [83]. The lobe-shape charge distribution of the d_z^2 dangling bond yields a much stronger overlap with the s-orbitals of the sample than can be achieved by an s-wave tip. As a consequence, the corrugation Δz measured by a d_z^2-orbital tip is more distinct compared to that measured by a s-orbital tip (see Fig. 3.4) and, therefore, can lead to STM images with increased lateral resolution [69]. In cases where the sample comprises lobe-shape orbitals, such as the Si dangling bonds studied in this thesis, the corrugation of the STM scan is even more ridged [see Fig. 3.4(c)].

High Bias Values – As elaborated above, the Tersoff-Hamann approximation is restricted to small bias values U. However, the atomic wires studied in this thesis are grown on semiconducting substrates (Si, Ge) and, therefore, require finite tunneling bias values. In particular, the extensively studied dangling bond state of the Si spin chains lies $\approx$ 0.5 eV above the Fermi level (see for example Sec. 5.4).

The following section discusses the effect of finite bias values on the tunneling current. Since an exact treatment of the high bias scenario is challenging, it is assumed that a finite bias does not affect the tip and sample wave functions ψ_μ and ψ_ν or their respective energy eigenvalues E_μ and E_ν. In fact, it shifts the sample DOS relative to tip DOS by the energy eU [71]:

$$I_T \propto \int_0^{eU} n_t(\pm eU \mp E) \cdot n_s(E, \vec{r_0}) dE, \tag{3.10}$$

where $n_s(E, \vec{r_0})$ is the DOS of the sample at $\vec{r_0}$, i.e. at the center of the tip, and $n_t(E)$ the DOS of the tip at energy E. All energies are given with respect to E_F. Depending on the polarity of the applied bias, the tunneling current is composed of electrons tunneling from

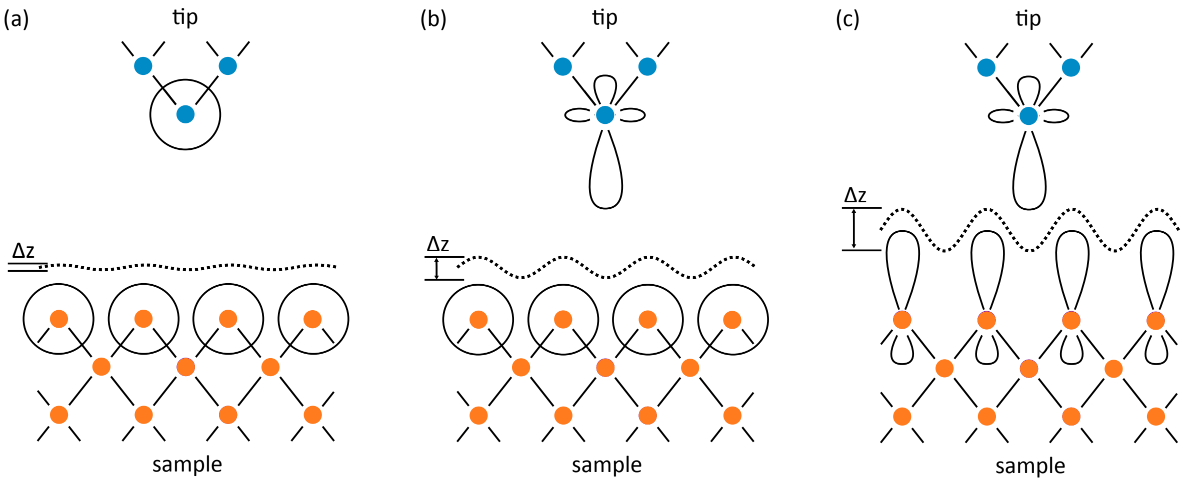

Figure 3.4: *Corrugation of a constant current STM scan for different tip and sample electronic states. (a) An s-wave tip scans a metal surface (s-orbitals). The STM line scan provides the superposition of the respective charge densities, and is only slightly corrugated. (b) The STM tip provides a* d_z^2*-state which is typically the case for W or PtIr tunneling tips. The overlap of s- and* d_z^2*-orbitals results in a stronger corrugated STM image compared to (a). (c) Sample which provides* sp^3*-orbitals (e.g. a silicon surface) is scanned by a* d_z^2*-tip. The STM contour shows the strongest corrugation. After [79] and [84].*

the occupied states of the tip to the unoccupied states of the sample ($U > 0\,\text{V}$) or from the occupied states of the sample to the unoccupied tip states ($U < 0\,\text{V}$) as depicted in Fig. 3.5. The contribution of n_s which is influenced by the tip-sample distance can be separated:

$$I_T \propto \int_0^{eU} n_t(\pm eU \mp E) \cdot n_s(E) \cdot T(E, eU) dE, \tag{3.11}$$

where $T(E, eU)$ can be written within the Wenzel-Kramers-Brillouin (WKB) approximation as [71]

$$T(E, eU) = exp\left(-2(d+R)\left[\frac{2m}{\hbar^2}\left(\frac{\phi_t+\phi_s}{2}+\frac{eU}{2}-E\right)\right]^{1/2}\right). \tag{3.12}$$

The decay rate κ introduced in Eq. 3.1 now depends on the work function of the tip (ϕ_t) and the sample (ϕ_s), the applied tunneling bias U, as well as on the total energy E. A close inspection of Eq. 3.12 reveals that the transmission coefficient $T(E, eU)$ is largest at $E = eU$ in case $U > 0\,\text{V}$. In case $U < 0\,\text{V}$, the largest value for $T(E, eU)$ is obtained at $E = 0 = E_F$. The tunneling process is visualized in Fig. 3.5 assuming a constant tip DOS. The length of the black arrows represents the energy dependence of the transmission probability. For $U > 0$, electrons tunnel from occupied tip states to empty sample states, thus, probing the unoccupied DOS of the sample. Since the tunneling current is dominated by electrons tunneling from states near E_F of the tip, a proper choice of the tunneling bias allows to selectively probe the sample DOS at different energies. Access to the occupied states of the sample can be achieved by applying a bias $U < 0$. However, the leading edge of the tunneling current is

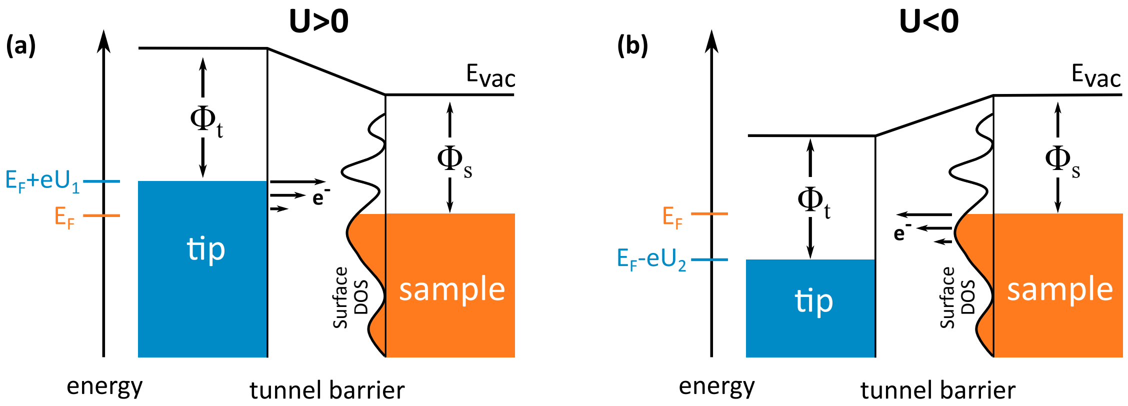

Figure 3.5: *Energy level diagram of the STM tunneling process for both tunneling bias polarities. The tip DOS is assumed to be constant and the length of the black arrows represent the energy dependence of the transmission coefficient. The sample is grounded in both cases. (a) For a negative potential at the tip ($U>0$ V), the unoccupied states of the surface DOS are probed. (b) For a positive potential at tip ($U<0$ V), STM is sensitive to the occupied states of the surface. After [85].*

always dominated by states near E_F of the sample. Thus, it is much easier to inspect the empty sample states rather than the filled states by changing the magnitude of tunneling bias. This fundamental difference will be important for the interpretation of the bias dependent STM images presented in Secs. 5.4, 5.7, 6.2, and 6.5.

3.1.3 Scanning Tunneling Spectroscopy

The previous sections demonstrated that constant current STM images usually display a convolution of topographic and electronic information of the sample, and that both aspects are often difficult to separate. A possible solution to overcome this issue is provided by STS, which allows for a more direct access to the sample DOS. The derivative of Eq. 3.11 leads to [85]

$$\frac{dI}{dU}(U) \propto e n_t(0) \cdot n_s(eU) \cdot T(eU, eU) + \int_0^{eU} n_s(E) \cdot n_t(\pm eU \mp E) \frac{dT(E, eU)}{dU} dE. \tag{3.13}$$

The tip DOS was assumed to be constant ($\frac{dn_t}{dU} = 0$). Neglecting the voltage dependence of the transmission coefficient $T(E, eU)$, which is responsible for the second term in Eq. 3.13, the differential conductivity dI/dU is directly proportional to the LDOS of the sample:

$$\frac{dI}{dU} \propto n_s(eU) \tag{3.14}$$

Experimentally, dI/dU and, therefore, information about the sample LDOS, can be obtained in two technically distinct ways. One possibility is to record the tunneling current as a function of the tunneling bias [I(U) curve] at a fixed sample location. Before the bias voltage is ramped, the tip-sample distance is determined by a set-point current I_{set} and a set-point bias U_{set}. During the I(U) curve acquisition, the feedback loop is turned off and the tip-sample distance stays constant. The numerical derivative of the I(U) spectrum then provides information about the sample LDOS at the respective location. However, typical I(U) curves contain too much noise to obtain a reasonable result by calculating dI/dU from a single I(U) curve. Therefore, averaging over a large number of spectra is often required. A means to overcome this issue is to measure dI/dU directly with a lock-in amplifier.

The Lock-In Technique – The basic principle of the lock-in technique is illustrated in Fig. 3.6. A small sinusoidal modulation bias $U_{mod}(t) = U_{mod}\sin(\omega_0 t)$, provided by a frequency generator, is added to the fixed tunneling bias U_T. The frequency of the modulation bias ω_0 is chosen such that it is higher than the cut-off frequency of the feedback loop. This is done in order to avoid any influence of the modulation on the tip-sample distance. Such a modulation of the tunneling bias results in a modulated tunneling current I(U(t)). A first-order Taylor-series expansion around U_T leads to:

$$I(U(t)) = I(U_T + U_{mod}\sin(\omega_0 t)) \approx I(U_T) + \underbrace{\frac{dI(U_T)}{dU}U_{mod}}_{\Delta I} \cdot \cos(\omega_0 t). \tag{3.15}$$

The amplitude of the current modulation ΔI – which is proportional to dI/dU and, therefore, reflects the sample LDOS – is detected with a lock-in amplifier by comparing its frequency and phase with the original modulation. This procedure results in a much higher signal-to-noise ratio than obtained by numerically differentiated I(U) curves. The energy resolution of a STS experiment performed with the lock-in technique is – aside from thermal broadening and electrical noise – determined by the amplitude of the modulation bias U_{mod} as illustrated in Fig. 3.6. According to Ref. [86], the energy broadening due to the bias modulation can be estimated by

$$\Delta_{mod} = \sqrt{3}\sqrt{2}\, eU_{mod} = 2.45\, eU_{mod}. \tag{3.16}$$

Of note, U_{mod} is the root mean square of the modulation amplitude. The energy broadening due to finite temperatures, considered a smear out of the Fermi function, can be estimated by [86]

$$\Delta_{therm} = 3.5\, k_B T. \tag{3.17}$$

The overall energy resolution is

$$\Delta E = \sqrt{\Delta_{therm}^2 + \Delta_{mod}^2} = \sqrt{(3.5\, k_B T)^2 + (2.45\, eU_{mod})^2}. \tag{3.18}$$

A small modulation amplitude therefore increases the energy resolution, but decreases the overall signal-to-noise ratio. All STS data presented in this thesis were recorded with $U_{mod} = 10\,\text{meV}$, which was necessary to obtain a sufficiently high overall signal. Since all spec-

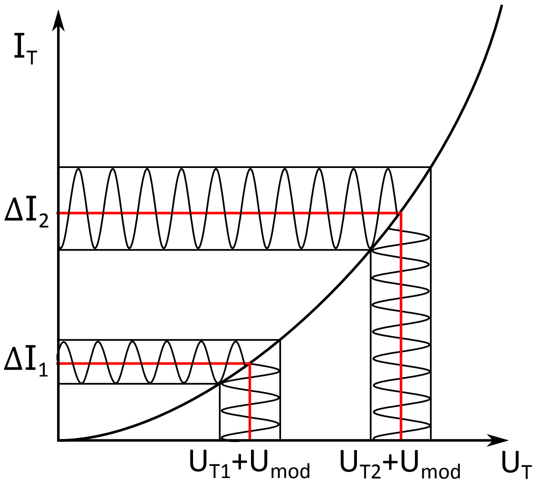

Figure 3.6: *Basic principle of the lock-in technique. The tunneling bias U_T is modulated by a small bias voltage U_{mod} with frequency ω_0. The resulting tunneling current modulation ΔI is detected. ΔI is proportional to differential conductivity dI/dU and, therefore, allows for a direct measure of the sample DOS. The signal ΔI_1 is smaller than ΔI_2 since the slope of the depicted I(U) curve at U_{T1} is smaller than at U_{T2}. After [87].*

troscopic measurements have been performed at a sample temperature of 77 K [i.e. $\Delta_{therm}(77\,\mathrm{K}) = 23\,\mathrm{meV}$], the modulation broadening does not significantly exceed the thermal broadening.

Grid Spectroscopy vs. dI/dU **Mapping** – Within this thesis, the lock-in technique described above has been be applied in two ways, namely as grid spectroscopy and dI/dU mapping. Grid spectroscopy combines the spatial resolution of constant current imaging with single spectra. However, the spectrum acquisition takes much longer than the scan time per pixel in a usual constant current image (about 10 s vs. 1-2 ms per pixel). Thus, a grid of pixels at which dI/dU spectra are measured is usually defined, as opposed to taking a spectrum at each pixel of the constant current image. This results in a reasonable measurement time, without limiting the spatial resolution of the simultaneously acquired constant current image. Although the spatial resolution of a grid spectroscopy may be limited, it contains the full spectroscopic information in the chosen energy range.

The second way the lock-in technique was applied was by scanning the surface with a fixed bias voltage. The obtained image provides the spatially resolved DOS at a fixed energy. These dI/dU maps can be recorded faster than grid maps and, therefore, often provide higher spatial resolution. However, dI/dU maps do not contain the full spectroscopic information and instead only show the LDOS at a fixed energy $E = eU$. Another important difference between grid spectroscopy and dI/dU mapping is their respective set-point, which determines the tip-sample distance during data acquisition. The set-point bias of dI/dU maps is necessarily given by the tunneling bias. Note that the absolute dI/dU signal does not only depend on the sample DOS but also on $T(E,U)$ (see Eq. 3.13), which, in turn, exponentially depends on the tip-sample distance d (Eq. 3.12). Thus, dI/dU maps have to be treated with care when interpreting them as the spatial dependence of the sample DOS at a given energy. For surfaces with strong spatial DOS variations, dI/dU maps may even show the opposite intensity relation than given by the sample LDOS [88]. In a grid spectroscopy, an arbitrary set-point can be selected, which then determines the tip-sample distance for the entire spectrum (with the feedback loop off). Here, a proper choice of the set-point prevents strong spatial deviations in the tip-sample distance d and, thus, provides more direct access to the spatial distribution of the sample DOS.

3.2 Low Energy Electron Diffraction

Starting from its discovery in 1927 by Davisson and Germer [89], diffraction of low-energy electrons developed into one of the most powerful techniques in surface science.

It can be applied to analyze the unit cell as well as the morphology of a surface and provides a quick and efficient control of sample preparation. More sophisticated applications like IV-LEED can provide detailed information about atomic positions within a unit cell [90]. All these variants of LEED are based on the wave nature of electrons [91]. The wave length $\lambda = \frac{h}{\sqrt{2m_e E_{kin}}}$ of low energy electrons – typical kinetic energy used in this thesis are $20-150\,\mathrm{eV}$ – is of a similar magnitude as atomic distances in solids ($\approx$ Å). Consequently, such electrons get diffracted at the atomic lattice creating a diffraction pattern which can be analyzed. The strong interaction of electrons with matter, for example, compared to x-rays, results in a high surface sensitivity. Fig. 3.7 displays the electron mean free path in a solid as a function of its kinetic energy [92]. The curve shows a minimum around $20-60\,\mathrm{eV}$, which is due to plasmon excitations [93]. Since the plasmon frequency depends on the electron density – a quantity which is roughly equal for all materials [93] – the curve does not show a significant material dependence and is therefore called *universal*. The mean free path in the energy range of interest is only several Å and limits the probing depth of LEED to 1-2 monolayer.

Depending on the information of interest, different theoretical descriptions of the diffraction process are available. In order to gain information about long range order, unit cell, and reconstruction of a surface, it is sufficient to describe the diffraction process by the geometrical theory [94]. Phenomena like spot intensity modulations in LEED patterns at a fixed electron energy can only be explained by the kinematic theory. Multiple scattering processes, which are neglected within the kinematic theory, are taken into account in the more complete but complex dynamic theory. The latter allows for determining atomic positions within a unit

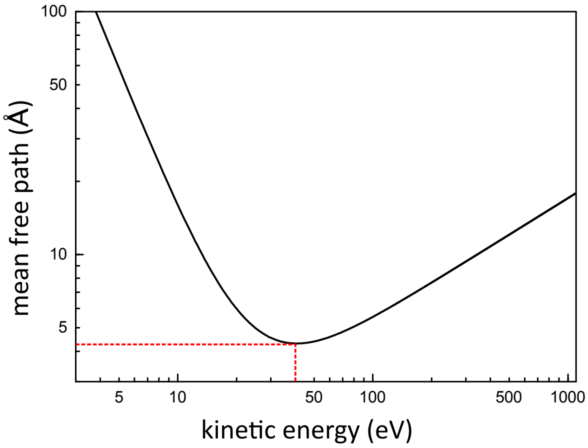

Figure 3.7: *Universal curve of electron mean free path in matter according to [92]. Low-energy electrons with E_{kin} = 20-150 eV have a mean free path of several Å explaining the high surface sensitivity of LEED and ARPES.*

cell from spot intensity modulations as a function of energy (IV-LEED) [94]. Within this thesis, LEED was primarily used to (1) check the preparation process of the stepped Si and Ge substrates, (2) optimize and – once a recipe has been established – quickly validate the atomic wire growth, and (3) identify the surface unit cell including temperature dependent superstructures. All these applications of LEED can be understood within the geometrical description that will be presented below.

3.2.1 Instrumentation

In this thesis, two different technical realizations of LEED have been used, namely, a conventional 3-grid LEED optics (Fig. 3.8) and a SPA-LEED. In both variants, electrons are emitted from a hot LaB_6 filament and focused by a Wehnelt cylinder. Afterwards, the electrons are accelerated (typically to 20-200 eV) and collimated by a lens system. Finally, the electrons leave the electron gun through a drift tube. In a conventional LEED setup, the drift tube and the sample are at the same potential such that the electrons pass through the field free space onto the sample. Typical beam diameters are 1 mm at the surface [94]. The diffracted electrons progress through three hemispherical concentric grids before they hit a fluorescent screen. The first grid is grounded to ensure the field free region between drift tube and sample. The second grid (supressor) lies on a negative potential slightly lower than the primary electron energy to filter inelastically scattered electrons. Subsequently, the electrons are accelerated by high voltage to a fluorescent screen, which displays the diffraction pattern. A third grid which is at the same potential as the second grid protects the second grid from

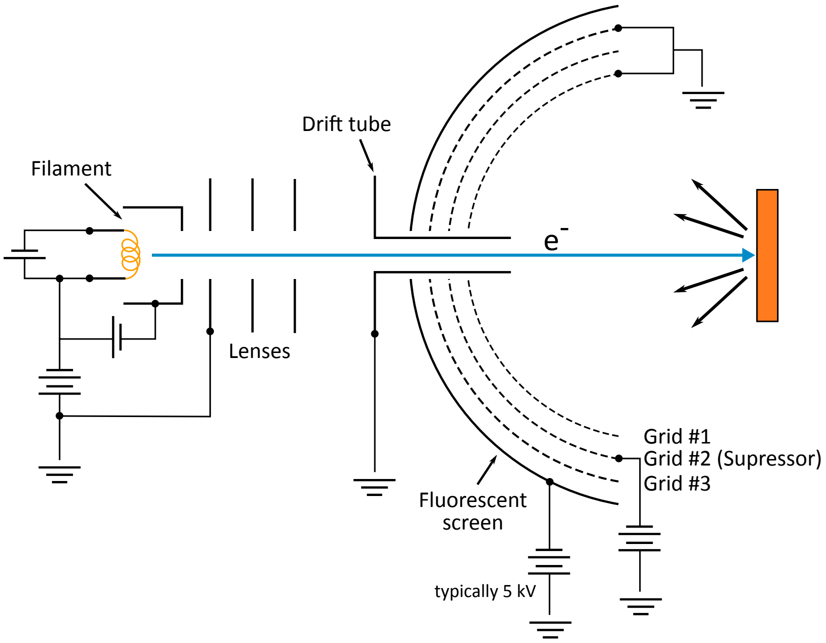

Figure 3.8: *Setup of a conventional 3-grid LEED optics. After [95].*

field distortions [94] by the screen high voltage. A digital camera mounted in a darkened box on the ex situ side of the LEED instrument is used to document the diffraction pattern displayed on the screen. In a SPA-LEED setup, the diffracted electrons are detected by a channeltron (instead of a fluorescent screen). The electron beam is guided by two sets of electrostatic deflection plates (octopoles) in order to vary the electron beam angle of incidence. The special arrangement of electron gun and channeltron position in combination with the two oppositely biased octopols plates results in a fixed angle between the incident electron beam and recorded diffracted electrons [90]. A variation of the incident angle therefore results in a special scanning mode in k-space [90]. For further details, refer to the excellent review from M. Horn-von Hoegen [90].

The SPA-LEED setup is superior to a conventional LEED since it allows for a close inspection of single diffraction spots as well as their profile analysis. This can provide information on sample properties like domain size, surface roughness, and defects [90]. Moreover, no spots [especially the (00) spot] are blocked by the electron gun and the beam can be scanned through k-space to obtain information about facet formation [90]. However, the acquisition time of a SPA-LEED image with reasonable resolution (typically several minutes) is much higher than for an "optical" LEED and can cause significant sample degradation as will be shown in Sec. 6.1.

Within this thesis a SPA-LEED has been used to obtain low temperature (10 K) LEED images of the Si(553)-Au surface (see Sec. 6.1). A detailed analysis of the surface morphology – in principle possible with a SPA-LEED – was not a focus of this work. The setup equipped with the standard LEED did not provide a cooling option to reach the temperatures of interest. Instead, it was used to study the wire growth and the unit cell of various Si/Ge-Au surfaces (cf. Secs. 4.2, 5.1, 5.2, and Appendix Secs. D and E).

3.2.2 Geometric Diffraction Theory

Electrons scattered elastically on a periodic lattice interfere constructively if they fulfill the Laue condition:

$$\vec{k} - \vec{k'} = \Delta\vec{k} = \vec{G} \quad \text{with} \quad \left|\vec{k}\right| = \left|\vec{k'}\right|. \tag{3.19}$$

To observe a spot on the screen, the difference between the wave vector of the incident electron $\vec{k}$ and that of the diffracted electron $\vec{k'}$ has to be a reciprocal lattice vector $\vec{G}$. For a three dimensional lattice, $\vec{G}$ can be expressed by a linear combination of the three reciprocal lattice vectors $\vec{b_1}$, $\vec{b_2}$ and $\vec{b_3}$:

$$\vec{G} = h\vec{b_1} + k\vec{b_2} + l\vec{b_3}, \tag{3.20}$$

with h, k, l being integer numbers. $\vec{b_1}$, $\vec{b_2}$ and $\vec{b_3}$ are related to the primitive basis vectors of the real space lattice $\vec{a_1}$, $\vec{a_2}$ and $\vec{a_3}$ as follows [96]:

$$\vec{b_1} = 2\pi \frac{\vec{a_2} \times \vec{a_3}}{\vec{a_1}(\vec{a_2} \times \vec{a_3})}, \qquad \vec{b_2} = 2\pi \frac{\vec{a_3} \times \vec{a_1}}{\vec{a_1}(\vec{a_2} \times \vec{a_3})}, \qquad \vec{b_3} = 2\pi \frac{\vec{a_1} \times \vec{a_2}}{\vec{a_1}(\vec{a_2} \times \vec{a_3})}. \tag{3.21}$$

Due to the low mean free path of low-energy electrons in solids one can assume that LEED in first approximation is only sensitive to the 2D lattice of the surface plane spanned by $\vec{a_1}$ and $\vec{a_2}$. As a consequence, $\vec{a_3}$ is infinitely large and the spacing between reciprocal lattice spots perpendicular to the surface becomes infinitely small.

A useful visualization of the Laue condition (Eq. 3.19) is the *Ewald construction*, which is shown for a conventional LEED experiment in Fig. 3.9. The Ewald construction for a SPA-LEED experiment looks slightly different (see e.g. Ref. [90]). The absence of any selection rule for $k_\perp$ is visualized by rods – so-called crystal truncation rods – at each reciprocal lattice vector of the surface. The radius of the Ewald sphere is set by the kinetic energy of the incoming electrons, i.e., by $\left|\vec{k}\right|$. The head of $\vec{k}$ has to touch a reciprocal lattice point and by convention is located on the surface plane [96]. The tail of $\vec{k}$ defines the center of the sphere. Every intersection of the Ewald sphere with a crystal truncation rod results in constructive interference and leads to an intensity spot on the screen. Hence, a LEED pattern presents an image of the reciprocal lattice of the surface. Fig. 3.9 displays a one-dimensional representation of the Ewald construction for a 2D lattice. The incoming electrons hit the sample perpendicular to the surface. A higher primary electron energy (dark blue circle) increases the radius of the Ewald sphere (light blue circle) as well as the number of scattering vectors which fulfill the Laue equation. Moreover, the scattering angle decreases. As a consequence, diffraction spots contract toward the (00) spot when increasing the primary electron energy. This effect was utilized to identify the (00) spot of various stepped surfaces (see Appendix Sec. B).

3.2.3 Diffraction Pattern of Stepped Surfaces

The atomic chain systems in focus of this thesis are grown via self-organization on stepped substrates. A long range step formation provides the basis for proper atomic wire growth. Thus, it is key to understand the LEED pattern given by a stepped surface. A stepped surface can be described by a convolution of a single terrace and a superlattice with periodicity L representing the step distance [see Fig. 3.10(a)] [97]. The Fourier transform of a single terrace of width $T = Na$ is given by the multi slit interference function

$$A(k) = \frac{sin^2(\frac{N}{2}ka)}{sin^2(\frac{1}{2}ka)} \tag{3.22}$$

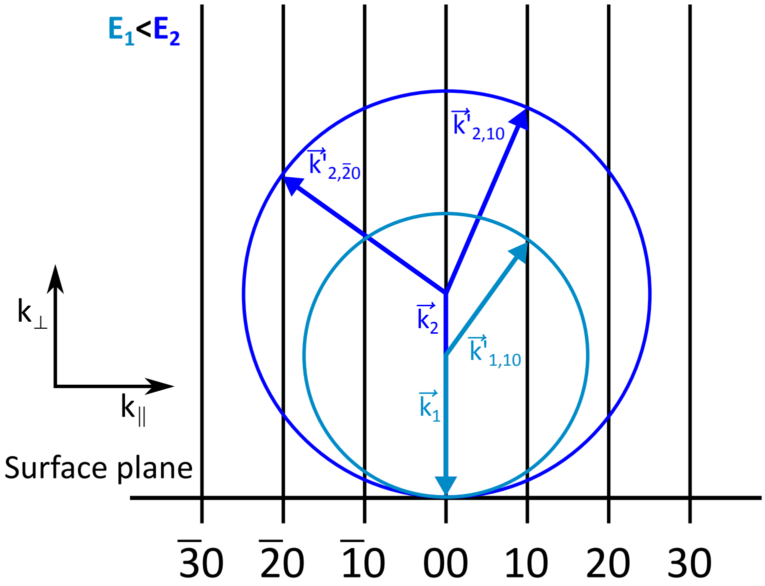

Figure 3.9: *1D representation of the Ewald construction for a 2D lattice and two different primary electron energies (dark and light blue circles). The primary electron beam is incident perpendicular to the surface. At each intersection of the Ewald sphere with a crystal truncation rod the Laue equation is fulfilled, and a diffraction spot may be observed on the screen. An increase of the primary electron energy increases the radius of the Ewald sphere and changes the orientation of the diffracted beams as exemplary indicated by* $\vec{k}'_{1,10}$ *and* $\vec{k}'_{2,10}$*. Moreover, the number of intersections with the rods increases and more spots occur on the screen (see e.g.* $\vec{k}'_{2,\bar{2}0}$*).*

with N being an integer and a the lattice constant of the terrace as pictured in Fig. 3.10(b). The Fourier transform of the superlattice is an array of rods separated by $\Delta k = 2\pi/L$. According to the convolution theorem, the Fourier transform of the stepped surface is given by multiplying the Fourier transform of the superlattice $\mathcal{F}(f_{sl})$ with the Fourier transform of the terrace $\mathcal{F}(f_{ter})$ as illustrated in 3.10(c). It is important to note that the stepped surface is now rotated such that the plane defined by the superlattice is oriented perpendicular to the incident electron beam. The rods of the fundamental terrace spots intersect the Ewald sphere several times. As a consequence, fundamental spots separate into subspots with a splitting proportional to the inverse terrace distance $1/L$. The number of subspots visible on the screen depends on the primary electron energy as illustrated by the Ewald construction in Fig. 3.10(c).

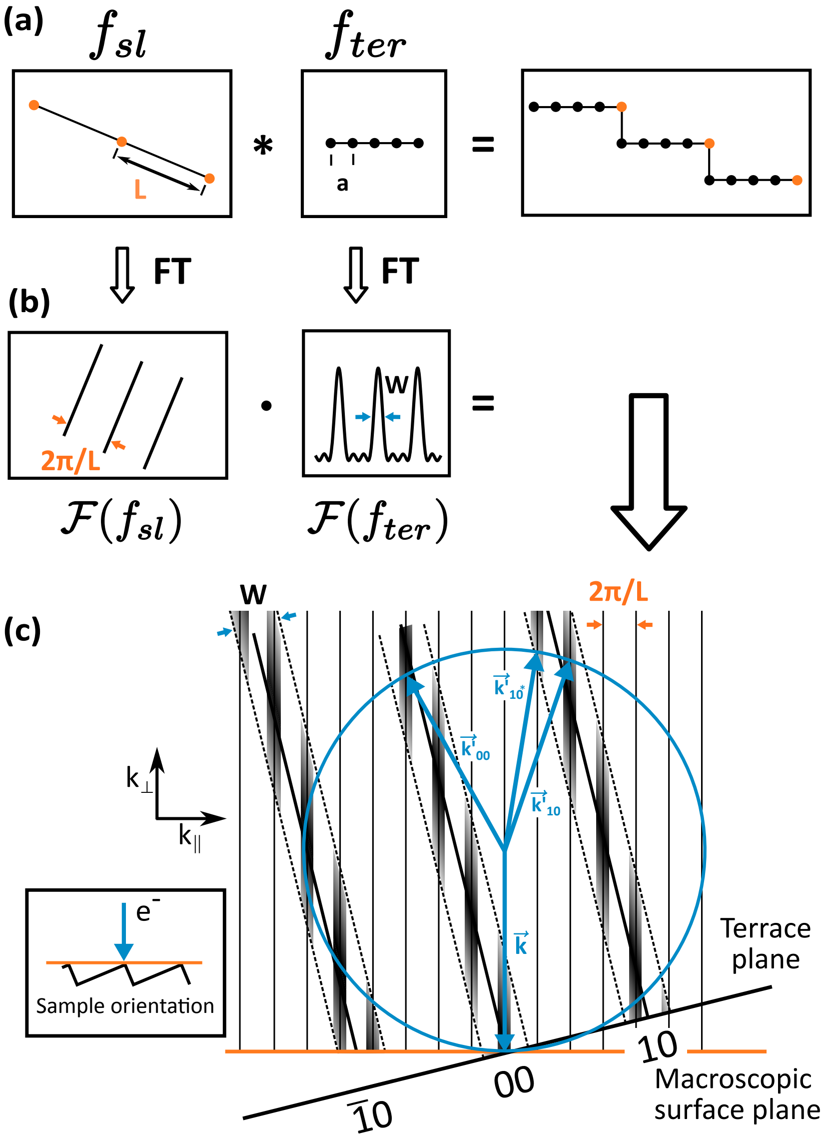

Figure 3.10: *LEED pattern formation of a stepped surface. (a) A stepped surface can be described as a convolution of a superlattice (f_{sl} with periodicity L) and a single terrace (f_{ter} with the atomic distance a). (b) Fourier transform of the superlattice $\mathcal{F}(f_{sl})$ and the terrace $\mathcal{F}(f_{ter})$. W is FWHM of the multi slit function. (c) Ewald construction for a stepped surface. The surface orientation with respect to the incident electron beam is depicted in the inset. The reciprocal space is composed by product of the Fourier transforms of the superlattice and the terrace. As a consequence, the main spots of the terrace can split into subspots. After [97].*

3.3 Angle-Resolved Photoelectron Spectroscopy

Photoelectron spectroscopy (PES) or photoemission spectroscopy summarizes different experimental variants that utilize the photoelectric effect to gain information about the electronic structure of a solid [98]. In this thesis, ARPES was utilized to analyze the band structure of the Si(553)-Au surface at different temperatures. The subsequent section will present the experimental and theoretical aspects relevant for the analysis and discussion of the ARPES spectra reported in Secs. 6.5 and 6.6. It follows the three step model of PES on the basis of Refs. [99–101].

A photon can release an electron from a solid if its energy $h\nu$ exceeds the binding energy E_B of the electron as well as the work function of the sample Φ_S. The kinetic energy distribution of the emitted electrons reflects the energy distribution of the bound electrons in the solid as illustrated in Fig. 3.11(a). The valence band as well as the core levels are subject to line broadening due to lifetime and resolution effects [101]. In the case of a metalic sample, the energy spectrum of the emitted electrons is terminated by the Fermi distribution [see Fig. 3.11(a)]. Notably, standard PES – contrary to STS – can only detect occupied states. To do so, the kinetic energy E_{kin} of the photoelectrons is measured by an electron energy analyzer. The respective binding energies E_B can then be calculated using the following equation:

$$E_{kin} = h\nu - \Phi_A - |E_B| \,. \tag{3.23}$$

Since E_{kin} is measured with respect to E_{vac} of the analyzer, Eq. 3.23 comprises the work function of the analyzer Φ_A instead of the work function of the sample Φ_s.

A well established although still simplified [101] description of PES is provided by the *three step model*, which divides the photoemission process into three separate steps [see Fig. 3.11(b)] [93]:

(1) Photoexcitation of the electrons.

(2) Transport of the excited electrons to the sample surface.

(3) Transition of the photoelectrons into vacuum.

The *first step* – the absorption of a photon and the excitation of a bound electron – can be modeled by a weak perturbation of the crystal:

$$H = H_0 + Oe^{-i\omega t}, \tag{3.24}$$

where H_0 is the Hamiltonian of the unperturbed system and O the operator of the time-dependent perturbation. The transition rate w_{fi} from an initial state i to a final state f of

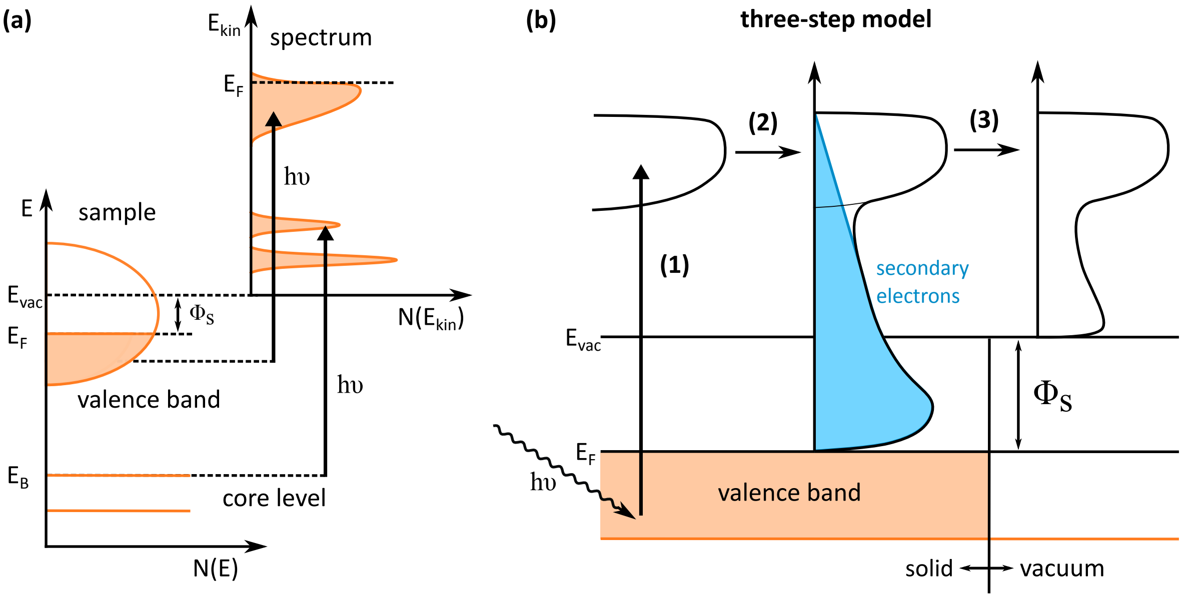

Figure 3.11: *(a) Energetics of the photoemission process. After [93]. (b) Illustration of the three step model of PES. After [93].*

the unperturbed system H_0 due to the perturbation O is described by Fermi's golden rule:

$$w_{fi} = \frac{2\pi}{\hbar} \left|\langle f \left|O\right| i\rangle\right|^2 \cdot \delta(E_f - E_i - h\nu). \tag{3.25}$$

$\delta(E_f - E_i - h\nu)$ ensures energy conservation. The perturbation is caused by the interaction of the electron with the electromagnetic field of the photon $\vec{A} = \vec{A}_0 e^{i(\vec{q}\cdot\vec{r}-\omega t)}$. A canonical replacement of the momentum operator in the unperturbed Hamiltonian [99, 100]

$$H_0 = \frac{\vec{p}^{\,2}}{2m} + V(\vec{r}) \quad \text{with} \quad \vec{p} \to \vec{p} - e\vec{A} \quad \text{(SI units)} \tag{3.26}$$

leads to

$$H = \frac{1}{2m}(\vec{p} - e\vec{A})^2 + V(\vec{r}) = \underbrace{\frac{\vec{p}^2}{2m} + V(\vec{r})}_{H_0} \underbrace{- \frac{e}{2m}(\vec{p}\cdot\vec{A} + \vec{A}\cdot\vec{p}) + \frac{e^2}{2m}\vec{A}^2}_{H_{per}}. \tag{3.27}$$

The part of the Hamiltonian describing the perturbation H_{per} can be simplified by making several assumptions. The quadratic term in $\vec{A}$ describes two-photon processes, which can be neglected for low light intensities produced by standard laboratory light sources [100]. Disregarding surface effects like surface photoemission ($\vec{\nabla}\vec{A} = 0$) [102] further simplifies H_{per} to $H_{per} = -\frac{e}{m}\vec{A}\cdot\vec{p}$. Since the photon wave length is large ($\lambda = 585$ Å for 21.2 eV) compared to atomic distances in a solid (∼ Å), the electromagnetic plane wave can be approximated as $e^{i\vec{q}\cdot\vec{r}} \approx 1$ (dipole approximation). $H_{per} = -\frac{e}{m}\vec{A}_0 \cdot \vec{p} \cdot e^{-i\omega t}$ then has the form of $Oe^{-i\omega t}$. Thus, the photoelectron current at energy E is given by

$$I(E) \propto \sum_{i}^{occ} \left| \langle f \left| \vec{A}_0 \cdot \vec{p} \right| i \rangle \right|^2 \cdot \delta(E_f - E_i - h\nu) \quad \text{with} \quad E = E_f. \tag{3.28}$$

Up to this point no assumption about the unperturbed system has been made. For example, i and f can be one electron states of a solid (independent particle picture) or N-electron many-body wave functions [99]. In case of non-interacting electrons, the photoemission intensity provides direct access to the sample DOS. ARPES, which in addition to the photoelectron's energy also detects its emission angle, then gives information about the band structure of the sample including band dispersion $E(\vec{k})$ and Fermi surface contour. If correlations are significant the PES spectrum can be modified and, consequently, the ARPES signal reflects the removal part of the spectral function rather than the band structure [101]. For example, significant electron-phonon coupling may manifest as a kink in the band dispersion [103]. The ARPES spectra presented in Secs. 6.5 and 6.6 have been inspected in terms of band structure and its temperature dependence. Correlation effects have not been the focus of the analysis and may require close up measurements with increased resolution. For details about the role of correlation effects in PES refer to e.g. [93, 100, 101].

The *second step* of the three step model comprises the travel of the photoelectron to the surface. Typical laboratory light sources (in this thesis: He-I line of a He discharge lamp with $h\nu = 21.2\,\text{eV}$) lead to kinetic energies of the excited electrons, which are close to the minimum of the universal curve discussed in Sec. 3.2. The mean free path of the photoelectrons is limited due to inelastic scattering, which explains the high surface sensitivity of ARPES and gives rise to a continuous background in the measured spectrum [see light blue area in Fig. 3.11(b)]. Quantitative spectra analysis requires a proper consideration of the background signal, as has been applied in Sec. 6.6.

The *third step* describes the transition of the photoelectron from the solid into vacuum. Only excited electrons with an energy higher than the sample work function Φ_S can leave the solid. Translational symmetry in the surface plane results in a conservation of the parallel component $\vec{k}_{\|}$ of the photoelectron momentum in the escape process ($\vec{k}_{\|}^s = \vec{k}_{\|}^v = \vec{k}_{\|}$) as depicted in Fig. 3.12 [101]. The momentum perpendicular to the surface is not conserved ($\vec{k}_{\perp}^s \neq \vec{k}_{\perp}^v$) due to the potential gradient perpendicular to the surface. Assuming a free electron final state leads to

$$\left| \vec{k} \right| = \frac{\sqrt{2mE_{kin}}}{\hbar}, \tag{3.29}$$

and relates the emission angle ϑ of the photoelectron to the parallel component of the electron's crystal momentum $\vec{k}_{\|}^s$ as follows:

$$\left| \vec{k}_{\|}^s \right| = \sqrt{k_x^2 + k_y^2} = \frac{\sqrt{2mE_{kin}}}{\hbar} \sin(\vartheta). \tag{3.30}$$

$\vec{k}_\perp^s$ can in principle be calculated using the following equation [101]:

$$\left|\vec{k}_\perp^s\right| = \frac{\sqrt{2m(E_{kin}\cdot\cos^2(\vartheta)+V_0)}}{\hbar}. \tag{3.31}$$

V_0 is the inner potential, which is in general unknown but can be determined by intricate experimental techniques or theoretical calculations [101]. For surface systems like the quasi-1D atomic wire arrays studied in this thesis, however, $k_\perp$ is irrelevant, so that the detection of E_{kin} as well as the emission angle ϑ is sufficient to measure the system's band structure $E(\vec{k})$.

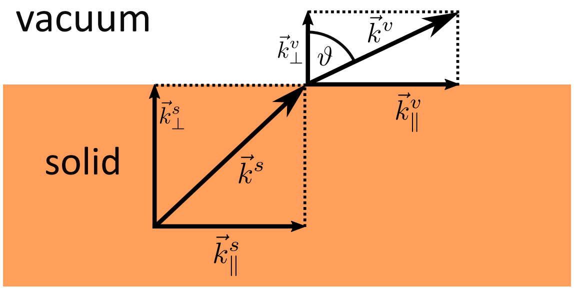

Figure 3.12: *Illustration of the conservation of momentum of a photoelectron leaving a solid. Translational symmetry in the x-y plane leads to conservation of the parallel component of the crystal momentum $\vec{k}_\parallel^s = \vec{k}_\parallel^v$. The momentum perpendicular to the surface plan is not conserved ($\vec{k}_\perp^s \neq \vec{k}_\perp^v$). After [104].*

3.4 Density Functional Theory

Density functional theory (DFT) is a numerical method that allows one to determine the ground state properties of a solid such as equilibrium structure, total energy, electronic structure, and phonon spectrum, etc. It may play a key role in the interpretation of experimental data but also has predictive power. In this thesis, it serves as a complementary method to the experimental techniques described previously. The following will briefly summarize the concept of DFT and introduce the basic terms relevant for the discussion of the DFT results presented in Chapt. 5, and Secs. 6.3 and 6.7. This section is inspired by an excellent talk given by S.C. Erwin at the ToCoTronics2016 Fall School in Würzburg [105].

The basis of DFT is formed by the following Hohenberg-Kohn theorems [106, 107]:

> **Theorem I:** The ground state (electron) density $n(r)$ of a bound system of interacting electrons in some external potential $v(r)$ determines this potential uniquely.
>
> **Theorem II:** There is a universal functional of the density $F[n(r)]$ – independent of $v(r)$ – which can be used to determine the ground state energy by minimization of $E[n] = \int v(r)n(r)dr + F[n(r)]$.

These theorems imply that there is a ground state electron density $n_0(r)$ that provides the ground state energy $E_0 = E[n_0(r)]$. In turn, any density different from $n_0(r)$ results in an energy higher than E_0 $[E(n \neq n_0) > E_0]$. Minimization of $E[n]$ leads to the famous Kohn-Sham equation [108]:

$$\left[-\frac{1}{2}\nabla^2 + v_s(r)\right]\psi_i(r) = E_i\psi_i(r), \tag{3.32}$$

which has the form of a one-particle Schrödinger equation. $\psi_i(r)$ are the one-electron Kohn-Sham orbitals and E_i are the Kohn-Sham eigenvalues. $v_s(r)$ is the effective Kohn-Sham potential given by

$$v_s(r) = v_{ext}(r) + \int \frac{n(r')}{|r - r'|}dr' + \underbrace{\frac{\delta E_{XC}[n(r)]}{\delta n(r)}}_{v_{XC}(r)}. \tag{3.33}$$

$v_{ext}(r)$ represents the potential energy of the crystal, which is determined by the atomic positions of the system. The second term of Eq. 3.33 accounts for the potential due to the average electron density. The latter term is the exchange-correlation potential $v_{XC}(r)$. It depends on the exchange-correlation functional $E_{XC}[n(r)]$, which, in turn, accounts for electron correlations [109]. The exact density of the many-body interacting system is given by [108, 110]

$$n(r) = \sum_{i=1}^{N} |\psi_i(r)|^2 . \tag{3.34}$$

Eqs. 3.32 – 3.34 constitute the famous Kohn-Sham equations. Their self-consistent solution reveals the ground state density $n_0(r)$, which can then be used to compute the ground state energy $E[n_0]$ [107]. The Kohn-Sham equations thus serve as a reference system for DFT to obtain the ground state density n_0 [110]. Instead of determining the universal functional $F[n]$ the new challenge in the Kohn-Sham formulation is to find useful approximations for $E_{XC}[n]$, which is in general unknown. Therefore, different exchange-correlation functionals are available. The various approximations reflect the physics of the electronic structure and come from outside of DFT [107]. A commonly used approach is the local density approximation (LDA), where $E_{XC}^{LDA}[n]$ is derived from the electron density of an uniform electron gas [107]. Although LDA is a very rough approach, only valid for systems with slowly varying particle density, it provides reasonably good result in many cases. An improvement of LDA is the generalized gradient approximation (GGA), which considers the gradient of the density as well [107]. There are different versions of GGA depending on how the density gradient is implemented. The GGA-DFT calculations presented in this thesis utilized the method developed by Perdew, Burke, and Ernzerhof (PBE) [111]. Electron correlation effects may be taken into account more precisely using the Heyd-Scuseria-Ernzerhof (HSE) hybrid functionals, which contain approximately 25% of exact exchange from Hartree-Fock theory [112]. The choice of the exchange-correlation functional has a significant impact on the physical properties of a system including the equilibrium lattice constant, electronic structure, and especially the magnitude of the band gap [113, 114] as will be discussed for Si(553)-Au in Secs. 5.3 and 6.5.

In order to compare the results from DFT with experimental STM data, simulated STM images have been created using the Tersoff-Hamann approximation [77] (see Sec. 3.1). Since the tunneling current depends on the LDOS, STM measurements at constant current and bias can be imitated by isosurfaces of the energy-integrated LDOS. It should be noted that no tunneling tip has been involved in these simulations, i.e. the simulations reflect an STM image recorded with an infinitely small tunneling tip. A more general aspect one has to keep in mind when comparing experimental data to DFT results is that DFT usually calculates ground state properties, while experimental STM and ARPES measurements always comprise a certain effect of the measuring probe on the system of interest (cf. Secs. 3.1 and 3.3).

4 Stepped Silicon Substrates

4.1 Crystallography of (*hhk*) Templates

At the first glance, a freestanding single atomic wire constitutes the perfects model system to study exotic 1D quantum phenomena like Peierls instabilities (see Sec. 2.1), TLL behavior, or soliton physics. However, a freestanding single atomic wire is, firstly, extremely difficult to realize experimentally, and, secondly, nearly impossible to address with today's experimental probes (see Chapt. 3). One opportunity to circumvent this problem is to adsorb metal adatoms on semiconducting substrates. In that process, the substrate serves as a template, which mediates the formation of self-assembled quasi-1D chain arrays. The embedding in a 3D environment disturbs the pure 1D character of the system and interactions between adjacent wires render the system at least quasi-1D. As outlined in Sec. 2.1, a coupling to higher dimensions is essential for the formation of long-range order, whereas thermal fluctuations suppress a long-range ordered ground state in a perfect 1D system. As an additional positive side effect, interactions with the underlying substrate may give rise to interesting modifications (see Chapt. 5) or even new quantum phenomena due to , e.g., their bondings to the adatoms ("orbital filtering") [115].

The choice of the substrate has significant influence on the properties of the resulting chain arrays and, thus, has to be considered carefully. One approach is to use planar semiconducting substrates with anisotropic surface lattice structures like Si(111) or Ge(001). Adsorption of In or Au atoms on theses surfaces leads to the extensively studied chain systems In/Si(111), Si(111)-(5×2)-Au and Au/Ge(001) discussed in Secs. 5.1 and 6.3. The atomic wires studied in this thesis have been grown on *stepped* Si (and Ge) substrates. Using these high-index substrates has the advantage that the atomic wires will exist only in one single domain determined by the step-edge orientation. In contrast, atomic wires grown on planar substrates usually form multi-domain surfaces [10, A8]. Moreover, the surface lattice structure of the substrate plays a secondary role. Instead, the wire spacing is determined by the terrace width of the substrate steps.

Stepped Si substrates can be achieved by cutting a Si(111) wafer against the [11-2] direction under a certain angle as illustrated in Fig. 4.1(a). Depending on the cutting angle α various stepped surfaces with Miller index *hhk* can be realized, each providing a different terrace width T. This enables a controlled modification of the model system's properties using

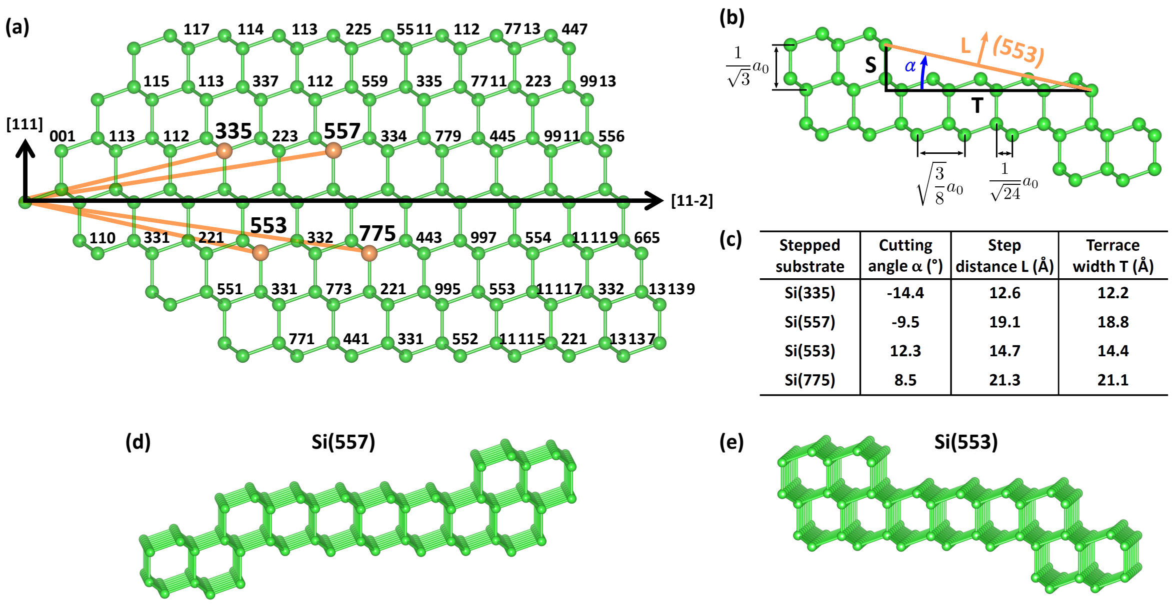

Stepped substrate	Cutting angle α (°)	Step distance L (Å)	Terrace width T (Å)
Si(335)	-14.4	12.6	12.2
Si(557)	-9.5	19.1	18.8
Si(553)	12.3	14.7	14.4
Si(775)	8.5	21.3	21.1

Figure 4.1: *(a) Side view on the (1-10) plane of the Si crystal lattice. Various stepped substrates can be obtained by cutting the 111 surface against the [11-2] direction under a certain angle. After [17]. (b) Side view on the Si(553) surface with step height S, step distance L, terrace width T and cutting angle α. (c) Table summarizing the geometric parameter of four Si(hhk) substrates which form stable surfaces upon Au adsorption. (d),(e) Perspective view on the Si(557) and Si(553) surfaces to illustrate the opposite terrace orientation of (hhk) surfaces with opposite cutting angle sign.*

different Si(hhk) substrates. The substrate step distance L can be calculated by [A3]

$$L^2 = S^2 + T^2 = \left(\frac{|h-k|}{2\sqrt{(3)}} \cdot a_0\right)^2 + \left(\left[\frac{2h}{3} + \frac{k}{3}\right]\sqrt{\frac{3}{8}} \cdot a_0\right)^2 \quad \text{with} \quad k = h \pm 2n, \tag{4.1}$$

where n is an integer, S the step height, and T the terrace width. a_0 is the lattice constant of the substrate material ($a_{0,Si} = 5.431$ Å). The basic geometrical considerations leading to Eq. 4.1 are illustrated by example for the Si(553) surface in Fig. 4.1(b). The Si(553) terrace width and step distance calculates to $T_{Si(553)} = (4 + 1/3)\sqrt{3/8} \cdot a_0 = 14.4\,\text{Å}$ and $L_{Si(553)} = \sqrt{[1/\sqrt{3} \cdot a_0]^2 + [(4 + 1/3)\sqrt{3/8} \cdot a_0]^2} = 14.7\,\text{Å}$. Notably, not all ($hhk$) substrates form stable reconstructions upon Au adsorption. For Si, four stable systems – Si(335)-Au, Si(557)-Au, Si(553)-Au and Si(775)-Au – are known (others may exist). The corresponding substrates and their respective cutting angle, terrace width, and step distance are tabulated in Fig. 4.1(c). The sign of the cutting angle determines the crystallographic orientation of the substrate as illustrated, by example, for Si(553) ($\alpha > 0°$) and Si(557) ($\alpha < 0°$) in Fig. 4.1(d) and (e). The steps of these two variants are oriented oppositely, which, for instance, has consequences for the structure of the step edge. Interestingly, the sign of the cutting angle seems to have only minor influence on the step-edge reconstruction after Au adsorption. Irrespective of the crystallographic orientation of the substrate, a Si honeycomb chain is formed at the step edge as will be shown in Chapt. 5.

4.2 Preparation of Si(*hhk*) Substrates

The Si(*hhk*) substrates used in this thesis were obtained from CrysTec GmbH as well as from Siltronix Silicon Technologies and were 2.5 mm wide, 10 mm long, and 275-525 μm thick. It was found that thinner samples (275 μm) are prone to bending during the intense flash cycles described below. Such bending could be avoided by using thicker samples (475-525 μm). Moreover, two variants, one with step direction parallel (A type) and one with step direction perpendicular (B type) to the 10 mm side (i.e. current flow direction parallel and perpendicular to the step direction), were available. The substrates were highly doped (0.01-0.1 Ωcm) in order to perform STM measurements at temperatures down to 4 K. Since heavily *p*-doped (boron) substrates can be subject to boron segregation to the surface [116, 117], only n-type (phosphorus) substrates have been used for the experiments shown in this thesis.

The substrate preparation contains several ex situ and in situ steps. While the in situ procedure has been fine-tuned for each substrate index, the ex situ preparation process is equivalent for all Si(*hhk*) substrates. First, the ex factory substrates are sonicated for 2 min in an acetone bath to get rid of the photoresist. Hydrocarbons are removed by subsequent baths in ultra-pure (purissimo grade) acetone, propanol and methanol for 2 min each. Second, residual methanol is blown off with dry nitrogen gas. Finally, the sample is mounted on the sample holder and transferred into the ultra-high vacuum (UHV) chamber (see Sec. A of the Appendix for further information about the sample holder and the experimental setups). The whole ex situ procedure is carried out in a laminar flow box providing a clean room environment.

In situ, the substrate is held at 600 °C via direct current heating for several hours to remove water, hydrocarbons, and other adsorbates from sample and sample holder. The sample temperature is monitored with an optical pyrometer (PA 20 from Keller HCW GmbH) at an emissivity of 40 %. In order to remove the oxide protection layer from the substrate, a short "flash" to 1380 °C, as illustrated in Eq. 4.2, is required.

$$\mathrm{RT} \xrightarrow{t=5\,s} 1380\,^{\circ}\mathrm{C} \xrightarrow{t=5\,s} \mathrm{RT}. \tag{4.2}$$

However, a flash to 1380 °C directly after the degas usually results in a pressure boost to $p \gg 1 \cdot 10^{-9}$ mbar in the UHV chamber, which may entail the formation of carbides [118]. To avoid such a pressure boost, several "pre-flashes" to $T \ll 1380\,^{\circ}$C were generally applied. To ensure a full removal of the protective oxide, several flash cycles (done according to Eq. 4.2) are recommended.

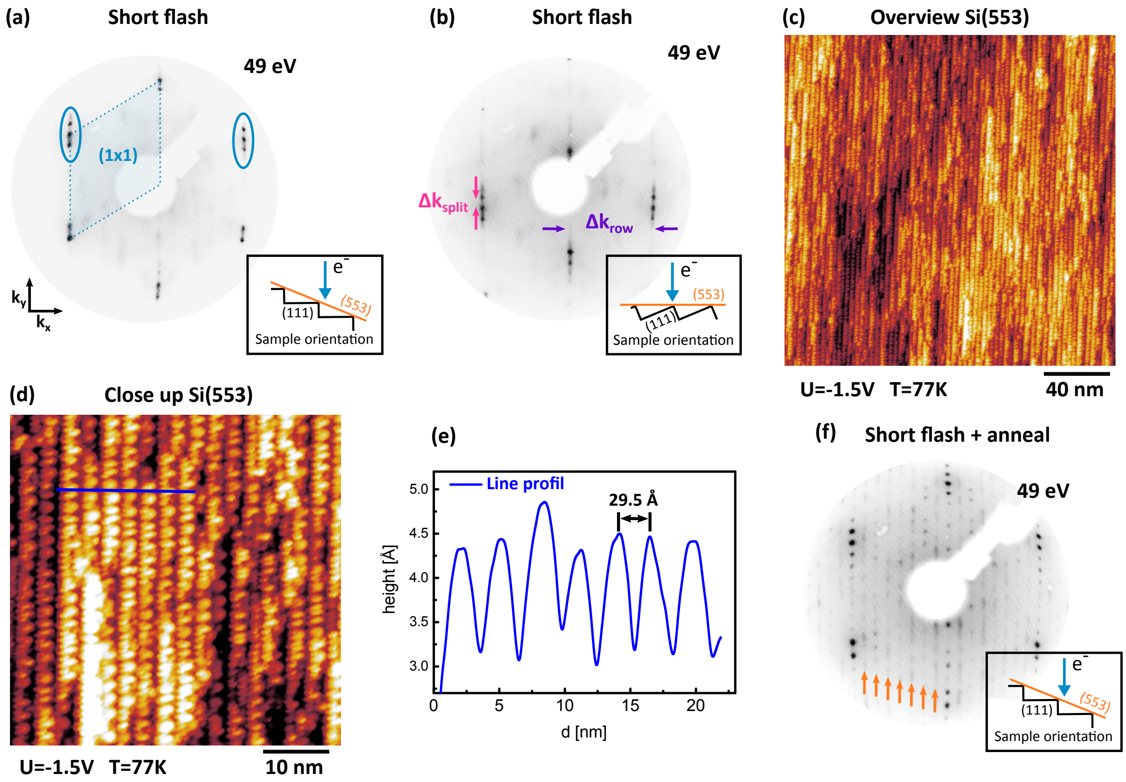

Figure 4.2: *(a) LEED image of a Si(553) surface after several short flash cycles according to Eq. 4.2 taken at 49 eV. The sample orientation with respect to the incident electron beam is sketched in the inset. The spots of the (1×1) unit cell (dashed blue) exhibit the characteristic spot splitting (blue ellipse) indicating the formation a regular step array. (b) Si(553) LEED image recorded with the (553) plane perpendicular to the incident electron beam. A quantitative evaluation of the spot spacings suggests the formation of double steps. (c) Overview constant current STM image (200 nm × 200 nm, $U = -1.5$ V, $I = 30$ pA, $T = 77$ K) of a Si(553) sample after several short flash cycles. No oxide residuals but regular steps are observed. (d) STM close-up image (50 nm × 50 nm, $U = -1.5$ V, $I = 30$ pA, $T = 77$ K). The terraces do not feature a clear periodic surface reconstruction. (e) Line profile along the blue line in (c) confirming the formation of Si(553) double steps. (e) LEED image of a Si(553) surface after a flash cycle followed by an anneal at 470 °C for 6 hours. Seven subspots chains (orange arrows) indicate the formation of a ×8 superstructure on terraces in step-edge direction.*

Si(553) – A representative LEED image of a Si(553) surface after the flash procedure described above is depicted in Fig. 4.2(a). The sample is rotated such that the electron beam is incident perpendicular to the (111) terrace plane as illustrated in the inset of Fig. 4.2(a). The diffraction pattern features the (1×1) spots of the Si lattice (corners of the blue rhomboid), which, in turn, are split into subspots indicating the formation of a regular step array as unraveled in Sec. 3.2. The ratio between the spot splitting (Δk_{split}) and the spot row distance in k_x direction (Δk_{row}) relates to the step distance L_{hhk} as below:

$$L_{hhk} = \frac{\Delta k_{row}}{\Delta k_{split}} \cdot a_{[\bar{1}10]} \tag{4.3}$$

where $a_{[\bar{1}10]}$ is the atom-atom distance along the step-edge direction (3.84 Å for Si). A quantitative analysis of the Si(553) LEED image shown in Fig. 4.2(b) reveals $L_{553} = (30.37 \pm 1.52)$ Å. The error of the method as applied here is relatively large and has been estimated at 5 % since systematic errors like image distortions [119] as well as projection errors caused by photographing the spherical LEED screen have not been corrected for the purpose of this estimate. The LEED analysis indicates the formation of (553) double steps ($d_{Si(553)} = 29.50$ Å), which has also been observed in Ref. [116]. An overview and a close-up STM image of the Si(553) surface are shown in Fig. 4.2(b) and (c), respectively. The overview image confirms a complete oxide removal and the formation of a regular step array. The line profile perpendicular to the steps [blue line in Fig. 4.2(c)] reveals a step distance of $L_{Si(553,STM)} = (29.5 \pm 0.5)$ Å confirming the formation of Si(553)-Au double steps implied by the LEED pattern. The error estimate is based on the reading error. The terrace structure itself [Fig. 4.2(c)] does not feature a distinct long-range periodicity along the step direction. This is compatible with the LEED image which does not exhibit any superstructure spots. However, a long-term anneal of the sample at 470 °C for several hours [120] results in a long-range terrace reconstruction with ×8 periodicity, as verified by ×8 superstructure spots in the LEED pattern [orange arrows in Fig. 4.2(d)]. A detailed STM analysis revealed a special Si adatom reconstruction on the terrace [120]. Nevertheless, the more time-efficient flash cycles according to Eq. 4.2 appear to be sufficient to prepare and refresh the Si(553) substrate for Au atomic wire growth (see Sec. 5.2). Moreover, no differences between A and B type step orientation, i.e. no signs for step bunching, were observed for Si(553). This might be explained by the small Si(553) terrace width, which is not sufficiently wide to develop a full (7×7) reconstruction.

Si(775) – For Si(775), a flash recipe similar to that of Si(553) proved to give a reasonable substrate quality:

$$\mathrm{RT} \xrightarrow{t=5\,s} 1300\,^{\circ}\mathrm{C} \xrightarrow{t=5\,s} \mathrm{RT}. \tag{4.4}$$

Si(775), however, tends to refacet much easier than Si(553) by, for example, exposure to intermediate temperatures for several tenths of a second (not shown here; see Ref. [121]). Moreover, it appears that samples with step orientation perpendicular to the current flow direction (type B) are more susceptible to such kind of step bunching. A LEED image of a Si(775) substrate is shown in Fig. 4.3(a). Again, the (1×1) spots show the characteristic splitting although it is less sharp compared to that of Si(553), indicating the formation of irregular steps. The STM overview image confirms the implication of the LEED image: A stepped surface is formed but consists of terraces of different width. The close-up image [Fig. 4.3(c)] gives a detailed view of the irregular step distribution. Contrary to Si(553), the Si(775) terraces are subject to a distinct reconstruction. Depending on the size of the (111) terrace, elements of the (5×5) and the (7×7) reconstruction can be identified [see bottom and top of zoomed-in image in Fig. 4.3(c)]. Similar reconstructions have been observed and

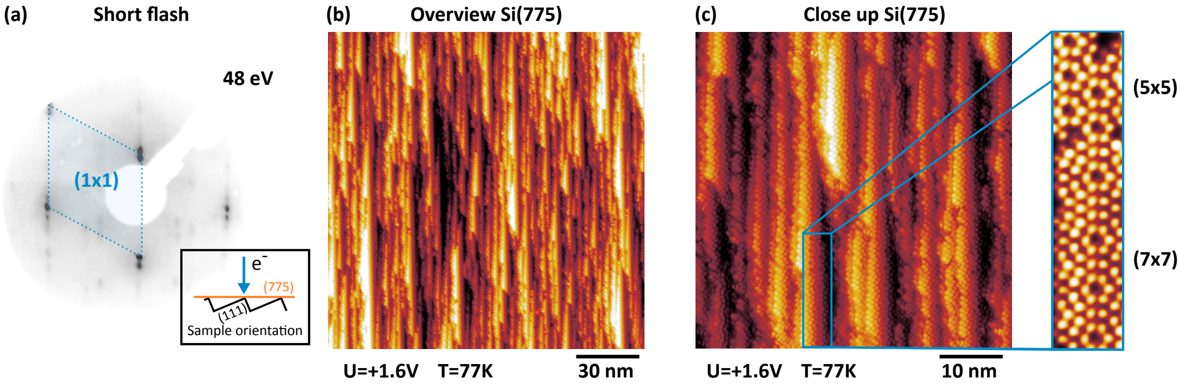

Figure 4.3: *(a) LEED image of a Si(775) substrate after several short flash cycles (Eq. 4.4) taken at 48 eV. The sample orientation with respect to the incident electron beam is illustrated in the inset. The spots of the (1×1) unit cell (dashed blue) exhibit the characteristic spot splitting implying the formation a stepped surface. Moreover, some light subspots indicate a reconstruction of the terrace itself (b) Overview STM image (150 nm × 150 nm, $U = +1.6$ V, $I = 100$ pA, $T = 77$ K) of a Si(775) sample after several short flashs. No regular steps but terraces of different width are observed. (c) STM close-up image (50 nm × 50 nm, $U = +1.6$ V, $I = 100$ pA, $T = 77$ K). Depending on the terrace width different reconstruction variants of the Si(111) surface like (5×5) and (7×7) can be identified (zoomed-in image).*

extensively studied for Si(557) [122]. Although there may be a thermal treatment that creates a perfectly regular Si(775) step array, the resultant substrate quality in this study, as presented in Fig. 4.3, is sufficient for excellent long-range Si(775)-Au atomic wire growth (see Sec. 5.2). Thus, no further effort has been made to optimize the substrate quality.

A regular step array on Si(557) substrates was achieved by several flashes to 1250 °C (data not shown here).

5 Spin Chains and Electron Transfer at Si(*hhk*)-Au Surfaces

5.1 Au Nanowires on Planar Si(111): The Parent System

The (5×2) Au reconstruction on planar Si(111) can be considered the *parent system* of the Si(*hhk*)-Au surfaces. Despite the fact that it was discovered much earlier than the Au induced high-index surfaces [123, 124], it comprises some structural key elements also found in the Si(*hhk*)-Au systems. Si(111)-(5×2)-Au has been intensively studied by various experimental and theoretical methods and was found to be, among other things, subject to a metal-insulator transition upon Si adatom doping [125]. Nevertheless, its structural model – the basis for the theoretical description of the experimentally observed phenomena – is still under debate today. As will be shown in the following section, disclosing the correct Si(111)-(5×2)-Au structure model is both a challenging task in its own right and an object lesson with instructive and substantial relevance for the search of proper Si(*hhk*)-Au models (see e.g. Sec. 5.7).

Three Competing Structure Models – During the last years three different structural models for the Si(111)(5×2)-Au surface have been controversially discussed in literature. A characteristic of all three candidate structures is that Au atoms substitute several Si atoms in the topmost layer. Nevertheless, the models differ in important details: The EBH model [126] – named after its inventors Erwin, Barke, and Himpsel – comprises a HCC built by Si atoms. Moreover, the (5×2) unit cell contains six Au atoms which is equivalent to a Au coverage of 0.6 monolayer (ML) [see Fig 5.1(a)]. It is important to note that a coverage of 1 ML corresponds to one Au atom per Si atom of the Si(111) surface, i.e. $7.83 \cdot 10^{14}$ atoms/cm^2. The Au reconstruction is composed by a single (S) and a double (D) Au row as marked in Fig 5.1(a). In the presence of Si adatoms – incorporated in the model between both Au chains and with $4a_0$ spacing along the chain direction – the periodicity of the Au rows doubles, which manifests in a dimerization of the Au double strand. Simulated STM images and the model's calculated band structure are in good agreement with the experimental results from STM and ARPES [126].

An alternative model was suggested in 2013 on the basis of Weissenberg reflection high-energy electron diffraction (W-RHEED) experiments. Surprisingly, the Si HCC – a central building block of the EBH model and of all Si(*hhk*)-Au systems (see below) – is missing in

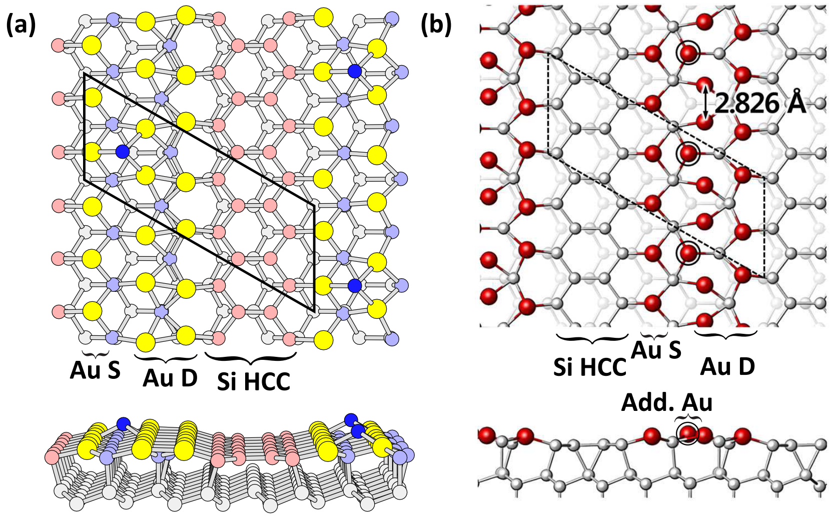

Figure 5.1: *(a) EBH model of the Si(111)-(5×2)-Au surface comprising a Si HCC (light red), six Au atoms per unit cell (yellow) arranged in a single Au row (S) and a dimerized double row (D), and Si adatoms (dark blue) adsorbed between the two Au row. The remainder atoms are Si (light blue and gray). Reprinted figure with permission from [126], Copyright 2009 by the American Physical Society. (b) KK model of the Si(111)-(5×2)-Au atomic wire system. Its unit cell contains 7 Au atoms (red). The additional Au atom, which is missing in the EBH model, is marked by a black circle. Moreover, the intrinsic KK model does not comprise Si adatoms. Reprinted figure with permission from [127], Copyright 2014 by the American Physical Society.*

this model. Instead, the unit cell is basically composed by six Au atoms arranged like a little "Eiffel tower" [128]. Due to its significant deviation from the existing models, the so-called Abukawa-Nishigaya (AN) model received a lot of attention. However, it did not withstand further theoretical and experimental tests: Reflectance anisotropy spectroscopy (RAS) [129] as well as surface x-ray diffraction (SXRD) data [130] rejected the AN model. In addition, relaxation of the atomic coordinates by means of DFT found the AN structure unstable due to energetically unfavorable seven-atom Si rings and undercoordinated Si atoms [129, 131].

Very recently, a third model, the Kwon-Kang (KK) model was proposed [127]. Similar to the EBH model, it comprises a Si HCC. However, its (5×2) unit cell contains one Au atom more than the EBH model, i.e, the Au coverage has increased to 0.7 ML compared to 0.6 ML for the EBH model. The additional Au atom is positioned between the single and the double Au row [see black circle in Fig. 5.1(b)] . As a consequence of the extra Au atom, the KK model features an intrinsic ×2 periodicity without Si adatoms. This is in contrast to the EBH model, which requires the incorporation of a Si adatom in every second (5×2) unit cell [resulting in an effective (5×4) unit cell] to reproduce the ×2 superstructure observed in LEED (Fig. 5.2) and STM (Fig. 5.3) experiments. The calculated band structure and simulated STM images based on the KK model are in good agreement with the results obtained from STM and ARPES measurements (as it is the case for the EBH model). Strikingly, the KK model can explain the experimentally observed metal-insulator transition after Si adatom adsorption [127]. In addition, recent SXRD [130, 132] as well as infrared spectroscopy (IR) [133] experiments

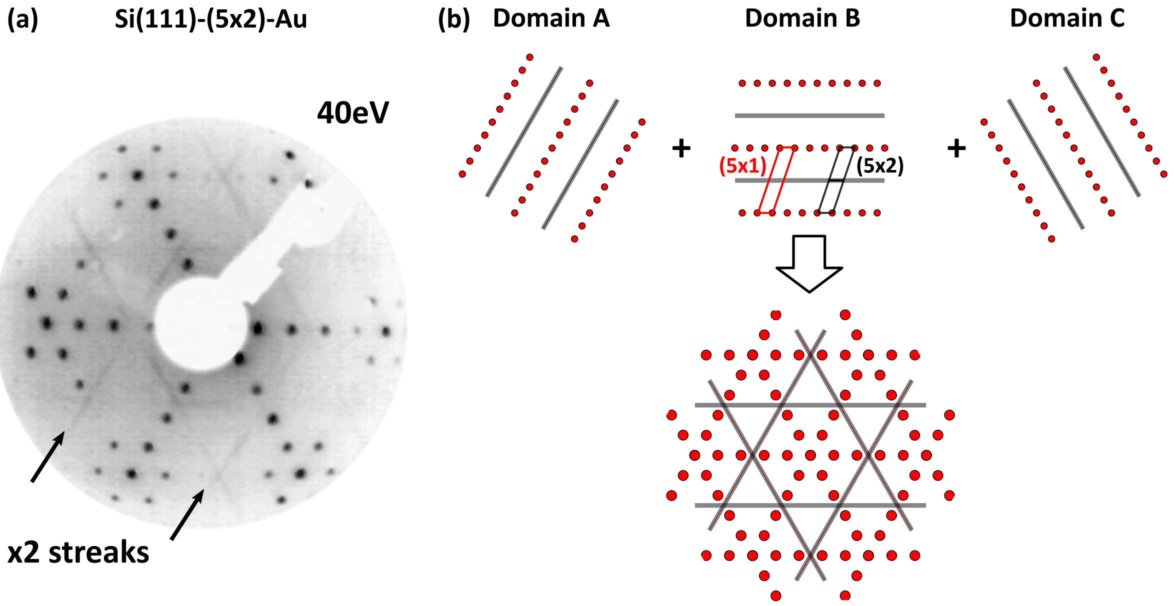

Figure 5.2: *(a) LEED pattern of the Si(111)-(5×2)-Au surface featuring all three rotational domains. ×2 streaks (black arrows) indicate the formation of a ×2 superstructure along the chain reconstruction. (b) Schematic composition of the LEED pattern shown in (a). Superposition of the three (5×2) domains A, B, and C give the experimentally observed pattern. (5×2) (black rhomboid) and (5×1) (red rhomboid) unit cells are marked exemplary in domain B.*

favor the KK model over the EBH model. From an STM point of view, a lack of high-resolution STM data in literature hinders a clear cut decision for one of the two models. Indeed, simulated STM images of both models are in reasonable agreement with the published experimental STM data [126, 127]. The experimental results presented in the following will attempt to fill this lacunae and aim to give further support to one of the promising structure candidates.

Surface Analysis by STM: Experimental Support for the KK Model – A well ordered Si(111)-(5×2)-Au sample was prepared by evaporating Au onto a clean Si(111)-(7×7) substrate held at 650 °C [134]. Surplus Au was desorbed by a postanneal at 900 °C. The threefold symmetry of the Si(111) substrate entails the formation of three domains rotated 120 ° against each other. Fig. 5.2(a) shows a LEED image of the Si(111)-(5×2)-Au surface. The pattern shares all three rotational domains of the (5×2) reconstruction as illustrated in Fig. 5.2(b) confirming the formation of multi-domains. Streaks halfway between the (5×1) spot chains are indicative for a ×2 superstructure along the chain direction [see Fig. 5.2(b) for the respective unit cells]. The observation of streaks rather than spots demonstrates a random registry instead of a fixed phase relation between adjacent chain structures [135].

STM images of the occupied and unoccupied states are displayed in Fig. 5.3. An apparent characteristic of both images are the randomly distributed Si adatoms which manifest themselves as bright disks (cf. Ref. [125]). The zoomed-in images give a detailed view of the chain

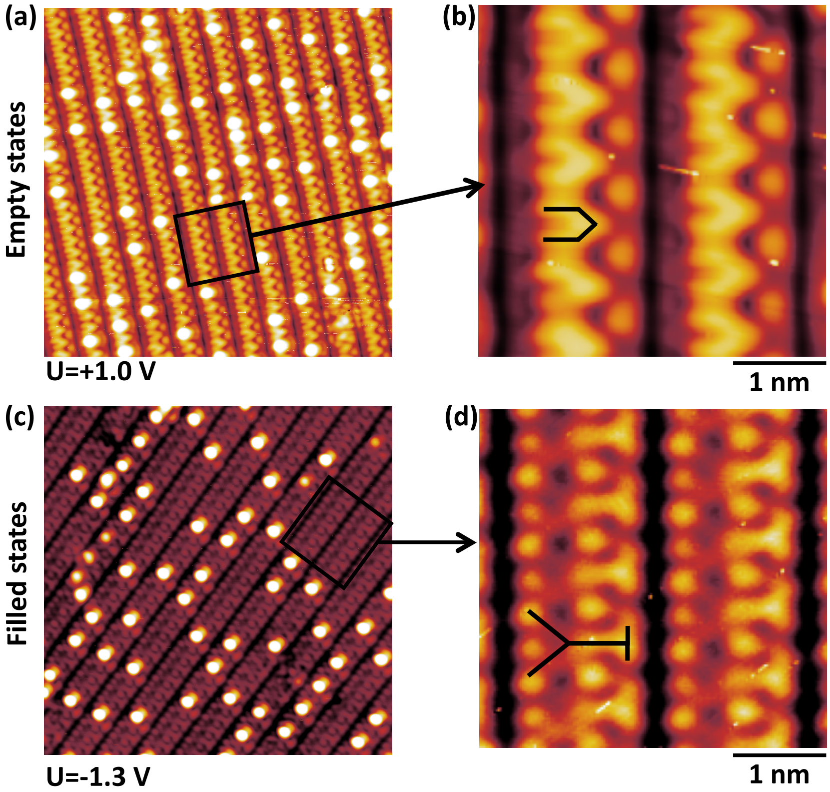

Figure 5.3: *Unoccupied (a) and occupied states (c) STM overview images of the Si(111)-(5×2)-Au surface. The randomly distributed bright disks are Si adatoms. (b), (d) Respective zoomed-in STM images illustrating the chain substructures visible in unoccupied and occupied states. The Au chain reconstruction appears V-shaped for the unoccupied states and Y-shaped for the occupied states (see black markers). All STM images are taken at $T = 77\,K$.*

substructure. Here, the empty states of the Au reconstruction appear V-shaped while the filled states emerge Y-shaped [see black markers in Fig. 5.3(b) and (d)].

A comparison of the experimental STM data with simulated STM images based on the KK model is given in Fig. 5.4. Conclusively, the V- and Y-shaped appearance observed experimentally recurs in the respective simulation. In addition, the STM images presented in Ref. [126] (Fig. 5.4 middle) suggest a good agreement with the KK model. However, Ref. [126] also states a close match of the STM data with the EBH model. A comparison with the high-resolution STM data presented in Fig. 5.3 confirms and even clarifies the close correspondence of the KK model with the experimental STM data (see Fig. 5.4). On the contrary, simulations based on the EBH model as shown in Ref. [126] do not match the data presented.

An additional possibility to distinguish between the EBH and KK model involves the amount of Au incorporated in the unit cell, which differs by 0.1 ML between both models. However, a determination of the correct Au coverage in the sub-monolayer regime is actually much more challenging than naively expected. A quartz micro balance allows to estimate the supplied amount of Au. In particular, using two cross-calibrated micro balances

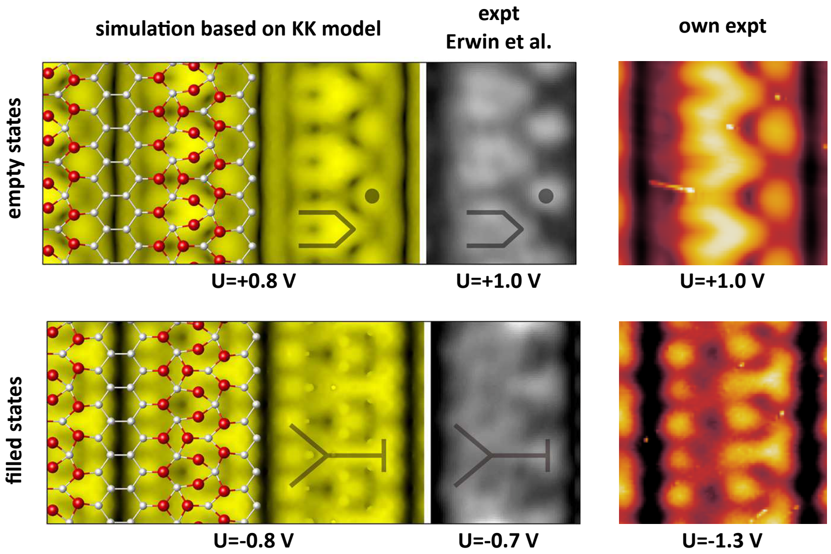

Figure 5.4: *Left: Simulated STM images based on the KK model for filled (+0.8 V) and empty (-0.8 V) states. Middle: Experimental STM images from Ref. [126]. Reprinted figure with permission from [127], Copyright 2014 by the American Physical Society. Right: Cut-out from STM images presented in Fig. 5.3 for better comparison with simulations.*

enables an accuracy well below 0.1 ML [136]. However, this method is not suitable for any Si-Au reconstructions due to their special growth requirements. The substrate requires to be held at elevated temperatures during growth (see Sec. 5.2) resulting in a reduced sticking coefficient or a postanneal, which comes along with a significant loss of adsorbate atoms. Both effects did not only lead to wrong coverage estimates in the past [17, 29] (and, thus, to wrong structural models) but also hinder an exact experimental coverage determination today.

Despite the fact that a direct experimental determination of the exact Au coverage has not yet been achieved, there are several strong evidences – including the STM images shown above – suggesting the KK model to be the correct structure of the Au atomic wires on planar Si(111). It is of substantial importance for the following results on stepped Si(*hhk*)-Au surfaces that the Si HCC, as a central part of the Au induced reconstruction on planar Si(111), is reinforced and that models without a Si HCC can be safely excluded.

5.2 Atomic Wire Growth on Stepped Si Substrates

The fabrication of long-ranged Si(*hhk*)-Au nanowires is a demanding task and requires subtle fine-tuning of the relevant parameters. The following section presents several practical approaches, which have been proved beneficial to achieve optimum (i.e. long-range ordered and low defective) atomic wire arrays.

The general preparation procedure is illustrated in Fig. 5.5. During the whole process excellent UHV conditions – here, typically a base pressure of $3 \cdot 10^{-11}$ mbar and a maximum pressure of $1 \cdot 10^{-10}$ mbar – are essential. As a first step, the respective Si(*hhk*) substrate is

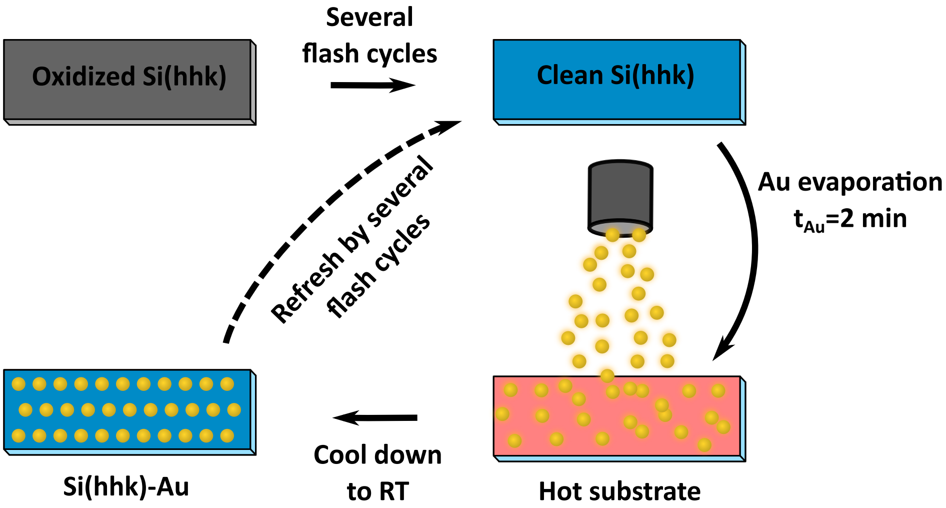

Figure 5.5: *Schematic of the general Si(hhk)-Au preparation procedure. After desoption of the oxide protection layer, Au is evaporated onto the hot Si(hhk) surface for 2 min. If the ideal Au coverage was provided, a long range ordered Si(hhk)-Au surface forms after cool down to RT.*

cleaned as described in Sec. 4.2. Then, a certain amount of Au is evaporated from an electron beam evaporator (EFM 3 from Omicron NanoTechnology GmbH) onto the substrate. During evaporation, the substrate is heated to elevated temperatures via direct current heating. The Au ion flux detected at the outlet of the evaporator serves as an indirect measure for the evaporated Au amount and allows to recapitulate equivalent evaporation conditions. In case of well chosen preparation parameters, an ordered Si(*hhk*)-Au atomic wire array forms after a cool down (typically in about 10 s) to RT. Noteworthy, there is no single ideal preparation recipe. Instead, a proper balance of evaporation time, substrate temperature, and supplied Au amount (each variable within a reasonable range) is required. In order to unravel this complex parameter interplay, both the evaporation time ($t_{Au} = 2\,\text{min}$) and the substrate temperature during evaporation ($T_{SA,\,Si(553)} = 600\,°\text{C}$ and $T_{SA,\,Si(775)} = 650\,°\text{C}$) were kept constant, while the provided Au amount was tuned to achieve optimum atomic wire growth. In this approach, the supplied Au amount is the only free and, therefore, crucial parameter. As a consequence, it has to be fine-tuned with high precision. Indeed, it seems that a less than 5 % deviation from the ideal Au amount (ion flux) leads to significantly lower sample quality.

There are other preparation procedures offered in literature [25,44,137] suggesting a postanneal for several seconds directly after Au evaporation at temperatures ranging from 830-1060 °C. This procedure can likewise lead to well-ordered nanowires, although the highest sample quality could be achieved by the recipe introduced above. Still, a postanneal allows to easily compensate too high Au coverage by gentle desorption of additional Au at elevated temperature and is, thus, an effective tool to study unexplored growth regimes like that of the Ge(*hhk*)-Au surfaces (see Appendix Secs. D and DAu). For the well-established Si(*hhk*)-Au surfaces, however, a postanneal turned out to be an additional, redundant parameter, which increases the complexity of the preparation recipe without providing better sample quality.

An immense advantage of using Si as a substrate material (instead of, for example, germanium, see Appendix Sec. E) is the possibility to refresh the substrate after Au deposition via direct current heating. Several flash cycles according to Eq. 4.2 or 4.4 completely release the adsorbed Au atoms and result in substrates equivalent to that after oxide removal. Thus, the very same substrate can be utilized for several subsequent evaporation trials, and allows for optimization of the preparation: increasing reproducibility and saving time. Having illustrated the general procedure to generate Au atomic wires on Si(*hhk*) templates, the next paragraph will focus on a growth characterization of the two most intensively studied Si(*hhk*)-Au systems in this thesis, namely, Si(553)-Au and Si(775)-Au.

5.2.1 Si(553)-Au and Si(775)-Au

The method of choice for an efficient large-area characterization of the atomic wire growth is LEED. Fig. 5.6(a) shows a LEED pattern of a Si(553)-Au surface with ideal Au coverage recorded at RT. Sharpe main spots reflect the (1×1) unit cell of the Si(553)-Au surface (black rhomboid) and indicate high quality 1D order. Their relative spacings $\frac{\Delta k_{[1\bar{1}0]}}{\Delta k_{[33\overline{10}]}} \cdot a_{[1\bar{1}0]} = (14.41 \pm 0.72)\,\text{Å}$ suggest the formation of regular Si(553) single steps ($L_{553} = 14.7\,\text{Å}$). The step-edge direction in real space is perpendicular to the spot chains as marked by the black double arrow. Halfway between the main spots streaklike intensity is observed [black arrows in Fig. 5.6(a)]. These ×2 streaks evidence the presence of a ×2 periodicity along the chain direction. Their origin is a period doubling of the Au chain, which is still partially present at RT [see zoom of Fig. 5.7(b)]. Further, the presence of streaks instead of sharp spots demonstrates that the Au chains do not show any phase correlation across the steps.

Fig. 5.6(b) provides a LEED pattern recorded close to the edge of the identical Si(553)-Au sample. At this position, the sample temperature was significantly lower during the evaporation process (550 °C compared to 600 °C in the central part), resulting in a higher sticking coefficient of the Au adsorbate atoms. In addition to the features observed in Fig. 5.6(a), $(\sqrt{3} \times \sqrt{3})$ spots can be identified (see red circles and red rhomboid for the $(\sqrt{3} \times \sqrt{3})$ unit cell). These spots represent the formation of Si(111)-$(\sqrt{3} \times \sqrt{3})$-Au facets, which comprise a Au coverage of 1 ML [29]. Such a pattern is thus indicative for excess Au coverage [29]. It can also be observed at the sample center when too much Au was offered during the evaporation. Fig. 5.6(c) provides a LEED image of well-ordered Si(775)-Au nanowires, as inferred from the sharp and regular spots chains. The spot spacing in $[55\overline{14}]$ direction is significantly smaller than that in the Si(553)-Au pattern ($[33\overline{10}]$ direction), which is a direct consequence of the larger Si(775)-Au terraces. Note that both images were recorded at nominally identical electron beam energies (45 eV). An analysis of the relative Si(775)-Au spot spacings suggests the formation of Si(775) single steps [$L_{775} = 21.3\,\text{Å}$; $\frac{\Delta k_{[1\bar{1}0]}}{\Delta k_{[55\overline{14}]}} \cdot a_{[1\bar{1}0]} = (21.9 \pm 1.1)\,\text{Å}$]. Moreover,

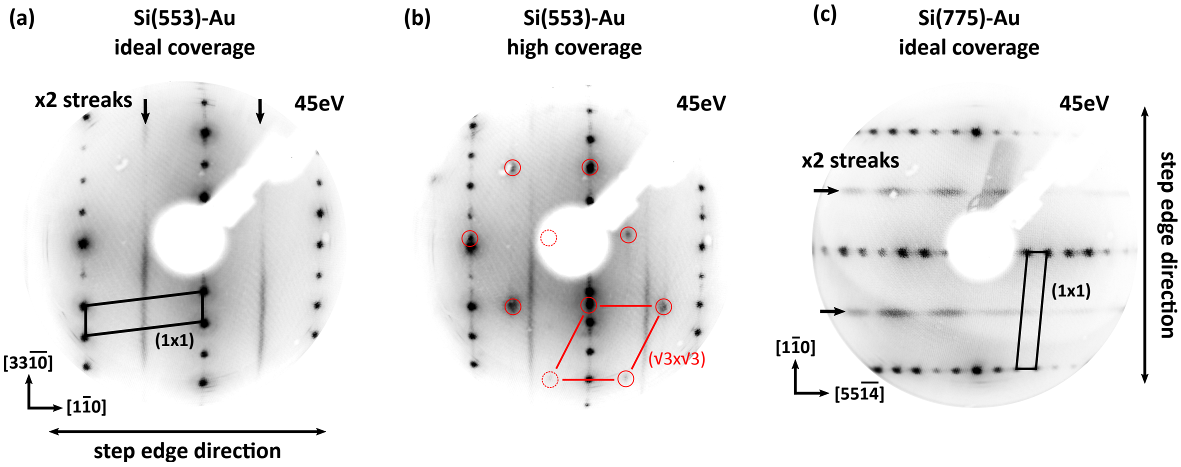

Figure 5.6: *(a) LEED pattern of a Si(553)-Au surface with ideal Au coverage. Sharp integer spot chains suggest high quality long range order. The (1×1) unit cell is marked by the black rhomboid. ×2 streaks indicate the presence of a ×2 superstructure. (b) LEED image taken at a colder area of the identical sample as in (a). The pattern is characteristic for Si(553)-Au with surplus Au coverage. The ($\sqrt{3} \times \sqrt{3}$) spots, marked in red, reflect the formation of high coverage Si(111)-($\sqrt{3} \times \sqrt{3}$)-Au facets. (c) LEED pattern of a Si(775)-Au surface with ideal Au coverage. ×2 streaks witness a ×2 superstructure along the chain direction. All images were recorded at RT.*

pronounced ×2 streaks can be identified in the Si(775)-Au pattern, implying the presence of chains with a ×2 superstructure. The origin of this superstructure as well as the intensity modulation of the ×2 streaks will be discussed in detail in Secs. 5.7 and 5.9.

5.2.2 Adsorbate-Induced Defects

Defects play a versatile role in real-world atomic wire systems. Thus, they are of relevance in several chapters of this thesis. One can distinguish two types of defects, namely, lattice defects and adsorbate induced defects. Both may terminate atomic wires, which gives rise to impurity potentials and to finite discrete wire lengths. It will be shown in Sec. 5.9 that lattice defects may act as dopants, and induce a localized, unpaired electron spin. Defects created by adsorbates are found to locally pin the low temperature phase of the Si step edge and, thus, have significant influence on the phase transition described in Sec. 6.6. Moreover, defects may act as phase defects and shift the phase of a superstructure along the wires (see Sec. 6.3). The following paragraph provides some general information about defects caused by adsorbates using the Si(553)-Au system as an example. Yet, the influence of defects on a specific physical issue will be discussed in detail in the respective sections.

Fig. 5.7(a) shows an STM image of the Si(553)-Au surface, which comprises a very low defect density of about 0.006 per (1×1) unit cell. Several chains do not host one single defect in the whole scan frame, i.e., their chain length exceeds 50 nm. Others are interrupted by defects, which are attributed to unintentional adsorption of various residual gas species [138]. Depending on the type of adsorbate, the respective defect length can vary by several lattice

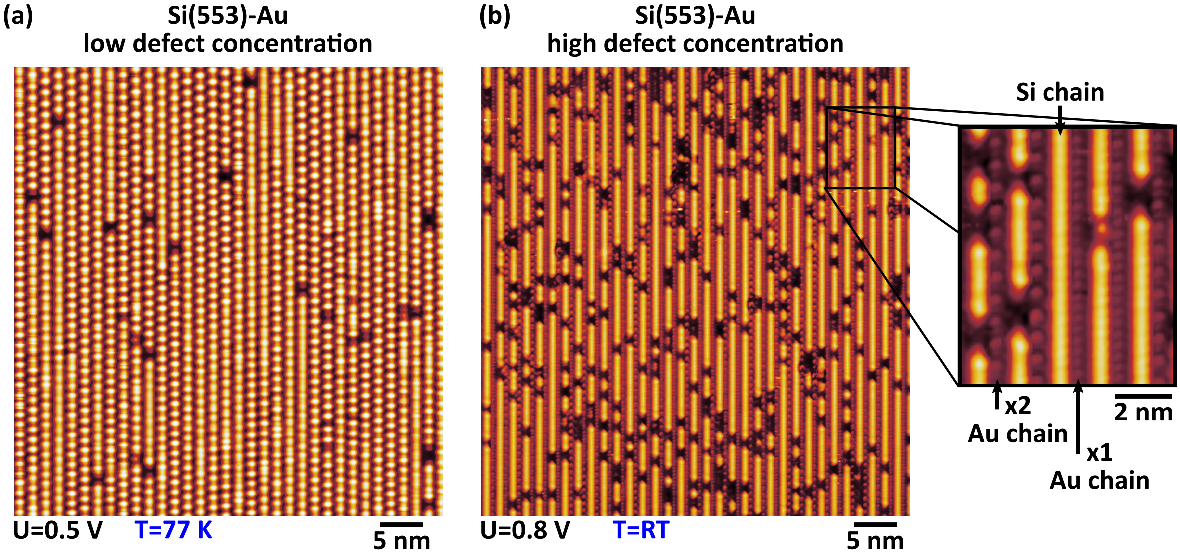

Figure 5.7: *(a) STM overview image of Si(553)-Au with low defect density (48 nm × 51 nm, $T = 77$ K, $U = +0.5$ V, $I = 5$ pA). Several Si step edges (bright) are free of any defect along the whole scan frame. (b) STM overview image of Si(553)-Au taken at RT (48 nm × 51 nm, $U = +0.8$ V, $I = 50$ pA). Compared to (a), the defect density at the Si step-edge chain is ten times higher. The Au chains, however, do not host any defect across the whole scan frame. Inset: Zoomed-in STM image to illustrate the different superstructures of the Au chains.*

constants [117, 138].

It is important to note that the bright rows in this image correspond to the Si step edges (see Sec. 5.4). These step-edge chains exhibit a ×3 periodicity, which is subject of the next section. The second chain type of the system, the Au chain, is not visible in this STM image.

The low defect concentration could be realized by optimized preparation parameters according to Subsec. 5.2.1. In addition, it appears that the exposure time to residual gas – despite a base pressure of $3 \cdot 10^{-11}$ mbar – has a significant influence on the defect density. Consequently, the time between sample preparation and transfer to the STM cryostat has to be reduced to minimum to obtain the lowest defect concentration. In particular, performing a LEED experiment after preparation leads to a significant increase of the number of defects, suggesting electron beam assisted adsorption of residual gas [139, 140] (see Sec. 6.1).

Fig. 5.7(b) presents an STM image of a Si(553)-Au surface with ten times higher defect density [0.06 per (1×1) unit cell] than in (a). Accordingly, the average chain length is much shorter than in Fig. 5.7(a). Of note, the image has been recorded at RT so that the bright Si chains show ×1 instead of a ×3 periodicity – a behavior that will be discussed in detail in Sec. 6.6. In addition, Fig. 5.7(b) not only displays the Si step edges, but also the Au chains lying in the trench between the bright Si chains [see black arrows in zoom of Fig. 5.7(b)]. Interestingly, the Au chains do not host one single defect but run with perfect structural order along the 51 nm wide scan frame. This suggests a selective adsorption behavior with preferential adsorption of residual gas atoms at the Si step edges. A plausible explanation for this behavior is given by the fundamentally different bonding network of the respective chain types: The Au chain is tightly incorporated in the middle of the Si(553) terrace. Instead, the Si atoms at the exposed step edges are only threefold coordinated, leaving behind one dangling bond for chemical bonding (see Fig. 5.8 for a structure model). In line with this explanation, it has been found that atomic hydrogen adsorbs in a two-stage process on the Si(553)-Au surface [A9]. First, the H atoms passivate the Si step edge. Subsequently, H atoms adsorb on terrace sites. The different susceptibility to residual gas adsorption may have consequences for the Si(553)-Au band structure observed in ARPES. Until today, no ARPES signal from the Si step edge has been detected in literature (see e.g. the ARPES data of Crain *et al.* in Ref. [137]. Instead, all published ARPES measurements are dominated by two parabolic quasi-1D bands which stem from the usually defect-free Au chains. A simple but reasonable explanation for this issue is that only high quality Si(553)-Au samples with low defect density give rise to a detectable signal from the Si step edge as will be demonstrated in Subsec. 6.5.1.

As a side remark, the zoomed-in image of Fig. 5.7(b) nicely confirms the coexistence of two different Au chain periodicities at RT [25]. Some chains exhibit a ×1 period while others still feature the LT ×2 phase (see Sec. 5.4 for details).

5.3 Spin Chain Proposal from DFT

A seminal DFT study by Erwin and Himpsel published in 2010 [1] suggests charge ordering at step edges of Si(553)-Au and Si(557)-Au. The footings of this work are well established structural models for both surface reconstructions. The following paragraph will review the main results of Ref. [1], using the example of Si(553)-Au – the most intensively studied member of the Si(*hhk*)-Au family in this thesis and in literature. The Si(557)-Au model will be discussed in Sec. 5.5.

Si(553)-Au Structure Model – Like all Si(*hhk*)-Au systems, the step edge of the Si(553)-Au surface is formed by a sp^2-hybridized Si HCC [green in Fig. 5.8(a)]. The terrace itself consists of a Au double strand, which corresponds to a Au coverage of 0.48 ML. There have been models comprising a monoatomic Au chain only [17,141–143]. However, the most recent SXRD and DFT studies are clearly in favor of the Au double row [1,22,28]. Relaxation within DFT finds a buckling of the Au dimeres. Specifically, the dimeres of the Au ladder are tilted in plane in alternating fashion from rung to rung along the chain axis. As a consequence, the Au chain features a period doubling with respect to the distance $a_0 = 3.84\,\text{Å}$ between two Si atoms along the step edge – a property which is in agreement with experimental findings obtained by LT LEED [25] (see Sec. 6.1) and STM [25,26] (see Sec. 5.4). Experimentally, the ×2 periodicity is still partially present at RT [see Fig. 5.7(b)] and manifests as ×2 streaks in the LEED pattern [Fig. 5.6(a)]. Noteworthy, a similar dimerization is also present in the EBH and KK model of the Si(111)-(5×2)-Au surface (cf. Sec. 5.1). A quantitative measure

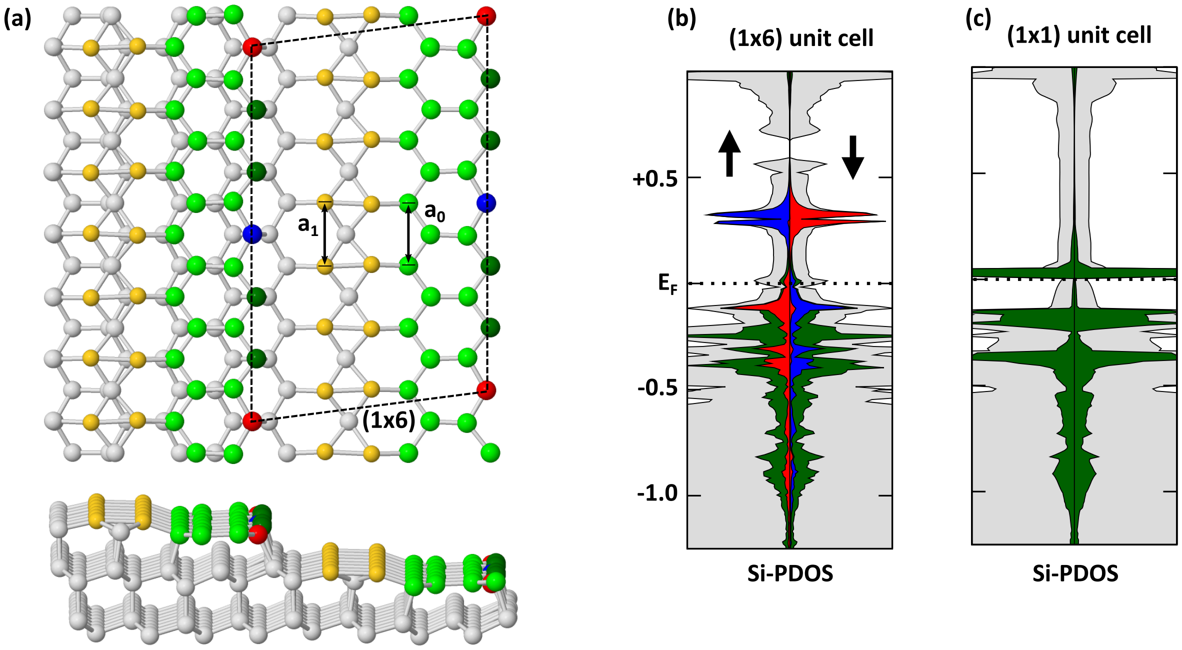

Figure 5.8: *(a) Top and side view of the Si(553)-Au structural model in its AFM ground state. Au atoms are yellow. All others are Si atoms. The terrace comprises a Au double strand. Neighboring Au dimers are buckled in opposite direction, leading to a ×2 period of the Au chain. Each step edge is composed by a Si HCC (green). Atoms directly at the edge are subject to charge ordering. Singly occupied step-edge atoms are color red (spin up) and blue (spin down). Dark green atoms are occupied by two electrons. The coupling between localized spins is AFM along and FM across the chains. Atomic coordinates provided by S.C. Erwin. (b) Si PDOS for the model shown in (a). The colors indicate the atomic origin of the respective states. Localized electrons give rise to an exchange split state with intense DOS about 0.4 eV above E_F. Spin-up states (left) as well as spin-down states (right) are displayed. (c) Si DOS of the model shown in (a), but constrained to the (1×1) unit cell. No charge order occurs. The unoccupied Si step-edge PDOS is localized close to E_F. (b) and (c) reprinted by permission from Macmillan Publishers Ltd: Nature Communications [1], Copyright 2010.*

for the dimerization is given by the dimerization parameter $d = (a_1 - a_0)/a_0$ [see Fig. 5.8(a)]. However, it is an intricate detail that d is sensitive to the choice of the DFT exchange-correlation functional as well as to the silicon lattice constant [A3]. Using the PBE functional results in $d = 0.04$ [1].

Spin Polarization of Every Third Step-Edge Atom – An apparent shortcoming of the model described is that "standard" DFT calculations reveal a ×1 periodicity at the Si step edge [22] and, thus, cannot explain the ×3 superstructure observed experimentally at LT [25, 26]. This issue could be solved in Ref. [1] by applying spin-polarized DFT calculation to the (1×6) unit cell of the above model [see Fig. 5.8(a)]. As a result, the Si step edge is subject to a charge ordering. In particular, every third Si step-edge atom is occupied by one, and, thus, spin-polarized electron. All other step-edge orbitals are doubly occupied, forming spin-compensated lone pairs. Consequently, the Si step edges host an ordered array of local magnetic moments, referred to as *spin chains*. In addition, the step edge bears a structural deformation with ×3 period. In detail, singly occupied Si atoms sit 0.3 Å lower than the surrounding nonpolarized Si atoms [1] [see side view in Fig. 5.8(a)]. Therefore, accounting for both local deformation and charge ordering, such spin chains may also be considered spin polarons [42]. The step-edge charge ordering manifests itself in the electronic structure by a prominent characteristic. The calculated Si PDOS comprises an exchange split state localized at every third singly occupied step-edge atom [cf. Fig. 5.8(b)]. Of particular interest for the experimental test of this proposal is the pronounced unoccupied minority spin state localized about 0.5 eV above the Fermi level. The magnitude of the exchange splitting depends on the detailed parameters of the DFT calculation, and suffers the general limitations of DFT in predicting exact exchange correlation energies [108, 109] (cf. Sec. 3.4). While PBE reveals an exchange splitting of about 0.5 eV [1], HSE increases the magnitude of the exchange splitting to about 0.8 eV [144]. A totally different electronic structure is found when the identical model is constrained to the (1×1) unit cell. Here, no exchange split state exists but the unoccupied Si step-edge DOS is localized close to the Fermi level [see Fig. 5.8(c)]. The perhaps most popular prediction of Ref. [1] is a magnetic ordering of the localized spins. Mapping results from DFT on a nearest-neighbor Heisenberg model reveals a strong AFM coupling of adjacent spins along the spin chain ($J_{\parallel} = +15\,\text{meV}$) and a weak FM coupling across the steps ($J_{\perp} = -0.3\,\text{meV}$).

In summary, this model embodies an alternative explanation for both LT superstructures observed experimentally. The ×3 period of the Si step edge is proposed to arise from charge ordering, and the ×2 periodicity of the Au chain is an inherent structural feature of the ground state model. This is in clear contrasts to earlier reports [25, 26], which attributed the origin of the respective chain superstructures to two independent Peierls distortions accompanied by a Fermi nesting-driven band gap opening.

5.4 Si(553)-Au: Formation of ×3 Spin Chains

This section provides an experimental test of the spin chain proposal described above by means of bias-dependent STM and local STS [A1].

Comparison of Experimental and Simulated STM Images – Fig. 5.9(a) displays three constant current STM images recorded at a fixed temperature (77 K), but at different tunneling biases. The two left images are sensitive to the unoccupied states ($U = +1.0\,\text{V}$ and $U = +0.1\,\text{V}$; $I = 50\,\text{pA}$), while the right image ($U = -1.0\,\text{V}$) probes the occupied states of the Si(553)-Au surface. For high positive tunneling bias (+1.0 V), the Si step edge – the bright chain in all three images – features a distinct ×3 periodicity. In particular, every third atom of the step edge appears brighter than its neighbors. Close to the Fermi level [$U = +0.1\,\text{V}$, middle image in Fig. 5.9(a)], no distinct ×3 periodicity can be identified, but the Si step edge displays a ×1 periodicity. This bias dependence, and especially the absence of a super-

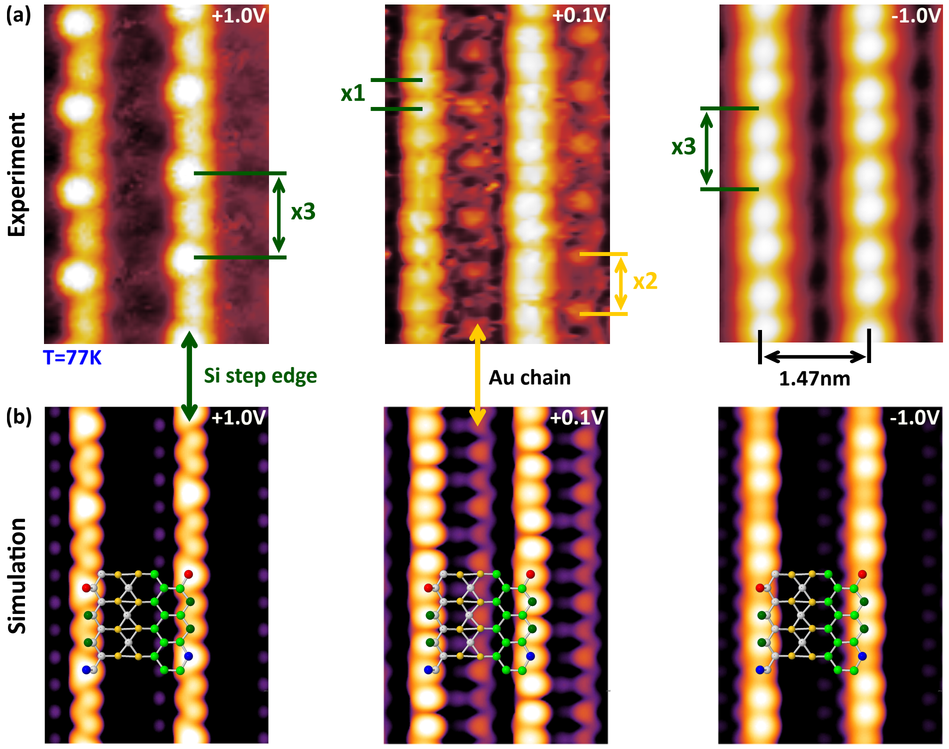

Figure 5.9: *(a) Experimental constant current STM images ($I = 50\,\mathrm{pA}$) of the Si(553)-Au surface for various bias values ($T = 77\,\mathrm{K}$). (b) Corresponding simulated constant current STM images based on the spin-polarized DFT ground state. A top view of the structural model is superimposed for easier comparison of atom positions to corresponding DOS accumulations in the simulation. Unoccupied state STM images adapted from [A1]. Simulated STM images provided by S.C. Erwin.*

structure close to the Fermi level, does not match to the simple Peierls picture suggested in previous works [25, 26].

Furthermore, the low bias image comprises clear signal from the second chain type of the surface. The Au chain manifests as circular, $2a_0$ spaced charge clouds located in between the bright Si chains. Both experimental STM images are in excellent agreement with simulated STM images (cf. Sec. 3.4 for technical details of the simulation) based on the charge ordered DFT ground state [see Fig. 5.9(b)]. The Si chain displays the same bias-dependent periodicity change in both experiment and simulation. Even the shape of the experimentally observed Si atoms is in striking agreement with the simulation. In both corresponding high bias pictures (+1.0 V) every third Si atom exhibits a bright triangular structure, while the less pronounced Si atoms between them feature a V-like shape. Apart from the Si chain, there is an excellent match with the appearance of the Au chain which is only visible close to E_F in simulated and experimental STM images. As an interesting detail, the buckled Au rungs are not directly reproduced in the simulated STM image. Instead, the Au chain manifests as charge clouds with doubled periodicity. Specifically, the highest DOS is localized between the two closer Au atoms of the right-hand ladder string. For easier identification of such details, the structural model is superimposed the simulation in Fig. 5.9(b). Experimentally, very similar ×2 periodic charge clouds are observed, giving additional support for the validity of the model. Further details about the Au chain, especially about its electronic structure and its influence on the Si step edge, will be discussed in Secs. 6.2 and 6.5 respectively. The following paragraph will instead focus on the Si step edge and on the origin of its bias-dependent periodicities.

In the DFT model, the prominent minority state $\approx +0.4\,\text{eV}$ above E_F, which stems from the spin-polarized Si atoms [see Fig. 5.8(b)], is responsible for the bias-dependent change from ×1 to ×3 periodicity. As mentioned in the previous section, this characteristic state vanishes if spin polarization is artificially constrained to be zero in the calculation [see Fig. 5.8(c)]. Then, all Si step-edge atoms exhibit identical unoccupied LDOS, which is located close to E_F. The experimental bias-dependent STM images indeed suggest the presence of such a localized "spin state". As introduced in Sec. 3.1, an STM image – in good approximation – displays the LDOS integrated from E_F up to the tunneling bias U. Consequently, the low bias STM image detects states close to E_F, but is *insensitive* to states located several tenth of an eV above E_F. The high bias scan ($U = +1.0\,\text{V}$), however, is *sensitive* to such a state, and, indeed, displays enhanced DOS at every third step-edge atom.

In addition to the close matching between experiment and theory for the unoccupied states, STM scans detecting the occupied states also fit to DFT modeling. The STM image recorded at $U = -1.0\,\text{V}$ [Fig. 5.9(a), right image] exhibits a ×3 periodicity, but with inverted intensity compared to that of the $+1.0\,\text{V}$ image. Here, just as in the calculation, the nonpolarized step-edge atoms appear bright, while the spin sites are less intense. Such appearance is not surprising having in mind that, first, the spin sites structurally sit slightly below the height of its nonpolarized neighbors and, second, occupied states STM images are dominated by states close to E_F of the sample (leading edge effect, cf. Sec. 3.1) – an energy position where DFT does not predict any spin state DOS. Notably, a more complete bias-dependent set of STM measurements with higher resolution is presented in Sec. 6.2. These data reveal subtle details about the Si-Au chain interaction, however, do not affect the fundamental results discussed in this paragraph.

Spin Chain Fingerprint Detected by Local STS – A more direct access to the LDOS can be obtained by local STS (cf. Sec. 3.1). Fig. 5.10 displays two different STS spectra, which represent the LDOS at the two characteristic positions of the Si step edge, namely, at the bright mesa atoms (red) and at the Si atoms in between (dark green). Both spectra have been recorded using the lock-in technique (see Sec. 3.1) with a modulation voltage of $U_{mod} = 10\,\text{meV}$. The inset displays the locally resolved dI/dU signal at $U = +440\,\text{meV}$, and results from a grid of dI/dU spectra performed over a certain sample area (cf. Sec. 3.1). Red and green stars mark the two characteristic step-edge locations. The most prominent feature of this local spectroscopy experiment is the distinct peak at $\approx +0.44\,\text{V}$ displayed by the spectrum taken at the bright mesa atoms (red). Its spatial origin as well as its energetic

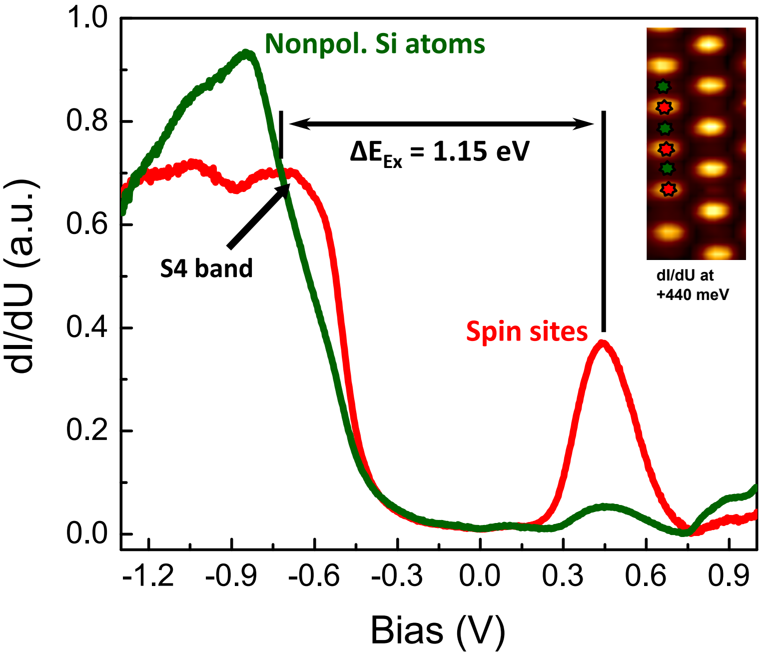

Figure 5.10: *dI/dU spectra taken at the two characteristic atomic positions of the Si step edge, i.e., the spin sites (red) and the nonpolarized Si step-edge atoms (green). Spectra have been recorded with the lock-in technique ($U_{mod} = 10$ meV, $T = 77$ K, $U_{set} = +0.2$ V, $I_{set} = 10$ pA). Inset: Locally resolved dI/dU signal at $U = +440$ meV. The red and green stars exemplarily mark the local position of the respective dI/dU curves. Both spectra have been offset-corrected using simultaneously recorded $I(U)$ curves as a reference. Several single-point spectra were averaged to improve statistics.*

position provide an excellent match with the minority spin state predicted by DFT. In turn, the green spectrum does not feature any pronounced DOS signal in the unoccupied states. The small peak at +0.44 V probably arises from the finite spatial resolution of the tunneling tip, i.e., it is an imprint of the intense DOS captured by the red spectrum. Such strong spatial variation of Si step-edge LDOS provides clear evidence for charge ordering. In addition to that, the one-to-one correspondence with the DFT prediction allows the conclusion that the step edges of the Si(553)-Au surface indeed host spin chains.

A corresponding state in the unoccupied energy range is also visible in two-photon photoemission experiments [144], which, however, does not feature local resolution but instead is representing an average over all atoms in both chains. Subsequently, an increased DOS signal at every third Si atom has been independently confirmed by other STS experiments [145,146].

Although it is much easier to disclose the energetically well separated minority spin state – be it by STS or by bias dependent STM – the majority spin state could also be detected. The red curve in Fig. 5.10 shows a peak in the occupied states at -720 meV, in good agreement with bias dependent dI/dU mapping and LT ARPES experiments presented in Sec. 6.5. This allows to determine the exchange splitting of the dangling bond spin state to about 1.15 eV – a value which is in reasonable agreement with DFT ($\Delta E \approx 1$ eV) [A3]. In fact, the rather large experimental value compared to the result obtained by PBE (0.5 eV) indicates an important role of electron correlations.

In summary, the results obtained by STM and STS give strong evidence for the formation of spin chains at the Si(553)-Au step edge as proposed by DFT. The question whether these spins order magnetically or not is impossible to address by a conventional STM experiment, which is only charge but not spin sensitive. Instead, spin-polarized scanning tunneling microscopy (SP-STM) is required to achieve spin sensitivity [147]. In order to check the AFM spin ordering predicted by DFT, SP-STM was applied in collaboration with J. Kemmer and M. Bode from Würzburg, Experimentelle Physik II. In situ Cr coating of conventional W tips resulted in an out-of-plane spin sensitivity as verified by measurements on a well-suited test system, namely, one ML of Mn on W(110) [148]. Interestingly, no significant difference between measurements performed with spin-sensitive tips and measurements with normal W tips could be detected. Based on this result, one can rule out an AFM spin ordering down to the measurement temperature of 56 K. Further results addressing the possibility of magnetic order in Si(553)-Au spin chains will be discussed in Sec. 6.1.

5.5 Si(557)-Au: Formation of ×2 Spin Chains

Structure Model and Chain Appearance in STM – The Si(557)-Au surface offers an interesting crystallographic contrast to that of Si(553)-Au, because its steps are oriented oppositely – a result of the reverse sign of the substrate cutting angle (see Fig. 4.1 in Chapt. 4). A complete structural model has already been published [1,34], and is largely consistent with earlier SXRD experiments [31]. This model – as it is the case for Si(553)-Au – is composed entirely of structural motifs from Fig. 1.1. Despite its different crystallographic orientation, the step edge is again a single-honeycomb graphitic silicon strip [see Fig. 5.11(a)]. The terrace itself accommodates a single Au chain, which does not dimerize but exhibits ×1 periodicity. The remainder of the terrace consists of a staggered double row of alternating Si adatoms (black) and unpassivated Si “restatoms” (blue) both separate by $2a_0$.

Fig. 5.11(b) shows an STM overview image of the Si(557)-Au unoccupied states which is dominated by two bright chains. According to previous STM studies [24, 149, 150], these chains correspond to the Si step edges and to rows of Si adatoms [see labeled arrows in Fig. 5.11(b)]. The randomly distributed bright protrusions are mainly due to lattice defects like misplaced Si adatoms [149]. Adsorbate induced defects manifest as discontinuities in the Si step edge but also as structureless bright protrusions [149]. Both chain types display a ×2 periodicity. For the adatom row, the ×2 spacing is an inherent structural feature. For the step edge, spin-polarized DFT calculations suggest the formation of a spin chain with ×2 periodicity. Specifically, half of the step-edge orbitals are found singly occupied and, hence, fully spin polarized, while the other half is doubly occupied. Noteworthy, each restatom

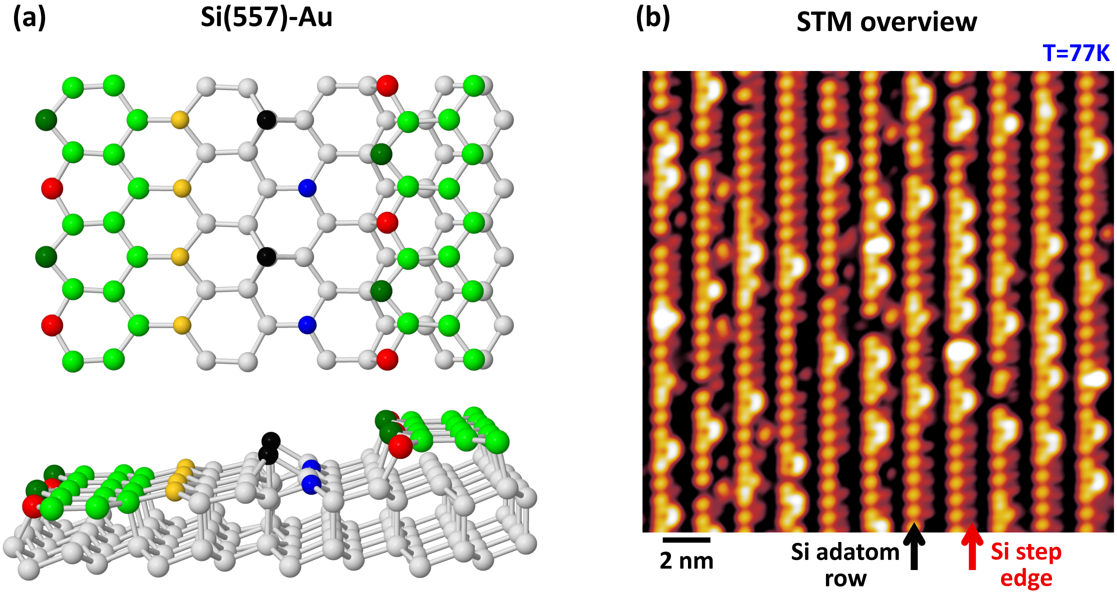

Figure 5.11: *(a) Top and side view of the Si(557)-Au structure model. The terrace itself hosts a monoatomic Au chain (yellow) with a_0 periodicity as well as a row of Si adatoms (black) with $2a_0$ spacing accompanied by unpassivated Si restatoms (blue). The step edge is built by a Si HCC (green), which is subject to the formation of a spin chain with ×2 spacing. Red atoms are singly occupied, dark green atoms are doubly occupied step-edge atoms. Atomic coordinates provided by S.C. Erwin. (b) STM overview image of the Si(557)-Au atomic wire array ($U = +1$ V, $T = 77$ K). Bright chains correspond to the Si adatom row (black arrow) and the Si step edge (red arrow). Randomly distributed bright protrusions are lattice defects like misplaced Si adatoms*

dangling bond is also found singly occupied and, thus, fully spin polarized [1]. However, the situation found for the restatoms is different from that at the step edge, which is subject to charge ordering with merely every second step-edge atom being spin polarized. As the restatoms show an inherent ×2 periodicity, the number of spin-polarized step-edge atoms and restatoms is equivalent.

Evidence for Step Edge Spin State from Local STS – Experimental support for the prediction of spin chains at the Si(557)-Au step edges comes from STS [see Fig. 5.12(a)]. The Si step-edge spectra feature a well-defined unoccupied state at about +0.5 eV (red curve). This is very likely the same characteristic minority spin state detected on Si(553)-Au (see previous section). Moreover, DFT predicts a state at a similar energetic position arising from spin polarization of every second step-edge atom [see Fig. 5.12(b)]. Noteworthy, previous STS studies reported a similar unoccupied state [149, 150] although it was not associated to spin chain formation. In addition, the small spacing and STM-broadened appearance of the halffilled dangling-bond orbitals make it infeasible to separately resolve the spectra for the two neighboring silicon step-edge atoms. Further support for the DFT modeling comes from the Si adatom spectrum [black curve in Fig. 5.12(a)], which comprise only one well-defined feature located above E_F, confirming the empty dangling bond of the Si adatoms.

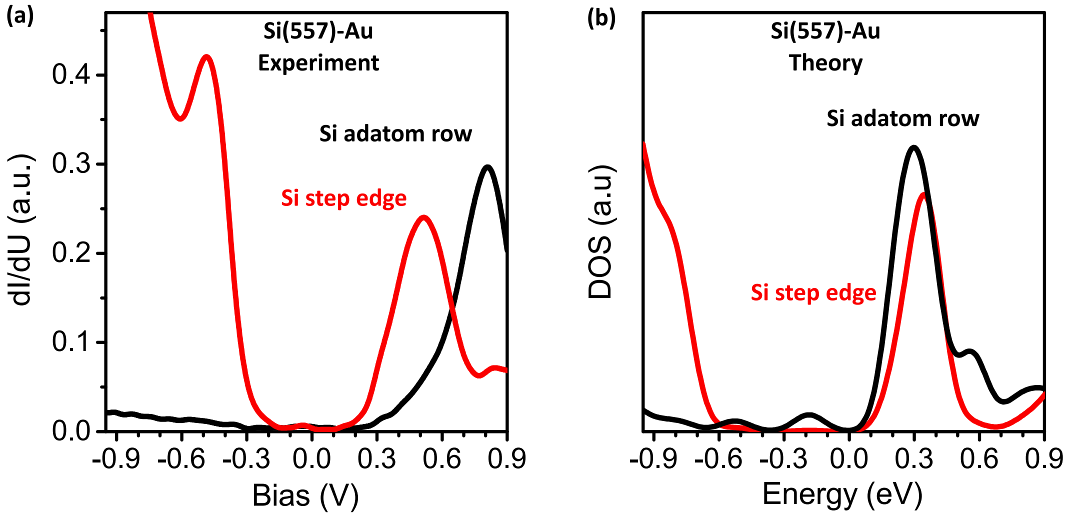

Figure 5.12: *(a) Local STS spectra taken at the two characteristic Si chains – adatom row and Si step edge – of the Si(557)-Au surface. The Si step-edge spectrum comprises an intense peak 0.5 V above E_F which provides evidence for spin chain formation. (b) LDOS for Si(557)-Au obtained by DFT/HSE calculations. The Si step-edge spectrum (red) shows a strong peak above and below E_F representing singly-occupied and doubly-occupied step-edge atoms. The adatoms, with its empty dangling bond orbitals, give rise to pronounced unoccupied DOS. Experimental spectra are in qualitative agreement with the LDOS given by DFT.*

Contrary to the case of Si(553)-Au, the Si(557)-Au step edges do not show a temperature dependence. For Si(553)-Au, the tripled periodicity observed at LT vanishes at RT. This is not the case for Si(557)-Au. Instead, the step edges retain their ×2 period up to RT [150,151]. A plausible explanation for this observation is given by the spin chain scenario. For Si(553)-Au DFT predicts a thermally excited spin hopping to adjacent lattice sites [42] – a finding which will be addressed experimentally in Sec. 6.6. For Si(557)-Au such hopping is unlikely since a spin hop to an adjacent lattice site results in a configuration with two spin sites directly next to each other – a situation which is energetically extremely unfavorable. This is likewise the reason why the Si(335)-Au step edges do not host spin chains as will be outlined in the following paragraph.

5.6 Si(335)-Au: Charge Order at the Step Edges

Si(335)-Au is the member of the Si(*hhk*)-Au family with the smallest terrace width. Thus, it is not surprising that its terrace comprises a single Au strand only (see Fig. 5.13). DFT calculations propose an average step-edge occupation of one electron, which does not result in a spin chain with ×1 periodicity. Instead, one-half of the step-edge orbitals are empty and one-half are doubly occupied [23, A3]. At the first glance, a spin chain with ×1 periodicity might be a plausible step-edge configuration since the exchange splitting of singly occupied atoms leads to an energy gain in DFT. However, a spin site spacing of only a_0 causes a huge

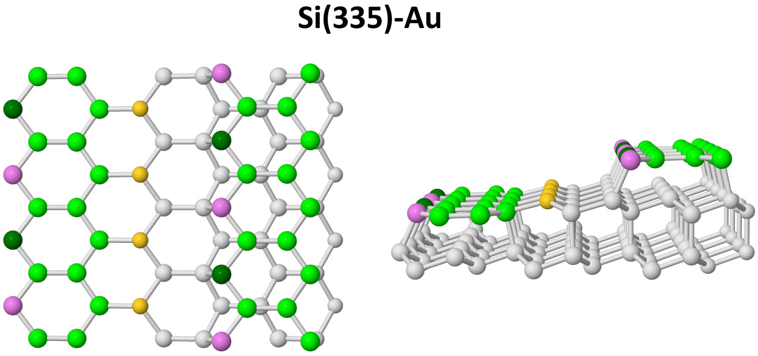

Figure 5.13: *Top and side view of the Si(335)-Au structure model. The terrace incorporates a monoatomic Au chain only (yellow). The step edge is built by a HCC of Si (light green). Si atoms directly at the step edge display a charge ordering such that half of the step-edge orbitals are empty (magenta) and half are doubly occupied (dark green). Atomic coordinates provided by S.C. Erwin.*

Coulomb energy penalty, which energetically forbids a spin chain with ×1 period [42,A3]. The step-edge charge order favored by DFT receives experimental support from bias-dependent STM experiments: Switching the sign of the tunneling bias, i.e., switching between occupied and unoccupied states, results in an inversion of the STM intensity at the step edge [33]. Such finding is fully consistent with one-half empty and one-half completely filled step-edge orbitals.

5.7 Si(775)-Au: Saturated Step Edges

Si(775)-Au comprises the largest step spacing of all members of the Si(hhk)-Au family ($L = 21.3\,\text{Å}$). Terraces are half again as wide as on Si(553)-Au, which is equivalent to two additional silicon unit cells. In contrast to its famous siblings with indices 553 and 557, Si(775)-Au was much less studied experimentally as well as theoretically. Only a few overview STM images [17, 152] and a ball-and-stick model [17], not tested with DFT, have been published in literature. The detailed atomic structure was unknown, as was the electronic configuration at the step edge and the presence of a phase transition. The following section will address these issues experimentally by STM and STS, and theoretically by DFT. The results are published in Ref. [A3].

New Structure Model – Fig. 5.14 shows two overview STM images of the occupied states (a) as well as the unoccupied states (b) of the Si(775)-Au surface respectively. These images reveal three rows of features (A, B, and C) separated by 21.3 Å, as well as occasional random defects which could be identified as Si-adatom vacancies and different types of misplaced Si adatoms (see Sec. 5.9). Each of the three rows exhibit a ×2 periodicity with respect to the silicon surface lattice constant $a_0 = 3.84\,\text{Å}$, although, it is much more pronounced in row B

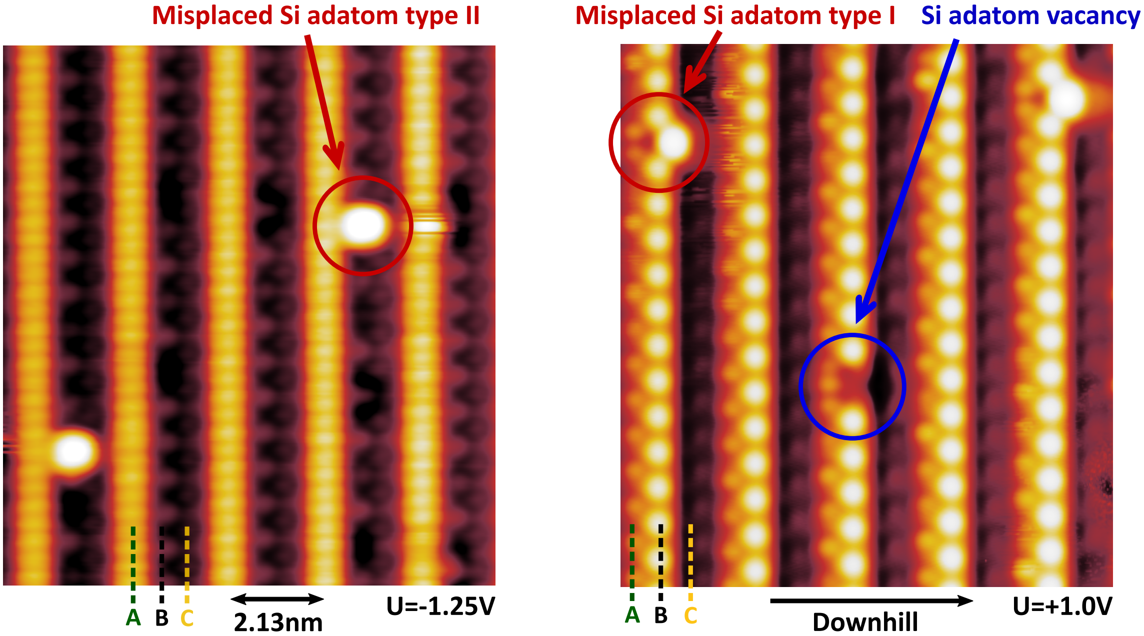

Figure 5.14: *Constant current STM overview images of the Si(775)-Au occupied (a) and unoccupied (b) states ($T = 77\,K$). Three different rows (A, B and C) can be identified. Several common native defects are labeled and will be discussed in detail in Sec. 5.9. (a) Adapted from [A4]. (b) Adapted from [A3].*

and C than in row A. These patterns do not change, within any row, between 5 K and 300 K as shown by the temperature-dependent STM study presented in Fig. 5.15. Hence, Si(775)-Au does not feature a transition to higher order periodicity in this temperature range, in contrast to Si(553)-Au (see Sec. 6.6). Notably, the Si(775)-Au STM images (Fig. 5.14) show a strong bias-dependent characteristics: The occupied state image ($U = -1.25\,\mathrm{V}$) is dominated by row A. For the unoccupied states, row B has the highest intensity. In this row different parts of a zigzag chain are highlighted by reversing the bias as will be discussed in detail below. Row C appears similar to the Au chain of the Si(553)-Au system [cf. Fig. 5.9]. In principle, the presented STM images are compatible with previous STM studies [17, 152], however, their improved resolution allows to identify the correct number of chain types as well as their superstructures. As a consequence, the ball-and-stick model proposed earlier [17] can be ruled out as a structure candidate. In contrast to the three atomic rows observed in Fig. 5.14, the ball-and-stick model shows only two chain types, and, thus, can safely be excluded.

Inspired by the STM images, a new structural model was developed in close collaboration with S.C. Erwin. In that process, DFT and in particular simulated STM images are utilized to proof the validity of the model. Fig. 5.16 displays the final result of this modeling. All motifs of the model are taken from Fig. 1.1, i.e., have already been found on other Si(*hhk*)-Au surfaces, although, there, arranged and combined in different ways. The step edge is again a graphitic Si honeycomb chain, as it is the case for all other members of the Si(*hhk*)-Au family. On the terrace a double chain of Au atoms incorporates in the topmost Si layer and

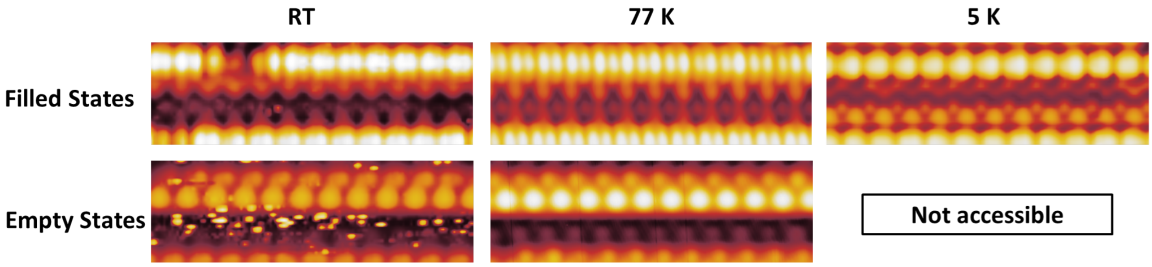

Figure 5.15: *Constant current STM images of the Si(775)-Au surface at various sample temperatures. Filled states images have been recorded at $U = -1.0\,V$ ($U = -0.95\,V$ for $77\,K$) and empty states are shown for $U = +1.0\,V$. All three chain types do not change their ×2 periodicity between room temperature and 5 K, which indicates the absence of a phase transition in this temperature window.*

repairs the surface stacking fault created by the Si HCC at the step edge. Noteworthy, this stacking fault occurs on Si(hhk) surfaces with $\alpha > 0°$ only , i.e. only on Si(553) and Si(775), implying that it is hardly a coincidence that just these two Au reconstructions form a Au double strand. The remainder of the terrace has a standard Si(111) crystal structure. The high number of dangling bonds of such surface is energetically costly, and, thus, in general reconstructs in the well-known (7×7) reconstruction. Such reconstruction is not possible on Si(775)-Au. Instead, the (111)-like region incorporates Si adatoms (black) to passivate most of its surface dangling bonds. The result is a double row of alternating adatoms (black) and unpassivated restatoms (blue) spatially shifted by a_0 and with ×2 periodicity each.

A comparison of simulated STM images based on this structural model to high-resolution experimental data is shown in Fig. 5.16(b). The respective occupied and unoccupied state images are in excellent agreement, and allow one to determine the atomic origin of all experimentally observed features. The bright row A dominating the filled state images corresponds to the unpassivated Si step-edge atoms. The zigzag row, labeled B, can be attributed to the staggered row of adatoms and restatoms. The experimental bias dependence of both rows is in excellent agreement with theory. For a more detailed bias dependent STM study see Fig. 5.21 presented further below. The clear zigzag appearance of row B for biases $\leq 0.3\,\mathrm{V}$ and the inversion of the relative intensities of adatom vs. honeycomb row that occurs at about 0.4 V provide additional support for the structure model presented. The third chain feature, row C, stems from the Au chain. Dimerization of the Au double strand manifests in a double row of staggered spots in STM with ×2 periodicity within each of the two rows. In particular, row C arises from the right-hand leg of the ladder formed by the Au chain. The additional row of weak spots, between rows B and C, come from the left-hand leg of the Au ladder. DFT calculations using PBE reveal a dimerization parameter $d = 0.08$, which is twice the Si(553)-Au value. Like for Si(553)-Au, the dimerization parameter is sensitive to the choice of DFT exchange-correlation functional and to the silicon lattice constant. In summary, the detailed structure, spacing, periodicities, and bias dependence of all elements

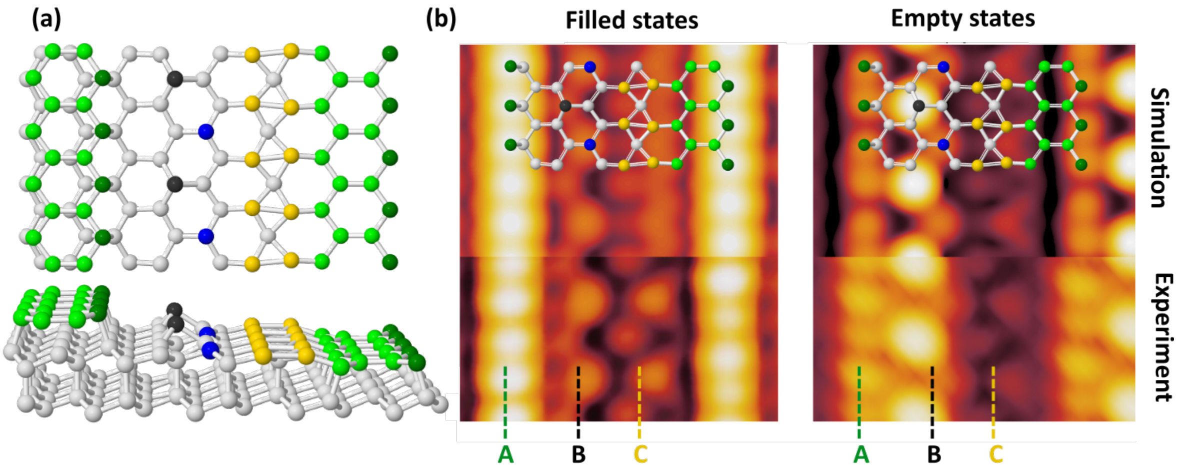

Figure 5.16: *(a) Proposed structure model for Si(775)-Au. Au atoms are colored yellow. All other atoms are Si. The step edge is a graphitic Si HCC (green). The terraces comprise a dimerized Au double chain as well as a row of Si adatoms (black) separated by $2a_0$ and accompanied by unpassivated Si restatoms (blue). (b) Comparison of experimental (bottom) and theoretical (top) STM images for filled and empty states ($U_{theo} = -0.8$ eV and $+0.8$ eV, $U_{exp.} = -1.0$ eV and $+1.0$ eV, $T = 77$ K). A top view of the structure model is superimposed the simulation for easier assignment of the various structural motifs. Simulation and experiment are in excellent agreement proofing the validity of the model presented in (a). From [A3].*

observed in experimental Si(775)-Au STM images are accurately explained by the proposed structural model.

Absence of Spin Polarization at the Step Edge – Having established a reasonable structure model for Si(775)-Au, one can address the electronic configuration of the Si step edge. Owing to its structural similarities to Si(553)-Au for which every third step-edge atom is completely spin-polarized, one may expect the formation of a spin chain. However, the Si(775)-Au step edge is completely non-spin-polarized within DFT. The reason for this difference is that there are enough electrons available to completely fill all dangling-bond orbitals at the Si(775)-Au step edge, resulting in doubly occupied lone pairs with zero spin polarization.

In order to test this theoretical finding experimentally, local STS was applied. Recall that the existence of spin polarization is intimately connected to the corresponding smoking gun electronic state found several tenth of an eV above E_F. Fig. 5.17 shows dI/dU spectra taken at the three distinct structure elements, namely, row A, B, and C. The spectrum characteristic for the step edge is strongly peaked at -0.8 eV and has no significant weight above the E_F. This is the signature of a fully occupied state, and, hence, is consistent with the DFT result of a non-spin-polarized lone pair at the Si(775)-Au step edge. The spectrum taken at the adatom row shows an intense peak at about +0.6 eV only. A peak in a similar energy region has also been observed for the Si(557)-Au adatom spectrum [Fig. 5.12(a)] and reflects the empty adatom dangling bond orbital. The smaller peak of the Si step edge and the Au

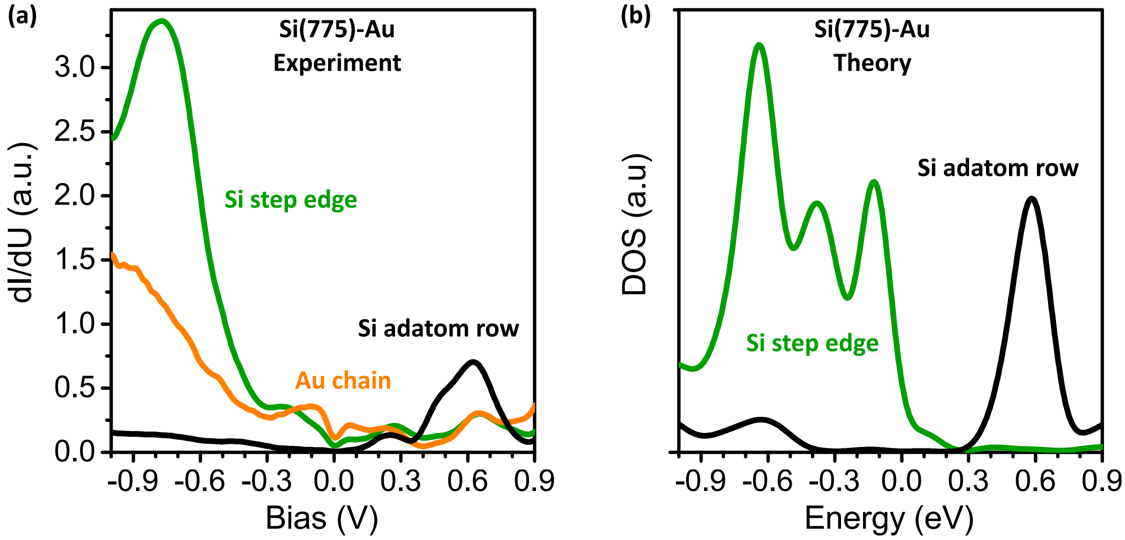

Figure 5.17: *(a) STS spectra taken at the three different structural elements of the Si(775)-Au surface at 77 K. Spectra have been recorded using the lock-in technique with a modulation bias* $U_{mod} = 10\,\mathrm{meV}$. *Several single-point spectra were averaged to improve statistics. The green spectrum peaks at -0.8 eV indicating double occupied step-edge orbitals. (b) Si(775)-Au LDOS from DFT/HSE calculations based on the model proposed in Fig. 5.16(a). From [A3].*

chain spectrum in this energy region is very likely an imprint of the intense adatom DOS due to the finite spatial resolution of the STM tip. The experimental STS spectra are in good qualitative agreement with the LDOS obtained from DFT/HSE calculations [see Fig. 5.17(b)]. Minor discrepancies like the detailed energy distribution of the step-edge DOS do not question the validity of the structure model but are in fact not surprising having in mind the limitations and approximations of DFT and STM (cf. Chapt. 3).

5.8 Electron Counting

The complete experimental and theoretical scrutiny of all four members of the Si(hhk)-Au family allows to verify the relationship between structural motifs and spin chain formation, and, thus, to understand why spin chains develop on some Si(hhk)-Au surfaces but not on others.

The step-edge atoms of the Si HCC form three covalent bonds leaving a single sp^3-orbital that is not part of any bond. Neglecting band dispersion, this orbital can be occupied by either zero, one or two electrons. Spin-polarized DFT calculations for all Si(hhk)-Au systems reveal that one-electron occupancy occurs with a large on-site exchange splitting (about 1 eV), resulting in the characteristic unoccupied spin state. This finding does not depend on any magnetic order in the system, and leads to the basic condition for spin chain formation: If the electron count is large enough to singly occupy some, but insufficient to doubly occupy all of the step-edge orbitals, local spin moments can form. In summary, two out of four

Surface	Average occupancy per step-edge atom	Individual occupancies	Spin chain formation
Si(335)-Au	1	2, 0	No
Si(557)-Au	3/2	2, 1	×2
Si(553)-Au	5/3	2, 2, 1	×3
Si(775)-Au	2	2	No

Table 5.1: *Summary of the average and individual step-edge orbital occupancy for each Si(hhk)-Au surface. Si(553)-Au and Si(557)-Au form spin chains at their respective step edges. Adapted from [A3].*

members of the Si(*hhk*)-Au family are subject to such spin chain formation. On Si(553)-Au, two-thirds of the step-edge orbitals are doubly occupied, and one-third are singly occupied, resulting in a spin chain with ×3 periodicity. On Si(557)-Au, one-half are doubly occupied, and one-half are singly occupied, forming spin chains with ×2 periodicity. On Si(335)-Au, half the step-edge orbitals are empty and half are doubly occupied, and spin chains do not develop. On Si(775)-Au, every orbital is doubly occupied. Again, no spin chains form. These *individual* step-edge occupancies revealed by DFT are summarized in Table 5.1.

The corresponding *average* occupancies can also be obtained by electron counting. From the average electron occupancies one can easily derive the individual step-edge occupancies which, in turn, give information about the existence and period of spin chains. The explicit counting has been elaborated by S.C. Erwin and is detailed in the Supporting Information of Ref. [A3]. The starting point of the counting is an hypothetical "ideal" step edge of Si(*hhk*)-Au surfaces, i.e., before any electrons transfer from or to the terraces took place. The Si honeycomb structure motif has first been identified on the Si(111)-M surfaces, which show a "honeycomb chain-channel" (3×1) reconstruction after adsorption of a metal (M represents the metal adsorbate) [153]. Its structure comprises Si honeycomb chains separated by single M chains (see Fig. 5.18), reflecting a minimal model of the Si HCC motive. In case M is an alkali metal, the outer atoms of the Si HCC are doubly occupied lone pairs. From this one can conclude that the "intrinsic" step edges of Si(*hhk*)-Au surfaces (before any electron transfer from or to the terraces) consist of doubly occupied Si step-edge atoms [153]. Using this electronic step-edge structure as a starting point, one can deduce the step-edge occupancy for all Si(*hhk*)-Au surfaces by accounting for the electronic contribution of additional structure motifs on the terraces and the DFT band filling of the parabolic Au induced bands (see Supporting Information of Ref. [A3]). The result of this procedure coincidences with the DFT outcome for all Si(*hhk*)-Au surfaces and suggests an *electron transfer* between the terrace and the step edge.

It should be noted that for Si(553)-Au the band filling of the inner Au band observed experimentally significantly deviates from the DFT value. One possible explanation for this discrepancy could be external electron doping of the Si(553)-Au surface by, e.g., substrate dopants or defects, as will be further discussed in Sec. 6.5.

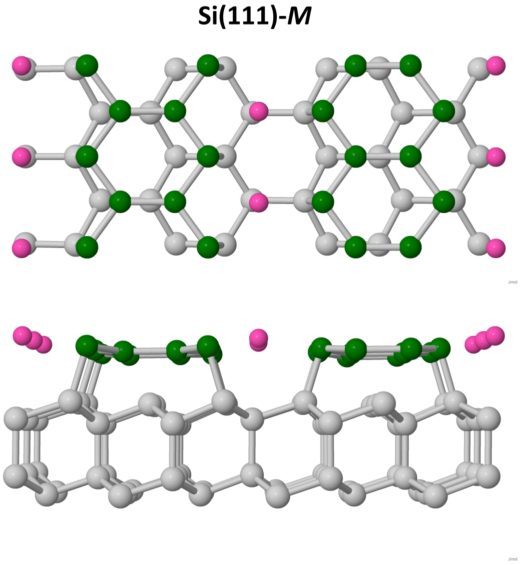

Figure 5.18: *Representative structure model for the Si(111)-(3×1)-M surface. In the model presented the metal adsorbate is Li. Magenta atoms represent Li atoms. All others are Si. The Si atoms in the top layer reconstruct in a honeycomb chain-channel structure (green) [153]. Atomic coordinates provided by S.C. Erwin.*

5.9 Creation and Suppression of Spin Chains

5.9.1 Doping-Induced Spin Chains in DFT

The completely non-spin-polarized step edge of Si(775)-Au offers an ideal test case for the idea of creating and manipulating spins on Si(*hhk*)-Au surfaces. The picture of electron counting and charge transfer developed above suggests that adding holes to Si(775)-Au creates local spin moments, as long as the holes localize at the step edge and not somewhere else. DFT results confirm and illuminate this notion in several ways. Adding holes to the ideal Si(775)-Au surface indeed results in a complete localization of the holes at the step edge. As a consequence, local magnetic moments emerge at the step-edge atoms. Although the total moment is equal to the number of added holes, each spin moment is partially delocalized along the step edge. The degree of spin delocalization depends on the number of added holes as demonstrated by the results shown in Fig. 5.19. For low hole concentration – reflected by a DFT calculation with one additional hole per eight step-edge atoms – the resulting spins partially delocalize along the step edge (see red curve in Fig. 5.19). For higher hole concentration, the spin moments get more localized as revealed by a calculation with one added hole per four step-edge atoms (green curve in Fig. 5.19). In case of a charged defect nearby, the spins get further localized (blue curve in Fig. 5.19), which will be discussed in detail below. This theoretical proof of principle implies that adding holes (or electrons) to Si(*hhk*)-Au systems may result in the formation or suppression of local spins. In particular, adding electrons to the Si(557)-Au and Si(553)-Au surface should suppress the intrinsic spin

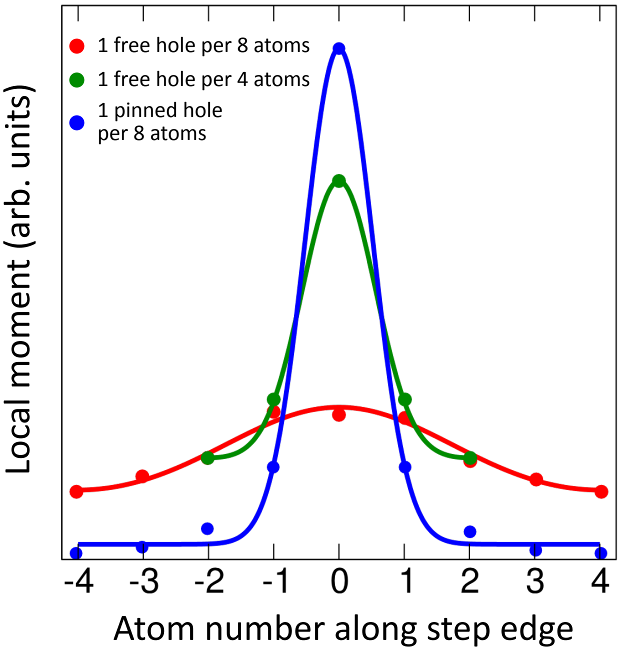

Figure 5.19: *DFT calculations demonstrating the formation of spin moments upon doping holes to the Si(775)-Au surface. Low hole concentration of one hole per eight step-edge atoms results in a partially delocalized spin along the step edge (red curve). Doping of one hole per four step-edge atoms reveals a more localized moment (green curve). A charged defect, i.e., a vacancy in the adatom row as presented in Fig. 5.20, pins the hole to the step-edge atom closest to the defect (blue curve). Curves are Gaussian fits to local magnetic moments obtained by DFT. From [A3].*

chains at their respective edges or result in spin chains with higher periodicity, depending on the amount of added electrons. The step edges of the Si(335)-Au surface should be subject to spin chain formation when adding additional electrons. The detailed spin site density, and, thus, the periodicity of the spin chain depends on the concentration of the added electrons. In turn, Si(775)-Au requires hole doping to render its step edges spin-polarized. An experimental verification of this basic doping strategy will be presented in the next paragraph.

5.9.2 Experimental Proof of Principle: Doping by Native Defects

The Si(775)-Au surface features several native defects, which typically occur with a concentration of 5-10 % (see Appendix Fig. F.9). These defects correspond to missing or missplaced atoms in the surface lattice structure and differ from the adsorbate-induced defects discussed in Sec. 5.2. Lattice defects are a natural part of the Si(775)-Au surface and can not be suppressed by minimal exposure time to residual gas atoms like it is the case for adsorbate induced defects. Extensive tuning of the growth parameter did not result in a significantly lower defect concentration.

Spin Site Inducing Defect – The following paragraph will demonstrate that one of these characteristic defects creates a single localized spin at the Si step edge. As a first step, electron counting for various lattice defects will be presented to give an intuitive understanding of this finding. Each Si adatom supplies four electrons. The three surface dangling bonds surrounding the adatom site form covalent bonds using three of the four electrons provided by the adatom. It is well known from DFT calculations and STS data (Fig. 5.17) that the surface dangling bond of the adatom is empty (Fig. 5.17). The fourth electron must thus reside elsewhere. DFT calculations reveal that this electron transfers to the nearest available step-edge orbital and creates a doubly occupied lone pair there. Reversing this analysis leads to the following fascinating result: Generating an adatom vacancy removes one electron from the doubly occupied lone pair, and, thus, should create a single spin at the step edge. The DFT results presented above show that the adatom vacancy indeed induces a spin site, which is localized at one step-edge atom (blue in Fig. 5.19). The origin of this localization is of electrostatic nature. Each spin created by an adatom vacancy is positively charged relative to the background of doubly occupied step-edge atoms. Due to electroneutrality of the whole system, each adatom vacancy is negatively charged. Hence there should exist an electrostatic attraction between the vacancy and the induced spin. The work to move the spin in the corresponding electric field is thus expected to follow $-q^2/\epsilon R$. This hypothesis has been tested by a series of DFT calculations where the spin is forced to localized at step-edge atoms nearby the step-edge atom closest to the vacancy. DFT total energy changes relative to the case of large spin-vacancy separation are plotted in Fig. 5.20(a). The resulting curve reflects the binding energy of the spin site and shows the expected $1/R$ behavior confirming an attractive electrostatic interaction. Noteworthy, these calculations show that the step-edge site closest to the vacancy is energetically most favorable and reveal a binding energy of 85 meV for the spin.

Experimental STM and STS measurements fully support the analysis presented above. Fig. 5.20(b) shows a simulated STM image (left) of the region around a Si adatom vacancy. The step-edge atom closest to the defect is now spin-polarized. This manifests itself as increased intensity when imaged at (high) positive biases due to the unoccupied exchange-split state of the induced spin. The experimental STM image [right in Fig. 5.20(b)] also shows enhanced intensity at the step-edge atom closest to the defect, and is perfectly in line with the simulation. Additional support is given by local STS. The tunneling spectrum taken at the defect-induced spin site [red spectrum in Fig. 5.20(c)] exhibits a distinct DOS maximum at 350 meV above the Fermi level. This unoccupied state is similar to the fingerprint spin state found at the Si(557)-Au and Si(553)-Au step edges, and suggests the formation of an localized spin at this particular step-edge site. As a cross-check, such a state is not present in the local spectrum taken at an unaffected step-edge atom [green in Fig. 5.20(c)], which shows no significant DOS above E_F. The peak at about 700 meV is very likely induced

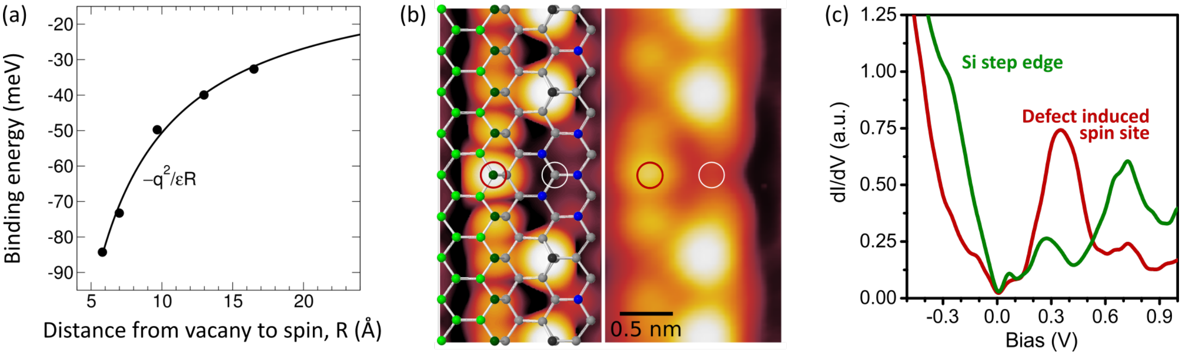

Figure 5.20: *(a) DFT total energy changes with respect to the case of large spin-vacancy distance. The 1/R behavior proofs an electrostatic attraction between vacancy and step-edge spin. The situation displayed in (b) corresponds to the lowest energy configuration with a binding energy of 85 meV. (b) Theoretical and experimental STM image of an adatom vacancy on Si(775)-Au. The missing adatom induces a spin site (red circle) at the step-edge atom closest to the vacancy (white circle), which manifests as increased intensity of this step-edge atom in both images. (a) and (b) adapted from [A3]. (c) Single point tunneling spectra taken on an unaffected Si step edge (green) and on the Si step-edge site closest to an adatom vacancy (red). The intense peak at approximately +350 meV suggests the formation of an unpaired spin at this step-edge site. From [A8].*

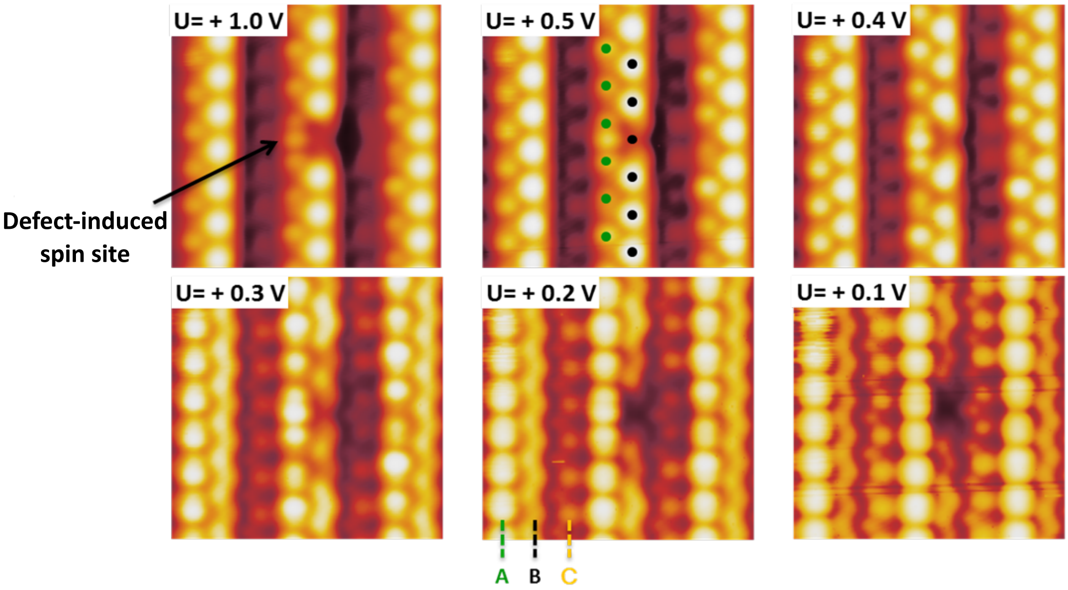

Figure 5.21: *Unoccupied states bias series of a region around a Si adatom vacancy on Si(775)-Au. The step-edge site closest to the adatom vacancy (black arrow) shows enhanced intensity for tunneling biases ≥+0.3 V, as expected for a step-edge atom hosting an unpaired spin. From [A3].*

by the adjacent Si adatom row located only a few Å away from the step edge [cf. adatom spectrum in Fig. 5.17(a)]. Further support comes from a bias dependent STM study of a region around an adatom vacancy which is presented in Fig. 5.21. The spin site is most pronounced at about 0.4 eV above E_F and can hardly be identified at +0.1 V and +0.2 V, as expected for an unoccupied state located at +0.35 eV. These results theoretically and experimentally demonstrate the fascinating possibility to turn the initially nonpolarized Si(775)-Au step edge into a spin-polarized state.

Other Defect Types – Aside the adatom vacncies, two other defects are commonly found on Si(775)-Au, namely two different types of misplaced adatoms. A structural model, simulated STM images, and experimental STM data for both misplaced adatom defects (Type I and Type II) are displayed in Fig. 5.22(a) and (b), respectively. In both cases, the theoretical simulation is in detailed agreement with the experimental STM images, giving excellent support for the proposed structural models. Misplaced adatom Type I acts as a phase defect. It interrupts the usual $2a_0$ spacing of normal adatoms, reducing the expected $4a_0$ spacing between the two adjacent normal adatoms to $3a_0$. As a consequence, the adatom row segments below and above the defect are (phase) shifted by a_0 with respect to each other [see black dots and stars in Fig. 5.22(a)]. This phase shift is not restricted to the adatom row. In fact, also the Au chain and the Si step-edge atoms exhibit an a_0 phase shift across the defect as visualized by the colored dots and stars in the unoccupied STM images taken at +0.5 V and +0.2 V. Such phase defects may be the reason for the observation of (intensity-modulated) ×2 streaks instead of ×2 spots in the Si(775)-Au LEED pattern [see Fig. 5.6(c)].

The effect of the misplaced adatom Type I on the step edge's electron concentration is easiest to evaluate in three stages: As discussed above, removal of a normal adatom and its four electrons transfers one hole to the step edge. Next, the entire row of normal adatoms on one side of this vacancy has to be shifted toward the vacancy by a_0, anticipating the actual spacing around the misplaced-adatom defect. This increases the total number of adatoms by one-half. Since the addition of half an adatom is equivalent to the addition of half an electron to the step edge, 0.5 holes have been added to the step edge so far. Sticking the removed adatom to its new misplaced site is equivalent to adding one electron. The overall net change induced by a misplaced-adatom defect is *0.5 additional electrons.* Consequently, the misplaced-adatom defect Type I should *not* create a spin at step edge. In agreement with the finding from electron counting, the experimental STM images of the region around adatom defect Type I do not show any evidence of spin-polarized step-edge atoms.

Electron counting for misplaced-adatom defect Type II follows the same line as for Type I. Contrary to Type I, misplayed adatom Type II does not create a phase defect. The adatom rows contiguous to the vacancy are not shifted by a_0 but show the same phase [see black dots in Fig. 5.22(b)]. Consequently, the total adatom number is not increased by 0.5 adatoms and the overall net change induced by misplaced adatom Type II is 0.5 electrons less than for

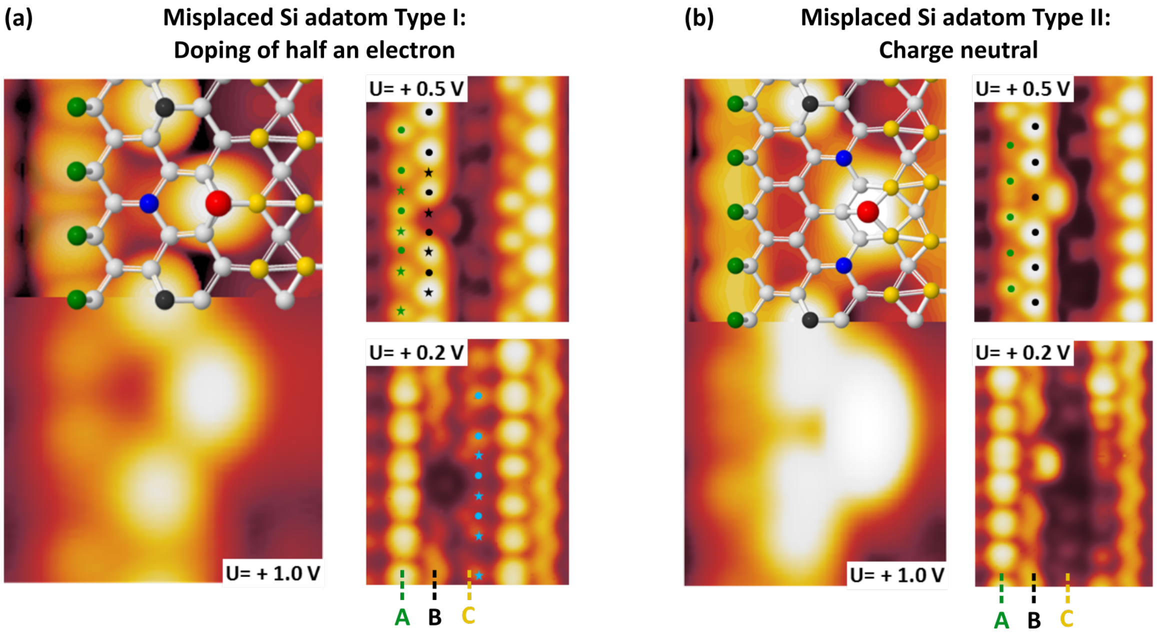

Figure 5.22: *(a) Structural model, simulated and experimental STM images of Type I misplaced-adatom defect. This phase defect disrupts the usual adatom spacing, as indicated by the colored dots and stars in the right-hand panels. (b) Structural model, simulated and experimental STM images for Type II misplaced-adatom defect. In contrast to the Type I defect, the Type II defect does not disrupt the adatom spacing, as demonstrated by the green and black dots in the right-hand panel. Both defect typs do not induce a spin site at the step edge since they are electron-donation (Type I) and charge neutral (Type II). From [A3].*

misplaced adatom Type I. Thus, Type II is *charge neutral* and should not induce any spin at step-edge atoms. The experimental STM images are consistent with this result. The step-edge atom closest to the vacancy does not show increased intensity, although the tunneling conditions are chosen such that they are sensitive to the characteristic unoccupied spin DOS.

In summary, three different unintentional defects of the Si(775)-Au surface have been studied. It has been consistently shown by STM, DFT, and electron counting that one of these defects is electron-donating (misplaced-adatom defect Type I), one is charge-neutral (misplaced-adatom defect Type II) and one is hole-donating (adatom vacancy). Only the hole-donating adatom vacancy renders the adjacent step-edge Si atom spin-polarized. These findings do not only evidence electron transfer between native defects and the Si step edge, but also provide further support for the fundamental picture of electron transfer between undisturbed Si(*hhk*)-Au terraces and their respective step edges.

5.9.3 Manipulation of Spin Chains: Alternative Approaches and Relevance for Other Material Systems

The findings presented above suggest to use STM atom manipulation [154] to create and arrange adatom vacancies on Si(775)-Au in order to realize spin chains with tunable spacings and length. Moreover, it demonstrates the feasibility to induce localized spins by doping, and reveals a pathway to use surface chemistry to create or suppress spin chains on Si(*hhk*)-Au surfaces. On the one hand, this can be realized by electron or hole donating adsorbates like I^-, Cl^- ,K^+, Li^+ (see Sec. 6.7). On the other hand, the threefold coordinated step-edge atoms offer perfect adsorption sites for step edge passivating adsorbates like hydrogen [A9].

An alternative approach is to fine-tune the growth conditions of the self-assembled atomic wire arrays as reported in Ref. [146]. In this work, a reduced Au coverage results in pristine Si terraces between each Si(553)-Au-like reconstructed terrace. The incorporated Si terraces increase the distance between Si(553)-Au terraces. Thereby, the charge ordering at the step edges is found to be suppressed [146]. The authors of Ref. [146] argue that this is due to strain induced by the additional Si (5×5) terrace and rule out a significant charge transfer from the pristine Si terrace. This argument is based on the step-edge periodicities found in bias-dependent STM images as well as on DFT calculations. However, DFT cannot confirm the absence of charge ordering at the step edge, but finds a spin chain with ×5 periodicity most stable. Irrespective of the clear experimental evidence for the absence of a spin chain at 77 K, the interpretation that strain is the driving force is not convincing and requires further support. Moreover, no STM measurements below 77 K have been performed so that there is still the possibility to detect a spin chain at lower temperatures, as predicted by DFT [146], and expected for an electron transfer of less than one-third an electron per step-edge atom.

The results presented above about controlling spins at the steps of Si(*hhk*)-Au are not limited to the specific choice of silicon or the high-index setup. Instead, they may be relevant – probably with interesting modifications – to other related material systems such as graphene and its intensively studied analogs with higher order number Z, like silicene [155–157], germanene [158–161], stanene [162, 163] and bismuthene [115] as well as their physical configurations, such as finite ribbons. To mention only a few recent findings in this context: First experimental indications for partially filled dangling bond orbitals at the zigzag edges of graphene nanoribbons have been found [36]. On planar graphene, vacancies in the graphene lattice [164] as well as adsorption of atomic hydrogen [165] were discovered to induce unpaired spins. Both of these papers create the impression that the detection of localized unpaired spins or spin chains equals the detection of magnetism. Noteworthy, this not the case since there is no necessity that localized spins order magnetically as will be discussed in Sec. 6.1. In fact, both papers do not provide experimental evidence for magnetic ordering of the localized spins.

Overview of Si(*hhk*)-Au Findings

The presented scrutiny of various Si(*hhk*)-Au surfaces by STM, STS, and DFT revealed the following results:

I) The KK model is the most promising structure model for the Si(111)-(5×2)-Au surface.

II) The step edges of the Si(553)-Au and the Si(557)-Au surface are subject to the formation of spin chains.

III) The Si(775)-Au surface comprises three different chain types, namely, a Si honeycomb chain at the step edge, a double strand Au chain, and a staggered adatom-restatom chain. All three chains have been combined in a new structural model which is in excellent agreement with the experimental data.

IV) The step edges of Si(775)-Au do not host spin chains. Instead, all step-edge orbitals are doubly occupied.

V) The formation of spin chains on Si(*hhk*)-Au surfaces is determined by the total electron count and charge transfer between the terrace and the step edge.

VI) Hole doping can render the Si(775)-Au step edges spin-polarized. An experimental verification of this DFT proposal was realized by native lattice defects. One of these defects – a vacancy in the adatom chain – induces a single magnetic moment which is localized at the step atom nearby the vacancy.

After having shown why spin chains form on some Si(*hhk*)-Au step edges but not on others, the next section will focus on the Si(553)-Au spin chains and various interactions with their atomic environment.

6 Si(553)-Au: Interactions of Si Spin Chains

6.1 Absence of Magnetic Order: Evidence for a 2D Spin Liquid

Notwithstanding the strong experimental evidence for the formation of spin chains, i.e. for charge ordering, at the Si(553)-Au step edges (Sec. 5.4), the question as to whether or not such uncompensated local spins order magnetically is still unanswered. The initial Si(553)-Au spin chain proposal in Ref. [1] found an AFM coupling of the localized spins along the step edge ($T = 0\,\mathrm{K}$). The presence of such a magnetic state at $T > 0\,\mathrm{K}$ seems to contradict the Mermin-Wagner theorem which states that quantum fluctuations prohibit any magnetic ordering above $T = 0\,\mathrm{K}$ in strictly 1D (or 2D) systems [7]. However, this is only valid for perfectly isotropic 1D or 2D set-ups. Even small anisotropic contributions lead to an effective suppression of fluctuations and the possibility for magnetic order at $T > 0\,\mathrm{K}$ [166]. Thus, in real-world systems, additional couplings with other dimensions – in the present case between neighboring step edges – can stabilize magnetic order at sufficiently low but finite temperatures.

Mapping the Si(553)-Au DFT results on a nearest-neighbor Heisenberg model yields a strong AFM coupling along the chains ($J_{\|} = 15\,\mathrm{meV}$) and a small, but finite, FM coupling perpendicular to the chains ($J_{\perp,1} = -0.3\,\mathrm{meV}$). These findings imply an overall AFM ground state. However, the STM and SPA-LEED data presented below reveal a spin site arrangement which differs from that assumed in the DFT proposal. In particular, spin sites of adjacent spin chains are found to be located in a centered geometry, which may have consequences for the magnetic ordering of the spins. The following section will first present the experimental results proofing the new lateral spin site arrangement and then discuss its implications for magnetic ordering of the Si(553)-Au spin chain array. Most of these results are published in [A6].

6.1.1 Centered Spin Site Geometry

Information from SPA-LEED – Fig. 6.1(a) shows a SPA-LEED image of the Si(553)-Au surface taken at 80 K. At this temperature, the Si step edges are subject to a ×3 spin chain formation. Consequently, one should observe some intensity at 1/3 and 2/3 positions

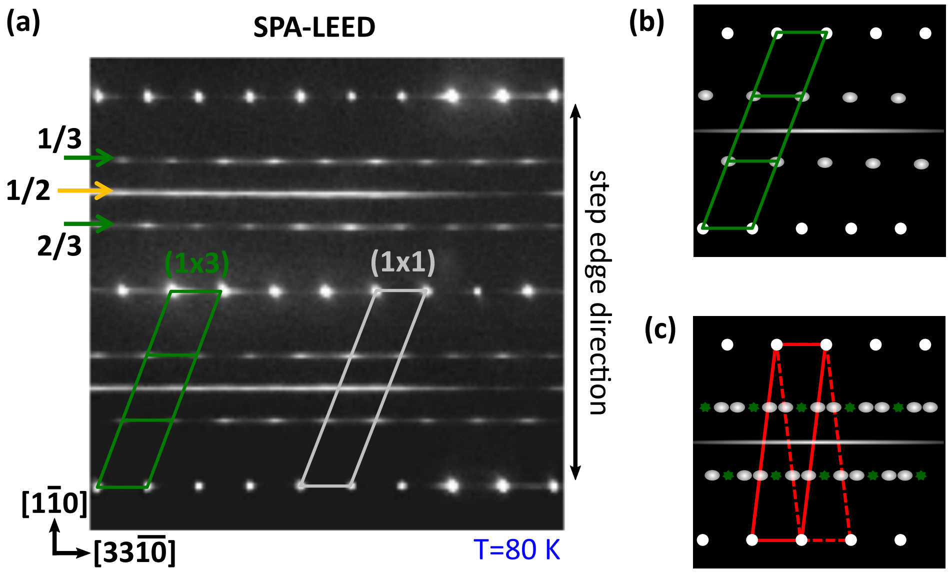

Figure 6.1: *(a) SPA-LEED pattern of the Si(553)-Au surface taken at $T = 80\,\mathrm{K}$ and 150 eV . The spot sequence at 1/3 and 2/3 positions between the row of integer spots originates from the step-edge spin chains and indicates a clear interwire coupling. Corresponding (1×1) and (1×3) unit cells are marked in gray and green respectively. (b) Sketch of the diffraction pattern based on the (1×3) unit cell shown in (a). (c) Diffraction pattern of the unit cell proposed by Ref. [1]. Gray ovals represent the expected diffraction spots at ×3 positions. Green stars mark the position of the diffraction spots observed experimentally. The red dashed line represents the mirror domain, which results in an additional diffraction spot sequence at ×3 positions. Adapted from [A6]. SPA-LEED image recorded by B. Hafke.*

in between the rows of integer order spots. In addition to the main spot rows and the ×2 streaks known from the RT diffraction pattern [Sec. 5.2 Fig. 5.6(a)], one can indeed identify a row of spots at these positions. The observation of spots rather than streaks suggests that adjacent spin chains show a non-negligible interaction, which results in a fixed phase relation between neighboring spin chains. From the position of the ×3 spots with respect to the integer spots one can derive the geometry of the (1×3) unit cell spanned by the spin sites [see green rhomboids in Fig. 6.1(a)]. Since all spin chains show a strict ×3 period, in principle, three distinct phase relations between adjacent spin chains are possible. Spin sites of neighboring steps can be shifted by either $1/2\,\mathrm{a}_0$, $3/2\,\mathrm{a}_0$, or $5/2\,\mathrm{a}_0$ along the step direction. Note that neighboring step-edge atoms show an intrinsic shift of $1/2\,\mathrm{a}_0$ due to the Si lattice structure (see e.g. Fig. 5.8). In reciprocal space, this results in three different lateral translational vectors, which may span the primitive unit cell. The DFT proposal from Ref. [1] assumed a phase shift of $1/2\,\mathrm{a}_0$ between adjacent spin chains. This corresponds to the red unit cell pictured in Fig. 6.1(c). A phase shift of $5/2\,\mathrm{a}_0$ results in a mirror symmetric situation (with respect to a mirror plan perpendicular to the step direction), which inevitably shows the same unit cell geometry [dashed red unit cell in Fig. 6.1(c)]. Such unit cells imply diffraction spots at the position of the gray ovals. However, these gray ovals do not coincide with the positions of the experimentally observed ×3 spots, which are marked by green stars in Fig. 6.1(c). The third

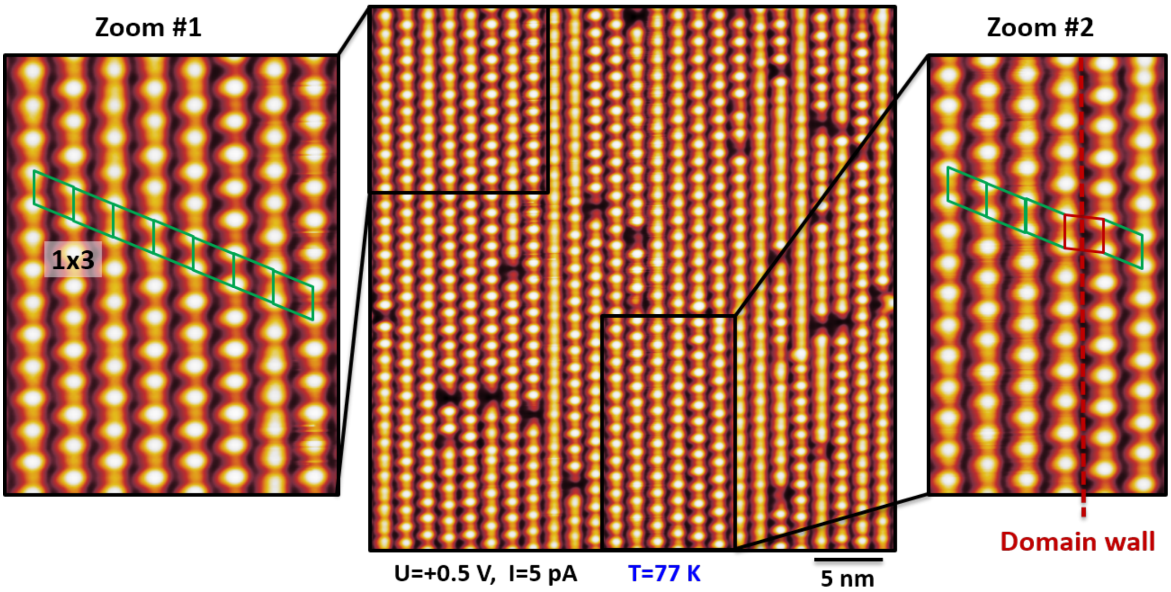

Figure 6.2: *STM image of the Si(553)-Au surface at 77 K depicting the empty states. The tunneling bias was chosen to be $U = +0.5\,V$ to highlight the (×3 periodic) Si step-edge atoms with partially filled dangling bonds. Zoom #1 shows a well ordered, eight chain wide area of the centered spin site arrangement. Zoom #2 depicts two ordered, centered domains separated by a linear domain wall, which locally exhibits the original structure proposed by Ref. [1]. Adapted from [A6].*

possible phase relation is a lateral shift of $3/2\,a_0$, which is equal to a centered arrangement of the spin sites. The corresponding unit cell is displayed in Fig. 6.1(b) as a green rhomboid. The expected diffraction pattern for this unit cell exactly matches the diffraction spots observed experimentally. A quantitative analysis of the spot profile of the ×3 spots along the $[33\overline{10}]$ direction reveals a correlation length of $\Gamma \approx 10\,\text{nm}$ perpendicular to the steps [A6].

Information from STM – The centered arrangement of the spin sites is also observed in real space by STM. Fig. 6.2 shows an overview STM image of the Si(553)-Au unoccupied states with particularly low defect concentration. The tunneling bias was chosen to be $U = +0.5\,\text{V}$ to emphasize the DOS of the spin sites. For the area shown in zoom # 1, the centered registry is preserved over a distance of eight chains, consistent with the correlation length extracted from the fit to the SPA-LEED line profile [A6]. Zoom # 2 depicts two antiphase translational domains (green unit cells) separated by a linear domain boundary, which locally exhibits the spin site arrangement assumed by Ref. [1] (red unit cell). Based on the STM and SPA-LEED results, one can conclude that there is a significant lateral interaction between the Si step edges despite their rather large separation of 14.7 Å.

Information from DFT – DFT calculations also prefer the centered spin site assembly. Compared to the old arrangement, it is favored by 1.6 meV per spin [A6]. This result agrees with an estimate of the Madelung energies of both geometries as detailed in Ref. [A6]. The

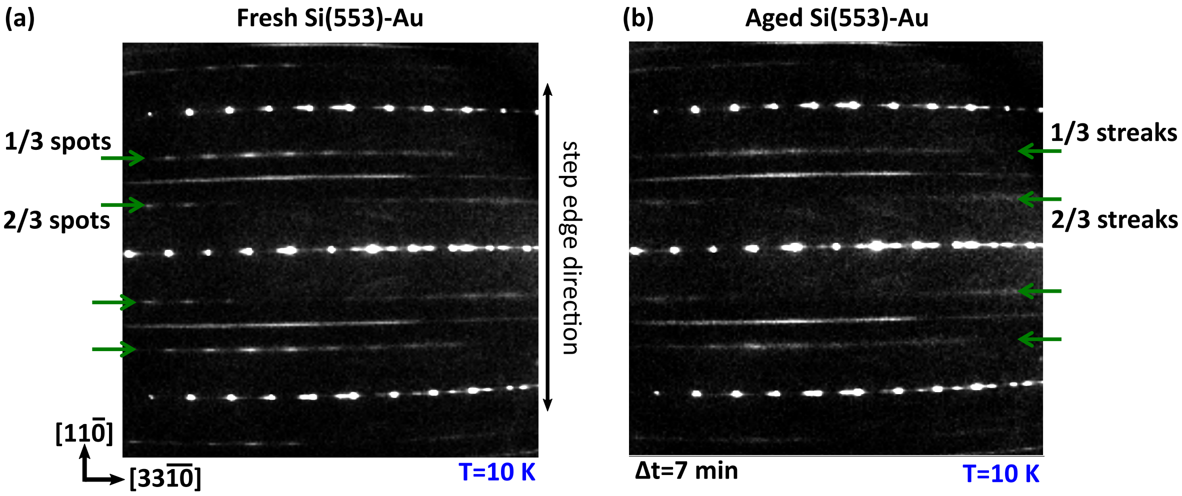

Figure 6.3: *(a) SPA-LEED pattern of a fresh Si(553)-Au surface taken at 10 K. The sample has been recleaned on the sample manipulator according to Eq. 7.1 given in the Appendix. When the sample reached its base temperature of 10 K, the SPA-LEED measurement was started. At 1/3 and 2/3 positions between the main spots, a sequence of spots is observed. (b) SPA-LEED pattern recorded 7 min after the image presented in (a). The ×3 spots are strongly elongated in [33$\overline{10}$] direction and, thus, appear streak-like. All other diffraction intensities are basically unchanged. The intensity between the integer spots is due to a refacetting of minor sample areas to other Si(hhk)-Au surfaces, but does not affect the detected aging effect.*

Madelung constant of the centered geometry, $\alpha_{centered} = 1.6488$, is larger than for the unit cell proposed earlier, $\alpha_{original} = 1.6475$. The difference corresponds to an energy difference of 2.1 meV per spin [A6]. Both calculations imply that the interaction between adjacent step edges is primarily Coulombic (electrostatic) and, thus, not driven by the coupling of local spin moments.

Effect of Defects – Noteworthy, earlier LEED and STM experiments revealed significantly lower correlation lengths [25, A1]. The LEED image presented in Ref. [25] displays streaks instead of spots at ×3 positions, suggesting a random registry between adjacent spin chains. This apparent discrepancy could be explained by time-dependent SPA-LEED experiments. Fig. 6.3(a) shows a SPA-LEED image of a fresh Si(553)-Au surface taken at 10 K. Before image acquisition, the sample was recleaned on the sample manipulator according to the recipe presented in the Appendix (Sec. C). At ×3 positions, a clear spot sequence is observed. Fig. 6.3(b) provides a SPA-LEED image taken on the very same surface, but 7 minutes after the image presented in (a). In this case, the ×3 spots are much more elongated in [33$\overline{10}$] direction and, thus, appear as streaks. This finding implies that the interwire correlation length has significantly reduced within 7 minutes. The reason for this decrease is an increase of the step-edge defects generated by exposure to residual gas atoms (base pressure of $1 \cdot 10^{-10}$ mbar). Moreover, the electron beam of the SPA-LEED appears to catalyze the defect generation. A high defect concentration results in a short average wire length, which, in turn, increases the number of domain boundaries in lateral direction (cf. Sec. 6.4). Therefore, the low-defective STM image presented in Fig. 6.2 could only be achieved by optimized sample preparation and minimal exposure time to residual gas atoms as detailed in Sec. 5.2.

6.1.2 Consequences for Magnetic Ordering

As already mentioned in the introduction of this section, DFT calculations of Ref. [1] predict a strong AFM coupling of the spins along the step edge and a weak FM coupling across the steps. The exchange constant $J_{\perp,2}$ for next-nearest-neighbor spins on adjacent chains was not calculated, but should be even smaller than $J_{\perp,1}$ due to the larger spin spacing [see Fig. 6.4(a)]. For the new centered spin site assembly, the situation is drastically different: The isosceles triangular spin arrangement results in a degeneracy of $J_{\perp,1}$ and $J_{\perp,2}$ [see Fig. 6.4(b)].

As a consequence, the spins are magnetically frustrated, since both (competing) exchange couplings cannot be satisfied simultaneously, and magnetic order is suppressed. Note that this does not depend on the sign of $J_\perp$. Such a geometry has been modeled theoretically by the anisotropic triangular Heisenberg spin-1/2 model [167, 168]. The model consists of 1D chains coupled in a zigzag fashion exactly as in the case of Si(553)-Au spin chains. The ratio of $|J_\perp|/J_\|$ interpolates between the ideal 1D chains ($|J_\perp|/J_\| = 0$) and the isotropic triangular lattice ($|J_\perp|/J_\| = 1$). It turns out that the ground state phase diagram depends on the ratio of $|J_\perp|/J_\|$ only. For the case of an isotropic triangular lattice, 120° Néel AFM order usually is the preferred ground state [167]. For a sufficiently strong anisotropy, ($|J_\perp|/J_\| < 0.8$) a quantum spin liquid (QSL) ground state is suggested [167,168]. The new spin site arrangement gives an exchange coupling constant of $J_\| = 16\,\text{meV}$ along the chains and $J_\perp = -0.4\,\text{meV}$ perpendicular to the steps [A6]. This results in a ratio of $|J_\perp|/J_\| = 0.025$, and, thus, places the Si(553)-Au spin chain array deep in the QSL regime.

The possibility for the formation of QSLs was proposed by Philip W. Anderson in 1973 [169]. A characteristic of spin liquids is that the spins do not order magnetically even at $T = 0\,\text{K}$, but rather fluctuate in a correlated fashion [170]. In particular, two adjacent spins form a so-called valence bond. Due to the antiferromagnetic interaction, they form a singlet state with $S = 0$. If each spin is part of a specific valence bond, i.e., each spin has its fixed valence bond partner, the system is in a so-called valence bond solid state [170]. In a spin liquid, however, the ground state is comprised of a superposition of many different pairings of spins, and is, thus, considered a resonating valence bond state [170]. An interesting feature of spin liquids is the possibility for exotic excitations such as spinons. In a 1D chain, a spinon manifests as a domain wall, while in a 2D QSL a spinon is created as an unpaired spin [170]. An experimental proof of a QSL state is very challenging. Nevertheless, experimental evidence for QSL properties have been detected in certain organic compounds [171] and anorganic quasi-2D bulk materials [172], both of which show triangular lattice geometry. For the first material, the absence of long-range magnetic order could be verified by temperature-dependent measurements of

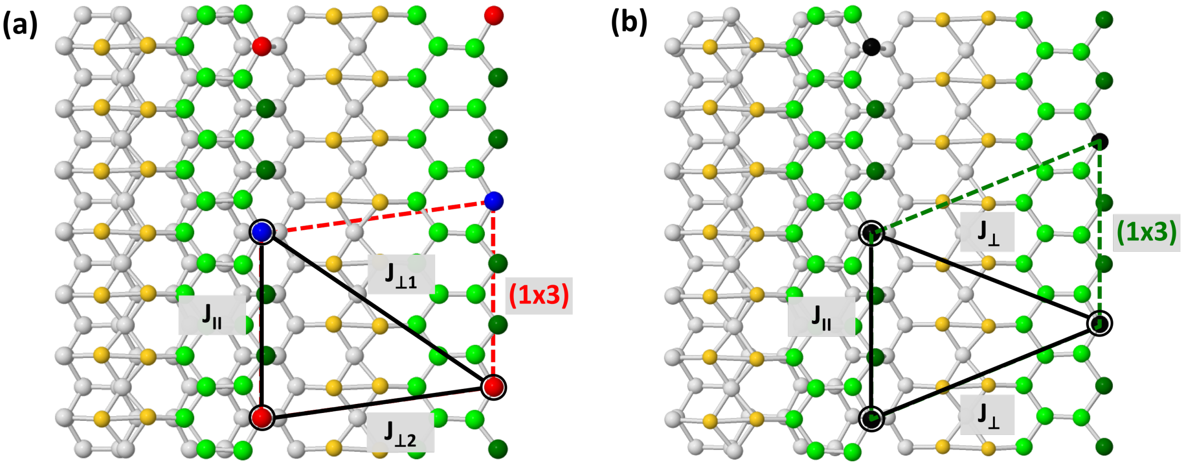

Figure 6.4: *(a) Si(553)-Au structure model according to Ref. [1]. The red and blue color of the spin-polarized step-edge atoms illustrates the proposed AFM spin ordering along the chain and the FM ordering across the steps. Nearest-neighbor spins across the step are basically arranged horizontally as marked by the (1×3) unit cell (red). (b) Structure model for the centered spin site arrangement as inferred from SPA-LEED and STM. The (1×3) unit cell is depicted in green. The centered geometry leads to a degenerate exchange coupling across the steps and, thus, to magnetic frustration. Atomic coordinates provided by S.C. Erwin.*

the magnetic susceptibility and nuclear magnetic resonance measurements [171]. For the latter, spinon excitations have been detected by neutron scattering [172]. However, it was subsequently discovered that the experimentally detected spinons are interacting 1D spinons rather than the spinons expected for a 2D spin liquid [170,173]. For the Si(553)-Au spin chains, experimental support for the presumed spin liquid scenario could be obtained by temperature-dependent measurements of the spin-susceptibility. Although such measurements are much more challenging for surface spins than for bulk materials, they may be realized by x-ray magnetic circular dichroism (XMCD) experiments [174].

6.2 Parity Breaking at the Si Step Edge

The Si(553)-Au atomic wire array is built by two different chain types – the Au double strand and the Si step-edge chain. Both types of 1D structures show a finite coupling between neighboring chains of *equal* type. As discussed in the previous section, neighboring spin chains exhibit a strong structural correlation. For the Au chains, the wiggled quasi-1D Fermi surface contour reflects a non-zero coupling between electrons confined in the Au chains of adjacent terraces [137] [or see Sec. 6.5]. However, since both chain types are interspersed, each could, in principle, also influence the other. The objective of the following section is to study such mutual interaction between directly neighboring Si and Au chains. It will be shown that the interaction is highly unidirectional. The Au chains modulate the charge distribution along the Si step edge, while the Si chains leave the Au chains unaffected. As a consequence, the parity of the step edge is broken, which, in turn, result in two step-edge variants with opposite directionality. The discussion of the results is structured as follows: First, the periodicity of Si step edge is examined, yielding two different, yet undetected sixfold modulations. Then, STS data evidence that the intensity modulation of the spin chains is of electronic nature. Finally, the origin of the step-edge modulations is traced back to interactions with the adjacent Au chains on either side. These findings are published in Ref. [A7].

Long-Range Modulations of the Si Step Edge – Fig. 6.5 presents constant current STM images of unoccupied states of the Si(553)-Au surface taken at various tunneling biases. The image series discloses two distinct long-range modulations of the Si step edge, which manifest at different bias values. At +0.7 V the Si step edge displays the well-known ×3 superstructure [25–27, 146, A1] (or Sec. 5.4). However, when looking at the STM image taken at +0.4 V [Fig. 6.5(b)], a small additional modulation can be identified: Every second spin site along the step edge appears brighter (site A) than the other (site B). This becomes evident in the line profile, which is taken along the dashed green line in Fig. 6.5(b) and presented in Fig. 6.5(f). The clear intensity difference between consecutive spin sites leads to an overall *sixfold* modulation along the Si step edge. It is important to mention that these STM images have been recorded with a nonmagnetic tunneling tip, and, thus, do not show any evidence for the AFM spin order proposed in Ref. [1].

The second long-range modulation is observed for low tunneling biases, i.e., close to the Fermi level. At $U \leq +0.2\,\mathrm{V}$ the spin sites do not exhibit any significant LDOS, and, thus, no distinct ×3 superstructure is observed. Instead, the step edge features a ×6 periodic structure which is reminiscent of “bones” connected by bright “joints” [see labels in Fig. 6.5(e)]. Both elements are formed by pairs of doubly-occupied Si step-edge atoms. For intermediate tunneling voltage, i.e., +0.3 V, the Si step edge shows a superposition of its low and high tunneling bias appearance: The bones and joints are still visible, while the two girdling spin-polarized Si atoms start to become prominent. In principle, all of these fine details of the

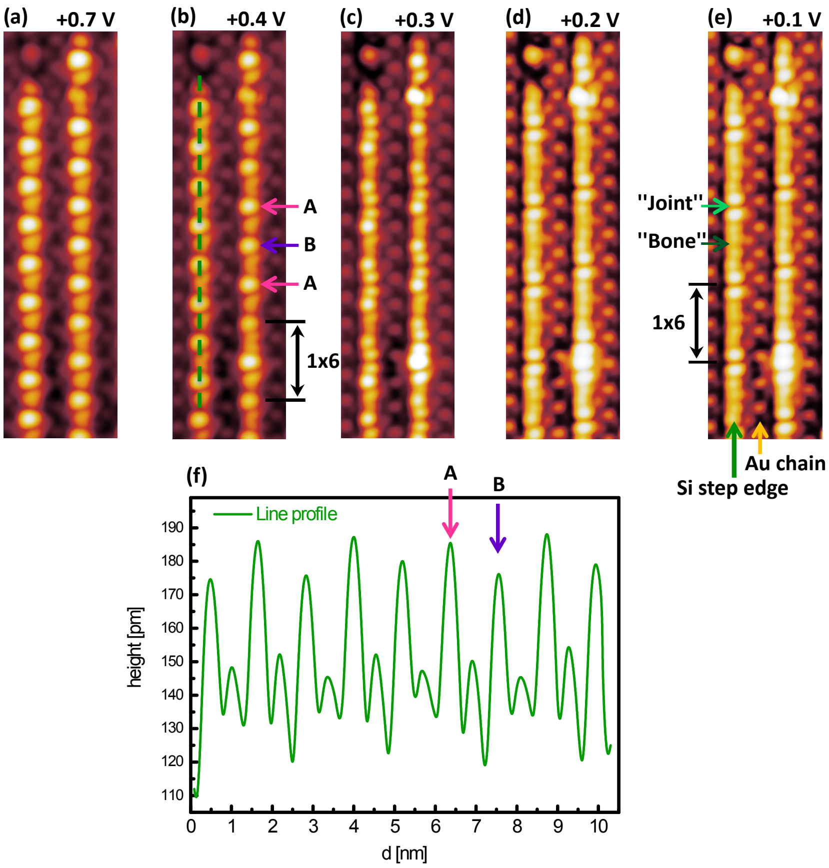

Figure 6.5: *(a)-(e) STM images of the unoccupied states of the Si(553)-Au surface at various tunneling biases ($T = 77\,\mathrm{K}$). (f) Line profile along the Si step edge at $U = +0.4\,\mathrm{eV}$ [dashed green line in (b)]. At a tunneling bias of +0.3 V and +0.4 V, spin sites A and B display a clear intensity difference (see magenta and purple arrows as well as the line profile) leading to a sixfold modulation of the spin chain. At low tunneling biases, the Si step edge exhibits a second ×6 periodicity, which manifests in a bone-and-joint like appearance of the non-spin-polarized Si atoms (see dark and light green arrows). At +0.3 V the Si chain exhibits a superposition of both ×6 intensity modulations. . From [A7].*

bias dependent step-edge appearance can be divined in the bias series presented in Ref. [A1] [see e.g. low bias image of Fig. 5.9(a)]. However, only the extremely sharp tip used to record the STM images of Fig. 6.5 allows for the interpretation presented above.

Energy-Shifted Spin Site DOS – Next, the intensity difference of consecutive spin sites will be analyzed in more detail. For this purpose, dI/dU maps in the energy range of the characteristic unoccupied spin state have been acquired [see Fig. 6.6(a)]. One can clearly identify localized DOS intensity with ×3 spacing in all dI/dU maps, even though their respective intensities vary with the set-point voltage. For low tunneling bias ($0.20\ldots0.30\,\mathrm{V}$), spin site A appears brighter than site B. With increasing bias both spin sites initially appear equivalent and then reverse their relative intensities, i.e., site B becomes more intense than A for bias voltages $\geq 0.45\,\mathrm{V}$. These observations indicate that the unequal appearance of spin

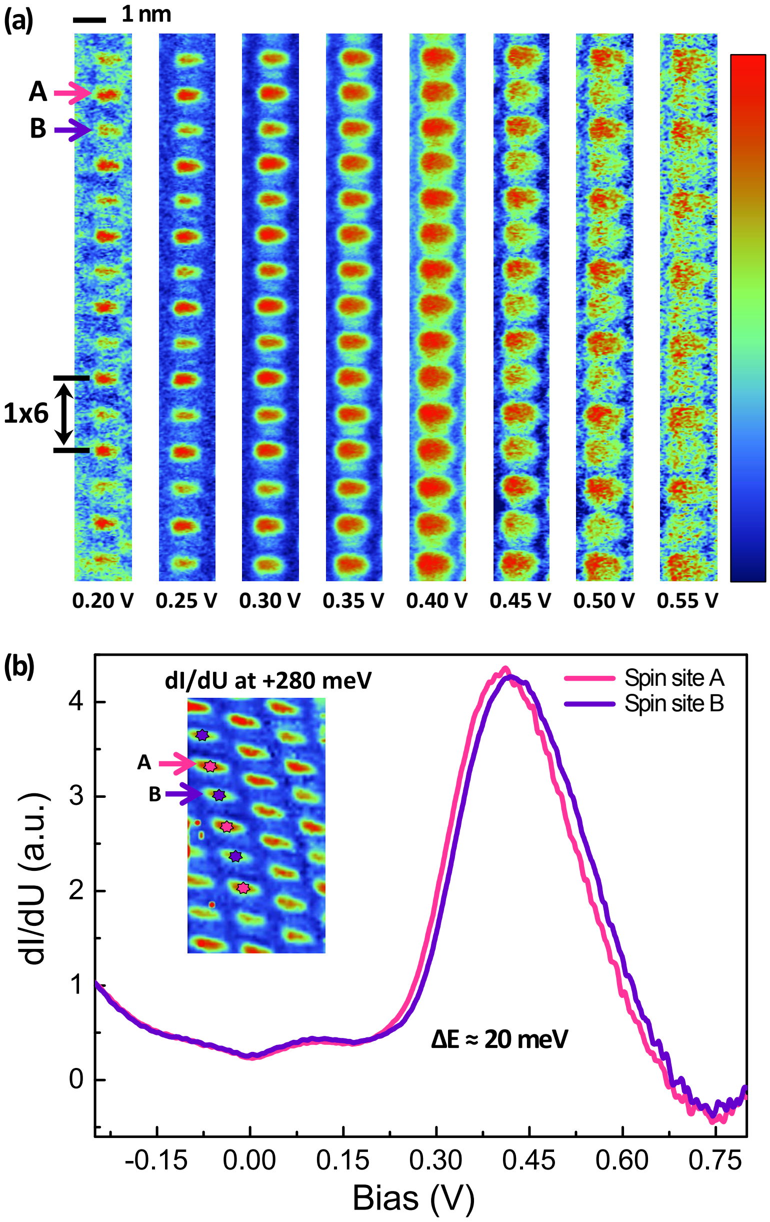

Figure 6.6: *(a) dI/dU maps of a Si step edge at various tunneling biases recorded at 77 K. At low tunneling bias, a clear DOS imbalance between neighboring spin sites is observed. This imbalance inverts for high tunneling bias, providing evidence for its electronic nature. (b) Local tunneling spectroscopy on different spin sites. Inset: dI/dU grid map at +280 meV. As indicated in the inset, the magenta and purple dI/dU curves represent spectra taken at spin site A and B respectively. The dI/dU curves of spin site A and B are found to be shifted by 20 mV with respect to each other. Both data sets have been recorded by the lock-in technique using a modulation amplitude of $U_{mod} = 10$ meV. For the dI/dU grid, the tip was stabilized at a set-point of $U_{set} = -0.3$ V, i.e., at an energy position where the DOS modulations along the step edge are small (see Appendix Fig. F.11), in order to avoid strong local deviations in the tip-sample distance. . From [A7].*

sites A and B in the topography images of Fig. 6.5 originates from an energy shift of their associated unoccupied DOS. Local STS measurements, as shown in Fig. 6.6(b), support this conclusion. The spectra measured at spin sites A and B display an energy shift between the respective spin DOS peaks of about 20 meV. Both the dI/dU maps and the tunneling spectra clearly demonstrate that the inequivalence between adjacent spin sites is electronic in nature rather than a topographic effect. Since both STS variants and STM topography reveal nominally identical results, a qualitative error due to set-point effects (see Sec. 3.1) can safely be excluded. The absence of any distinct structural motif with ×6 periodicity is supported by missing ×6 features in the electron diffraction patterns presented in Figs. 6.1 and 6.3. In these images, no intensity at ×6 positions between the integer order spot rows is observed.

Directional Si Step Edges – But what is the origin of the energy-shifted DOS? To answer this question, the second chain type of the system – the Au chain – plays an essential role. As outlined in Sec. 5.3, the Au dimers, which reside on the terraces of Si(553)-Au, are slightly tilted in an alternating fashion from rung to rung along the Au ladder. This tilted dimer structure is not directly resolved in STM images. Instead, circular charge clouds with ×2 periodicity are detected, which is in perfect agreement with the simulated STM images [see low bias images of Fig. 5.9]. According to the DFT-simulated STM images, LDOS accumulates in between the closer Au atoms of each strand of the ×2 periodic Au double chain. The charge clouds, thus, not only represent the tilted Au ladder, but also allow for an analysis of the phase relation of neighboring Au chains, which will be important for the subsequent arguments.

Fig. 6.7(a) provides STM images taken at +0.3 V. At this particular bias, the STM images feature both the bone-and-joint structure formed by the nonpolarized Si atoms as well as the inequivalent DOS of spin site A and B. Consequently, these close ups of the Si step edges reveal a finely modulated pattern, rendering the atoms with different intensity. As a key characteristic, the A and B atoms and the bone-and-joint segments (as marked in the images) do not show the same intensity. This is in contrast to the simple picture expected for isolated Si chains with a dangling bond on every third site, which would imply a mirror plane perpendicular to the chain direction. In this case, such a mirror plane is obviously lacking, i.e., the parity of the step edge is broken. Instead, two different step-edge variants exist, which show opposite directionality. The two variants have been labeled as "forward" and "backward" Si chains. They are directional in a sense that they cannot be mapped onto each other by translation. More specifically, the "forward" chain in the image on the left of Fig. 6.7(a) is characterized by the following repeat sequence (from top to bottom): spin site B – joint segment – spin site A – bone segment. In contrast, the "backward" chain in the image on the right displays the reversed sequence: Site B is encountered prior to site A, while the joint and bone segments maintain their position.

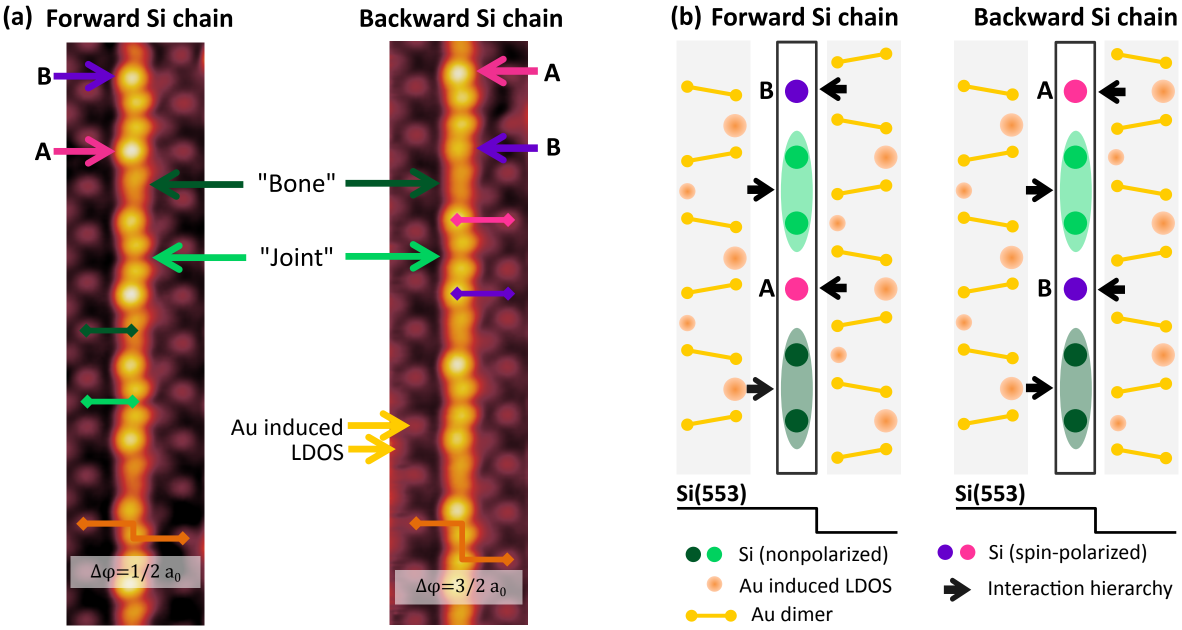

Figure 6.7: *(a) Constant current STM images of two Si step edges with opposite directionality ($U = +0.3$ V). The forward Si chain (left image) is characterized by the repeat sequence: spin site B – joint segment – spin site A – bone segment. For the backward Si chain (right image), site A and B are interchanged, leading to the sequence: spin site A – joint segment – spin site B – bone segment. Magenta and purple pointers mark the fixed phase relation between the Au charge clouds of the right-sided Au chain and the spin sites A and B. Green markers illustrate the fixed phase relation of the bone-and-joint elements to the left-sided Au chain. (b) Schematic of the interaction hierarchy between Au chains and the enclosed the Si step edge. The Au chains induce a parity breaking of the surrounded step edge and render it directional. The directionality of the step edge is determined by the phase relation of the surrounding Au chains. From [A7].*

Unidirectional Au-Si Chain Interaction – As a next step, the origin of the parity-breaking and the determining factors of the step-edge direction are discussed. Here, the neighboring Au chains and their phase relation play a major role. A phase shift of $\Delta\varphi = 1/2\, a_0$, where a_0 is the distance between two Si atoms along the step edge, leads to a forward Si chain, whereas $\Delta\varphi = 3/2\, a_0$ results in a backward Si step edge [see orange markers in Fig. 6.7(a)]. The background of this simple relationship can be understood by inspecting the phase shifts between the step edge features and the neighboring Au chains. The position of the inequivalent spin sites is determined by the Au chain of the adjacent *downhill* terrace, i.e., not the same-level terrace. This corresponds to the Au chains to the right of the spin chains pictured in Fig. 6.7(a): The bright spin sites A are always located next to the charge clouds of the downhill Au chain, while the darker spin site B always sits between the Au charge clouds [see magenta and purple markers in Fig. 6.7(a)]. The inequivalence of the nonpolarized Si atoms, i.e., their bone-and-joint appearance, is also found to be Au chain induced. Contrary to the spin sites, the nonpolarized Si atoms respond to the Au chain located on the *same* terrace, as can be concluded from their strict phase relation: The joint structures always appear between the charge clouds of the left-side Au chain, as indicated by the light green markers in Fig. 6.7(a). The bone elements, in turn, are located next to the charge clouds of the left-side Au chain [dark green marker in Fig. 6.7(a)].

As outlined previously, the transverse phase correlations of both chain types is fundamentally different: The spin chains exhibit a distinct interwire coupling, which results in a fixed phase relation between neighboring spin chains (see Sec. 6.1). The Au chains do not show any fixed phase correlation. Instead, the phase between adjacent Au chains switches randomly between $1/2\,a_0$ and $3/2\,a_0$ as evidenced by ×2 streaks rather than ×2 spots in the diffraction pattern (see Subsec. 5.2.1). As a consequence, no preference for either of the two step-edge variants exists. Instead, forward and backward step edges should be evenly distributed across the Si(553)-Au surface.

Fig. 6.7(b) provides a visualization of the experimental observation from the structural point of view. The tilting of the Au dimers, i.e., the local charge distribution in the Au chains, influences the specific elements of the neighboring step edge, and lifts the degeneracy of their DOS, as reflected by the color coding of the step edge and the arrows. The Au chain on the right of the spin chain (neighboring terrace) affects the *spin sites* and the left-sided Au chain (same terrace) the *nonpolarized* Si atoms.

A deeper insight into the interaction mechanism can be obtained by recalling the periodicities of both chain types. Remarkably, the Au chain does not show any reminder of a ×6 superstructure, see Fig. 6.7(a). Thus, the spin chain and its distinct ×3 periodicity do not affect the Au chain, whereas the Au chain imprints its ×2 periodicity on the Si step edge, lending it a long-ranged ×6 modulation. Hence, one can conclude that the net result of the interaction is unidirectional, in that the Au chains affect the step edges but not vice versa.

In summary, the close up inspection of the Si(553)-Au atomic chain array unveils a complex DOS modulation of the Si(553)-Au step edges, which has been overlooked in previous STM experiments with lower resolution [25–27, 43, 44, 146, A1]. The modulation can be explained by a subtle interaction between the Au and Si chains, which is hierarchical in nature. Specifically, the Au chains modulate the Si step edges, breaking their parity and lending them directionality, while the Si chains leave the Au chains unaltered. Such unilateral interaction is an interesting finding per se, but also plays a key role in understanding the observation of coupled solitons, as discussed in the next section.

6.3 Coupled Solitons

6.3.1 Deconfined Setup

Solitons are solitary wave packets, which maintain their shape when they propagate. In solid state physics, they manifest as domain walls between two degenerate ground states of 1D chains. The basic properties of solitons have been elaborated in the theory section using perhaps the most prominent example of polyacetlyen (see Sec. 2.2). One of the major obstacles to observing solitons is that many real-world electronic systems are not strictly 1D, but only quasi-1D due to strong anisotropy. Even an infinitesimal coupling between chains leads to a confinement force between the solitons, i.e., an attractive, constant force, which does not decay with distance. The mechanism is illustrated in Fig. 6.8(a). Here, two interacting chains with two different ground states A and B each are displayed. The ground states are shifted relative to each other by one lattice site, and are energetically degenerate. The lower chain #2 permanently displays ground state B, while the upper chain changes its ground state from A to B and back to A by introducing two domain walls. Although the ground states of the isolated chains are degenerate, the coupled chains favor one configuration (E_0) over the other (E_1). As a consequence, the two domain walls (i.e. solitons) cannot move independently from each other, but are *confined*, irrespective of whether they exist in the same chain or in different chains. This is due to an energy penalty $\Delta E \propto (E_1 - E_0) \cdot x$, which increases in a linear fashion with the distance x between the domain walls.

The setup of Fig. 6.8(a) would, for example, be conceivable for an atomic wire reconstruction formed on a planar surface where the mechanism governing the soliton behavior is exclusively determined by the phase relationship of the deposited adatom chains. One example of this would be the In/Si(111) chains discussed in the introduction of this thesis (Chapt. 1). In these wires, single solitons can only be observed in the case of occasional trapping by impurities or defects [15,16]. Mobile solitons are primarily observed in pairs [15], as expected for a confined setup. Interaction with structural defects results in a transient trapping of one of the two solitons, which enables the detection of single, mobile solitons [15]. The Si(553)-Au surface, however, provides a fundamentally different setup. It is comprised of two different chain types with – most importantly – dissimilar periodicities. This situation is sketched in Fig. 6.8(b). One chain has a ×3 periodicity, and, thus, provides three degenerate ground states, which are shifted by one or two elementary units respectively [see Fig. 6.8(c)]. The second chain has two different ground states, and is similar to either chain depicted in Fig. 6.8(a) in this regard. Contrary to Fig. 6.8(a), where solitons result in two energetically distinct configurations (with E_0 and E_1), the coupling of chains with incommensurate periodicities provides degenerate configurations with identical energy per unit length (always E_2). Consequently, there is no linear confining potential $V(x) = (E_1 - E_0) \cdot x$ between the solitons. Instead, solitons can move independently. The Si(553)-Au atomic wire array – comprising ×3 spin chains and ×2

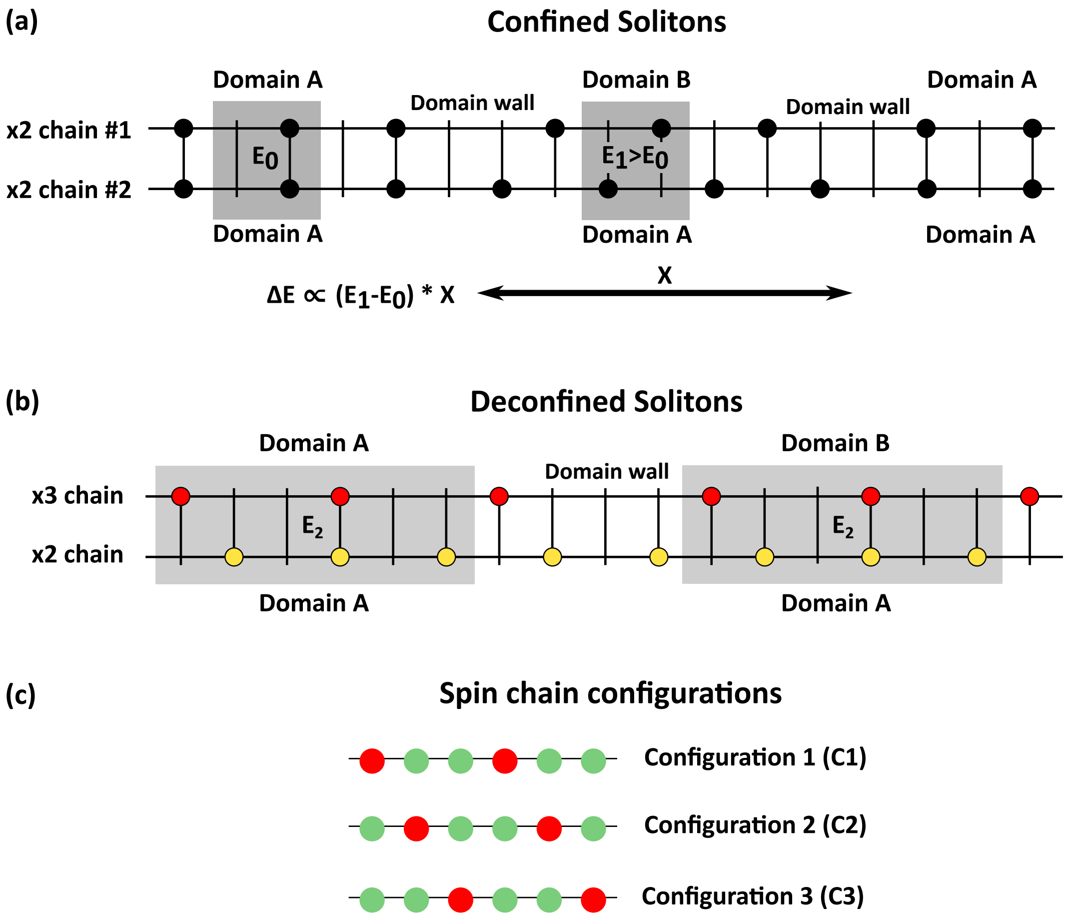

Figure 6.8: *Formation of confined and deconfined solitons, depending on the phase registry of interacting chains. (a) Coupled chains with two degenerate ground states, A and B, respectively. Domain walls lead to two configurations of the coupled system with different energies $E_1 > E_0$. As a consequence, the two domain walls are confined, as their separation x costs the energy $\Delta E \propto (E_1 - E_0) \cdot x$. (b) Chains with two and three degenerate ground states respectively. All domain-wall-induced energy configurations have the same energy. Consequently, domain walls can move freely in such a system. (c) The three different ground states of a spin chain with ×3 periodicity.*

Au chains that interact with each other (see Sec. 6.2) – is, thus, a perfect model system to observe single, deconfined solitons.

6.3.2 Real Space Soliton Observations in Si(553)-Au

Coupled Au and Si Chain Solitons – Fig. 6.9(a) shows a close-up, high-resolution STM image, which captures soliton processes and implicitly encodes the time evolution of such processes. Fig. 6.9(b) displays the same surface segment as (a). Both images were taken in quick succession, but differ in the slow scan direction of the tunneling tip: (a) was scanned from left to right (“forward scan") and (b) from right to left (“backward scan"). The tunneling bias voltage ($U = +0.3\,\mathrm{V}$) has been chosen such that the measurement is sensitive to parts of the characteristic unoccupied spin site DOS localized at every third Si step-edge atom (see

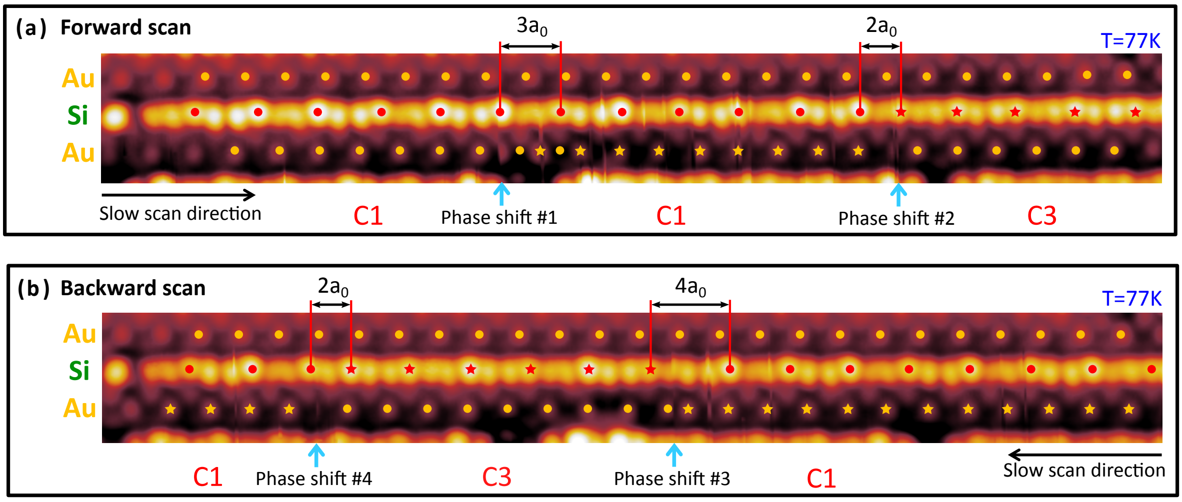

Figure 6.9: *STM constant current images ($U = +0.3$ V) of a single spin chain and two surrounding Au chains, comparing two subsequent images with opposite line-feed direction. In particular, the fast scan direction is vertical, i.e., the slow scan movement is horizontal as indicated by the black arrows (also see schematic in Fig. 6.10). The Au chain exhibits several phase shifts as marked with the cyan arrows. The orange dots and stars highlight the position of the Au charge clouds. Stars mark domain A. Dots mark domain B. Most Au chain phase shifts come hand in hand with a phase shift in the spin chain as indicated by the red symbols marking the spin site positions. The configuration of the spin chain is encoded in the red symbols. Red stars represents configuration C1 and red dots configuration C3.*

Sec. 6.2), while also displaying the charge clouds of the Au chains. As a consequence, the spin sites appear brighter than the doubly occupied step edge atoms, with the result that the Si step edge – the bright chain in the middle of the images – features the well-known ×3 periodicity as marked by the red dots in Fig. 6.9(a). Note that the scanning bias is the same as for the images presented in Fig 6.7(a). The step edge thus features an additional ×6 modulation due to the unilateral interaction with the Au chains as explained in Sec. 6.2. This modulation, however, is not of major importance for the observation of coupled solitons.

The bright Si step edge is surrounded by two Au chains [see labels in Fig. 6.9], with one located on the same terrace as the step edge and one located on the terrace below. Both chains exhibit the characteristic circular charge clouds with ×2 spacing representing the Au ladder with its tilted Au dimers (see Sec. 6.2). For clarity, the Au charge clouds are marked by orange dots and stars.

Based on this general static setting, the next paragraph addresses the the dynamic effects encoded in such STM images step by step: The cyan arrows mark positions at which the phase of the lower Au chain suddenly shifts. As a consequence, some parts of the STM image display domain A (orange dots) while others display domain B (orange stars) of the Au chain. To further visualize the phase shifts encoded in the images, the ×2 spaced orange dots marking the Au charge clouds on the left side of what is referred to as “phase shift #1” have been continued across the phase shift. While the dots coincide with the Au charge clouds on the left of the phase shift, they are in between the Au charge clouds on the right of this phase shift. This observation indicates the presence of a single soliton, which has propagated through the Au chain during the STM measurement, and, thereby, shifted its phase by a_0. Note that only the lower Au chain shows signatures of passing solitons, while there are no such signatures in the upper Au chain.

Characteristic of the process, a phase shift in the Au chain (labeled as "phase shift #2" to #4 in Fig. 6.9) appears together with a change of the spin chain configuration in most cases. In order to visualize the configuration of the spin chain, spin sites have been marked with red dots (configuration C1) and red stars (configuration C3) respectively. Configuration C2 is not observed in the images presented. To the left of phase shift #2 the spin chain presented in Fig. 6.9(a) displays configuration C1. At the position of phase shift #2, however, the configuration of the spin chain changes from C1 to C3, as witnessed by an apparent spin site spacing of only $2a_0$. The spin chain has shifted by a_0 to the left, which can only be explained by soliton movement along the step edge as the scan was being taken. Since the STM images show rather abrupt changes of the initial intensity pattern of the chains, one can infer that the soliton induced process occurs on a faster timescale than the image recording process (see Subsec. 6.3.2 for details). Hence, the images indicate that the solitons are not frozen, but rather highly mobile. Consequently, solitons can not be observed directly, but only indirectly through shifts in the ground state configurations of the chains once the solitons have passed. It is characteristic of the data presented that solitons in the spin chain and solitons in the Au chain are detected more or less simultaneously (as seen, for example, at phase shift #2 in the image). This strongly suggests that the spin chain and the Au chain soliton move jointly through the respective chains, as the solitons are coupled to each other.

Soliton Scanning Procedure – Before analyzing the individual soliton events observed in the STM scans presented in Fig. 6.9, it is important to illustrate the STM scanning procedure. This will help to understand the formation of the STM data and to explain why such images can only be obtained when solitons travel through the chains during the scan. For this purpose, the schematic in Fig. 6.10 considers an example sequence of coupled soliton passings, and sketches the effective STM image obtained when scanning the surface while these solitons pass through the chains. The tunneling tip scans perpendicular to the chain structures line by line, i.e., the slow scanning direction is along the chains as indicated by the black meander on the bottom of Fig. 6.10. At time t_1, one soliton passes through the lower Au chain, and another passes through the spin chain. As shown in the center panel of Fig. 6.10, one can indirectly infer this soliton event at t_1 through the continuation of the STM scan, which now shows the spin chain in configuration C2 and the Au chain in phase B, as compared to configuration C1 and phase A before t_1. The panel above, indicated by the label "C3" on the right, shows that, at time t_2, another two coupled solitons have passed, flipping the spin chain into configuration C3 and the Au chain back into phase A.

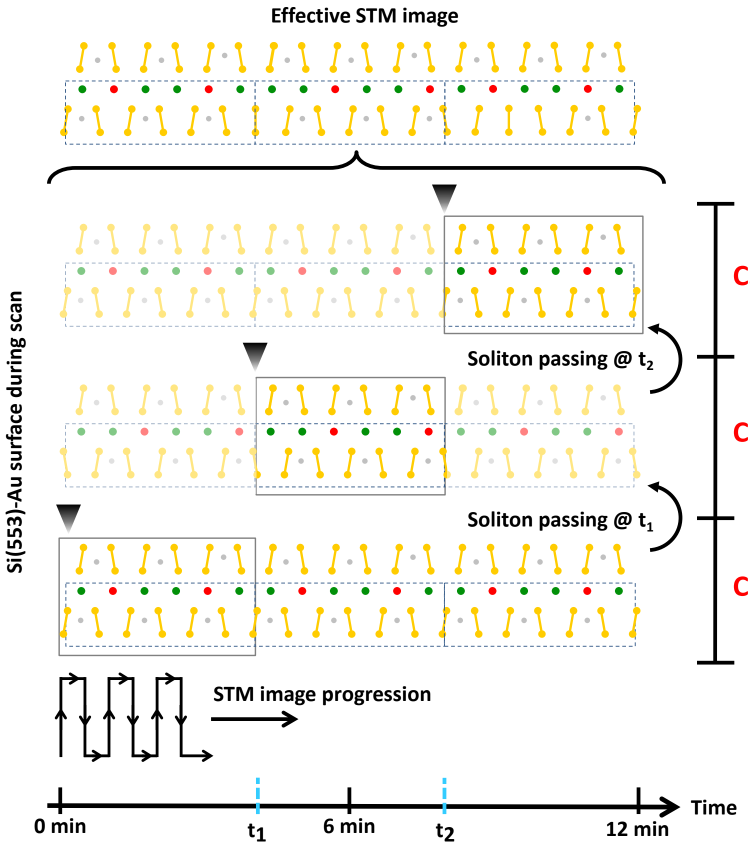

Figure 6.10: *Schematic diagram of the STM measurement procedure to illustrate the generation of the STM images presented in Fig. 6.9. The tunneling tip, represented by the black triangle, scans perpendicular to the chain structures line by line, i.e., the slow scanning direction is along the chains as indicated by the black meander. Yellow dumbbells represent dimers of the Au double-strand chains. The Si step edge is sketched by using red and green dots. At the point in time when solitons pass through the chains (t_1 and t_2), the phases of the Au chain and the spin chain shift. The effective STM image is a composition of the chains' respective configuration during the scan, and is dependent upon the on moment and number of soliton passings occurring during the image acquisition.*

Hence, the STM images presented are temporal compositions of the chain configurations at the times the respective images are taken. Irrespective of its shortcomings, the chosen method of image recording – *fast* scan in the direction perpendicular to the chain direction, and *slow* scan along the chains – is fully adequate to capture the coupled movement of Au and spin chain solitons. The STM data presented in Figs. 6.9 and 6.11 were obtained with a scan speed of 0.8 ms per pixel (fast scan direction), which results in a time distance of 1.3 sec between two pixels in the slow scan direction. Noteworthy, the images are ≈ 70 pixel wide cut-outs of 800 pixel wide scan frames.

Passings of Various Coupled Solitons – Having clarified the STM image formation, various soliton passings documented in the images of Fig. 6.9 will now be analyzed in further detail. Clear evidence that the chains alter their configuration during the STM scans can be

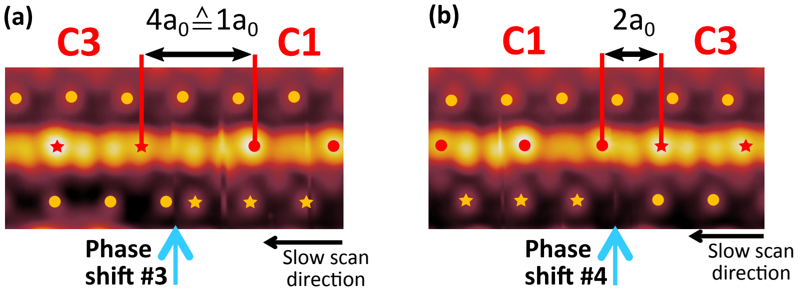

C1-C3 spin chain soliton

C3-C1 spin chain soliton

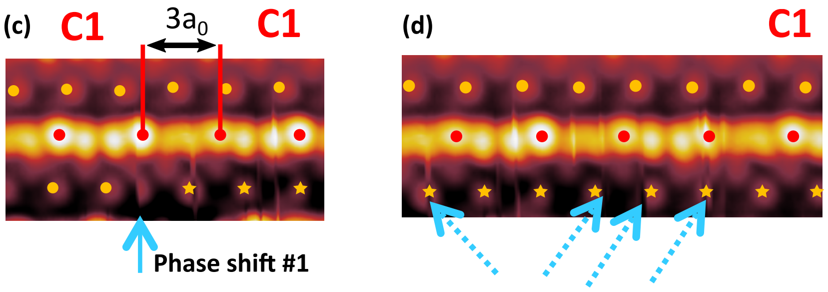

Pure directionality flip

Passing of soliton pairs

Figure 6.11: *(a),(b) Coupled Au and spin chain soliton passing. Slow scan direction is from right to left as marked by the black arrow. At phase shift #3 in (a) the Au chain's phase changes from B to A and the spin chain's configuration from C1 to C3. At phase shift #4 in (b) the Au chain's phase changes from A to B and the spin chain's configuration from C3 to C1. The spin chain soliton observed in (b) is the anti-soliton of the spin chain soliton observed in (a). (c) Single Au chain soliton passing. No phase shift in the spin chain is observed. Intensity changes of the spin sites after the Au chain soliton passing are due to the unidirectional interaction of the Au chain with the Si step edge. (d) Multiple passings of coupled soliton pairs. A passing of coupled soliton pairs does not change the spin chain phase at larger distances as marked by the red dots.*

seen in that Fig. 6.9(a) and (b) depict the same chain (see e.g. the defect at the left end of the chains) scanned at different points in time. Although the chain is identical, particular chain segments appear in different configurations during the forward and backward scan respectively. For example, the right part of the Si step edge shows the C3 configuration for the forward scan and the C1 configuration for the backward scan. Moreover, the soliton passings are observed at different locations in the two scans.

Fig. 6.11 displays close-up images of the characteristic soliton passing points of Fig. 6.9. Fig. 6.11(a) and Fig. 6.11(b) show two Au chain solitons, which are coupled to two different spin chain solitons. At the phase shift #3 [Fig. 6.11(a)], the spin chain flips from configuration C1 to configuration C3 as the slow scan direction was from right to left. This corresponds to a shift of the spin site by $-a_0 \,\hat{=}\, 2a_0$. At phase shift #4 [Fig. 6.11(b)], the spin chain exhibits the reversed phase shift, namely flipping from configuration C3 to configuration C1. Hence, the spin chain soliton in Fig. 6.11(b) may be considered the anti-soliton of the spin chain soliton in Fig. 6.11(a). Fig. 6.11(c) displays an Au chain soliton which is not accompanied by a spin chain soliton, as one can easily infer from red dots marking the spin sites (this spacing continues to be $3a_0$). Instead, only the relative intensity of adjacent spin sites inverts at the point where the Au soliton has passed (i.e., at the point indicated as "phase shift #1"). This observation is in perfect agreement with the results presented in Sec. 6.2. A phase shift of the lower lying Au chain – as is the case in Fig. 6.11(c) – results in an interchange of site A and B, mediated by the unidirectional interaction of the Au chain with the spin chain. As a consequence, the directionality of the step edge flips at "phase shift #1". The fact remains that in the event depicted in Fig. 6.11(c) no spin chain soliton is involved. Instead, the spin chain only witnesses the Au chain soliton and confirms the unidirectional interaction between the Au chain and the spin chain reported in Sec. 6.2. While all of the dynamic events discussed so far can readily be interpreted with single solitons in each chain, the section of Fig. 6.9(a) enlarged in Fig. 6.11(d) indicates that several soliton pairs have propagated through the Au chain. At the locations indicated by the dashed cyan arrows, the phase of the Au chains appears to change for a time of approximately one second (1-2 line scans) before flipping back to its initial configuration. The same seems to happen for the spin chain, as the Au chain phase shifts appear to be accompanied by short, spike-like intensity changes in the spin chain. As expected for soliton pairs, their numerous passings do not alter the spin chain configuration at larger distances, resulting in regular $3a_0$ periodic spin sites (red dots).

Phase Defects – Aside from the mobile solitons discussed above and the frozen solitons detected at the In/Si(111) surface, the phase of an atomic chain can also be altered by intrinsic structural defects. Such phase defects are in most cases immobile (at least at low T), and do not host the characteristic topological properties of solitons (see Sec. 2.2). In order to avoid confusion with the solitons in the focus of this section, this paragraph will discuss some phase defects observed on Si(553)-Au step edges. Contrary to the STM images presented in Fig. 6.9, the images displayed in Fig. 6.12 do not show any indication of dynamic events during the scan. Instead, they exhibit the static setting of two different Si step edges both interrupted by a defect. The defects are adsorbate-induced as outlined in Subsec. 5.2.2. In both cases, the defects intercept the regular ×3 spacing of spin sites along the step edge, as indicated by the red symbols. Red dots mark the spin sites of the left step-edge segment, and are continued across the defects with ×3 spacing in order to depict the defect-induced phase shift of the spin chain. On the left side of the defects, the dots match the spin site positions, while this is not the case on the right side of the defects. There, spin sites are marked by red squares [Fig. 6.12(a)] and stars [Fig. 6.12(b)]. The effective defect-induced phase shift is different in both step edges displayed. In Fig. 6.12(a), the spin site spacing across the defect is $7a_0$ resulting in an effective phase shift of $+a_0$. For the step edge shown in Fig. 6.12(b), the effective phase shift is $+2a_0$. Notably, the spin site spacing across the defect in both cases is not a multiple of $n \cdot 3a_0$ (with n being an integer), illustrating that defects can create phase shifts at the Si step edges.

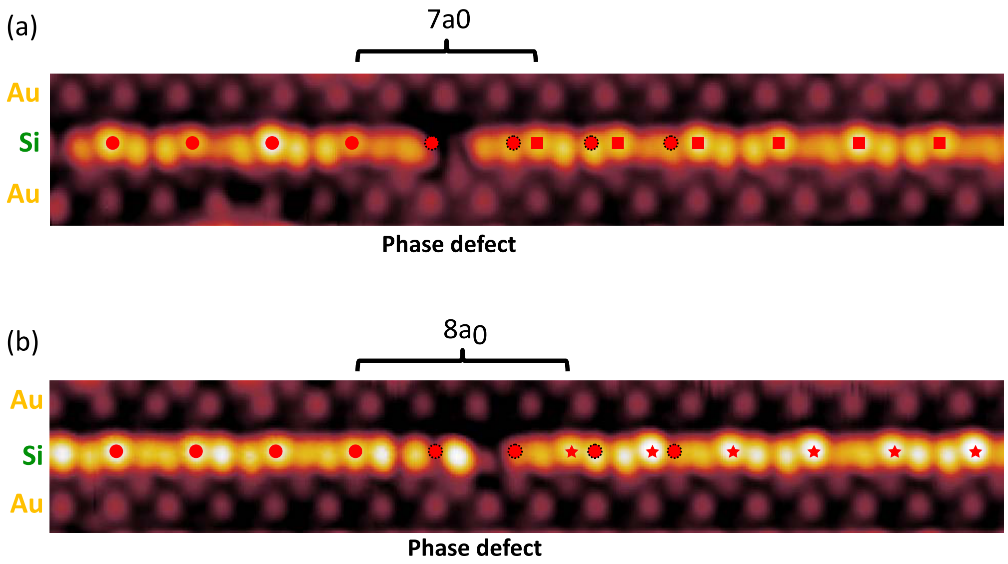

Figure 6.12: *Constant current STM images of two different Si(553)-Au step edges interrupted by defects. In both cases, the phase of the spin chains changes across the defects. In (a), the spin chain is shifted by* $+a_0$*. In (b), the defect induces a phase shift of* $2a_0$*. Red dots mark spin sites on step-edge segments to the left of defects, and are continued across the defect maintaining their* $\times 3$ *spacing for illustration purposes. Red squares and stars mark spin sites of the step-edge segments to the right of the defect. Dots indicating the normal spacing continuation (dashed black outline) do not align with the red squares and stars, illustrating the phase shifts induced by the defects.*

6.3.3 DFT Modeling

The high propagation velocity of the solitons hinders their direct observation by STM. In order to reveal various properties of the Si(553)-Au solitons, DFT calculations have been performed by S.C. Erwin [175]. For this purpose, a long Si(553)-Au supercell built of ten (1×1) cells has been modeled. At one end of the supercell, the Au chain is set to configuration A and at the other end to configuration B. Relaxation of the atom coordinates reveals a soliton formation in the center of the structure [see Fig. 6.13(a)]. The Au chain soliton is characterized by a twist of the Au dimers from $d=-0.2$ to $d=0.2$ (or vice versa as the sign of the dimerization for the intrinsic structure alternates between adjacent dimers). The domain wall is quite thin and appreas to span approximately four Au dimers [see Fig. 6.13(a)]. Fig. 6.13(b) shows the dimerization parameter d extracted from the DFT calculation as a function of the dimer number. The data points follow the typical S-shape expected for a soliton (cf. Sec. 2.2). A fit of the data to Eq. 2.16 reveals a soliton width of $\xi_{Au}=1.5a_0$. This is significantly smaller than the width found for solitons in polyacetlyene ($\xi_{PA}\approx 7a_0$) and In/Si(111) ($\xi_{In}\approx 10a_0$). The formation energy of the Au chain soliton is determined to be about 200-300 meV. In addition, DFT finds an extremely small activation barrier of about 4 meV. A simple estimate based on the Arrhenius equation ($R = R_0 \cdot e^{-E_{act}/kT}$) implies that the Au solitons appear mobile at all temperatures above $\approx 2\,\mathrm{K}$ (assuming an attempt frequency of $R_0 = 10^{12}$ Hz and

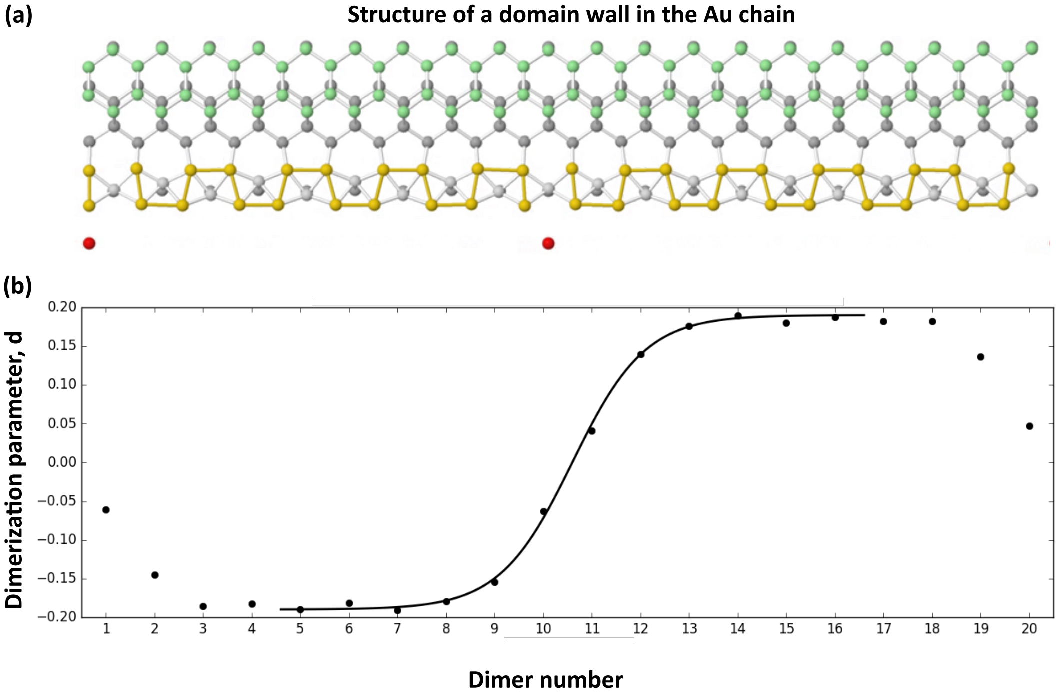

Figure 6.13: *(a) DFT modeling of a Au chain soliton using a supercell containing ten (1×1) unit cells. The soliton is characterized by a continuous twist of the Au dimers to a dimerization with opposite sign. The center of the soliton is marked by the red dot. (b) Dimerization parameter d for each dimer across the Au chain soliton. Values have been multiplied by ±1 to eliminate the distracting sign alternation of adjacent dimers. A fit of Eq. 2.16 to the DFT data points reveals a domain wall width of 1.5a_0. From [175].*

a moving rate $R = 1/10\,\mathrm{Hz}$). This finding is consistent with the STM observations.

For the spin chain, two different types of solitons exist. The first type corresponds to a local spin spacing of $2a_0$ and is referred to as heavy soliton. For the second type – the anti-soliton of the first and referred to as light soliton – the spacing is $4a_0$. The formation energy of such a soliton pair is estimated to be 25 meV at most [42]. Compared to the formation energy of the Au chain soliton (200-300 meV), the formation of a spin chain soliton requires much less energy. The activation barrier for the spin chain solitons is found significant higher than for the Au chain soliton, namely, 14.5 eV and 16.1 meV for light and heavy soliton, respectively [175].

In order to investigate the experimentally observed coupled solitons with DFT, a supercell with one spin chain soliton and one Au chain soliton has been modeled. Fig. 6.14(a) shows the DFT total energies for eight versions of this supercell. The cells differ in the distance between the Au and the Si soliton ranging from 0 to $7a_0$. From these calculations one can read two important facts: First, the lowest energy setting is that with zero distance between the solitons. This suggest that two independently propagating solitons (a spin chain and a Au soliton) are likely to bind together as they pass each other, and will move in a coupled fashion thereafter. The corresponding lowest energy structure is shown in Fig. 6.14(c). Second, there are energy maxima at $+a_0$ and $-a_0$ separation. These maxima indicate an activation barrier that the solitons have to surmount to split up (or to bind together). Fig. 6.14(b) displays the results of Fig. 6.14(a) in two separate data sets, one for even values of separation and one for odd values of separation. This version of presentation allows the quickly extract the absolute numbers of two important energies: The coupled configuration is favored by 5 meV compared to a large soliton spacing, which corresponds to a Au-Si soliton binding energy $E_{B(Au-Si)} = 5\,\text{meV}$. The activation barrier for the coupled splitons to split up is $E_{split} = 23\,\text{meV}$. Note that the lack of left-right symmetry is not an artifact of the calculation but rather has its origin in the unidirectional Au-Si interaction described in Sec. 6.2. The scenario suggested by the calculation is fully consistent with the experimental result presented above, and clearly explains why coupled solitons are observed in most cases.

(a)

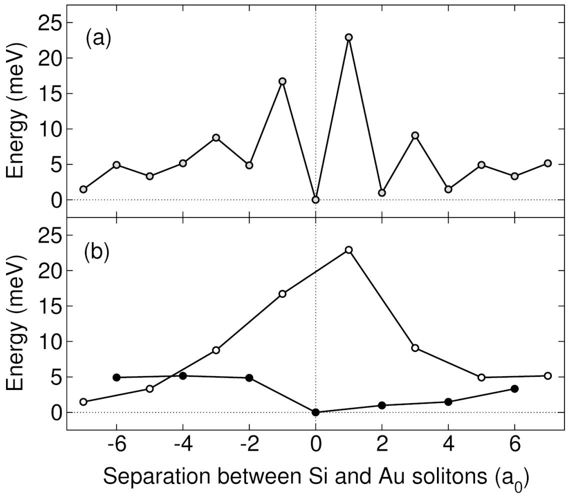

(b) **Deconfined solitons in Si(553)-Au**

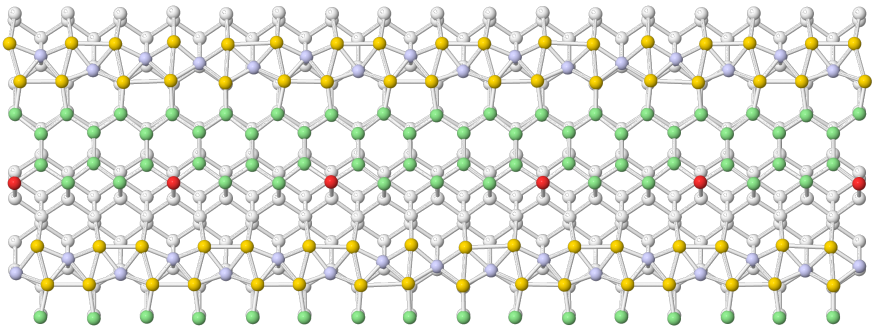

Figure 6.14: *(a) DFT relative total energies for eight different Si(553)-Au supercells each containing a Au and a spin chain soliton. The distance between the solitons has been varied from 0 to $7a_0$. Zero distance between both solitons is energetically favored compared to all other distances and serves as energy reference (0 meV). (b) Data points of (a) but split in two curves. The black (white) circles display energies for even (odd) values of soliton separation. (c) Structure of lowest energy. In this configuration the distance between the Au chain and spin chain soliton is smallest. From [175].*

6.4 Excitation of the Si Step Edge

6.4.1 Previous Results

It has recently been shown that the spin chain ground state can be "excited" by injecting electrons from the STM tunneling tip to the Si(553)-Au surface [43]. At sufficiently low temperatures (e.g. 60 K), the Si step edge changes its apparent periodicity from ×3 to ×2 upon increasing the tunneling current [43]. The so-called "excited state" (×2) has been found to have a limited lifetime before it falls back into the ground state (×3). This can be seen in STM images taken at intermediate tunneling currents, which show a superposition of the ground state and the excited state (see Fig. 2 of Ref. [44]). The tunneling current required for the excitation decreases with temperature (see Fig. 4 of Ref. [44]). At very low T (e.g. $T < 13\,\mathrm{K}$), the excitation is triggered by such low tunneling currents that the ground state of the Si(553)-Au spin chain can no longer be imaged by STM. Instead, STM images display the excited state with its ×2 periodicity. Extrapolating the temperature- and current-dependent STM measurements indicates that a current of the order of fA or lower is sufficient to excite the ground state at $T = 7\,\mathrm{K}$ [44]. A meticulous analysis of the excitation dynamics revealed the following characteristics of this current-induced transition: (i) the lifetime of the excitation is on the timescale of milliseconds [43], (ii) there is no energy barrier for the decay of the excited state and the decay mechanism is independent of the excitation, (iii) the excitation frequency is increased by higher tunneling currents, and (iv) the transient doping efficiency strongly depends on the spatial location of the excitation and is more likely at Si spin sites. Despite these detailed observations, a complete and consistent physical picture of the excitation scenario is still missing. One reason for this is the lack of a structural model for the excited phase. It has been suggested and supported by DFT calculations that the excited state could be a spin chain with ×2 periodicity induced by electron doping [43]. However, this contradicts an analysis of the spatial positions of the ×2 protrusions, which revealed that they are actually located *between* Si step-edge atoms [44]. Therefore, a simple ×2 spin chain cannot explain the excited state. The following paragraph presents an alternative explanation for the nature of the excited state.

6.4.2 The Excited State: Superposition of Different Ground States

High Tunneling Current – Fig. 6.15(a) displays an identical Si(553)-Au step edge for various tunneling currents. All other scan parameters have been kept constant. The low current image displays the well-known ×3 spin chain superstructure. This changes with increasing tunneling current in agreement with previous reports [43, 44]. At $I = 400\,\mathrm{pA}$, the step edge features a ×1 peridocity with maxima *in between* lattice sites as indicated by the dashed blue line. The authors of Ref. [44] speculated that the shifted ×1 charge maxima might stem from Si HCC atoms located one row behind the Si step-edge atoms. This would

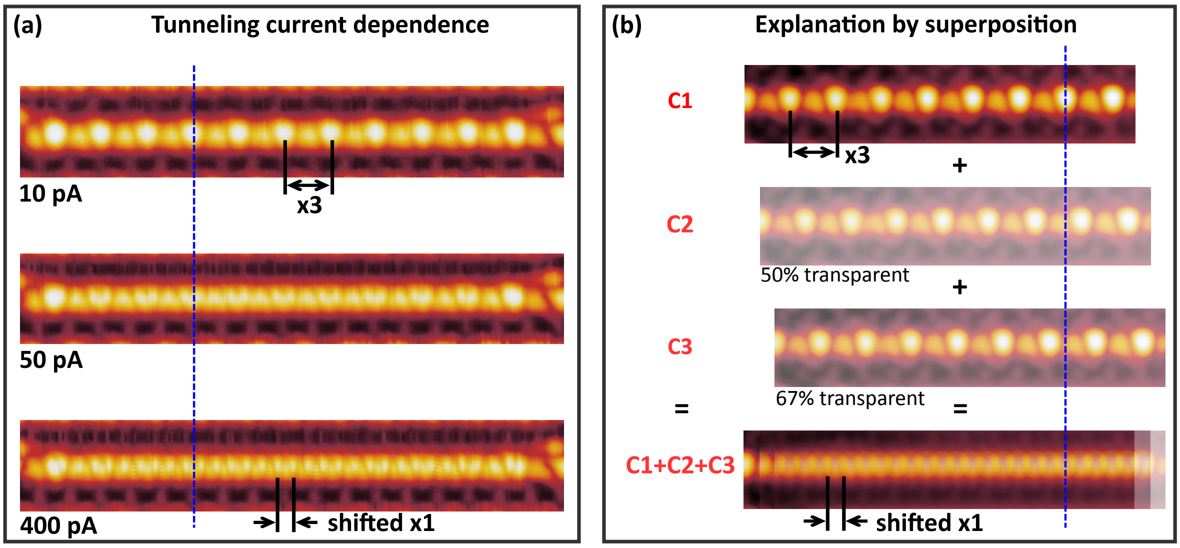

Figure 6.15: *(a) Constant current STM images of an identical Si(553)-Au step edge for various tunneling currents ($U = +1.0$ V, $T = 77$ K). At low tunneling current (10 pA), the step edge features the well-known ×3 superstructure. For a high current (400 pA) a ×1 periodicity with maxima between lattice sites is observed (see dashed blue line). (b) Superposition of three variants of the same spin chain STM image ($U = +1$ V). The images are shifted by a_0 with respect to each other, representing the three different spin chain configurations C1, C2, and C3. The superposition image (each configuration contributing 33 %) is a replica of the high current STM image.*

match their spatial position in the chain direction, since the Si row second closest to the step edge is shifted by $0.5a_0$ with respect to the Si step-edge atoms (cf. structure model presented in Fig. 5.8). However, this atomic assignment would also imply a lateral shift of ≈ 0.14 nm in the direction perpendicular to the step edge. Such a shift is not observed in the data presented in Fig. 6.15(a). Instead, an alternative explanation for the high current step-edge appearance is given in Fig. 6.15(b). For this purpose, three different variants of a Si(553)-Au step edge STM image have been superimposed. The three images differ by a horizontal shift of a_0, representing the three different ground state phases C1, C2, and C3 of a Si spin chain [cf. Fig. 6.8(c)]. The superposition image coincides with the high current experimental STM image. As it is the case in the high current STM scan, its intensity maxima show a ×1 spacing, and are located in between Si step-edge atoms (as indicated by the dashed blue line). This finding discloses that the high current STM images first reported in Refs. [43, 44] actually display a superposition of the three possible spin chain ground state configurations. It is important to mention that the lateral extension and form of the spin sites, as displayed in STM, have a strong impact on the superposition pattern. One might expect that a superposition of three shifted ×3 chains would result in a ×1 chain with maxima *at* the lattice sites. However, the rather large lateral extension and triangular shape of the spin sites in STM leads to a superposition pattern with ×1 maxima *in between* lattice sites.

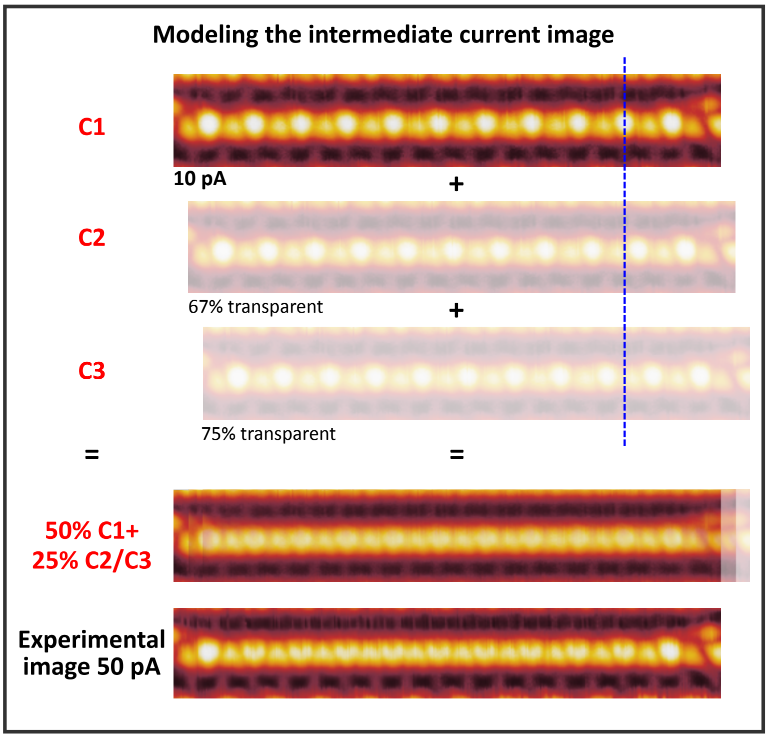

Figure 6.16: *Top: 10 pA STM image presented in Fig. 6.15(a). Below: Two variants of the 10 pA image, each shifted by a_0 with respect to the other, mimicking the spin chain configuration C2 and C3 respectively. C2 image features 67 % transparency and C3 75 %. Superposition of the first three images results in an image comprised of 50 % C1, 25 % C2, and 25 % C3 respectively. The superposition matches the experimentally observed intermediate tunneling current (50 pA) STM image (bottom).*

Intermediate Tunneling Current – Fig. 6.16 provides an explanation for the Si step-edge appearance at intermediate tunneling currents, i.e., for the 50 pA image in Fig. 6.15(a). Essentially, the appearance can once again be mimicked by a superposition of the spin chain configurations. In contrast to the modeling of the high current image, which requires equal contribution of all three spin chain configurations, the intermediate current image is best reproduced by an imbalanced contribution of the different spin chain configurations, namely, 50 % C1, 25 % C2, and 25 % C3. This modeling suggests that the tunneling current flowing between the tip and sample forces the spin chain to switch its configuration frequently during the STM scan. For an intermediate tunneling current, the ground state configuration (C1) is still dominant, but C2 and C3 contribute significantly to the STM image. For a high tunneling current, all configurations exist with equal probability.

Effect of Discrete Chain Length – In principle, all three spin chain configurations are energetically degenerate. However, in real-world systems, defects terminate the step-edge chains, resulting in finite and discrete chain lengths. Finite chains can be categorized into three groups characterized by their absolute chain length. In general, chains featuring a length

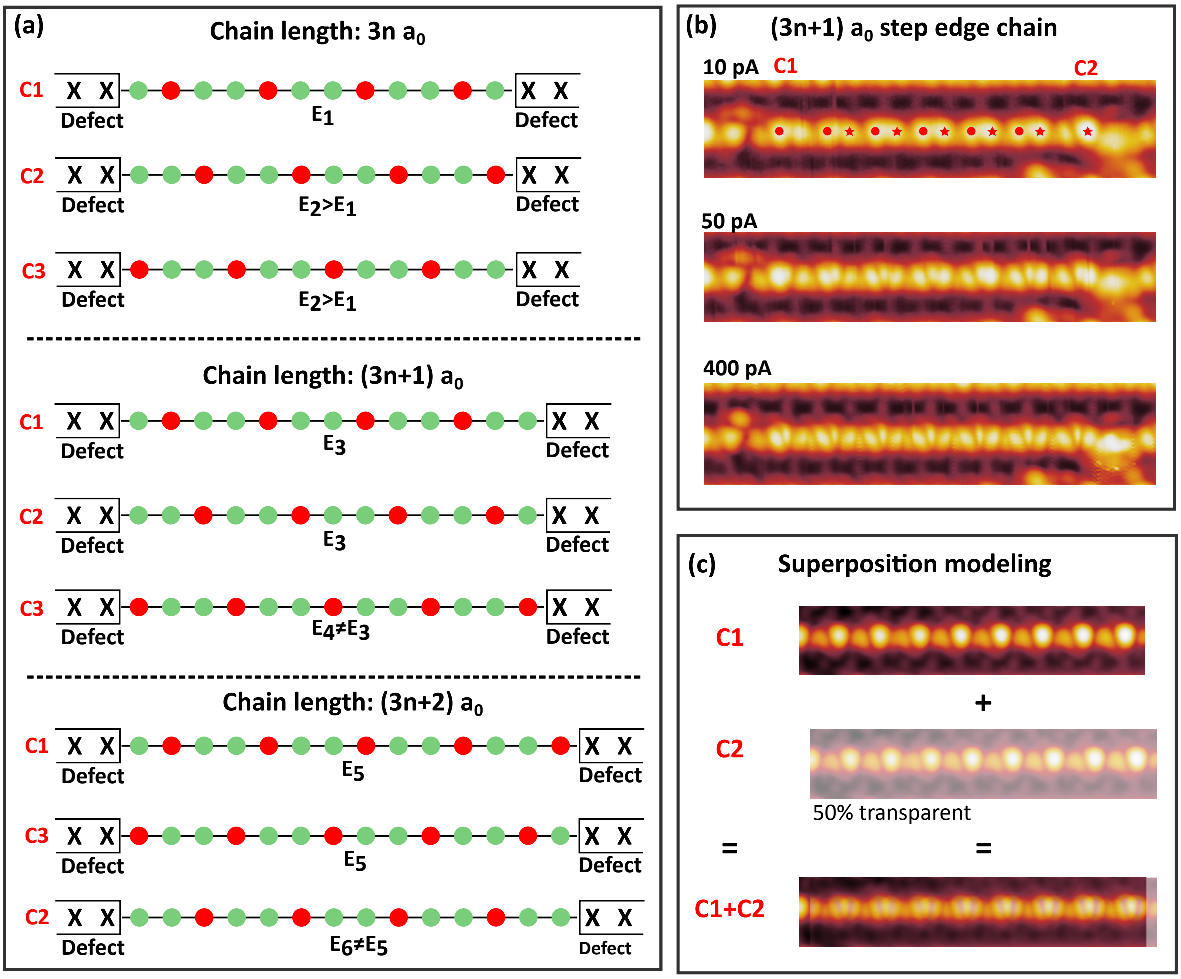

Figure 6.17: *(a) Various spin chain configurations for the three absolute wire length categories of* $3n \cdot a_0$, $(3n+1) \cdot a_0$, *and* $(3n+2) \cdot a_0$. *The finite wire length lifts the degeneracy of the three spin chain configurations. Consequently, some configurations are energetically more favorable than others, as indicated by the energy labels* E_1 - E_6. *The hierarchies of theses energies are educated guesses based on the experimental STM data and require a verification by e.g. DFT. (b) Constant current STM of an identical Si step edge with a length of* $(3n+1) \cdot a_0$ *(here* $22a_0$*) for different tunneling currents. The low current image (10 pA) displays two spin chain configurations, each pinned at one chain end as marked by the red stars and dots. With increasing tunneling current, the step-edge appearance changes, showing a tulip-like pattern at 400 pA. (c) Modeling of the high current image shown in (b). The tulip pattern can be reproduced by a superposition of two spin chain configurations (50 % C1 and 50 % C2).*

of $3n \cdot a_0$, $(3n+1) \cdot a_0$ and $(3n+2) \cdot a_0$, with n being an integer, exist [see Fig. 6.17(a)]. As a consequence of the discrete chain length, the degeneracy of the three spin chain configurations is lifted. In particular, for a $3n \cdot a_0$ wire length, the configuration labeled C1 in Fig. 6.17(a) is energetically more favorable than the one labeled C2 and C3, as can be inferred from Ref. [27]. In this experimental study, the discrete chain length was found to determine whether or not a distinct ×3 pattern can be observed, for wires shorter than $\approx 10\,\mathrm{nm}$. Specifically, a clear ×3 spin chain is imaged by STM for a wire length commensurate with $3a_0$ [27]. For a wire length of $(3n+1) \cdot a_0$ and $(3n+2) \cdot a_0$, fluctuating patterns are observed [27]. The absolute chain length can, in principle, be defined in different ways, since the crossover region between the defect and the chain does not feature a clear-cut chain end (see Ref. [117] for details). Moreover, various defects, which differ in shape, extension, and bias dependence, exist on the Si(553)-Au surface [117, 149, 176]. For consistency reasons, the method used in Ref. [27] has been applied. Here, the wire length is essentially determined to be the distance between the two bright protrusions (i.e. spin sites) terminating the finite step edge plus an additional $3a_0$.

Fig. 6.17(b) displays an STM image of a Si step edge with a length of $(3n+1) \cdot a_0$ (here $22a_0$). In contrast to the distinct ×3 pattern of the step edge shown in Fig. 6.15(a) (wire length $3n \cdot a_0$; $33a_0$), this step edge features two different spin chain configurations, each pinned at one chain end [see red markers in 10 pA scan of Fig. 6.17(b)]. With increasing tunneling current, the step-edge appearance changes, and exhibits a pattern which is reminiscent of tulips. This tulip pattern can be modeled by an overlay of *two* of the three spin chain configurations [see Fig. 6.17(b)], which implies that electrons tunneling between the tip and the sample induced a flip between only two of the spin chain configurations.The different behavior compared to the step edge presented in Fig. 6.15(a), in which all three configurations contribute at high tunneling currents, can be explained by the different wire length categories of the two finite chains. In particular, a energetic hierarchy, as suggested in Fig. 6.17, seems to determine the current dependent behavior.

Pinning at Defects – In addition, all of the observations above suggest that the “excitation” of a spin chain into other configurations is more likely to occur in the center of the finite step edges. Close to the terminating defects, the spin chain exhibits one specific configuration, while the center of the chain displays a superposition pattern [see, for example, 400 pA image of Fig. 6.15(a) or 50 pA image of Fig. 6.17(b)]. This observation implies a pinning by defects similar to what has been observed in the course of the temperature dependent spin chain studies presented in Sec. 6.6.

Consistency with Previous Results – At first glance, the results presented above seem to contradict the works of Polei *et al.*, which report a ×2 step-edge periodicity for high tunneling currents as opposed to the ×1 discussed above. However, the high current images from that studies can be reproduced by a superposition of the respective low current images (not shown here). The origin of the slight ×2 modulation in their high current images will be explained in the following paragraph.

6.4.3 Excited State at 4 K

As outlined in the introduction of this section, it is not possible to observe the ×3 spin chain pattern at 4.3 K in STM. Instead, the step edge displays the "excited" ×2 pattern [44]. The following paragraph will discuss the step-edge pattern observed at 4.3 K in terms of the nature of the excited state revealed above.

Fig. 6.18 presents high-resolution Si(553)-Au STM data obtained at a sample temperature of $T = 4.3\,\mathrm{K}$. Si(553)-Au STM images recorded at such low temperatures have not been reported before. For a bias value sensitive to the spin site DOS [see Fig. 6.18(a)], the Si chain features an overall ×2 periodicity. More specifically, the step-edge chain exhibits asymmetric burger-like charge cloud pairs, which are formed by a fundamental ×1 periodicity. Adjacent charge clouds show a small intensity difference as well as a pair building [see line profiles in Fig. 6.18(d)], which leads to the ×2 modulation of the step edge. The maxima of the step-edge protrusions (×1) are located between the lattice sites of the step-edge atoms as can be inferred from the structural model overlay. Moreover, two step edge variants can be identified: a forward and a backward step edge. The origin of these two variants can be traced back to the unidirectional interaction between Au and Si chains described in detail in Sec. 6.2. Once again, the directionality of the step edge is determined by the registry of the surrounding Au chains ($3/2\,a_0$ vs. $1/2\,a_0$) as illustrated in Fig. 6.18(c). These findings support the conclusion that the subtle ×2 modulation is a consequence of the Au-Si chain interaction, while the intrinsic step-edge periodicity is in fact ×1. In particular, the Au chain on the neighboring downhill terrace seems to induce a slight pairing of the ×1 charge clouds, i.e., it determines the position of the center of the burger structure. The Au chain on the same level terrace, in turn, imprints the asymmetry to the burger structure (i.e. bigger and smaller "burger halves"). The bottom line of this analysis is that the Si step edge essentially features a ×1 periodicity with maxima between step-edge lattice sites. This is exactly the same observation made for the high tunneling current images recorded at 77 K [see Fig. 6.15(a)]. Consequently, one can draw the conclusion that both step-edge appearances have the same origin, namely, the superposition of the three distinct spin chain configurations. Additional support for this interpretation comes from the LT SPA-LEED measurements presented in Fig. 6.3. Although recorded at a very low temperature (10 K), the pattern still features ×3 streaks/spots, suggesting that the ×3 spin chain state is the ground state of the step edge. The ×2 pattern observed in LT STM data must, therefore, be induced by the STM measurements procedure, i.e., by the tip-sample interaction.

For lower tunneling bias, the step edge of the 4.3 K image displays a different pattern, namely, the bone-and-joint segments also identified in the 77 K data [see Fig. 6.18(b)]. This

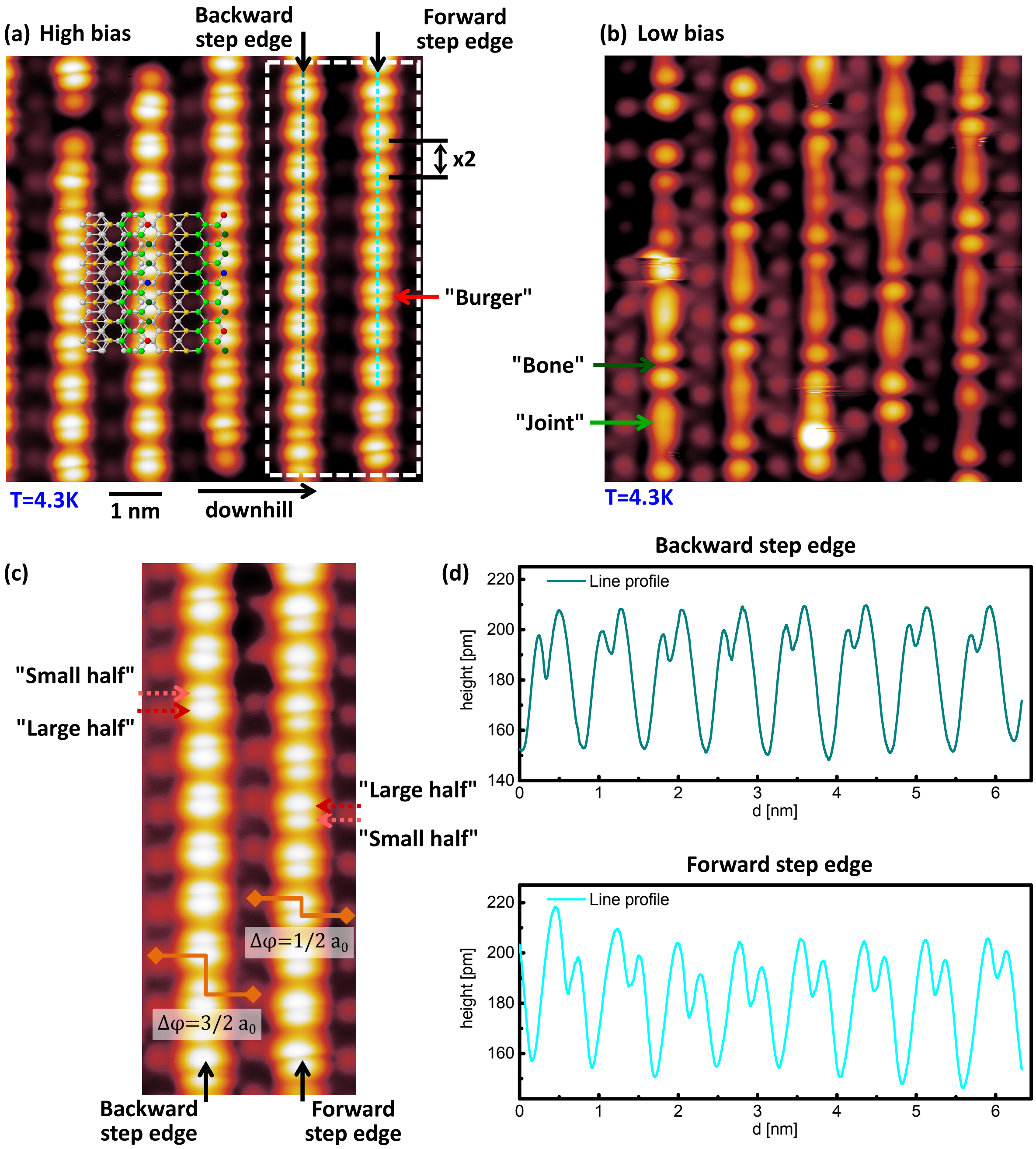

Figure 6.18: *(a),(b) Unoccupied states STM images of an identical Si(553)-Au sample area recorded at 4.3 K. At high tunneling bias [(a), $U = +1.0\,\mathrm{V}$, $I = 100\,\mathrm{pA}$], the step edge features a $\times 2$ periodicity built by $\times 1$ charge clouds exhibiting a burger-like appearance (see labels). The structural model overlay has been aligned with respect to the Au charge clouds which are not expected to show any shifts between 77 K and 4.3 K. Two chain types with opposite directionality are observed. At low tunneling bias [(b), $U = +0.3\,\mathrm{V}$, $I = 50\,\mathrm{pA}$], the step edge features the bone-and-joint structure well-known from the 77 K data. Notably, the given bias values have to be handled with caution, a band bending may lead to a significant offset voltage. (c) Enlargement of two step-edge chains with different directionality [dashed white box in (a)]. The directionality of the step edges is determined by the phase relation of the adjacent Au chains (see orange markers). (d) Line profiles of the dashed light and dark cyan lines in (a).*

finding suggests the presence of one distinct spin chain configuration rather than a superposition of all three variants in case the step edge is scanned with low tunneling bias. This bias dependence allows one to speculate that the step-edge “excitation” depends not only on tunneling current and temperature, but also on the scanning bias.

In summary, it has been shown that a superposition of the three distinct ground state configurations of the Si spin chain provides a reasonable explanation for the “excited” step-edge state reported earlier. Several superposition combinations have be identified depending upon the discrete wire length and the magnitude of the tunneling current. Nevertheless, a complete physical picture of this step-edge “excitation” is still missing, and requires further modeling, for example, by DFT. A plausible interpretation comprises the excitation of the solitons by the tunneling current. However, it is not clear how solitons interact with the defects on Si(553)-Au. The solitons detected in the In/Si(111) wires are able to pass through defects [15]. Moreover, defects have been found to trap solitons via Coulomb interaction and strain fields [15, 16]. The latter has not yet been observed for Si(553)-Au solitons, suggesting a different defect interaction compared to the In/Si(111) solitons.

6.5 Details of the Electronic Structure

6.5.1 Band Structure from ARPES

Quasi-1D Au Bands – Fig. 6.19(a) displays a band map of the Si(553)-Au surface measured by means of ARPES at LT (50 K), i.e., a temperature at which the step edges feature ×3 spin chains. The map shows the intensity of the photoelectrons as a function of binding energy and momentum along the Γ_0 - K_0 - M_1 direction of the (1×1) surface Brillouin zone (SBZ) [see inset in Fig. 6.19]. The band structure is dominated by two parabolic bands labeled with S1/S2 (outer band) and S3 (inner band). These bands have been observed and characterized in various ARPES experiments [25, 137, 146, 177] and DFT studies [1, 22]. According to DFT, they essentially originate from silicon atoms in the center of the terrace, but are nonetheless Au-induced [22, A3]. In particular, S1/S2 is derived from a hybridization of the Au atom of the right-hand leg of the Au ladder with the Si atom located between the Au dimers, whereas S3 is associated with a hybridization of the left-sided Au ladder atoms and Si atoms located between the Au chain and the step edge [22, 177]. Nevertheless, they are usually referred to as “Au bands” in literature.

According to DFT studies, both Au bands are subject to a Rashba-type spin splitting. In particular, the splitting is found to be much smaller for S3 than for S1/S2 [1, 178]. Experimentally, the spin-splitting of the outer Au bands was initially verified only indirectly by an avoided band crossing of the original S1/S2 band with its backfolded counterpart S1*/S2* induced at the ×2 zone boundary [20]. Specifically, bands with different spin quantum number (S1 and S2* as well as S2 and S1*) cross each other, while bands with identical quantum number (S1 and S1* as well as S2 and S2*) interact, and form minigaps of less than 100 meV at their hypothetical crossing point [20]. Backfolding and avoided crossing are also visible in the band map presented in Fig. 6.19(a). Direct confirmation of the spin-splitting of the outer Au bands was later achieved by spin-resolved ARPES measurements [178, 179]. However, the predicted splitting of the inner Au band has not yet been confirmed experimentally, as the very small splitting appears to be beyond the resolution limit of current spin-ARPES instrumentation [178, 179].

The Si(553)-Au Fermi surface, as displayed in Fig. 6.20, shows a clear wiggling, reflecting the quasi-1D character of the electrons confined in the Au chains. In order to quantitatively compare the Au induced band structure measured with results obtained in earlier studies, a tight binding fit according to the model given in Ref. [137] was applied. The hopping ratios of $t_1/t_2 = t_{\|}/t_{\perp} \approx 10$ obtained for S3 and $t_1/t_2 = t_{\|}/t_{\perp} \approx 46(39)$ for S1(S2) confirm the quasi-1D character of the Au bands, and concur with the values reported in Ref. [137]. The complete band parameters attained by the fit can be found in Tab. 7.1 of the Appendix. Notably, the SBZ is shifted by half a reciprocal lattice vector in k_y direction compared to Ref. [137], resulting in a different phase of the wiggled Au bands, and, thus, a different sign for t_2.

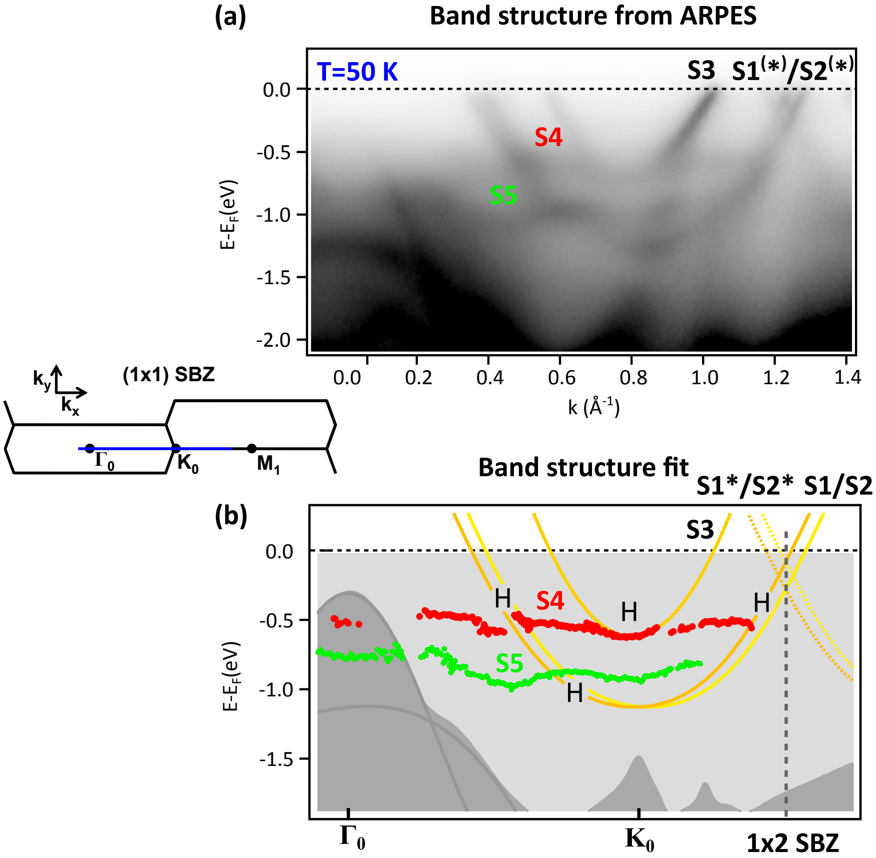

Figure 6.19: *(a) Band map of the Si(553)-Au surface along Γ_0 - K_0 - M_1 (inset) taken at 50 K ($h\nu = 21.2$ eV). Aside from the well-known Au bands (S1/S2, S3) two weakly dispersing bands (S4 and S5) can be identified. (b) Fits of the band map presented in (a). The Au induced bands S3 (orange), S1/S2 (dark/light orange) and their backfoldings S1*/S2* (dashed dark/light orange) at the (1×2) SBZ have been fitted with a tight binding model [137]. The red and green dots represent the maxima the weakly dispersing bands S4 and S5 respectively obtained by a maximum finding algorithm using the first and second derivative. S4 and S5 seem to hybridize with the Au bands as indicated by the black "H". Data acquisition and evaluation performed by L. Dudy.*

The Au band fillings, as determined by ARPES, are $n_{ARPES}(\mathrm{S1}) = 0.56$ and $n_{ARPES}(\mathrm{S2}) = 0.52$ (i.e., $n_{ARPES}(\mathrm{S1/S2}) = 0.54$ for each branch of the Rashba split band pair), and $n_{ARPES}(\mathrm{S3}) = 0.29$, which is once again in agreement with previous reports [17,25, 137]. The margin of error for these filling factors has been estimated at the maximum of 3 % due to uncertainties in the sample alignment. Importantly, the band fillings obtained do not match any commensurable nesting conditions, thereby excluding a simple Peierls scenario.

Moreover, the filling values do not coincide with the results from DFT. While the discrepancy is rather small for the outer Au band – $n_{DFT}(\mathrm{S1/S2}) = 0.5$ [1, 22] – the theoretical band filling for the inner Au band S3 deviates considerably from the experimental value [$n_{DFT}(\mathrm{S3}) = 0.167$] [A3]. One possible explanation for the mysterious discrepancy could be external doping of the Si(553)-Au surface by, e.g., substrate dopants or defects. This assumption is consistent with doping experiments in which the band filling of S3 was found

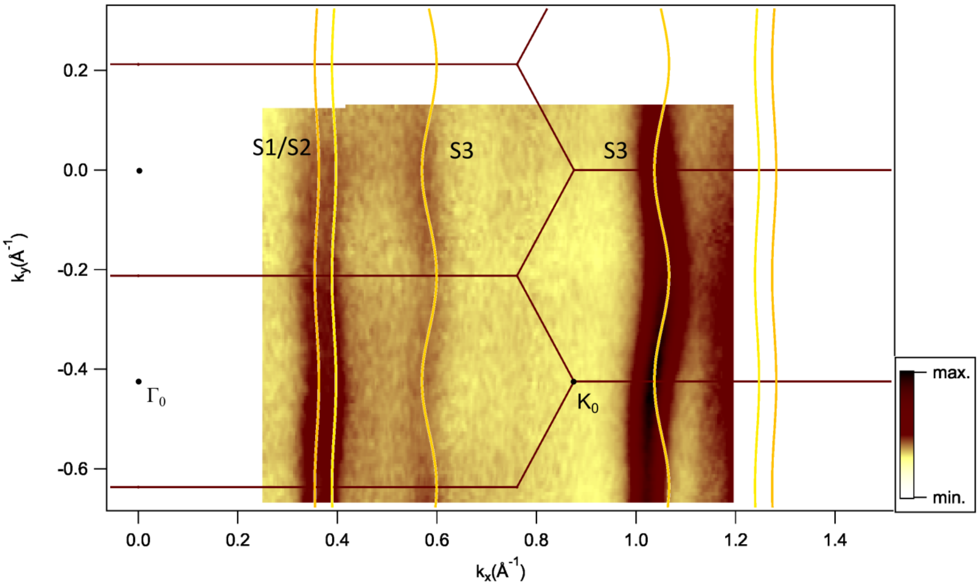

Figure 6.20: *(a) Fermi surface ($E_F \pm 30$ meV) of the Si(553)-Au measured by ARPES ($T = 11$ K) together with a tight binding fit (orange lines) according to the model presented in Ref. [137]. Note that this model ignores the Rashba splitting of S1/S2. The results of the fit are listed in Tab. 7.1 of the Appendix. The (1×1) SBZ is superimposed the data. Compared to the original study by Crain et al. [137], the SBZ is shifted by half in k_y direction. Data acquisition and evaluation performed by L. Dudy.*

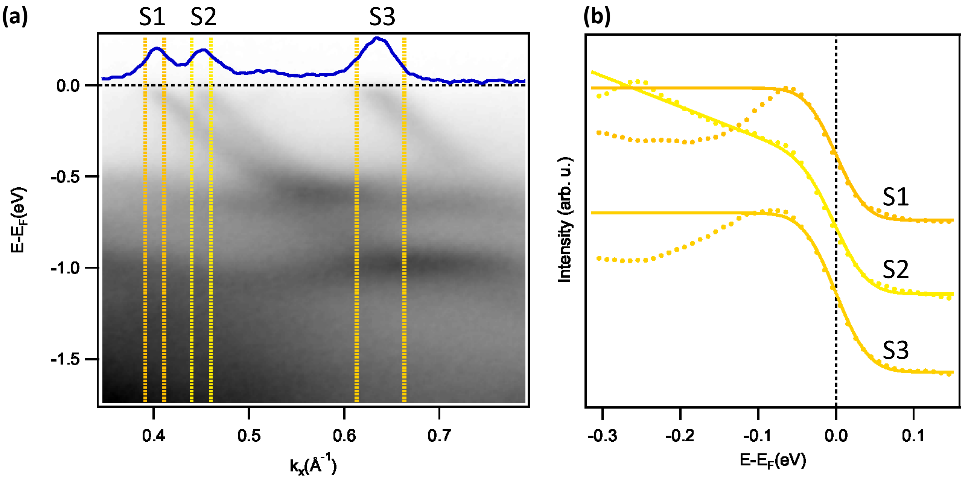

Figure 6.21: *(a) Band map of a Si(553)-Au surface recorded by means of ARPES at 11 K. Extrinsic shifts of the spectrum due to surface photovoltage effects have been carefully corrected. (b) EDCs taken at k_F of the S1, S2, and S3 bands (orange dots). The dotted orange lines in (a) mark the integration window of each EDC. Orange lines represent a Fermi distribution function convoluted with a Gaussian of 30 meV width to consider the experimental broadening. Data acquisition and evaluation performed by L. Dudy.*

to be highly sensitive to the dopant concentration, while S1/S2 remained essentially unaffected [177].

It should be noted that LT ARPES measurements on Si(*hhk*)-Au surfaces suffer a photovoltage shift [25], which has been carefully corrected by the energy difference between the S5 band (see below) and the leading edge of the S3 band. The amended ARPES band structure displayed in Fig. 6.21 indicates metallic behavior. All three Au bands disperse through the Fermi level, and are cut off by a Fermi edge. The latter is pictured in Fig. 6.21(b): The EDCs taken at k_F of the respective bands follow a Fermi distribution function convoluted by a Gaussian, which accounts for the experimental broadening.

Majority Spin Site State – In addition to the Au-derived bands, the LT band map [Fig. 6.19(a), $T = 50\,\mathrm{K}$] is comprised of two almost non-dispersive surface bands (S4 and S5) at a binding energy of $E_{B,S4} = (690 \pm 50)\,\mathrm{meV}$ and $E_{B,S5} = (1000 \pm 50)\,\mathrm{meV}$ respectively. Interestingly, both bands show a very small band width of only 100-200 meV, suggesting that they stem from rather localized electronic states. The lower lying band labeled S5 has been observed in another ARPES experiment [137]. Its origin has never been clarified in literature, and will be discussed in further detail below. On the contrary, the S4 band has *not* been observed in previous ARPES experiments [1, 25, 137, 146]. A comparison with local STS results presented in Fig. 5.10 indicates that the *S4 band* should be assigned to the majority band of the *dangling bond step-edge spins*. The red curve in Fig. 5.10 features a peak in the occupied states at about -720 meV in addition to the characteristic unoccupied spin site DOS. This is in line with the energetic position of the S4 band seen in ARPES.

The detection of a weakly dispersing band associated with the dangling bond spins in ARPES uncovers a long-standing mystery [146]. There could be several reasons why this band remained undetected in ARPES for such a long time: First, the band shows a strong temperature dependence, and, thus, can only be detected at sufficiently low temperatures (below ≈ 100 K; see Sec. 6.6). Moreover, the occupied spin state is located at higher binding energies than suggested by PBE based DFT calculations [1, 146] (see Sec. 5.3). Another possibility is that the intensity of S4 might significantly depend on the photon energy. Synchrotron ARPES experiments [17, 137, 146] have been performed at higher photonenergies, e.g., 34 eV or 46 eV, due to higher photoemission cross sections for the Au-induced surface bands [19]. In addition, the polarization of the photon beam may play a role.

Most likely, however, is that the defect concentration of the samples studied elsewhere [17, 137, 146] was too high to observe the spin state (see time-dependent ARPES study in Sec. 6.6). This is not surprising, since most synchrotron endstations are not dedicated to excellent atomic wire growth as it may be the case in specialized home laboratories. In addition, synchrotron experiments are typically performed in one to two weeks, including the transfer of the preparation recipe to a different chamber, rendering the preparation of a low-defective Si(553)-Au sample a difficult task. The importance of a low defect concentration becomes evident in the time-dependent ARPES analysis presented in Fig. 6.28 of Sec. 6.6. These experiments demonstrate an exceptional fast smearing of the S4 band (which ends up in its complete disappearance) with increasing exposure time to residual gas atoms, i.e., with increasing step-edge defect density.

Contrary to expectation, neither band shows a clear periodicity, e.g., ×3 as suggested by the real space spin site spacing. Instead, S4 and S5 seem to hybridize with the Au bands [see "H" labels in Fig. 6.19(b)], resulting in a slight non-periodic wiggling of both bands. Thus, no tight binding model was fitted to S4 and S5. Instead, the red and green dots plotted in Fig. 6.19(b) represent the respective maxima obtained from a maximum finding algorithm.

The atomic assignment of S5 is not as clear cut as for S4. Keeping the structural model in mind, one would expect two additional weakly dispersing bands, namely, one derived from the nonpolarized Si step-edge atoms and one from the left-sided Si atoms of the HCC. DFT predicts the band derived from the nonpolarized Si atoms in approximately the same energy region as the majority spin state [144]. The band associated with Si atoms from the opposite side of the HCC is predicted several tenths of an eV below the band of the nonpolarized step-edge atoms (i.e., at a binding energy of about 1 eV). This fits the energetic position of S5, suggesting that S5 stems from Si atoms located at the left side of the HCC. Additional support for this assignment comes from the temperature-dependent behavior of the S5 band. In contrast to S4, S5 does not show a significant bleaching with increasing temperature (see Sec. 6.6). Such behavior is expected for a band associated with the left side Si HCC atoms, but not for the nonpolarized step-edge band which should show a similar temperature-dependent behavior as the spin site band (see Sec. 6.6). Thus, one can draw the conclusion that *S5* originates from the *left-sided atoms of the Si HCC.* Further experimental support for this assignment comes from dI/dU mapping of the occupied Si(553)-Au states as presented in the following paragraph.

6.5.2 Local Density of States

Indications for Metallic Au Chains – Fig. 6.22 displays dI/dU spectra taken at different characteristic locations of the Si(553)-Au surface. The spectra have been extracted from the same spectroscopy grid as the spectra presented in Fig. 5.10. However, their spatial dependence has been evaluated with more differentiation in order to gain additional insight into the electronic structure of the distinct chain elements. The orange curve represents spectra taken at the position of the Au atoms. Magenta and purple curves have been recorded at spin sites A and B, while the light and dark green spectra have been taken at the position of the joint and bone segments. All spectra show a finite LDOS at E_F, indicating metallic behavior (see enlargement of Fig. 6.22). In contrast to the spectra presented in Refs. [146,A1], the Au chain dI/dU signal does not exceed the Si signals at the Fermi level. Instead, all spectra show similar, but finite dI/dU intensity. The reason for the different relative intensities is

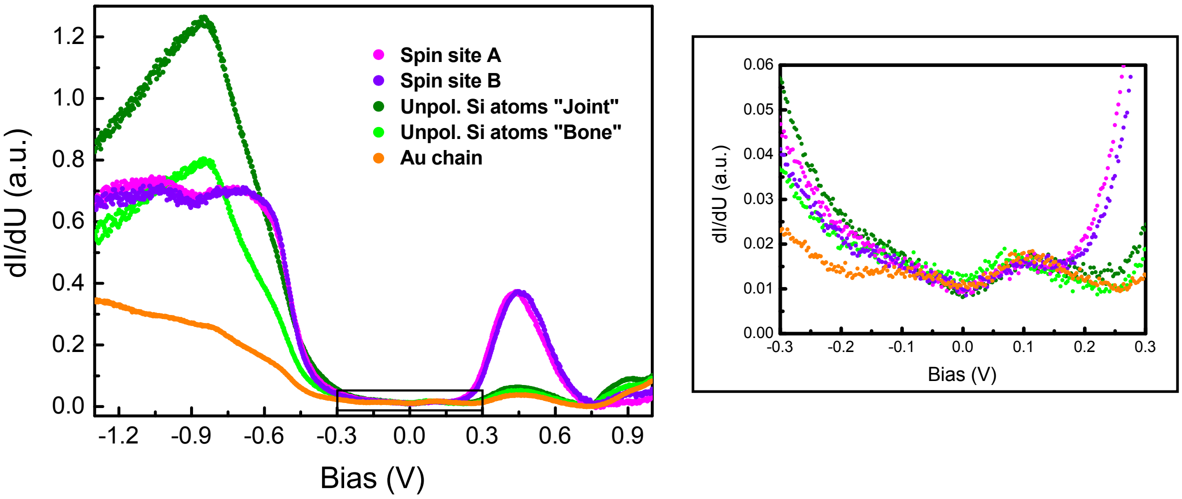

Figure 6.22: *Local STS on various, characteristic elements of the Si(553)-Au surface. Grid spectroscopy has been performed with the lock-in technique ($U_{mod} = 10$ meV) at 77 K. A set-point of $U_{set} = +0.2$ V was chosen to avoid strong local variations in the tip-sample distance. Spectra have been offset-corrected using simultaneously recorded I(U) curves as a reference. Inset: enlargement of the area around the Fermi level (black box). All spectra show finite DOS at E_F.*

that the set-point bias for this spectroscopy grid was chosen closer to E_F ($U_{set} = +0.2$ V) to minimize set-point effects (cf. Sec. 3.1). Nevertheless, the finite Au LDOS indicates that the Au chains are metallic even at LT, thereby excluding the textbook Peierls scenario suggested in earlier studies [25, 26]. This finding is consistent with the results from ARPES and the detection of plasmon excitations [A4] (see below). The spectra recorded at the position of the spin sites confirm the energy splitting of the unoccupied spin DOS peak discussed in Sec. 6.2. For the occupied states, a much smaller splitting, if any, is observed. The two curves recorded at the nonpolarized Si step-edge atoms have identical shapes but different intensities. The spectrum representative for the joint segments displays an overall higher intensity than the spectrum recorded at the bone segments. This suggests that the inequivalent intensities of bone and joint segments observed in constant current STM images (see Sec. 6.2) come from an LDOS imbalance rather than an LDOS splitting as is the case for the spin sites. Thus, the unidirectional interaction between Au chains and Si step edges appears to be even more complex than discussed in Sec. 6.2: The Au chain located at the same level terrace induces a DOS imbalance to the nonpolarized step-edge atoms, while the Au chain of neighboring downhill terrace creates an energy splitting of the spin site DOS.

Majority Spin Site State – To further scrutinize the occupied LDOS of the Si step edges, bias dependent topography images and dI/dU maps have been recorded simultaneously on an identical Si(553)-Au sample area (see Fig. 6.23). The topography images [Fig. 6.23(a)-(e)] are fully consistent with the data presented in Fig. 5.9 and support the spin chain scenario as outlined in Sec. 5.4. Although the local resolution of these images is lower than in Figs. 6.5

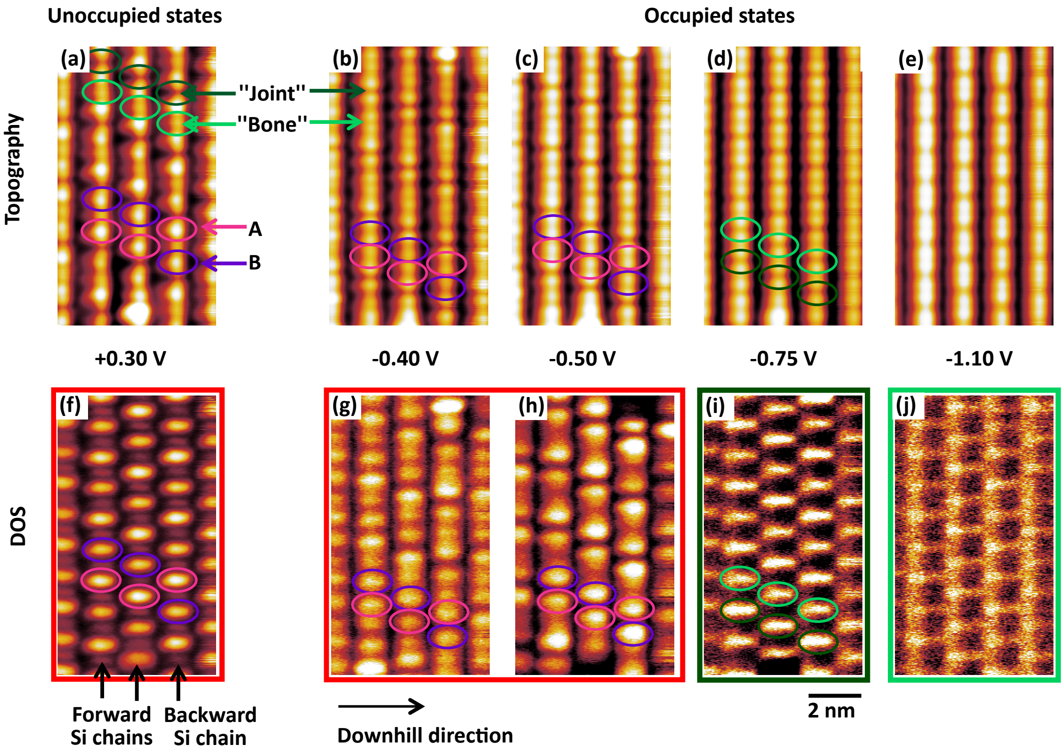

Figure 6.23: *Si(553)-Au constant current STM images [(a)-(e)] and dI/dU maps [(f)-(j)] for various tunneling biases ($T = 77\,K$). dI/dU maps have been recorded simultaneously with the topography images using the lock-in technique ($U_{mod} = 10\,\mathrm{meV}$). All images display the identical sample area comprising two forward and one backward Si step-edge chain. dI/dU maps taken at -0.40 V and -0.50 V [(g) and (h)] reveal clear spin site DOS. The corresponding topography images do not display any spin sites, but rather bone-and-joint segments. At -0.75 V [(i)], the dI/dU map is dominated by the DOS of the nonpolarized step-edge atoms. At even higher negative bias [-1.10 V; see (j)], DOS from the left-sided atoms of the Si HCC is visible.*

and 6.9, the step-edge charge modulation and its different chain segments (spin sites A and B, bones and joints, cf. Sec. 6.2) can be readily identified (see labels in Fig. 6.23). The lower local resolution is due to a relatively blunt tunneling tip, which is well suited for spectroscopy experiments like dI/dU mapping [71]. The dI/dU map of occupied states ($U = +0.3\,\mathrm{V}$) is fully consistent with the maps presented in Fig. 6.6(a). A clear intensity difference between adjacent spin sites is visible. Although the topography images for negative bias voltages are dominated by the nonpolarized step-edge atoms (cf. Sec. 5.4), the corresponding dI/dU maps at $U = -0.4\,\mathrm{V}$ and $U = -0.5\,\mathrm{V}$ [Fig. 6.23(g) and (h)] clearly feature the occupied spin site state. The maps show highest intensities *between* the nonpolarized Si atoms imaged in the corresponding topography scan as indicated by the magenta and purple ellipses. On the contrary, the dI/dU map taken at $U = -0.75\,\mathrm{V}$ displays intensity clouds at the centers of the bone and joint segments respectively (see green ellipses), suggesting the presence of states stemming from the nonpolarized step-edge atoms in this energy region. For even higher negative biases [$U = -1.10\,\mathrm{V}$, (j)], dI/dU signal is found at the left-sided atoms of the Si HCC.

Although dI/dU maps display only a relative DOS contrast and are prone to set-point effects (see Sec. 3.1), the results obtained are in line with the grid spectroscopy data presented in Fig. 6.22, and provide additional support for the assignment of the S4 and S5 bands seen in ARPES. An extended bias series for both unoccupied and occupied states is displayed in the Appendix (Fig. F.10 and Fig. F.11).

As a side note, adjacent DOS clouds observed in the dI/dU maps show a pronounced intensity difference. This modulation is a consequence of the unidirectional Au-Si chain interaction discussed in Sec. 6.2, and can be utilized to identify the atomic origin of the respective intensities. The sample area imaged is comprised of two forward and one backward Si step edge [see labels and colored ellipses Fig. 6.23(a) and (f)]. In particular, bone segments of adjacent step edges feature a phase shift of $-1.5a_0$, as indicated by the green ellipses in Fig. 6.23(a). Neighboring spin sites of the same type display a phase shift of $-1.5a_0$ between the left and central step-edge chain and $-4.5a_0$ between the central and right step edge [see magenta and purple ellipses in Fig. 6.23(a)-(c) and (f)-(h)]. The DOS clouds dominating Fig. 6.23(g) and (h) show the same intensity pattern, which indicates to their spin site origin. DOS clouds in Fig. 6.23(i), on the other hand, display the intensity pattern of the joint and bone segments as stressed by the green ellipses. In conjunction with their local position, this suggests that these DOS clouds are derived from nonpolarized Si atoms.

In summary, the enhanced scrutiny of the occupied step-edge LDOS offered by STS, uncovered (i) the majority state of the spin sites, (ii) a state stemming from the lone-pair step-edge atoms, and (iii) DOS from left-sided Si HCC atoms. Their absolute and relative energetic positions are in agreement with the two low-dispersive bands found in ARPES. Although much easier to detect in the unoccupied states, the complex step-edge charge modulation induced by the Au-Si chain interaction also occurs for the occupied states.

Au Channel Width – In the framework of this thesis, the plasmon excitations of various Si(*hhk*)-Au systems have been investigated in close collaboration with colleagues from the University of Hannover [A4]. For this purpose, plasmon dispersions have been recorded by means of electron energy loss spectroscopy [180]. 1D-like dispersions could indeed be detected on various Si(*hhk*)-Au systems. However, these dispersions feature a significant influence of the Au wire spacing as well as the actual width of conducting Au chains. In particular, the Au chain width was found to have a much stronger impact on the dispersion than the Au chain spacing. In this context, an experimental estimate for the actual width of the Au conduction channel was required. This has been realized exemplarily by local STS measurements on the Si(553)-Au surface. Fig. 6.24(a) displays a dI/dU map close to the Fermi level (+6.4 meV). The spectroscopy set-point was chosen such that the Au chain spectra feature a higher dI/dU signal close to E_F than the Si spectra. Consequently, the image shows a modulated electron density with finite width and highest intensity at the position of the Au chain [see topography overlay in the lower part of Fig. 6.24(a)]. Although it has been shown that relative intensities

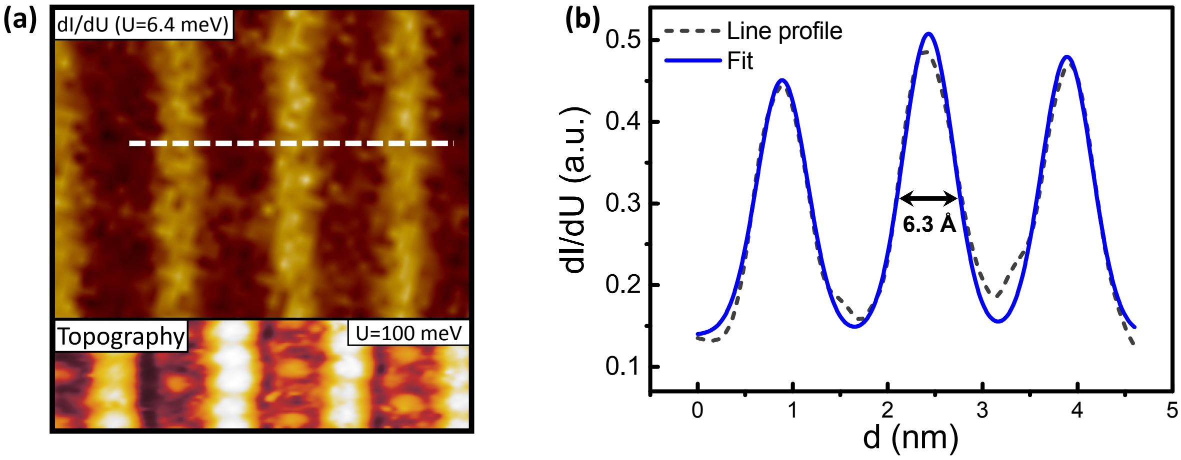

Figure 6.24: *(a) Bottom: Constant current STM image of the Si(553)-Au surface taken at $U = +100\,\text{meV}$ and 50 pA. Top: dI/dU grid map of a Si(553)-Au sample area recorded with the lock-in technique ($U_{mod} = 10\,\text{meV}$, $U_{set} = -0.3\,\text{V}$, $I_{set} = 40\,\text{nA}$) displayed close to E_F ($U = +6.4\,\text{meV}$). The dI/dU signal is significantly enhanced at the Au chain position. From [A4]. (b) Line profile along the dashed white line in (a). Blue: Gaussian fit to the profile revealing a wire width of (6.3 ± 0.3) Å. The dI/dU data have been offset-corrected using simultaneously recorded $I(U)$ curves as a reference.*

depend on the spectroscopy set-point (cf. Sec. 3.1), this approach is well suited to determine the width of the Au channel. A fit to the line profile taken along the dashed white line reveals a full width at half maximum of (6.3 ± 0.3) Å of the electron density modulation. This value comparable with the effective wire width (7.5 Å) determined from the plasmon dispersion [A4].

6.6 Temperature Dependence of the Si Step Edge: Thermal Creation of Solitons

It has long been known that both chain types of the Si(553)-Au surface show a pronounced temperature dependence [25,26]. The STM data presented in Fig. 6.25(a) and (b) confirm the temperature-dependent superstructures previously observed [25,26]: At RT, the well-known LT superstructures (×3 for the Si step edge and ×2 for the Au chain) cannot be detected. Instead, both chain types display a ×1 periodicity in STM. Moreover, a temperature-dependent band gap opening was inferred from ARPES measurements [25], leading to the interpretation of these observations as two Peierls instabilities, driven by nesting in the metallic surface bands. Historically, the S1/S2 bands (nearly half-filled) have been assigned to the Au chain and the S3 band (close to 1/3 filled) to the Si step edge [25]. At present, several experimental and theoretical findings safely exclude such a Peierls interpretation: (i) The well-established Rashba splitting of S1 and S2 casts doubt upon the ARPES measurements of Ref. [25], which have claimed a different temperature-dependence for S1 and S2. Moreover, the ARPES data presented in this thesis suggest a metallic behavior of the Au chain at LT (see Subsec. 6.5.1), which is consistent with the metallic Au chain behavior detected via STS (Subsec. 6.5.2). (ii) The assignment of the S3 band to the Si step edge is incorrect. S3 is, in fact, not connected to the Si step edge, but is rather Au chain induced (cf. Sec. 6.5). In addition, the formation of spin chains at the Si(553)-Au step edges is by now well established, excluding a Peierls-like CDW for this chain type (cf. Sec 5.4).

The spin chain scenario provides a promising alternative explanation for the temperature-dependent step-edge superstructure. Molecular dynamics and kinetic Monte Carlo simulations predict a hopping of the spin sites between adjacent lattice sites to be responsible for the high-temperature step-edge appearance [42]. It has been found that, at sufficiently high temperatures, the spin sites essentially move like a random walker (no defects considered). At very low temperatures (about 30 K), spin hopping freezes out, restoring the ×3 ordered spin chain. In addition, a small temperature window (30-35 K) has been found in which correlated hopping behavior occurs, preserving at least a short-range ×3 ordering. Defects can significantly increase the given freeze-out temperature [42]. This scenario plays an important role in the interpretation of the following temperature-dependent ARPES and STM data.

6.6.1 K-Space Point of View

RT vs. LT ARPES Band Structure – Fig. 6.25(b) shows two ARPES band maps recorded at RT and 50 K respectively. The major difference between the two maps is the missing S4 band in the RT data set [see also fits presented in Fig. 6.25(c)]. This band has been associated with the Si step-edge atoms (for a complete discussion of the LT band structure see Sec. 6.5). As a result, the S4 band serves an additional opportunity (aside from real-

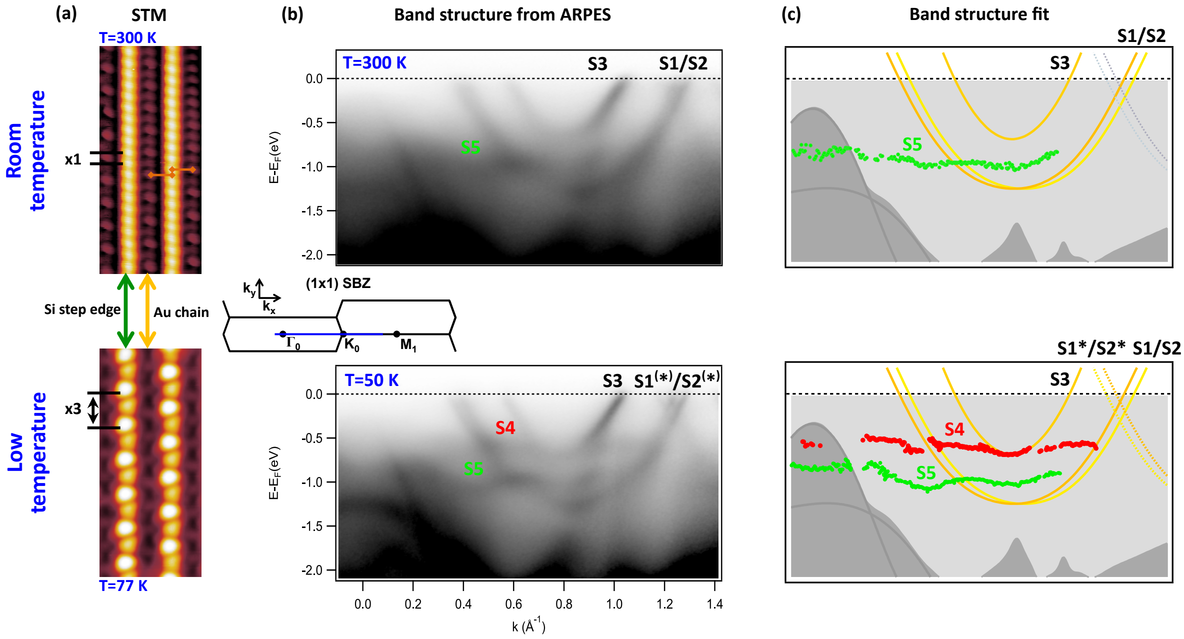

Figure 6.25: *(a) RT (top) and LT (bottom) STM image of the Si(553)-Au surface taken at a bias value sensitive to the unoccupied dangling bond spin DOS ($U = +1.0\,V$). At LT the step edges feature a distinct ×3 periodicity. At RT, no superstructure is observed, but the step edges exhibit a ×1 periodicity. The ×1 maxima are at positions of step edge lattice site as indicated by the orange markers. The Au chains display a ×2 periodicity at LT. At RT, the two right Au chains displayed show a ×1 periodicity, while the left Au chain features a ×2 periodicity. (b) Band map of the Si(553)-Au surface along Γ_0 - K_0 - M_1 (inset) recorded at RT (top) and LT (bottom). The LT, image is the same as presented in Fig. 6.19. The weakly dispersing band S4 is only visible at LT. (c) Fits of the respective band maps presented in (b). The Au induced bands S3 (yellow), S1/S2 (dark/light yellow), and S1*/S2* (dashed dark/light yellow) have been fitted with a tight binding model [137]. The red and orange dots represent maxima of Gaussian fits to the band intensity of the weakly dispersing bands S4 and S5 respectively. Data acquisition and evaluation performed by L. Dudy.*

space STM experiments) to study the temperature-dependent behavior of the Si(553)-Au spin chains in detail. One additional and less important difference is that the backfolded S1*/S2* bands, which can clearly be identified in the LT band map, are only slightly visible at RT. This is consistent with the result from STM imaging. In this case, only some Au chains show a distinct ×2 superstructure, while others feature a ×1 periodicity [see Fig. 6.25(a) or Fig. 5.7(b)]. This observation may be explained by a flipping of the tilted Au dimers at a rate faster than the STM measurement timescale.

Temperature-Dependent ARPES Study – Fig. 6.26 presents the temperature dependence of the S4 band. In contrast to all other surface bands, the spin band gradually spreads out with increasing temperature, as can be inferred by the temperature-dependent EDCs plotted in Fig. 6.26(a). Most pronounced in this heating cycle is a decrease of the S4 peak accompanied by a filling up of the intensity minimum at about −200 meV. Upon subsequent cooling, S4 reappears, and the intensity minimum at about −200 meV recovers. This re-

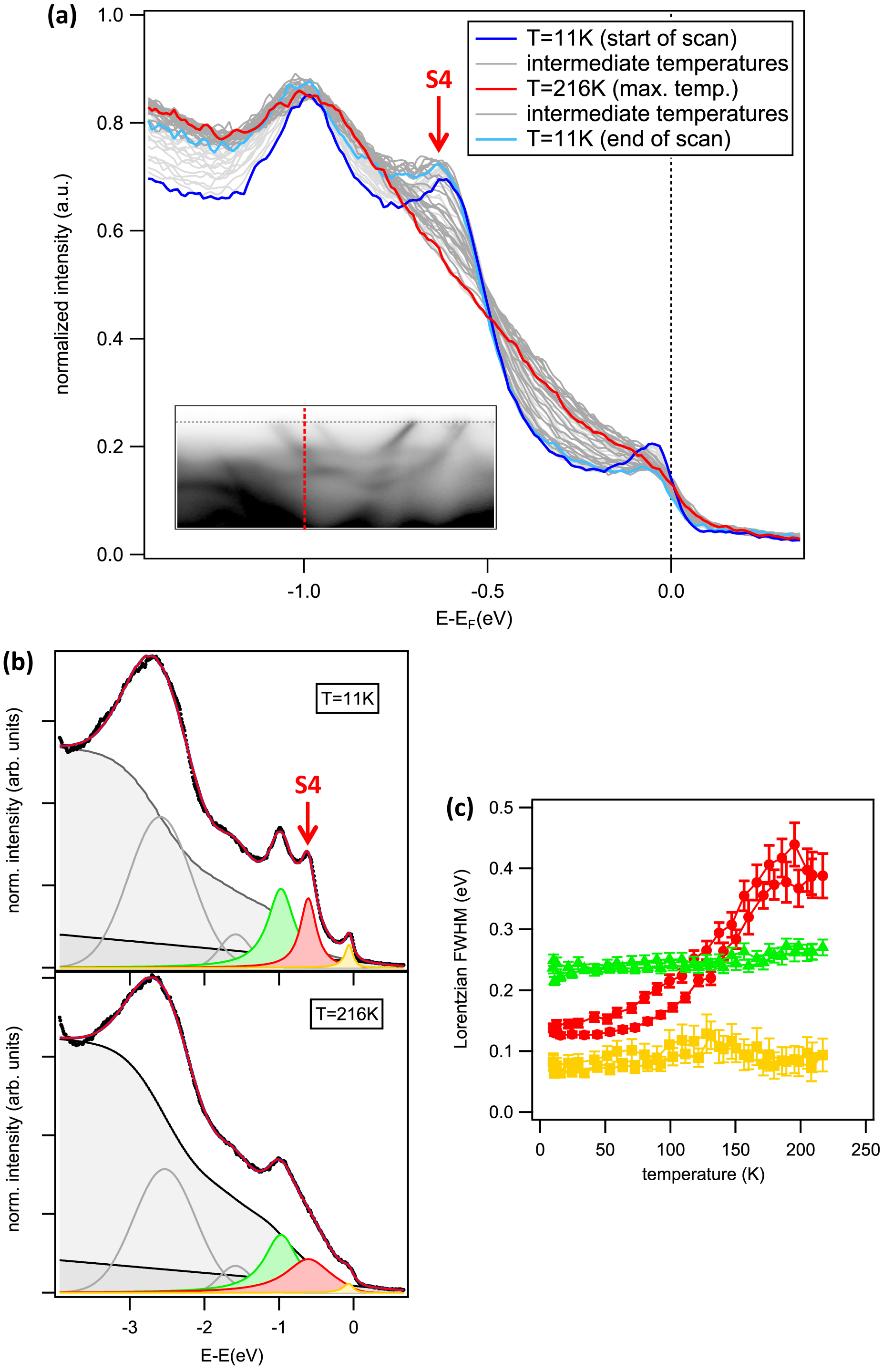

Figure 6.26: *(a) Normalized EDCs along the dashed red line (see inset) for a complete heating-cooling cycle (11 K – 216 K – 11 K). (b) Line-fitting shown for EDCs recorded at 11 K and 216 K respectively. S4, S5, and the leading edge of Au bands have been fitted by Lorentzians. Background intensity has been modeled by a linear background (dark gray), which accounts for photoelectrons generated by He II light, as well as a Shirley-type background (light gray) [181]. The Si(553)-Au sample has been refreshed before each ARPES measurement as described in the text. (c) FWHMs obtained by the line-fitting as a function of temperature. S4 shows a clear broadening with increasing temperature. S5 and the S3 Fermi cut off essentially maintain their width during the full heating-cooling cycle. Data acquisition and evaluation performed by L. Dudy.*

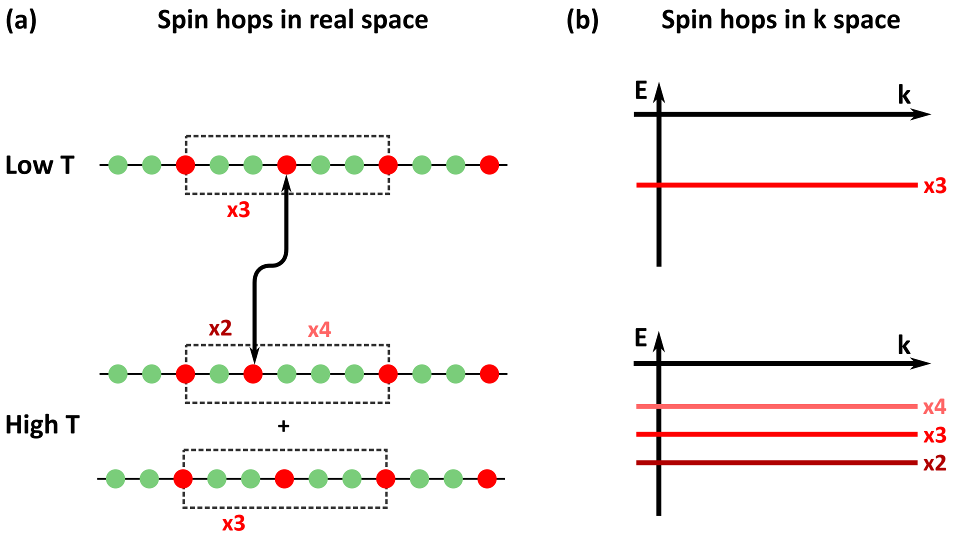

Figure 6.27: *(a) Top: Real-space spin chain at low temperatures. All spin chains show ×3 spacing. Bottom: Real-space spin spacing at elevated temperatures. Spin hops may occur leading to a local spin spacing of $4a_0$ and $2a_0$. (b) Top: Band structure sketch at low temperatures. ×3 spaced spins give rise to a localized state at a particular binding energy. Bottom: Band structure sketch at elevated temperatures. ×2 and ×4 spaced spin sites lead to states which are localized at a different binding energy when compared to the spins separated by $3a_0$. Consequently, the ARPES spectrum will feature spreading intensity at elevated temperatures.*

versibility excludes any sample degradation during data acquisition. Note that the sample was recleaned before each temperature step by applying a special “recovery” heating sequence (moderate heating to 600 °C for 5 sec followed by a short flash to 850 °C after 60 sec) in order to prevent aging effects during the heating sequence. A similar cleaning procedure has been applied by other groups [19, 21], and was both cross-checked and optimized by subsequent LT-STM measurements (see Appendix Sec. C).

A quantitative analysis of the temperature dependent ARPES band structure has been performed by fitting the respective EDCs using a global fitting model. In this model, background intensity has been modeled by combining a linear background and a Shirley-type background [181]. The linear background accounts for photoelectrons generated by He II light. The Shirley background considers inelastically scattered photoelectrons [181]. S4 (red), S5 (green), and the leading edge of the Au bands (orange) have been fitted with Lorentzians. The two panels of Fig. 6.26(b) show the line-fitting model for a low temperature (11 K) and a high temperature (216 K) example. Fig. 6.26(c) displays the FWHMs of S4, S5, and the S3 Fermi cut-off as a function of temperature. This analysis reveals a strong broadening of the S4 band with increasing temperature. Such broadening is not observed for S5 nor for the leading edge intensity of S3. Instead, both essentially maintain their width during the entire heating-cooling cycle, demonstrating that the broadening of S4 is indeed a temperature effect rather than an experimental artifact. The constant increase of the S4 FWHM with temperature suggests a second-order phase transition, i.e. an order-disorder-type transition at the Si step edge.

One possible explanation for the spreading of the step-edge band observed is the occurrence of spin site hops. Such spin hops lead to different local spin site spacings of $4a_0$ and $2a_0$ [see Fig. 6.27(a)], and correspond to the formation of soliton-antisoliton pairs (cf. Sec. 2.2). DFT calculations reveal a formation energy of 25 meV per soliton-antisoliton pair [42] – an energy which can easily be provide by elevated temperatures. The spin states which correspond to the $4a_0$ and $2a_0$ spaced spin sites are expected at a different binding energy than that of the $3a_0$ spaced spin sites as illustrated in Fig. 6.27. Since spin hops occur more frequently for elevated temperatures [42], the spin state intensity as seen in ARPES broadens with increasing temperature.

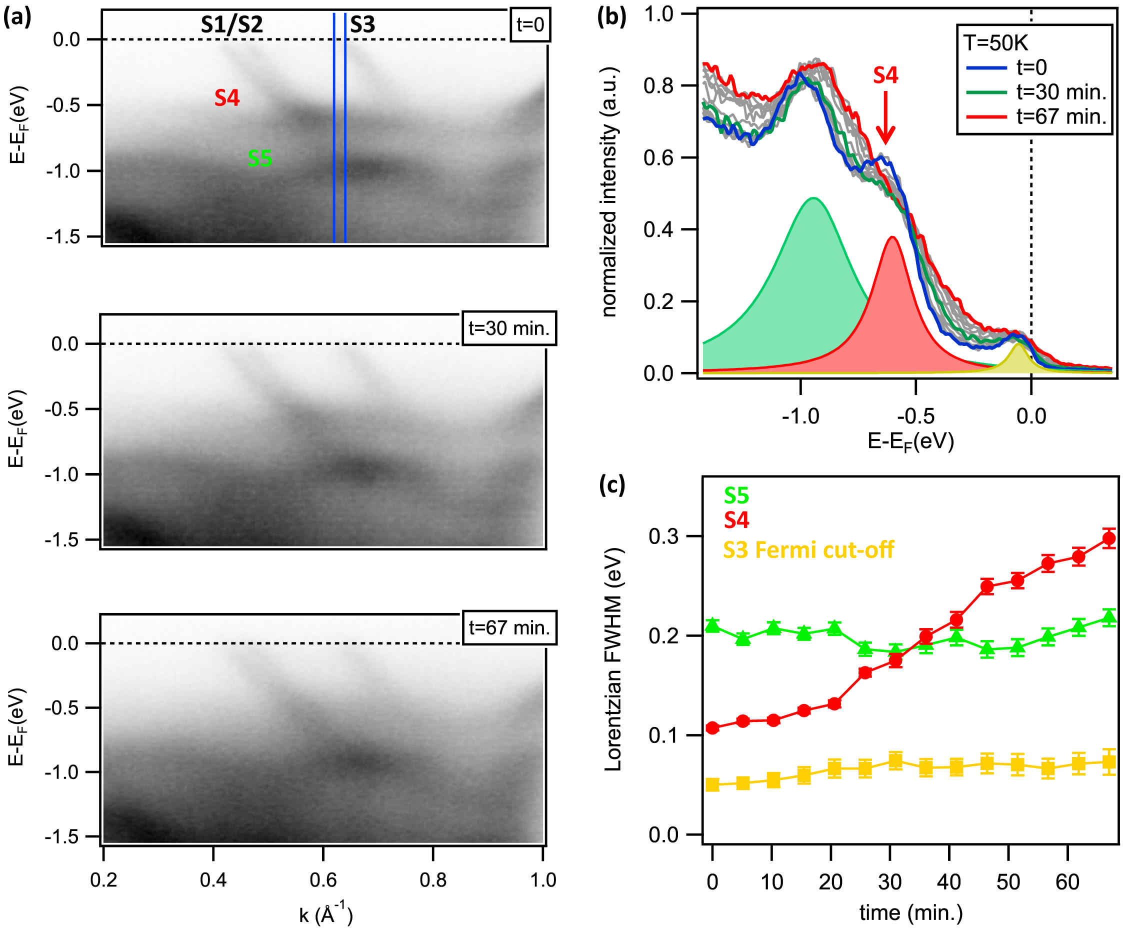

Figure 6.28: *(a) LT (50 K) Si(553)-Au band structure from ARPES measured directly after sample recovery (top), after 30 min (middle), and after 67 min (bottom) of exposure to residual gas atoms (base pressure of* $1 \cdot 10^{-10}$ *mbar). (b) Time-dependent EDCs along the stripe marked by the blue lines in top panel of (a). (c) FWHMs obtained by the line-fitting of the EDCs as a function of UHV exposure time. With increasing time, a smearing of the S4 band can be identified, while S5 and the S3 Fermi cut-off remain essentially unaffected. Data acquisition and evaluation performed by L. Dudy.*

Effect of defects – Support for this scenario comes from time-dependent ARPES measurements presented in Fig. 6.28. The top panel of Fig. 6.28(a) shows the LT band structure of the Si(553)-Au surface comprising the surface bands S1-S5 discussed above. After 67 min in UHV, the S4 band can hardly be identified. All other bands are still clearly visible [see Fig. 6.28(a) bottom panel]. A track of the band structure over time [Fig. 6.28 (b) and (c)] demonstrates the exceptional fast smearing of the S4 band, while all other bands remain essentially unaffected. An explanation for this behavior is given by the selective defect formation described in Subsec. 5.2.2. In this paragraph, STM experiments demonstrate that the Si step edge is much more susceptible to adsorbate-induced defect formation than the other structure elements. This matter of fact indicates that the fast broadening of the S4 step-edge band goes hand in hand with an increase of the step-edge defect density. The time-dependent SPA-LEED results presented in Sec. 6.1 support such selective adsorbate-induced defect generation at the step edge.

Importantly, the time-dependent behavior of the surface bands shows a conspicuous similarity to their temperature-dependent behavior. Just like a spin site hop, a step-edge defect locally interrupts the ×3 spin site spacing, and yields a smearing of the S4 step-edge band. This correspondence provides additional evidence for the spin hop scenario suggested by the ARPES results and the DFT calculations of Ref. [42]. To further verify this interpretation, temperature-dependent STM measurements have been performed and will be discussed in the following section.

6.6.2 Real-Space Point of View

STM Studies at Various Temperatures – Constant current STM images recorded at various temperatures between 77 K and 160 K reveal a change of the step-edge periodicity in this temperature range [see Fig. 6.29(a)]. At 77 K, all step edges feature the well-known ×3 periodicity. At 130 K, a ×3 period can only be identified in the vicinity of defects. All other chain segments display a ×1 periodicity. The ×1 maxima occur *at* the position of step-edge lattice sites, as in the case of the RT STM images [see orange markers in Fig. 6.25(a)]. Notably, this is in contrast to the high-current and low-temperature observations showing a step-edge appearance with ×1 maxima *between* lattice sites (Sec. 6.4). The position dependence along the step edge (×3 near defects and ×1 away from defects) suggests that defects act as nucleation centers, which mediate the condensation of the low temperature phase. Consequently, the defect concentration has significant influence over the transition temperature revealed by area averaging experimental techniques like SPA-LEED or ARPES. In turn, the step edges of a Si(553)-Au sample lacking any such pinning defects would show a pure ×1 periodicity at 130 K. Similar defect impacts have been observed for the In chains on Si(111) [182] and the 2D CDW system Sn/Ge(111) [61].

At the first glance, the STM image recorded at 160 K looks quite similar to that recorded

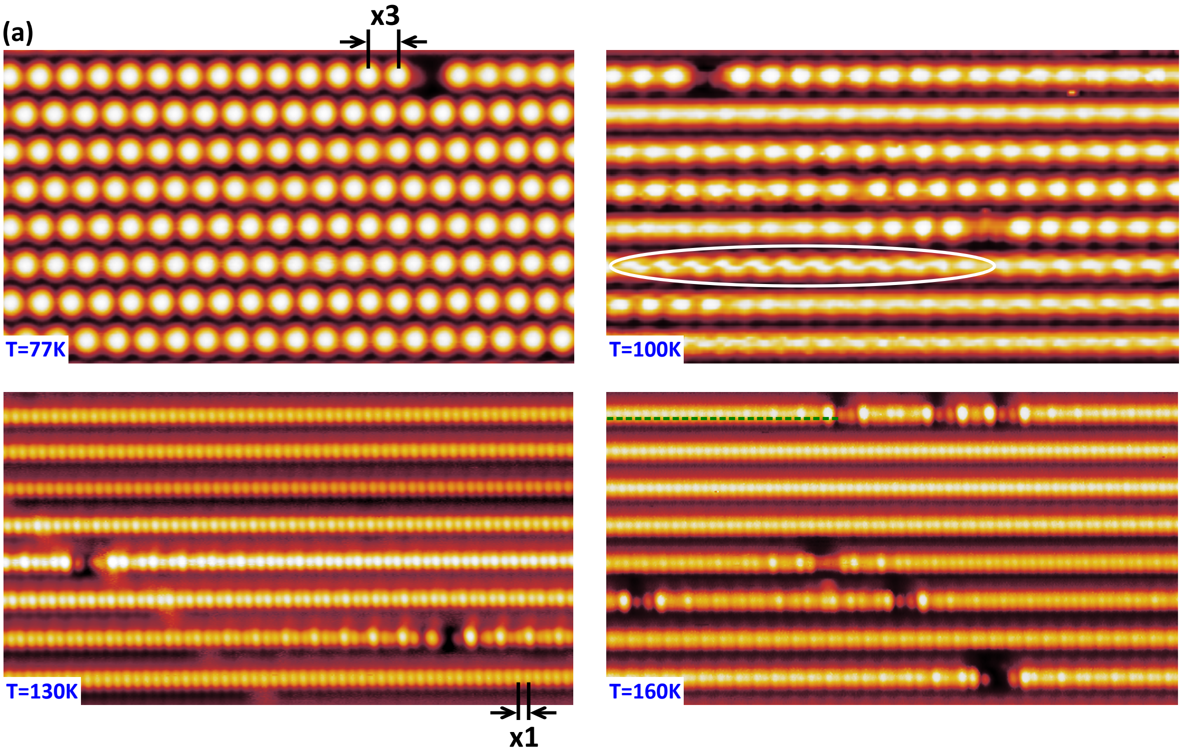

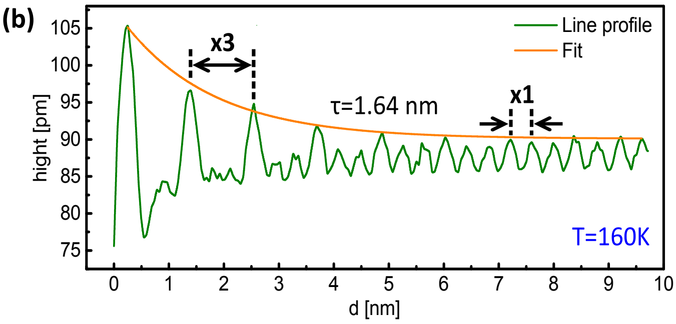

Figure 6.29: *(a) For constant current, 24.3 nm × 12.2 nm wide, Si(553)-Au STM images obtained at various sample temperatures (77 K, 100 K, 130 K, 160 K). All images have been recorded with equivalent scanning parameters ($U = +0.7\,V$, $I = 10\,pA$). At 77 K, all step edges of the scan frame display a ×3 periodicity. For higher temperatures (130 K or 160 K), most chain segments show a ×1 periodicity. The ×3 period can only be observed in the proximity of defects. (b) Line profile along the dashed green line of the 160 K image displayed in (a). Close to the defect, the step edge features a ×3 period, which becomes less pronounced with increasing distance from the defect. An exponential fit to the ×3 peak maxima reveals a decay length of $\tau = (1.64 \pm 0.18)$ nm [$(4.26 \pm 0.47)\,a_0$]. The given error corresponds to the fitting error.*

at 130 K. However, the extent of the ×3 periodic segments away from the defect is reduced compared to the 130 K image. In particular, the intensity of the ×3 charge clouds decays exponentially with the distance from the defect, as can be seen in the line profile taken along the dashed green line in the 160 K image [Fig. 6.29(b)]. A fit to the ×3 maxima of this particular profile with an exponential decay function $[f(x) = y_0 + A_0 e^{-(x-x_0)/\tau}]$ reveals a decay length of $\tau = (4.26 \pm 0.47)\,a_0$. The given error is the error of the fit. An evaluation of several chain ends observed at 160 K yields $\tau_{160\,\mathrm{K}} = (3.28 \pm 0.53)\,a_0$. In this case, the error corresponds to the statistical error, which is quite large, as not only the sample temperature, but also the local defect environment (type and density) and the absolute chain length (in particular for shorter chains) influences the decay length. Nevertheless, the average decay length observed at 130 K $[\tau_{130\,\mathrm{K}} = (8.07 \pm 1.46)\,a_0]$ is clearly larger than that at 160 K, proving a distinct temperature effect. Such an observation is consistent with the spin hop scenario proposed in Ref. [42]. Away from the defects, the spin sites hop at a rate much faster than the STM image recording process, resulting in an effective ×1 periodicity in the STM image. Closer to the defect, the hopping rate is significantly reduced due to pinning caused by the defect [42]. At 100 K, several spin chains reveal some fuzzy patterns (see white ellipse). Theses are due to spin hops occurring during the STM scan as will be shown below.

Time-Dependent STM Study: Observation of Spin Site Hops – Fig. 6.30(a) displays a constant current STM image of a defect terminated Si step edge recorded at 100 K. In order to detect any time-dependent changes in the step-edge pattern, the same line along the center of the step edge (dashed gray line) has been scanned continuously over a certain period of time [Fig. 6.30(b)]. Indeed, the staggered line profiles evidence many changes in the spin site arrangement along the step edge. These changes manifest as lateral a_0 or $2a_0$ shifts of some of the bright maxima representing the spin sites. Fig. 6.30(c) displays two line profiles recorded in quick succession ($\Delta t = 2.4\,\mathrm{s}$): one before (red) and one after (blue) a particular step-edge pattern swap. An analysis of the spin site spacings reveals that the step edge is in one particular spin chain configuration (C1) before the swap [left panel of Fig. 6.30(c)]. After the swap, it features two distinct configurations with each pinned to one chain end, as illustrated by the dark and light green markers in the right panel of Fig. 6.30(c). A similar pattern has been observed at 77 K for chains with $(3n+1)\,a_0$ chain length (see Sec. 6.4). The superposition of both line profiles presented in Fig. 6.30(d) illustrates that a lateral $+a_0$ shift of several spin sites of the left-sided step-edge segment is responsible for the change of the step-edge pattern. Such a shift can be created by the *formation and propagation of a soliton-antisoliton pair*, i.e., a spin site hop as sketched in Fig. 6.27(a).

It is important to acknowledge some limitations of the STM measurement technique, which prevent an analysis of the spin hop propagation along the wire. The applied STM variant of recording a time-trace of a particular step-edge profile is suited perfectly for witnessing changes in the step-edge pattern. However, the scanning nature of the STM measurement

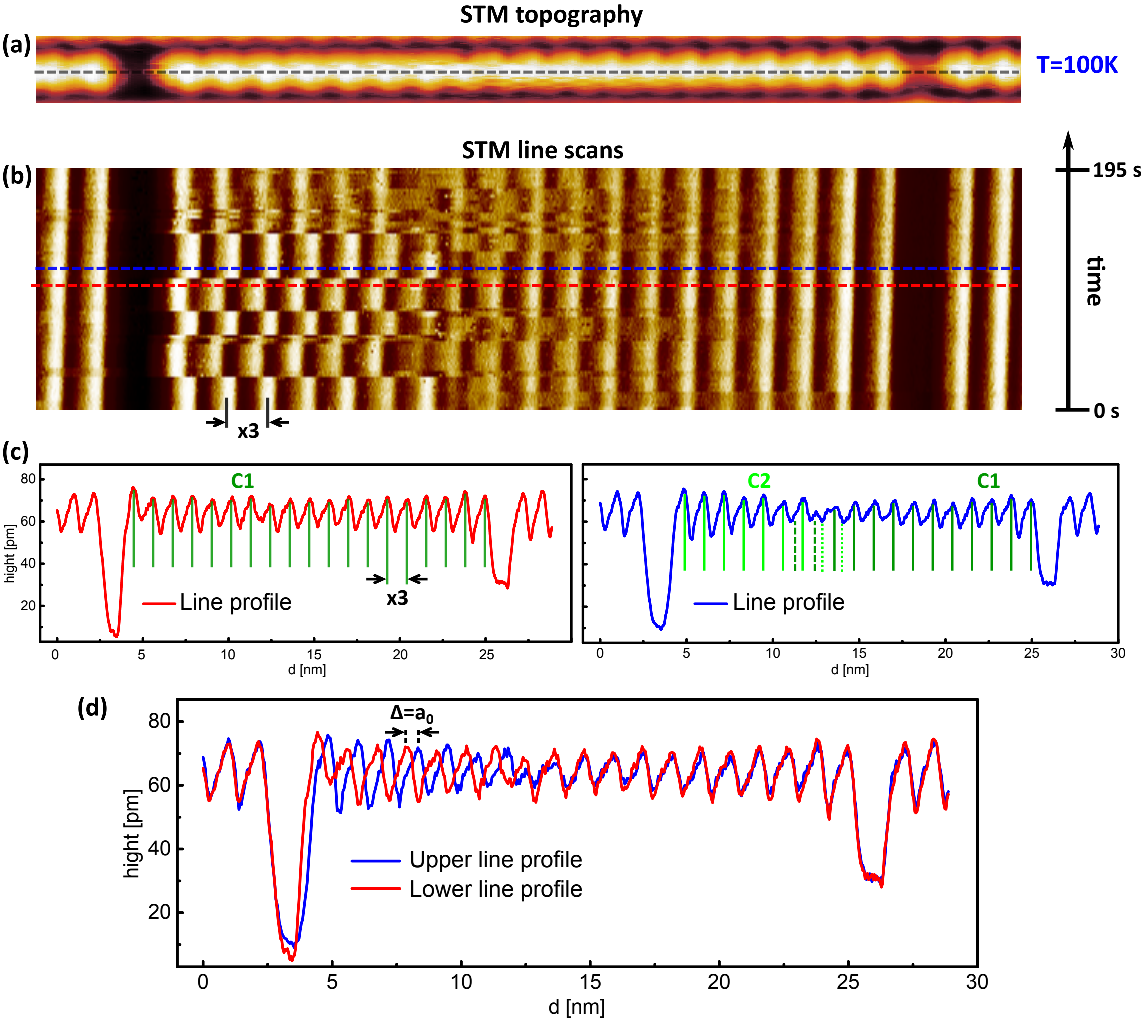

Figure 6.30: *(a) Constant current STM image of a Si step edge terminated by defects recorded applying the fast scanning direction parallel to the step edge ($T = 100\,K$, $U = 0.7\,V$, $I = 10\,pA$). (b) Stacked STM line scans taken along the dashed gray line in (a) with the oldest line profile at the bottom. The step-edge pattern at the left side of the finite chain changes several times during the time trace. (c) Two example line profiles recorded immediately before (red) and after (blue) a step-edge pattern swap. Light and dark green markers are equally spaced by a_0 to illustrate the respective spin site spacings. The red profile displays only ×3 spaced spin sites, i.e., only one spin chain configuration. The blue profile shows two different configurations, with each pinned to one chain end. (d) Superposition of both line profiles in (c) to demonstrate the $+a_0$ lateral shift of several spin sites at the left part of the step-edge chain.*

procedure does not allow for obtaining information regarding the propagation of the spin hops. Nevertheless, the observation of local changes in the real-space spin site positions is in line with the theoretical proposal of Ref. [42], and substantiates the explanation for the temperature dependence of the S4 band seen in ARPES.

In summary, the complementary STM and ARPES analysis of the Si(553)-Au spin chains' temperature dependence reveals an order-disorder transition, which manifests in real- as well as in k-space, and can be traced back to the formation and propagation of soliton-antisoliton pairs, i.e., single spin hops. Defects are found to play an important role in this scenario acting as pinning sites which locally stabilize the LT phase.

6.7 Electron Doping via Potassium Adsorption

Since the total electron count significantly determines the spin chain formation of the Si(*hhk*)-Au surface, it should be possible to create or suppress Si spin chains via doping. In particular, it has been demonstrated experimentally in Sec. 5.9 that a native, hole-doping defect can induce a spin site at the Si(775)-Au step edges. suppress Si spin chains via doping. In particular, it has been demonstrated experimentally in Sec. 5.9 that a native, hole-doping defect can induce a spin site at the Si(775)-Au step edges. An alternative approach is to evaporate additional, doping adsorbate onto Si(*hhk*)-Au surfaces. In case of Si(553)-Au, electron doping is expected to destroy or modify its step edge spin chains (cf. Sec. 5.9.1). Promising electron donating candidates are alkali metals like Li, Na and K, which have a low electronegativity and tend to release their valence electron to the surface. Upon the aforementioned elements, K comprises the lowest electronegativity and its electron doping effect has proven successful in several surfaces science experiments [183–185].

The following section will demonstrate the successful modification of the Si(553)-Au (electronic) structure by potassium adsorption. Upon K doping basically two effects on the Si(553)-Au electronic structure are observed: a MIT in the Au chains and a modification of the charge distribution at the Si step edge.

6.7.1 Doping with Adsorbates Reported in Literature

It has been shown that it is possible to dope the Si(553)-Au surface with external dopants, namely, additional Au and Ag atoms [177]. With increasing doping concentration an increase of the band filling of the inner Au-induced band S3 is observed. The outer Au bands S1/S2 remain more or less unaffected, as tracked by ARPES measurements. The authors of Ref. [177] explain the partial doping by a selective adsorption of the additional Au atoms. Specifically, the dopants adsorb at positions between the Au ladder and the honeycomb chain, i.e., close to the Au and Si atoms which hybridize to form the inner Au band S3. Therefore, the additional Au atoms donate charge to the S3 band but not to the S1/S2 band.

This scenario is qualitatively supported by DFT calculations, although some open questions remain: The structural model which best matches the experimentally determined extra Au coverage and which reproduces the energy shift of S3 cannot explain the bright protrusions observed in the STM images. These protrusions suggest a Au adsorption at the Si step-edge atoms which, in turn, cannot explain the energy shift of S3. A combination of the two models (see Fig. 5(d) of Ref. [177]) provides an explanation for both the ARPES and the STM results. However, the Au coverage theoretically required (0.24 ML for 0.25 eV shift) is much larger than the value obtained experimentally (0.048 ML for 0.15 eV shift). Unfortunately, the authors do not state how they determined the amount of extra Au coverage, which is a challenging and error-prone task (see Sec. 5.1). In addition, the doping experiments have only been carried out at room temperature, and, therefore, do not allow for an investigation into the response of the Si spin chain to the Au doping.

Apart from additional Au atoms, a joint work with colleagues from the ISAS Institut, Berlin and the Italian National Research Council, Rome has shown that Si(553)-Au can be doped by hydrogen adsorption [A9]. In particular, it was discovered that H atoms prefer to adsorb at the Si step edge. This passivates and, in turn, destroys the Si(553)-Au spin chains, and induces insulating behavior of the initially metallic Au bands [A9].

6.7.2 Effect on the ARPES Band Structure

In order to systematically study the influence of electron doping to a Si(553)-Au surface, a fixed amount of K has been evaporated, step by step, from a K dispenser source (SAES Getters S.p.A.) onto the Si(553)-Au sample. To ensure a high sticking coefficient and to avoid any contamination from cooling and warming of the sample between RT and LT, K was evaporated directly onto the cold sample mounted at the manipulator of the ARPES chamber ($T = 11\,\mathrm{K}$). One evaporation step is defined by a particular direct current heating sequence ($0\,\mathrm{A} \xrightarrow{t=5\,s} 1\,\mathrm{A}$ for 20s $\xrightarrow{t=30\,s} 3.5\,\mathrm{A}$ for 20s $\xrightarrow{t=10\,s} 6.5\,\mathrm{A}$ for 40s $\xrightarrow{t=10\,s} 0\,\mathrm{A}$) of the K dispenser mounted in the field of view of the sample with approximately 40 cm distance.

Transformation of the Spin Site Band – After each evaporation step of the series, the Si(553)-Au band structure was tracked by means of ARPES. Selected band maps along the Γ_0 - K_0 - M_1 direction are displayed in Fig. 6.31(a). This data set reveals several interesting modifications of the band structure with increasing K coverage. After about 10 K-evaporation-steps, the spin site band *S4 transforms* to a cosine-like band with a maximum at the K point of the (1×1) SBZ and a binding energy of about 0.4 eV [see S4* label in Fig. 6.31(a)]. This observation suggests a modification of the step-edge electronic structure by K adsorption. The S4* band is reminiscent of the nonpolarized step-edge band obtained by DFT calculations restricted to the (1×1) unit cell (Fig. 3(d) of Ref. [1]), but may also stem from a spin chain with a periodicity different from ×3 (e.g. from a spin chain with ×4 periodicity as discussed below). Consequently, one may speculate that electron doping achieved by K adsorption manipulates or even destroys the spin chains at the Si(553)-Au step edges. This issue will be revisited further below.

Band Gap Formation – With increasing K concentration, the band filling of both the inner (S3) and outer (S1/S2) Au-induced bands gradually increases, suggesting an electron transfer from the doping adsorbates to the Au chains. At a band filling of 0.35 for S3 and 0.59 for S1/S2 no further increase is observed [see Fig. 6.31(b)]. Instead, the bands appear to turn over, and a *band gap* emerges.

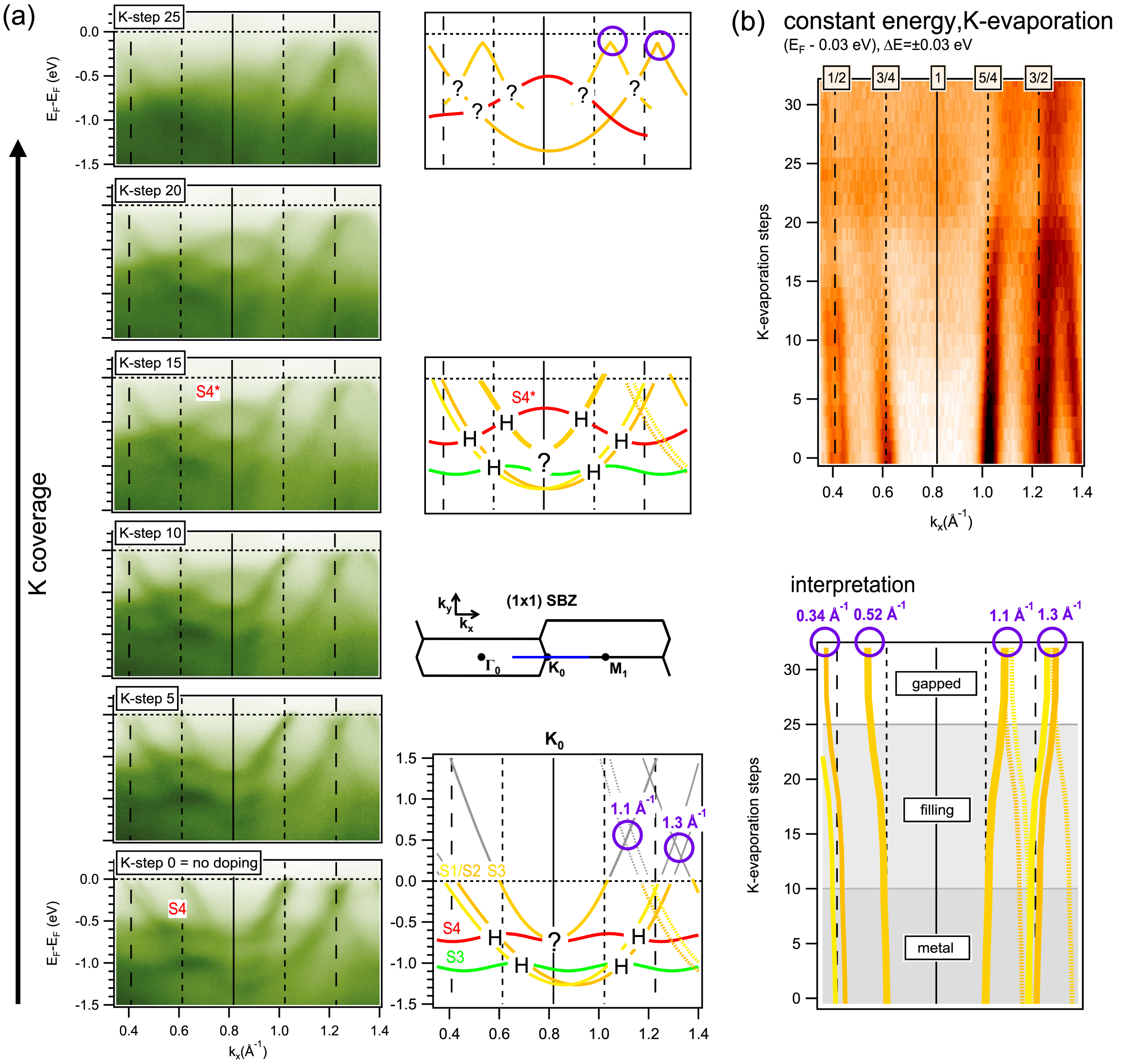

Figure 6.31: *(a) Selected ARPES band maps of the Si(553)-Au surface doped by step-wise K adsorption. The K coverage increases from the bottom up. Major changes in the band structure are sketched in the three panels on the right. (b) Top: Staggered momentum distribution curves at a constant energy of $-30\,\text{meV}$ ($\Delta E = \pm\,30\,\text{meV}$) for each K evaporation step. Both Au-induced bands are subject to an increase of their band filling as well as to a band gap opening. Bottom: Sketch of band behavior with increasing K doping based on the ARPES data above. ARPES data recorded and evaluated by L. Dudy.*

6.7.3 Dimerization Gap Induced Metal-Insulator Transition

Exclusion of a Peierls Scenario – One possible explanation for the emerging band gap observed that must considered is a doping-induced Peierls transition. In this scenario, doping electrons from the adsorbed K atoms fill up the metallic Au bands until nesting conditions are fulfilled and a band gap forms due to Fermi surface nesting (cf. Sec. 2.1). However, the experimentally observed filling factors do not match any (commensurate) conditions for nesting, rendering a doping-induced Peierls scenario unlikely.

Energy Gap in the Unoccupied DFT Band Structure – An alternative explanation is available from DFT band structure calculations. The metallic Au bands feature hybridization gaps at particular band crossings, which are located well above the Fermi level of the undoped system [see Fig. 6.32(a)]. Specifically, gaps occur at the hypothetical crossing point of an original Au band and the backfolded band of the other Au induced band, i.e., when S3 encounters S1*/S2* and when S1/S2 encounters S3* respectively. These calculations suggest the realization of a MIT by shifting the Fermi level upwards (through electron doping) until it lies in the hybridization gap.

Such a scenario fits to the behavior of the Au bands during the series of K evaporations. A clear merging of the respective original and shadow bands is observed between step 15 and 25. Moreover, the maxima of the gapped Au bands [$k_{cross\#1} = 1.10\,\text{Å}^{-1}$ and $k_{cross\#2} = 1.30\,\text{Å}^{-1}$] are in agreement with the extrapolated band crossings of the undoped system [see band structure sketch in Fig. 6.31(a) bottom]. It should be noted that DFT and ARPES do not show a perfect match. However, this can be traced back to the different band fillings of the calculated S1/S2 and S3 bands as well as their different relative energy offsets compared to the ARPES bands. This results in different absolute numbers for E_{cross} and k_{cross}, but does not put into question the proposed doping-induced MIT.

Dimerization Gap due to Tilted Au Ladder Structure – In order to unveil the origin of the energy gaps at the crossing of S3 with S1*/S2* and S1/S2 with S3*, DFT calculations of three different simple model systems were performed by S.C. Erwin [see Fig. 6.32(b)] [175]. All setups consist of two parallel linear chains of hydrogen atoms (one s-orbital per atom). For case A, the atoms are equally spaced along each chain. The band structure of this system consists of two cosine bands (B1 and B2) shifted in energy and folded back at a fictive ×2 zone boundary (X-point) of the BZ. For case B, the atoms are shifted by $\pm\Delta$ in chain direction reflecting the tilted Au dimers of the Si(553)-Au surface. As a consequence of the (symmetric) atomic displacement, a gap opens at the crossing of the backfolded B1 band and the B2 band [red circle in Fig. 6.32(b)]. However, neither band shows a gap opening at the zone boundary – exactly as is the case for the Si(553)-Au DFT and ARPES band structure. Gaps at the zone boundary only occur in case of an inequivalent atom displacement in both chains ($|\Delta_1| \neq |\Delta_2|$,

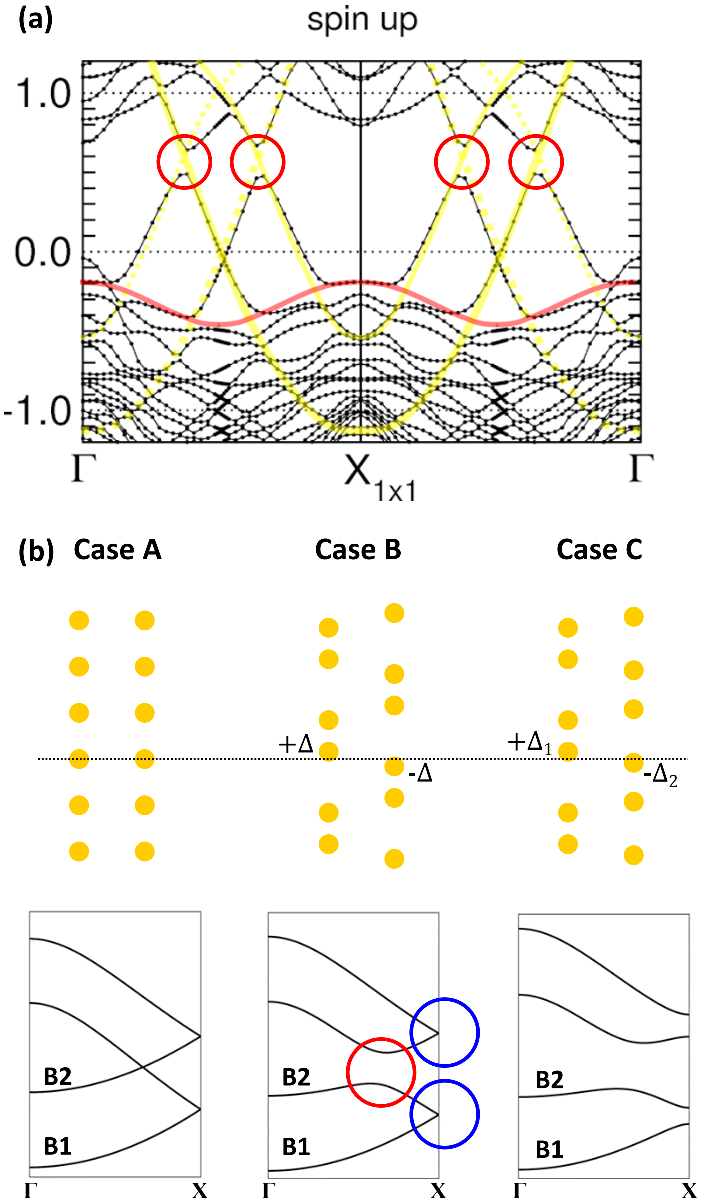

Figure 6.32: *(a) DFT Band structure of a Si(553)-Au (1×2) unit cell with spin polarization on every second step-edge atom enforced by perturbing its height [175]. Original and backfolded Au bands are marked by yellow lines and dots, respectively (see labels). The Au bands show a dimerization gap above E_F (red circle) when the inner (outer) Au band crosses the backfolded outer (inner) Au band, respectively. (b) DFT band structures (bottom) for three different variants of a two parallel, linear chains of hydrogen atoms (top). In case A, all atoms are spaced equally along the chain. In case B, each atom is shifted by ±Δ in chain direction compared to the atomic positions in case A. In case C, the magnitude of the atomic displacement |Δ| is different for each chain. Calculations performed by S.C. Erwin [175].*

case C). The asymmetric displacement breaks a glide-plane symmetry, which lifts the band degeneracy at the zone boundary [175]. This simple toy model analysis uncovers that the presence of gaps at particular band crossings in the Au chain band structure is determined by the symmetry of the Au ladder. In particular, it suggests that gaps at the crossings of S3 with S1*/S2* and S1/S2 with S3* are a direct consequence of the tilted dimer structure of the Au ladder and, thus, provides additional evidence for the tilted dimer structure of the Si(553)-Au Au chain proposed in Refs. [1,22].

6.7.4 K Adsorption in Real Space

To obtain information about adsorption sites of K as well as K induced modifications of the step-edge pattern, STM measurements on the Si(553)-Au+K system have been performed. Since the STM apparatus is connected to a different UHV system than the ARPES machine, a one-to-one comparison of the results obtained by both techniques is not possible. Moreover, Si(553)-Au+K samples could only be generated via different evaporation procedures. In particular, the STM chamber only allows for K evaporation onto a Si(553)-Au sample at RT which is subsequently cooled to 77 K before the STM measurements are started. K evaporation directly onto a cold sample sitting on the STM sample stage is not possible since K adsorbed at the STM wiring may cause an oxidation damage when venting the system. The different sample temperatures during evaporation may lead to a significantly different sticking coefficient. Moreover, it is very likely that K atoms evaporated onto the Si(553)-Au surfaces are highly mobile at RT. This assumption is based on similar experiments in which a submonolayer of Pb atoms has been evaporated on the Si(553)-Au surface [186, 187]. Even at temperatures well below RT, the Pb atoms are found to diffuse along the steps. Moreover, unpublished DFT calculations addressing Na adsorption on the Si(553)-Au surface suggest highly mobile Na atoms at RT [175]. These different evaporation procedures applied before ARPES and STM measurements hinder a one-to-one comparison of the results obtained by each method. Nevertheless, the STM analysis presented below provides some basic information about K adsorption effects in real space.

Random Distributed Decorations – Fig. 6.33(a) displays an STM image of a Si(553)-Au surface after K adsorption. One can easily identify randomly distributed spot-like decorations, which may be attributed to K atoms. Similar decorations have been observed on the Ge(001)-Au atomic wire system after K evaporation [188]. A subsequent STM scan [Fig. 6.33(b)] of an identical sample area implies that some of the adsorbates are either still mobile at $T = 77\,\mathrm{K}$ or are affected by the tunneling tip. At the areas marked by the blue circles, decorations disappear during the scan. Moreover, some chain segments exhibit a fuzzy appearance (see, for example, white rectangles in Fig. 6.33), suggesting the movement of atoms along the chain (cf. Ref. [186]). Topography images recorded at a lower positive bias [+0.7 V in Fig. 6.33(c)]

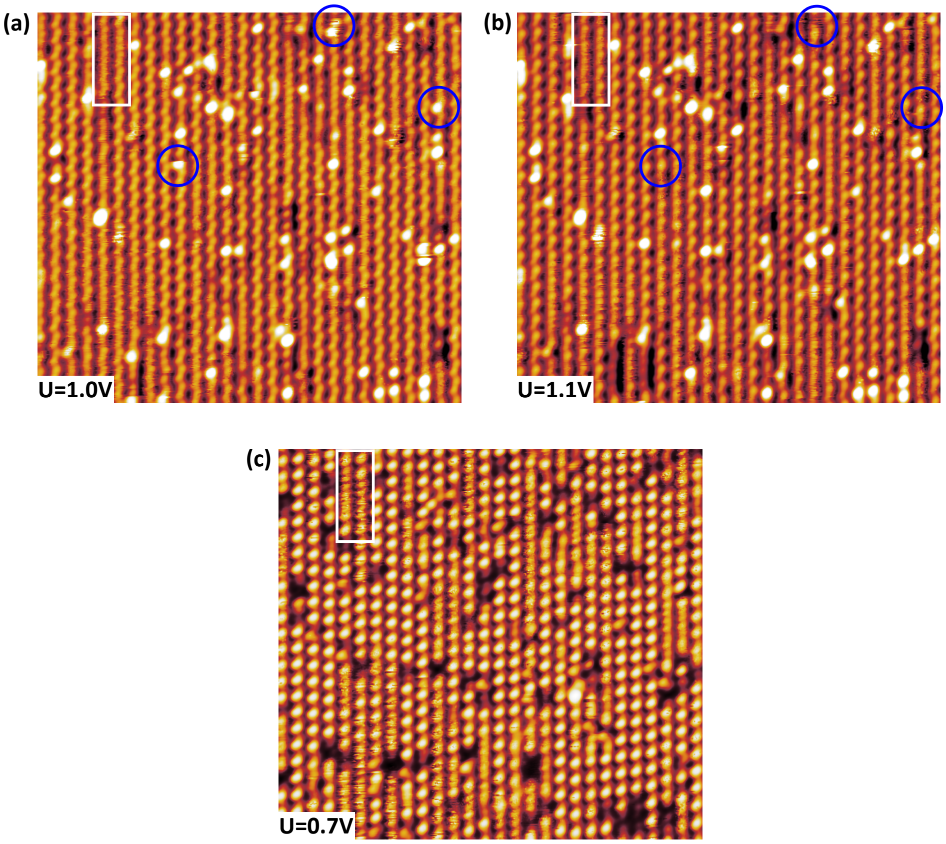

Figure 6.33: *Bias-dependent STM overview images of an identical Si(553)-Au sample area after K evaporation ($T = 77\,K$). Images presented in (a) and (b) have been recorded in direct succession. Some of the bright decorations induced by K evaporation disappear during the scan (blue circles). The image acquired at +0.7 V (c) displays exceptionally low intensity at the position of the decorations. Some chains feature fuzzy segments irrespective of the tunneling bias as indicated by the white rectangles.*

display exceptionally low intensity at the position of the decorations. These findings suggest that the K induced decorations host an unoccupied electronic state at about +1.0 eV. It should be noted that a similar bias dependence has been detected for the decorations induced by K evaporation on Ge(001)-Au [188].

Regular Adsorption Sites – In addition to the randomly distributed decorations, the STM step-edge appearance has indeed changed after K evaporation. In particular, a bias-dependent STM scrutiny suggest a site-specific adsorption of K atoms as well as a modification of the Si step edge charge distribution. The step edges presented in the +1.0 V image of Fig. 6.34 display a zigzag pattern composed of two rows with ×4 period. This is in strong contrast to the single row appearances and ×3 periodicity of the bare Si(533)-Au step edges (cf. Sec. 5.4). The two rows forming the zigzag chain show a different bias dependence. At $U = +1.0\,\text{V}$, both elements display equal intensity. All other images are dominated by the left-sided elements of the zigzag chain. dI/dU maps recorded at different biases confirm the implications from

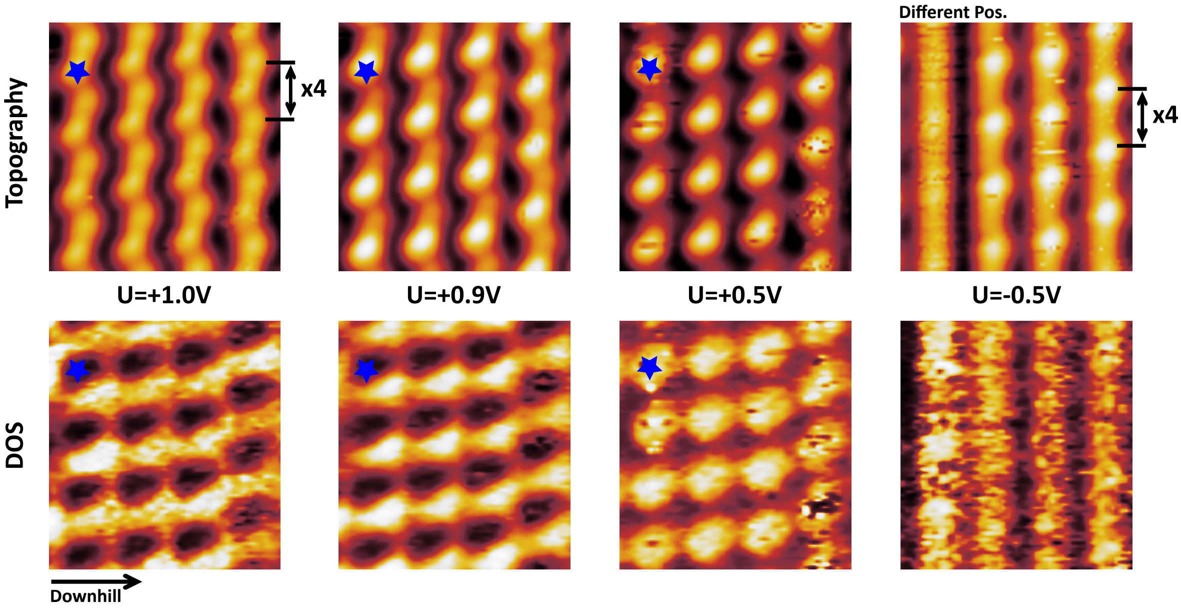

Figure 6.34: *Bias dependent close-up constant current STM images (top) and dI/dU maps (bottom) of an identical Si(553)-Au sample area after K evaporation ($T = 77\,K$). Blue stars mark equivalent sample positions for better comparison of topography and dI/dU maps. At +1.0 V, a zigzag chain composed of two shifted rows with ×4 periodicity is observed. All other topography images are dominated by the left-sided row of the zigzag chain. dI/dU maps recorded at a high positive bias (+1.0 V and +0.9 V) show highest intensity at the position of the right-sided row, while the map obtained at+0.5 V is dominated by the signal from the left-sided row.*

the topography images. The left-sided row of the zigzag chain dominates the scans at +0.5 V and −0.5 V, while the right-sided row features its highest intensity in the maps obtained at +1.0 V and +0.9 V. The bias dependent behavior as well as the respective local position of each row suggest that the left row corresponds to the Si step edge, while the right row could be induced by K adsorption at specific lattice sites.

Proposal for a Structure Model – An educated guess of a structural model based on the results presented above is displayed in Fig. 6.35. In this proposal, the step edge is subject to a ×4 spin chain, while K atoms reside at particular hollow sites between the step edge and Au chain. To verify this model, three different potassium adsorption sites haven been tested by DFT. K adsorption at the hollow site as shown in the model is found more favorable by 20 meV compared to adsorption at T_4 lattice sites (labeled with “C” in Fig. 6.35). Adsorption at the position marked with “B” is found unstable and converges to the hollow site adsorption upon relaxation. This DFT total energy analysis is in line with the model suggested by the STM data. However, it is worth mentioning that the model presented is highly speculative and needs further verification. Such verification could be achieved using complementary DFT calculations as well as ARPES and LT-STM measurements performed on an identical sample. The latter could be realized using a UHV system comprising both an LT-STM and an ARPES

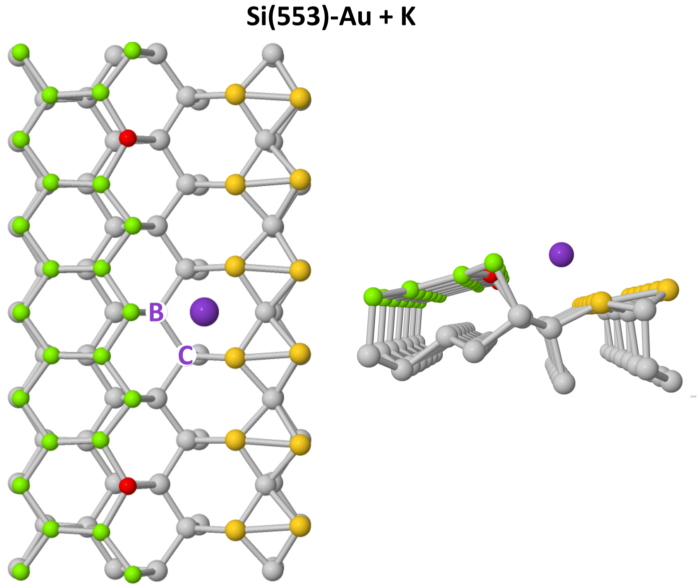

Figure 6.35: *Top and side view of a possible structure model of the Si(553)-Au after K adsorption. The K atom (purple) occupies a hollow site directly opposite of a nonpolarized step edge atom. The step edge is forced to exhibit a ×4 spin chain (red atoms are spin-polarized). In addition two other K adsorption sites marked by "B" and "C" have been tested with DFT. The structure displayed is found energetically most favorable. DFT calculations performed by S.C. Erwin [175].*

setup.

Nevertheless, it could be shown that potassium doping not only leads to a rigid shift of the Au-induced surface bands, which culminates in a MIT, but also to a modification of the step-edge charge distribution and K adsorption at specific lattice sites.

7 Conclusion

In conclusion, the research presented in this thesis has demonstrated that Au-induced atomic wires stabilized on stepped Si substrates provide a fascinating playground for studying the formation and interaction of Si spin chains. Specifically, the Si(553)-Au atomic wire system has been found to be much more versatile than reasonably expected. For example, the ×3 spin chains found on Si(553)-Au have proven susceptible to both their intrinsic atomic environment and to external parameters such as sample temperature, doping adsorbates, and the STM tunneling tip.

Formation of Si Spin Chains – The basis for the exploration of the interaction phenomena alluded to above has been the experimental verification of a theoretical proposal [1] suggesting the presence of spin chains at the step edges of the Si(553)-Au atomic wire array. This has been achieved by bias-dependent STM and STS experiments, which reveal a situation coinciding with the ground-state properties predicted by DFT [A1]. A deeper understanding of the spin chain formation on various Si(*hhk*)-Au surfaces has been obtained by exploiting the tunability provided by Si(*hhk*) substrates. A study of two additional Si(*hhk*)-Au systems – Si(775)-Au and Si(557)-Au – using again the complementary approach of STM/STS on the one hand and DFT on the other hand, has revealed that the step-edge charge distribution and, thus, the spin chain formation is governed by the total electron count of the respective terrace structure in combination with a charge transfer between the terrace and the step edge [A3]. A further experimental verification of this picture has been realized as a result of an unintentional hole-doping defect, which was found to induce a single localized spin at the step-edge atom closest to the defect [A3]. These findings demonstrate that the filling of the step-edge dangling bond orbitals can be modified on the atomic scale, and suggest to utilize atom manipulation techniques [154] or external dopants to tailor Si spin chains at will. In this respect, initial attempts made using the adsorption of potassium atoms on the Si(553)-Au surface have proven successful.

Interacting Si Spin Chains – The Si(553)-Au spin chain has been found to be highly susceptible to its embedding in a 3D environment, which comprises the supporting substrate and adjacent atomic chains of identical or different type. With regard to this, a distinct interwire coupling between neighboring spin chains has been identified. A cooperative SPA-LEED, DFT, and STM analysis has found a centered arrangement of adjacent spin sites, which has interesting implications for the potential magnetic ordering of the localized spins [A6]. The centered configuration leads to magnetic frustration, and may entail a quantum spin liquid ground state. Thus, the Si(553)-Au surface may extend the rather limited number of real-world candidate systems for spin liquid behavior in an anisotropic triangular lattice [189].

The interspersed array-like setup of the Si(553)-Au surface comprising Au chains on the terraces and Si chains at the step edges not only leads to couplings between chain structures of the same type, but also between different wire types, i.e., between directly neighboring Au and Si chains. This interaction has been identified to be highly unidirectional. High-resolution STM and STS experiments have shown that the Si chains respond to their immediate Au chain environment but not vice versa [A7]. As a direct consequence of this interaction, the parity of the Si step edges is broken, and two different step-edge variants of opposite directionality emerge. This finding contradicts the simplified view of the Si(553)-Au atomic wire array consisting of two decoupled chain subsystems.

The Versatile Role of Solitons in Si(553)-Au Atomic Wires – Beyond the aforementioned static properties of the Si(553)-Au surface, mobile solitons have been detected in both the Au chain and the Si step edge. Interestingly, the Au chain and the spin chain solitons are found to bind together rather than moving independently, as has been uncovered by high-resolution STM images and supported by DFT calculations. Although various types of (frozen) solitons have detected in other quasi-1D surface systems like $NbSe_3$ [38] and the In chain reconstruction on Si(111) [4], a coupling of solitons, each of which living in adjacent (but different) wire types, has not been observed before.

In addition, solitons also have been identified to be responsible for the temperature-dependent behavior of the Si(553)-Au step edges. A detailed tracking of the step edges' electronic structure over a wide temperature range by means of ARPES revealed an order-disorder-type transition. The basis for this analysis was the initial identification of a weakly dispersing surface band associated with the Si spin chains in the LT band structure obtained by ARPES. Time-dependent STM experiments at elevated temperatures identified spin hops (i.e., soliton-antisoliton pairs) to be responsible for the apparent temperature-dependent step-edge behavior, which previously had been assigned to a Peierls transition [25, 26].

Aside from these thermal excitations of solitons, it has been shown that a similar excitation of solitons can be realized by the STM tunneling tip, i.e., by the tunneling electrons. In fact, the low-temperature and high-current STM data obtained can well be explained by a superposition of the three equivalent ground states of the step-edge spin chain. In conclusion, the observation of one out of three possible (static) spin chain configurations suggests a pinning mechanism, e.g., promoted by chain-terminating defects.

For the future, one may think of time-resolved pump-probe diffraction experiments [190] to gain deeper insight into the versatile and likewise fascination role of solitons on the Si(553)-Au surface.

Manipulation of the Si(553)-Au Atomic Wires by Doping – A controlled manipulation of the Si(553)-Au surface has been achieved by the stepwise adsorption of potassium atoms. On the one hand, doping with potassium increases the band filling of the Au-induced surface bands and drives the initially metallic Au chains into an insulating state. With the help of DFT calculations, a dimerization gap in the unoccupied electronic structure of the intrinsic Si(553)-Au surface has been identified as the precursor of the MIT. A very similar result has been realized by adsorption of hydrogen atoms to the Si(553)-Au, as demonstrated in a joint study with colleagues from Rome and Berlin [A9]. On the other hand, potassium adsorption also modifies the Si step edge. With increasing potassium coverage, the initial spin chain electronic state has been observed to transform into a new band with lower binding energy. In the STM experiments performed, a regular adsorption of potassium atoms on the terraces accompanied by a change in the step-edge charge distribution has been detected.

Both experiments suggest a successful modification of the Si(553)-Au spin chains, and, thus, provide additional support for the electron transfer scenario demonstrated [A3]. The possibility to tune and manipulate the Si(*hhk*)-Au atomic wire systems on the atomic scale, which has proven successful in the present thesis, enables an exceptional and rather new approach to study 1D quantum phenomena (and in particular spin chains), which will certainly lead to interesting research results in the future.

Appendix

A Experimental Setups

The Sample Holder – In order to handle and prepare the 10 mm × 2.5 mm stepped semiconductor substrates in UHV, the sample pieces are mounted on a direct current sample holder from Omicron NanoTechnology GmbH (see Fig. A.1). In this setup, the sample is clamped between two molybdenum sheets at either side. One of the two sides is electrically isolated from the base plate and the threaded rods with ceramic washers. To inject the heating current required for the surface preparation, the sample holder is contacted at the isolated side as well as the base plate. The holder is compatible with both the LT-STM and the ARPES system. This enables investigation of an identical sample with both techniques without dismounting the sample.

The STM Setup – All STM experiments presented in this thesis have been performed with a commercial LT-STM from Omicron. The STM is part of a UHV setup comprising a preparation and an analysis chamber, both featuring a base pressure of $3 \cdot 10^{-11}$ mbar. The preparation chamber is equipped with electron beam evaporators (EFM3 from Omicron), a sputter gun (IQE 11 from SPECS Surface Nano Analysis GmbH), and an alkali metal dispenser source (alkali dispenser from SAES Getters mounted on a current feedthrough), which are utilized for the preparation of the Si/Ge(hhk)-Au nanowires. The samples mounted at the manipulator can be heated by direct current or a resistive heater. To quickly check the

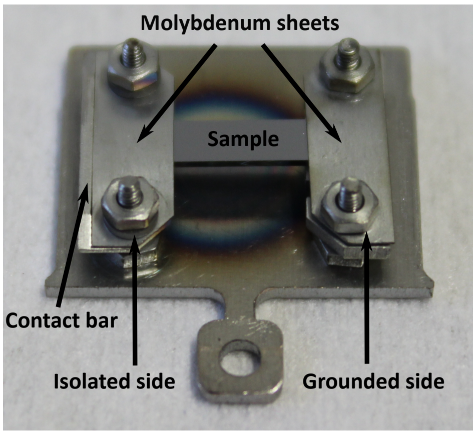

Figure A.1: *Stepped silicon sample mounted on a direct current sample holder from Omicron.*

surface quality after preparation as well as to perform a first scrutiny of the various atomic wire systems, an optical LEED (SPECTALEED from Omicron) is installed.

STM measurements can be performed at base temperatures of 300 K, 77 K, and 4.3 K. Cryogenic temperatures are realized by connecting the STM stage with two bath cryostats filled with liquid nitrogen (LN_2) or liquid helium (LHe). Temperatures in between the base temperatures can be realized by a restive heater mounted at the sample stage.

The ARPES Setup – The ARPES experiments presented in this thesis have been performed at a different UHV system, hosting a home-built ARPES machine. The setup comprises a high-intensity He duoplasmatron lamp (21.2 eV; "UVS 300" from SPECS) and a SPECS "Phoibos 100" electron analyzer (24 meV energy resolution). A six-axis goniometer ("Carving" manipulator from SPECS) provides access to the complete k-space. The sample mounted on the manipulator can be cooled by LHe (continuous flow cryostat) down to 10 K. Counter heating allows for temperature dependent measurements (see Sec. 6.6). In addition, this chamber is equipped with a commercial SPA-LEED (Omicron), which has been utilized to obtain the LT diffraction pattern presented in Fig. 6.3. The sample transfer from the LT-STM to the ARPES chamber was performed under UHV conditions, using a home-built UHV suitcase evacuated by a non evaporable getter (NEG) pump from SAES Getters ($p_b \approx 1 \cdot 10^{-9}$ mbar). Before each ARPES measurement, the samples have been refreshed while mounted on the manipulator by a special direct current heating cycle, which will be described below.

B Determination of the Downhill Direction

In order to compare experimental and theoretically simulated STM images of stepped atomic wire surfaces, it is essential to know the downhill direction in the respective STM images, i.e., the downhill direction of the stepped sample analyzed. This has been realized experimentally with energy dependent optical LEED experiments.

Since the manipulator in front of the optical LEED is limited to axial rotations about the axis along the 10 mm side of the sample [see Fig. B.2(a)], Type A samples (cf. Sec. 4.2) are required to determine the downhill direction. The left image in Fig. B.2(b) shows a LEED pattern of a well-ordered Si(553)-Au surface recorded at 45 eV. In order to detect the (0,0) spot of a surface facet, the energy of the LEED electron beam has been ramped during image acquisition [see right image in Fig. B.2(b)]. Specifically, the exposure time of the digital camera has been set to 10 s and the beam energy has been increased from 45 eV to 90 eV while the image has been recorded. The obtained photograph tracks the movement of the LEED spots upon electron beam energy variation. As has been demonstrated in the Sec. 3.2, the spot trace points towards the (0,0) spot of the respective LEED pattern. For a Si(553)-Au sample with the incident electron beam oriented perpendicular to the macroscopic sample surface, the (553)-(0,0) spot is found below the electron gun [see crossing of dashed blue in

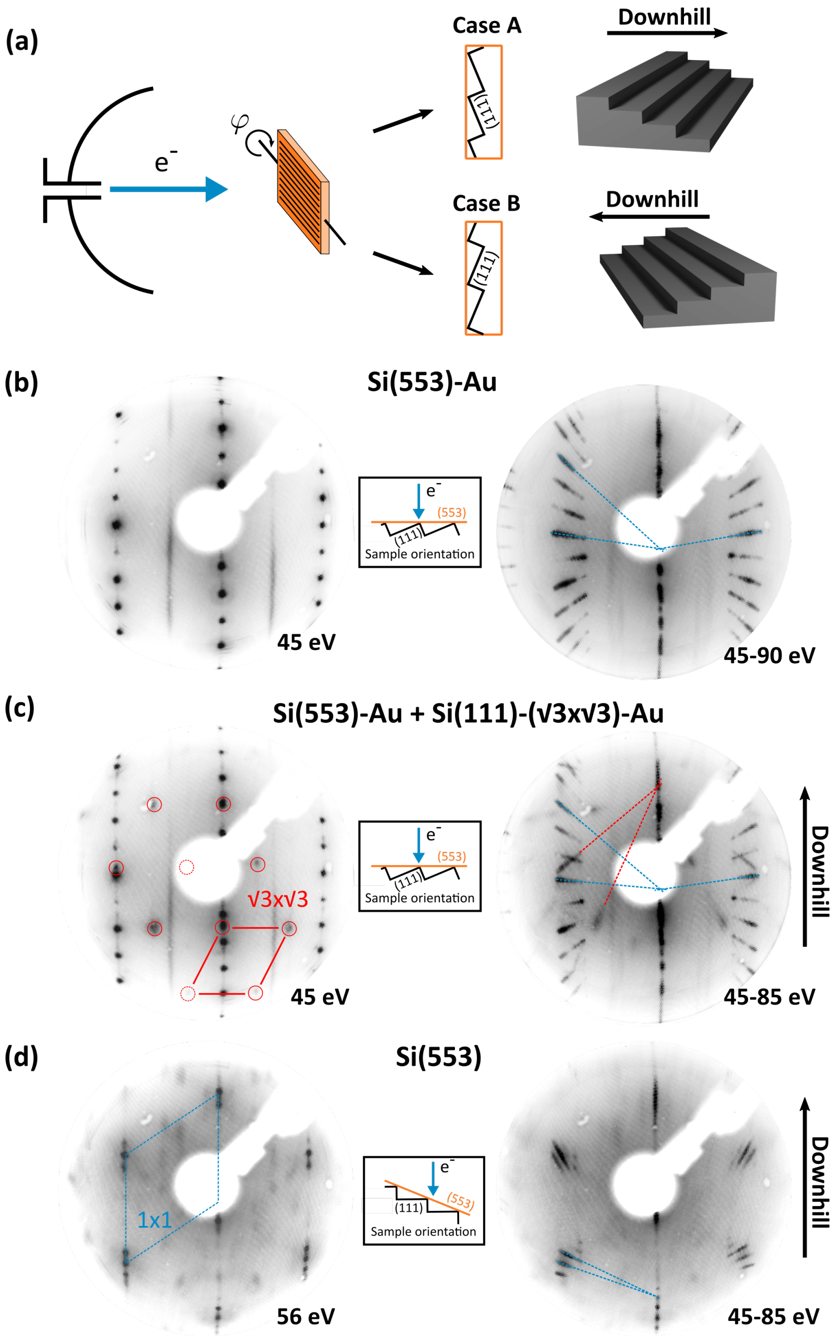

Figure B.2: *(a) Experimental setup to determine the downhill direction of a stepped surface via LEED. Type A samples are required to distinguish between the two possible downhill directions. (b) Left: LEED image of a well-prepared Si(553)-Au surface. The left pattern has been recorded at 45 eV. For the right image the electron beam energy has been increased from 45 eV to 90 eV during image acquisition with the digital camera (10 s exposure time). The (0,0) spot of the (553) plane is hidden by the electron gun. (c) Left: LEED image of a Si(553) sample with surplus Au coverage taken at 45 eV. Si(553)-Au as well as Si(111)-($\sqrt{3} \times \sqrt{3}$)-Au facets coexist. $\sqrt{3}$ spots are marked in red. Right: LEED image of the same surface but recorded while the electron beam energy has been varied from 45 eV to 85 eV. The respective spot traces (exemplary marked by the blue and red dashed lines) visualize the (0,0) spots of the respective surface orientations. (d) Left: LEED images of a Si(553) substrate recorded in tilted geometry (see inset) at 56 eV. In the right image, the electron beam energy has been ramped from 45 eV to 85 eV during image acquisition. The (0,0) spot of the (111) surface is behind the electron gun. The (0,0) spot of the (553) plane is located below the center of the image as can be inferred from the spot trace of the splitted (1×1) spots.*

right image of Fig. B.2(b)]. The method described above can utilized to identify the downhill direction of a stepped surface, as will be demonstrated using Si(553)-Au as an example.

The left image of Fig. B.2(c) displays a LEED pattern of a Si(553)-Au surface with surplus Au coverage for a fixed electron beam energy (45 eV). As a consequence of the high Au coverage, a refaceting of the surface occurs, and Si(553)-Au and Si(111)-($\sqrt{3} \times \sqrt{3}$)-Au facets coexist (cf. Sec. 5.2). By ramping the electron beam energy, the (0,0) spots of the two coexisting surface orientations can be identified [right image in Fig. B.2(c)]. The (553)-(0,0) spots is again hidden by the gun (see blue dashed lines). In contrast, the (0,0) spot of the (111) orientation is located *above* the electron gun (crossing of dashed red lines). From this, one can infer the downhill direction of the stepped sample. In particular, a tilt of the sample by $\varphi = +12.3\,^\circ$ is required to bring the (111)-(0,0) spot behind the gun, i.e., the investigated sample corresponds to "case A" [cf. Fig. B.2(a)]. For a "case B" sample, the (111)-(0,0) is located *below* the gun, and a sample tilt of $\varphi = -12.3\,^\circ$ has to be applied to realize a normal incident electron beam to the (111) terraces.

This method can likewise be applied for a bare Si(553) substrate. The left image of Fig. B.2(d) displays a LEED pattern of the identical Si(553) sample after Au desorption. The split (1×1) spots display a centered arrangement around the electron gun, suggesting an incident electron beam perpendicular to the (111) terraces. This pattern could be realized by a tilt of the sample by $\varphi = +12.3\,^\circ$, indicating a "case A" downhill direction. As a crosscheck, the electron beam has been ramped during image acquisition [right image of Fig. B.2(d)]. The spot trace of the splitted (1×1) spots reveal the (553)-(0,0) spot below the gun as expected of the determined downhill direction.

Once knowing the step orientation of a sample mounted on the sample holder, it is straight forward to trace back the downhill direction in the STM images.

C Recovery of Si(553)-Au Samples

After a certain time of residual gas exposure or a sample transfer between LT-STM and ARPES chamber, a significant loss of sample quality was observed. This degradation was simulated by putting a well-prepared Si(553)-Au sample [see Fig. C.3(a)] into the fast entry load-lock ($p = 5 \cdot 10^{-8}$ mbar) for 25 min. STM and LEED experiments clearly evidence the adsorption of residual gas atoms [see Fig. C.3(b)]. The LEED pattern shows an increase of the diffuse background intensity accompanied by a loss of spot intensities. In particular, the ×2 streaks are only slightly visible. An STM overview scan discloses a surface completely covered with adsorbates.

In order to recover the sample, the following two-step direct current heating sequence was applied:

$$\mathrm{RT} \underbrace{\xrightarrow{t=5\,s} 600\,^\circ\mathrm{C}\ \text{for}\ 5\,\mathrm{s} \xrightarrow{t=5\,s}}_{\text{Step \#1}} \mathrm{RT}\ \text{for}\ 60\,\mathrm{s} \underbrace{\xrightarrow{t=5\,s} 850\,^\circ\mathrm{C}\ \text{for}\ 5\,\mathrm{s} \xrightarrow{t=5\,s}}_{\text{Step \#2}} \mathrm{RT}. \tag{7.1}$$

The first step aims for the desorption of residual gas atoms, and is usually accompanied by a short pressure boost. The second step ensures a reassembly of the surface after adsorbate desorption. During the second step, no further pressure boost occurs. The process can be repeated many times without suffering a significant loss of sample quality. This is in contrast to the one step process suggested in Refs. [19, 21], which can only be repeated several times without sample degradation. A plausible explanation for this difference may be a considerable loss of Au atoms when combining adsorbate desorption and surface reordering in one step. The sample refresh is analyzed by LEED and STM experiments subsequent to step #1 and step #2 of the recovery sequence [see Fig. C.3(c) and (d)]. After step #1, no Si(553)-Au spots but rather (1×1) spots are observed. The STM overview scan reveals a rough, disordered sample surface. After step #2, LEED and STM images indicate a well-ordered Si(553)-Au atomic wire array. No significant difference to the freshly prepared sample can be identified [cf. Fig. C.3(a)].

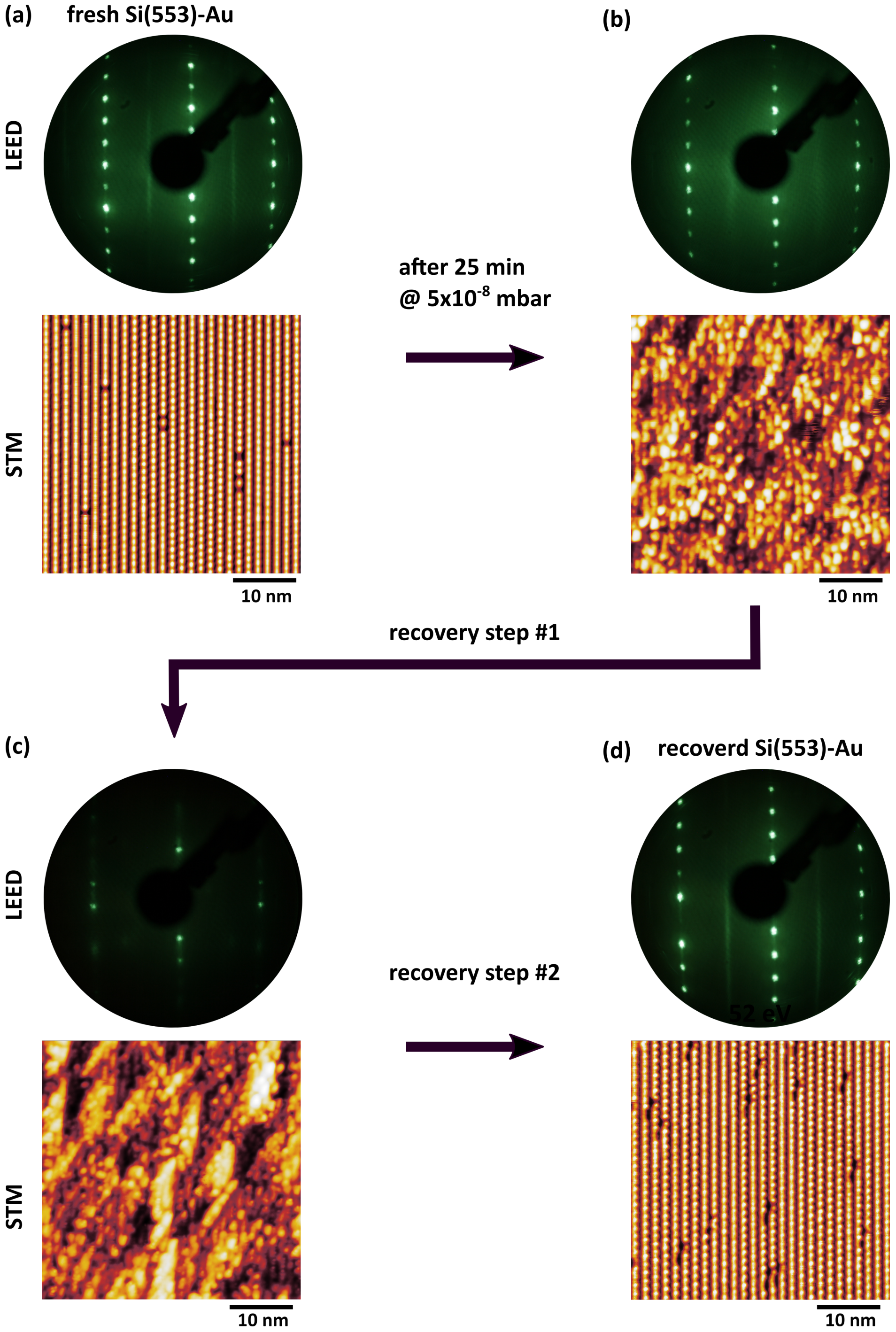

Figure C.3: *LEED patterns (52 eV, $T = RT$) and STM overview scans (39 nm×39 nm, $U = +0.5$ V, $I = 5$ pA, $T = 77$ K) of a Si(553)-Au sample after each step of the recovery sequence: (a) directly after preparation, (b) after storage in the load lock at a base pressure of $p = 5 \cdot 10^{-8}$ mbar for 25 min, (c) after the first step of the recovery sequence, (d) after the complete sample recovery. No significant difference between the fresh and the recleaned sample can be identified.*

D Ge(*hhk*) Substrates

To extend the zoo of quasi-1D model systems, various Ge(*hhk*) substrates have been utilized. Before Au evaporation a proper pretreatment is required, which significantly differs from that of Si(*hhk*). Ex situ, the ex factory substrates are, at first, sonicated in the triple organic bathes as described above for the Si(*hhk*) substrates. Second, wet-chemical etching in Piranha solution followed by a thermal oxidation step according to Ref. [191] is applied. This procedure is well established for the preparation of Ge(001) substrates [191]. The etching step is expected to remove the protective oxide layer as well as contaminants that have not been removed by the triple organic bath. The protective oxide is subsequently rebuilt by the thermal treatment. Although inevitable for the Ge(001) preparation, the second step appears be redundant for Ge(*hhk*) preparation: No significant difference between Ge(*hhk*) samples treated with triple organic only and etched samples could be observed. In situ, the protective oxide layer is removed by several cycles of Ar^+ ion sputtering accompanied by thermal annealing via direct current. The detailed process parameter for the respective Ge(*hhk*) substrates are given in Ref. [192].

Ge(553) – Fig. D.4(a) displays a LEED pattern of a Ge(553) sample after several sputter and anneal cycles. The (1×1) spots feature a splitting, which is characteristic for a stepped surface [blue ellipse in Fig. D.4(a)]. The magnitude of the observed spot splitting [$\frac{\Delta k_{row}}{\Delta k_{split}} \cdot a_{[\bar{1}10]} = (29.4 \pm 1.5)\,\text{Å}$, $L_{Ge(553)} = 15.4\,\text{Å}$] indicates the formation of Ge(553) double steps, just as observed for Si(553) [cf. Fig. 4.2(a)]. Despite a higher overall surface roughness, the STM overview image of the Ge(553) surface [Fig. D.4(b)] appears very similar to that of Si(553) [Fig. 4.2(c)]. The step distance obtained from STM [$(30.0 \pm 1.2)\,\text{Å}$] confirms the formation of Ge(553) double steps.

Ge(557) – A LEED pattern of a Ge(557) substrate after several sputter and anneal treatments is presented in Fig. D.5(a). Beside the split (1×1) spots (light blue ellipse), several additional spot rows (green arrows) are observed, indicating a ×5 superstructure along the chains. A quantitative analysis of the spot spacing [$\frac{\Delta k_{row}}{\Delta k_{split}} \cdot a_{[\bar{1}10]} = (33.8 \pm 1.7)\,\text{Å}$), $L_{Ge(223)} = 16.5\,\text{Å}$] yields the formation of Ge(223) double steps. This is in contrast to the other Si(*hhk*) and Ge(*hhk*) substrates studied within the framework of this thesis, but similar to what has been observed for Si(557). In general, Si/Ge(*hhk*) substrates maintain their surface orientation beyond in situ surface preparation. For Si(557), however, different preparation procedures yield various stepped surface orientations [193] (and references therein). Specifically, a refaceting to Si(223) triple steps has been observed for a Si(557) substrate prepared with the current direction perpendicular to the steps [194]. For the studied Ge(557) substrates, the heat current flow direction was perpendicular to the step direction (type B), too. Independent of the detailed preparation parameter, no Ge(557) surface could be realized. Instead, always faceting

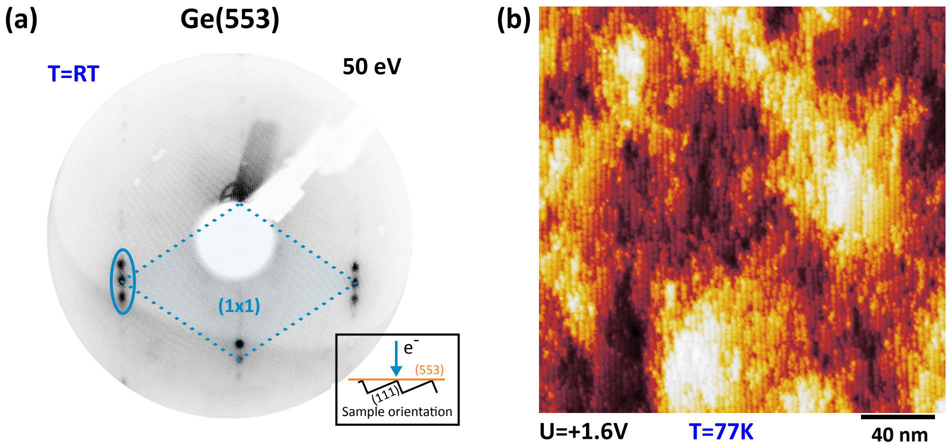

Figure D.4: *(a) LEED image of a Ge(553) substrate after several sputter and anneal cycles taken at 50 eV. A splitting of the (1×1) spots characteristic for stepped surfaces is observed (blue ellipse). The (1×1) unit cell is indicated by the dashed blue rhomboid. (b) STM overview scan of the Ge(553) surface (200 nm × 200 nm, $T = 77\,K$, $U = +1.6\,V$).*

into Ge(223) occurred. Based on this finding one may conclude that Ge(557) is unstable. An alternative scenario is that the company selling the nominal Ge(557) wafer applied a wrong cutting angle ($\alpha_{Ge(557)} = -9.4^\circ$ vs. $\alpha_{Ge(223)} = -11.4^\circ$).

The STM overview image of the Ge(557) substrate after in situ preparation presented in Fig. D.5(b) displays up to 30 nm wide terraces covered with periodic chain structures. An analysis of the interchain distance [(32.7 ± 0.5) Å] confirms the formation of Ge(223) double steps. Along the chains, three different features characterized by their unoccupied states STM appearance can be identified [see left panel of Fig. D.5(c)]. There are paired circular protrusions oriented perpendicular to the step direction [red ellipse in Fig. D.5(c)]. Further, spade-like (blue ellipse) and butterfly-like (green ellipse) features can be observed. The unoccupied state appearance of the two latter elements suggests that these elements are composed by Ge adatoms [see left panel of Fig. D.5(c) and Chapt. 5 for various Si adatom reconstructions]. These three characteristic building blocks occur with varying distance and sequence along the terraces. Neighboring paired protrusions show a minimal distance of $5a_0$, which is consistent with the ×5 superstructure spots observed in LEED. A complete decoding of the reconstruction is beyond the scope of this thesis. For this purpose, a scrutiny with STM only is insufficient. Instead, additional efforts, such as SXRD experiments or DFT simulations, are required. Moreover, the preparation conditions which lead to the Ge(223) double steps should be further verified by, e.g., testing Ge(557) substrates from a different supplier and with current flow direction parallel to the steps. Notwithstanding, the Ge(223) double steps are well suited for the growth of Ge(335)-Au as well as Ge(557)-Au atomic wires as described in Sec. E.

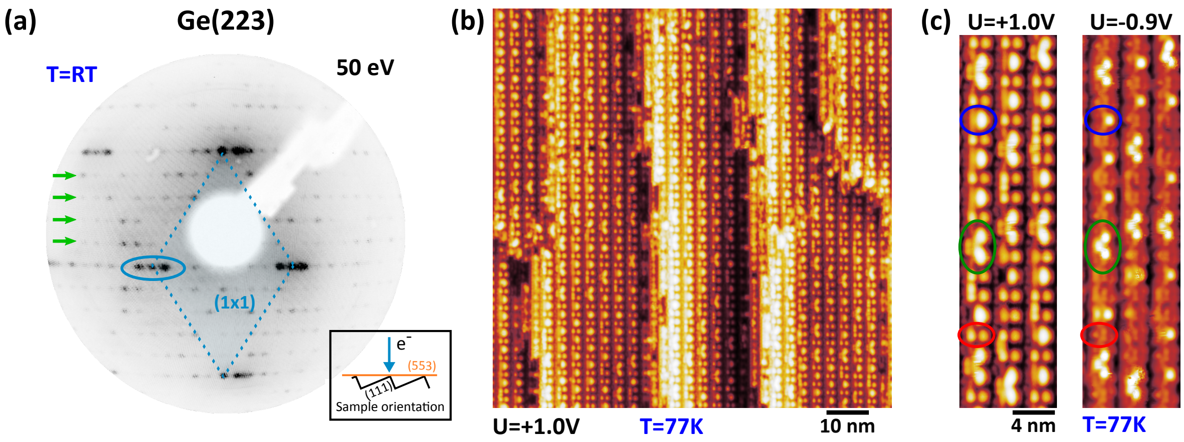

Figure D.5: *(a) LEED image of a nominal Ge(557) substrate after several sputter and anneal cycles taken at 50 eV. A splitting of the (1×1) spots, characteristic for stepped surfaces, is observed (blue ellipse). The (1×1) unit cell is indicated by the dashed blue rhomboid. The spot distances suggest the formation of Ge(223) double steps. Superstructure spots (green arrows) indicate the formation of an ×5 superstructure along the chains. (b) STM overview scan of the Ge(223) surface (93 nm × 93 nm, $T = 77$ K, $U = +1.0$ V, $I = 50$ pA). (c) Unoccupied states ($U = +1.0$ V) and occupied states ($U = -0.9$ V) zoomed-in STM images of an identical Ge(223) sample area (10 nm × 39 nm, $T = 77$ K, $I = 10$ pA). Three characteristic elements can be identified: paired protrusion (red ellipse), spade-like elements (blue ellipse), and butterfly-like elements (green ellipse).*

E Au Chains on Ge(*hhk*): An Alternative Spin Chain Model System?

The Si(*hhk*)-Au family offers certain degrees of tunability obtained by the specific choice of the high-index substrate (Sec. 4.1). Yet another handle is given by the substrate material. A promising option is to use Ge(*hhk*) instead of Si(*hhk*) templates – an approach that has not been attempted to date. Germanium, just like silicon, is a group-IV element, which crystallizes in a diamond lattice. In terms of lattice constant, both differ by only 4 % ($a_{Si} = 5.43$ Å vs. $a_{Ge} = 5.66$ Å). These structural similarities give reason to expect similar growth behavior. Moreover, Au atomic wires on a planar Ge substrate, namely Ge(001), are well established [A8]. In contrast, both substrate materials comprise several differences. The different atomic sizes and bonding characteristics cause distinct reconstructions of the respective (111) surfaces [195]. In particular, surface preparations including heat treatments result in a $c(2{\times}8)$ structure for Ge(111) [196] and in a $(7{\times}7)$ reconstruction for Si [197], despite of their identical crystal and valence-electron structure. Moreover, the band gap of Ge (0.66 eV) is about half as big as that of Si (1.12 eV), giving rise to modified electronic properties by, e.g., better screening of localized charges [A2]. Further, Ge is much heavier than Si ($Z_{Ge} = 32$ vs. $Z_{Si} = 14$), resulting in a stronger spin-orbit coupling (SOC). An issue of particular interest is whether Ge(*hhk*)-Au atomic wires are also prone to the formation of spin chains. The first step to answer this question is to explore the formation of Au induced reconstructions on various Ge(*hhk*) substrates, which is the objective of the following chapter.

E.1 Ge(557)-Au

In order to grow Ge(557)-Au chain structures, nominal Ge(557) substrates have been utilized. As described in Sec. D these kind of substrates are prone to refacet into Ge(223) surfaces during in situ preparation. Nevertheless, evaporation of a certain submonolayer amount of Au onto such a template can result in a well-ordered Ge(557)-Au atomic wire array. A corresponding LEED image [Fig. E.6(a)] features main spot rows with Ge(557)-Au spacings [$\frac{\Delta k_{row}}{\Delta k_{main}} \cdot a_{[\bar{1}10]} = (20.2 \pm 1.0)$ Å, $L_{Ge(557)-Au} = 19.9$ Å]. In addition, the diffraction pattern comprises ×2 streaks, suggesting the presence of a ×2 superstructure at RT [black arrows in Fig. E.6(a)]. Detailed growth parameters are given in Ref. [192]. Notably, a refresh of the Ge(*hhk*) substrates after Au adsorption is possible, but requires time-consuming sputter and anneal cycles. This is in contrast to Si(*hhk*), which can be refreshed easily via

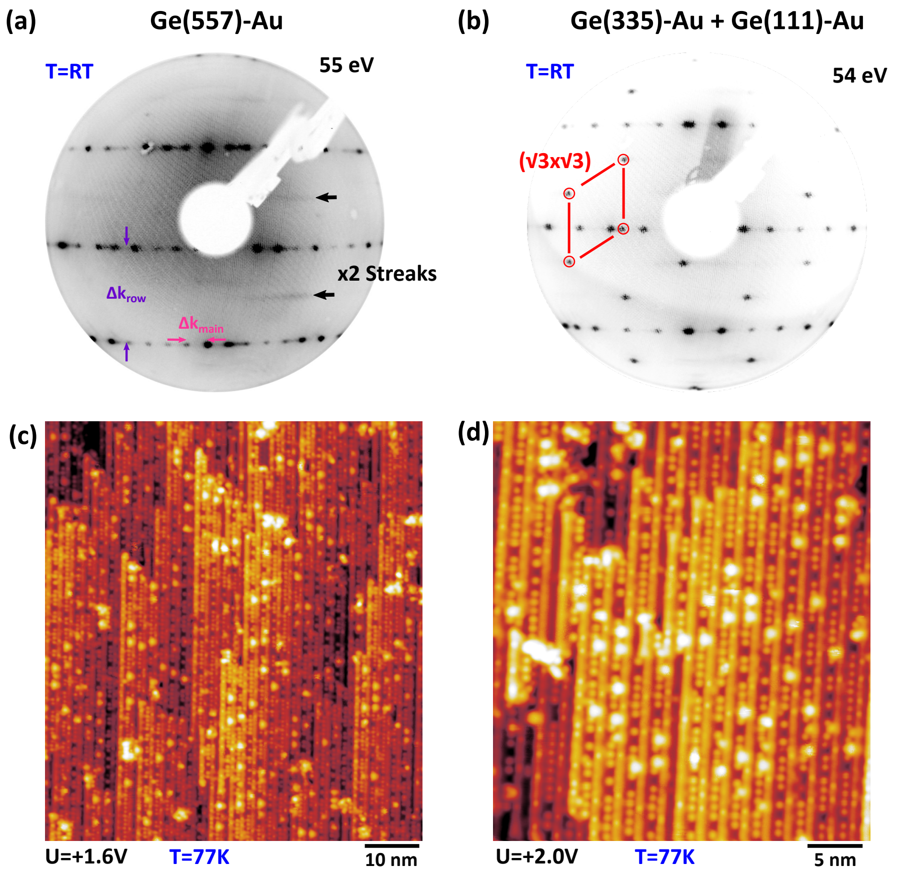

Figure E.6: *(a) LEED image of a Ge(557)-Au surface taken at 55 eV. Black arrows mark ×2 streaks. (b) LEED image (54 eV) of a nominal Ge(557) substrate after surplus Au adsorption. A faceting to Ge(335)-Au and Ge(111)-($\sqrt{3} \times \sqrt{3}$)-Au is observed. (c) STM overview image of the Ge(557)-Au surface (70 nm × 78 nm, $T = 77$ K, $U = +1.6$ V, $I = 50$ pA). (d) STM close-up image of the Ge(557)-Au surface (34 nm × 38 nm, $T = 77$ K, $U = +2.0$ V, $I = 100$ pA). Some chain elements are reminiscent of features known from Si(557)-Au.*

direct current flashes to high temperatures. In case a higher amount of Au than required for ideal Ge(557)-Au growth is provided, the formation of coexisting Ge(111)-($\sqrt{3} \times \sqrt{3}$)-Au and Ge(335)-Au facets can be realized. The LEED pattern shown in Fig. E.6(b) displays distinct $\sqrt{3}$ spots (red circles) as well as regular main spot rows with Ge(335)-Au spacings $[\frac{\Delta k_{row}}{\Delta k_{main}} \cdot a_{[\bar{1}10]} = (13.2 \pm 0.7)$ Å, $L_{Ge(335)-Au} = 13.1$ Å]. A similar refaceting has been reported for Si(557) after Au evaporation [29]. For an ideal Ge(557)-Au Au coverage, no $\sqrt{3}$ spots can be observed. Instead, the LEED image presented in Fig. E.6(a) comprises Ge(557)-Au spots only. An STM overview scan of a Ge(557)-Au sample reveals a regular atomic wire array [see Fig E.6(c)]. The chain spacing of (20.0 ± 0.3) Å suggests the formation of a Ge(557)-Au surface ($L_{Ge(557)-Au} = 19.9$ Å). The given error corresponds to the reading error. The zoomed-in image presented in Fig. E.6(d) comprises some features that are reminiscent of the chain structures observed on Si(557)-Au. In particular, two chain types can be identified. One type manifests as a bright, structureless filament sprinkled with small, irregular distributed charge clouds. The second type is characterized by rather periodic (×2) circular charge clouds that are reminiscent of the silicon adatom row known from Si(557)-Au and Si(775)-Au. In addition, the surface hosts randomly distributed, bright proportions. Similar features have also been observed on Si(557)-Au, Si(775)-Au as well as Si(111)-Au, and have been identified as (misplaced) Si adatoms (see Chapt. 5). Although they have some obvious similarities with their Si cousins, the Ge(557)-Au chains are interrupted by many defects, which hinder a clear-cut identification of superstructures.

E.2 Ge(335)-Au

The previous section demonstrated that Ge(335)-Au chains can form on a nominal Ge(557) substrate after Au adsorption, suggesting an exceptional stability of the Ge(335)-Au surface. In order to realize a pure Ge(335)-Au wire array (i.e. without Ge(111)-Au facets on the same sample), pre-cut Ge(335) substrates have been utilized. Evaporation of Au on a carefully prepared Ge(335) substrate (see Ref. [192] for detailed sputter and anneal parameters) results in well-ordered Ge(335)-Au wires. The LEED image comprises Ge(335)-Au main spot rows $[\frac{\Delta k_{row}}{\Delta k_{main}} \cdot a_{[\bar{1}10]} = (12.8 \pm 0.6)$ Å, $L_{Ge(335)-Au} = 13.1$ Å] as well as ×3 streaks [black arrows in Fig. E.7(a)]. The latter indicates the presence of a ×3 superstructure at RT. The STM scan presented in Fig. E.7(b) confirms the evaluation of the LEED spot spacings and reveals a wire distance of (13.0 ± 1.0) Å. Along the wires, a short-ranged ×3 periodicity, repeatedly interrupted by defects and adsorbates, is observed [green dots in Fig. E.7(c)]. Thus, one may speculate whether the Ge(335)-Au surface hosts ×3 spin chains. However, this requires further verification by, e.g., a detailed (bias-dependent) STM scrutiny on low-defective samples as well as DFT modeling. Nevertheless, it has been shown that Au adsorption on Ge(335) stabilizes an anisotropic atomic wire reconstruction.

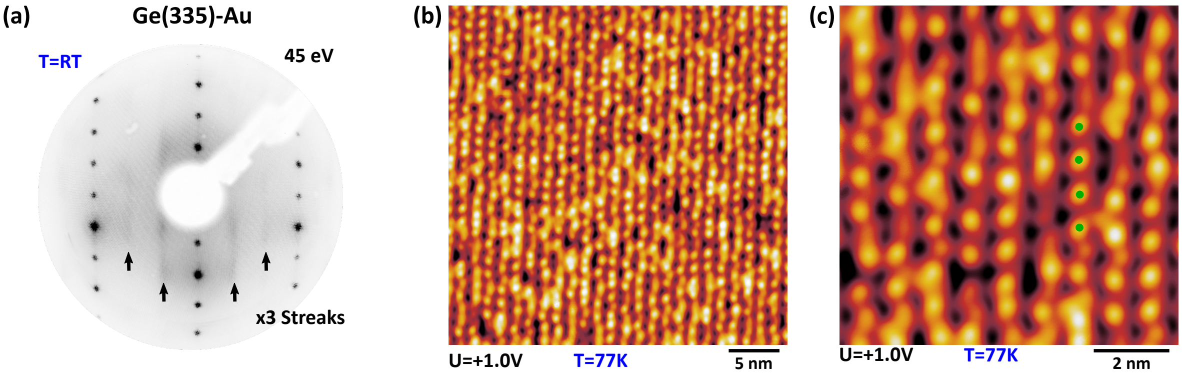

Figure E.7: *(a) LEED image of a Ge(335)-Au surface taken at 45 eV. Black arrows mark ×3 streaks. (b) STM overview scan of the Ge(335)-Au surface (31.5 nm × 31.5 nm, $T = 77\,K$, $U = +1.0\,V$, $I = 50\,pA$). (c) STM zoomed-in image of the Ge(335)-Au surface (12 nm × 12 nm, $T = 77\,K$, $U = +1.0\,V$, $I = 50\,pA$). The chains are interrupted by many defects/adsorbates. Some undisturbed chain segments show a ×3 periodicity as exemplarily marked by the green dots.*

E.3 Faceting of Ge(553) to Ge(221)-Au

Contrary to expectation, evaporation of Au on a Ge(553) substrate does not yield Ge(553)-Au wires, yet instead, a Ge(221)-Au surface forms. The LEED pattern after Au adsorption features main spots spacings which reveal a wire distance of $\frac{\Delta k_{row}}{\Delta k_{main}} \cdot a_{[\bar{1}10]} = (12.1 \pm 0.6)\,\text{Å}$. This suggests the formation of a Ge(221)-Au surface ($L_{Ge(221)-Au} = 12.0\,\text{Å}$). Moreover, the LEED pattern comprises $(\sqrt{3} \times \sqrt{3})$ spots, indicating a faceting of the surface [red circles in Fig. E.8(a)]. Interestingly, the main spot rows show a different relative alignment than in the LEED patterns of all known Si(*hhk*)-Au reconstructions. In particular, adjacent main spot rows are *not* shifted by half of the intrarow spot distance. This results in a rectangular (1×1) unit cell [see black rectangle in Fig. E.8(a)] instead of a rhombohedral unit cell as known from Si(*hhk*)-Au (cf. Sec. 5.2). Likewise, in real space, the substrate lattices of adjacent terraces are not shifted by $0.5a_0$. This finding substantiates the assumption that a Ge(221)-Au reconstruction has been realized: A (221) terrace is composed by an odd number of full atomic row distances in the direction perpendicular to the step edges ($T_{221} = (\mathbf{3} + 1/3)\sqrt{3/8} \cdot a_0$). Contrary, all stable Si(*hhk*)-Au terraces comprise an even number of full atomic row distances perpendicular to steps (e.g., $T_{553} = (\mathbf{4} + 1/3)\sqrt{3/8} \cdot a_0$). This registry is confirmed by the real space STM data. The scan presented in Fig. E.8(b) exhibits bright, filament-like chains separated by $(11.8 \pm 1.0)\,\text{Å}$ ($L_{Ge(221)-Au} = 12.0\,\text{Å}$). The dark trenches between the bright rows are cluttered by circular charge clouds which are reminiscent to substrate adatoms known from some Si(*hhk*)-Au surfaces. Interestingly, adjacent charge clouds are aligned horizontally instead of featuring a $0.5a_0$ shift [see green dots in Fig. E.8(b)]. This is fully consistent with a Ge(221) structure, which does not show a $0.5a_0$ shift of adjacent terrace lattices.

In summary, several stable Ge(*hhk*)-Au surfaces could be realized. Like for Si, Ge(557)-Au as well as Ge(335)-Au wire arrays exist. By contrast, a Ge(553)-Au surface could not be created. Instead, the Ge(553) substrate refacets to Ge(221)-Au after Au adsorption. Un-

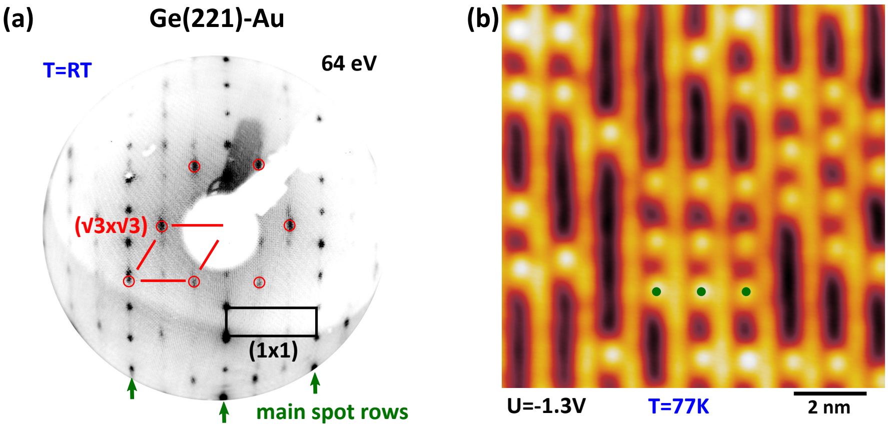

Figure E.8: *(a) LEED image of a Ge(553) substrate after Au evaporation taken at 64 eV. The spot spacings of the main spot rows (green arrows) indicate the formation of a Ge(221)-Au surface. The black rectangle reflects the (1×1) unit cell.* $(\sqrt{3}\times\sqrt{3})$ *spots are marked in red. (b) STM scan of the Ge(221)-Au surface (10 nm × 10 nm,* $T = 77\,K$, $U = -1.3\,V$, $I = 50\,pA$*). The random charge clouds, exemplarily marked by the green dots, are reminiscent to substrate adatoms known from the Si(hhk)-Au surfaces. Their horizontal alignment fits the terrace structure implied by the rectangular unit cell.*

fortunately, all discovered Ge(hhk)-Au surfaces comprise a rather high defect density. To unambiguously answer the question whether some of these stable Ge(hhk)-Au surfaces host spin chains or not, a further reduction of the defect density is required. Promising approaches in this respect are improvements of the UHV conditions and modifications to the usual growth procedure. Low-defective wire growth should enable a comprehensive characterization of the chain periodicities and the electronic structure, followed by the development of structure models for the respective surfaces in order to verify the existence of spin chains on Au stabilized stepped Ge surfaces. Moreover, temperature-dependent STM and ARPES measurements may yield the presence of temperature-dependent superstructures or signatures of a Peierls transition on these novel atomic wire systems.

F Additional Figures

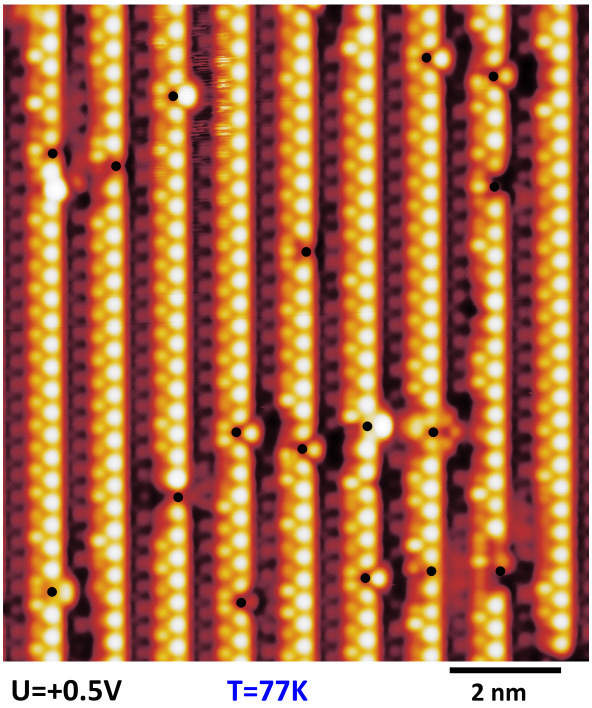

Figure F.9: *STM overview scan of the Si(775)-Au surface (19.2 nm × 21.1 nm, $U = +0.5$ V, $T = 77$ K). Adatom defects are marked by black dots. The adatom defect density per (1×2) unit cell of this particular scan is 7.6 %.*

Band	E_0[eV]	t_1[eV]	t_3[eV]	t_2[eV]
S3	1.35	1.08	0	-0.11
S2	0.04	0.73	0.065	$< \|0.024\|$
S1	-0.16	0.63	0.065	$< \|0.024\|$

Table 7.1: *Parameter of the tight binding fit to Au chain bands shown in Fig. 6.20. The values are in good agreement with results obtained by the authors of Ref. [137]. The shift of the SBZ by half a reciprocal lattice vector in k_y direction compared to Ref. [137] results in a different phase of the wiggled Au bands, and, therefore, in a different sign for t_2 of S3. t_2 of S1 and S2 is below the resolution limit of the ARPES measurement.*

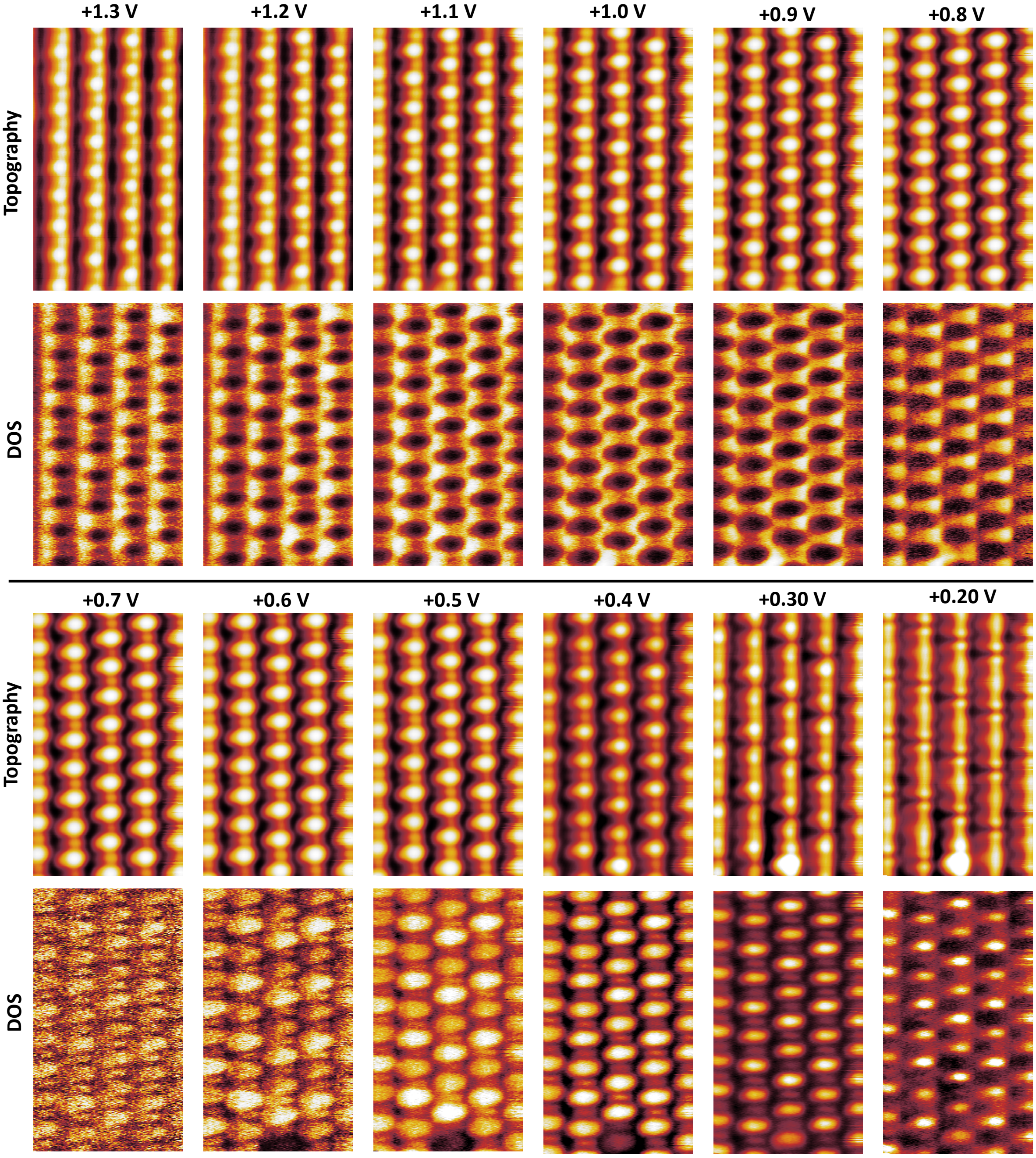

Figure F.10: *Unoccupied Si(553)-Au constant current STM images (top) and dI/dU maps (bottom) for various tunneling biases ($T = 77\,K$). dI/dU maps have been recorded simultaneously with the topography images using the lock-in technique ($U_{mod} = 10\,meV$). All images images display the identical sample area comprising two forward and one backward Si step-edge chain (cf. Fig. 6.23).*

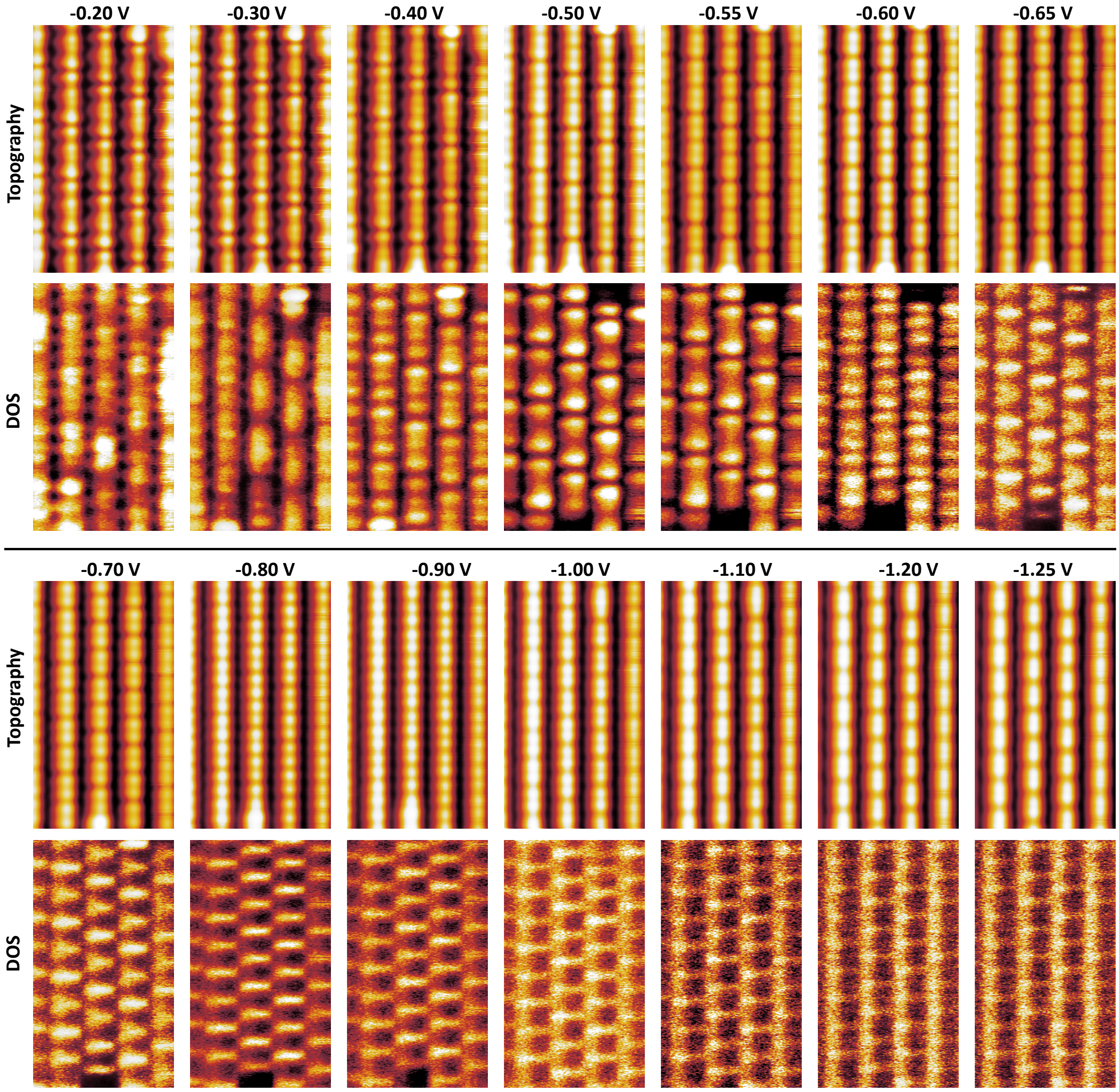

Figure F.11: *Occupied Si(553)-Au constant current STM images (top) and dI/dU maps (bottom) for various tunneling biases ($T = 77\,K$). dI/dU maps have been recorded simultaneously with the topography images using the lock-in technique ($U_{mod} = 10\,\mathrm{meV}$). All images images display the identical sample area comprising two forward and one backward Si step-edge chain (cf. Fig. 6.23).*

List of Own Publications

[A1] J. Aulbach, J. Schäfer, S. C. Erwin, S. Meyer, C. Loho, J. Settelein and R. Claessen, *Evidence for Long-Range Spin Order Instead of a Peierls Transition in Si(553)-Au Chains*, Phys. Rev. Lett. **111**, 137203 (2013).

[A2] S. Glass, G. Li, F. Adler, J. Aulbach, A. Fleszar, R. Thomale, W. Hanke, R. Claessen and J. Schäfer, *Triangular Spin-Orbit-Coupled Lattice with Strong Coulomb Correlations: Sn Atoms on a SiC(0001) Substrate*, Phys. Rev. Lett. **114**, 247602 (2015).

[A3] J. Aulbach, S. C. Erwin, R. Claessen and J. Schäfer, *Spin Chains and Electron Transfer at Stepped Silicon Surfaces*, Nano Letters **16**, 2698 (2016).

[A4] T. Lichtenstein, J. Aulbach, J. Schäfer, R. Claessen, C. Tegenkamp and H. Pfnür, *Two-dimensional crossover and strong coupling of plasmon excitations in arrays of one-dimensional atomic wires*, Phys. Rev. B **93**, 161408 (R) (2016).

[A5] S. Glass, F. Reis, M. Bauernfeind, J. Aulbach, M. R. Scholz, F. Adler, L. Dudy, G. Li, R. Claessen and J. Schäfer, *Atomic-Scale Mapping of Layer-by-Layer Hydrogen Etching and Passivation of SiC(0001) Substrates*, The Journal of Physical Chemistry C **120**, no. 19, 10361 (2016).

[A6] B. Hafke, T. Frigge, T. Witte, B. Krenzer, J. Aulbach, J. Schäfer, R. Claessen, S. C. Erwin and M. Horn-von Hoegen, *Two-dimensional interaction of spin chains in the Si(553)-Au nanowire system*, Phys. Rev. B **94**, 161403 (R) (2016).

[A7] J. Aulbach, S. C. Erwin, J. Kemmer, M. Bode, J. Schäfer and R. Claessen, *Parity breaking in a double atomic chain system*, Phys. Rev. B **96**, 081406 (R) (2017), Editors' suggestion.

[A8] L. Dudy, J. Aulbach, T. Wagner, J. Schäfer and R. Claessen, *One-dimensional quantum matter: gold-induced nanowires on semiconductor surfaces*, Journal of Physics: Condensed Matter **29**, no. 43, 433001 (2017).

[A9] C. Hogan, E. Speiser, S. Chandola, S. Suchkova, J. Aulbach, J. Schäfer, S. Meyer, R. Claessen and N. Esser, *Controlling the Local Electronic Properties of Si(553)-Au Through Hydrogen Doping*, submitted (2017).

[A10] M. R. Scholz, V. A. Rogalev, L. Dudy, F. Reis, F. Adler, J. Aulbach, A. Fleszar, L. J. Collins-McIntyre, L. B. Duffy, H. Yang, Y. L. Chen, T. Hesjedal, Z. K. Liu, M. Hoesch, S. Muff, J. H. Dil, J. Schäfer and R. Claessen, *The topological surface state of α-Sn on InSb(001) as studied by photoemission*, submitted (2017).

[A11] T. Wagner, J. Aulbach, R. Claessen and J. Schäfer, *Regular Au-induced Atomic Wires on Stepped Ge(hhk) Surfaces*, manuscript (2017).

[A12] J. Aulbach, S. Erwin, M. Greiter, R. Thomale, R. Claessen and J. Schäfer, *Soliton Drag in Atomic Wires at a Substrate Step Edge*, manuscript (2017).

[A13] J. Aulbach, L. Dudy, R. Claessen and J. Schäfer, *Order-Disorder Transition in Silicon Spin Chains*, manuscript (2017).

Bibliography

[1] S. C. Erwin and F. Himpsel, *Intrinsic magnetism at silicon surfaces*, Nat. Commun. **1**, 58 (2010).

[2] R. Peierls, *Quantum Theory of Solids*, Clarendon Press, Oxford (1964).

[3] F. D. M. Haldane, *'Luttinger liquid theory' of one-dimensional quantum fluids. I. Properties of the Luttinger model and their extension to the general 1D interacting spinless Fermi gas*, Journal of Physics C: Solid State Physics **14**, 2585 (1981).

[4] S. Cheon, T.-H. Kim, S.-H. Lee and H. W. Yeom, *Chiral solitons in a coupled double peierls chain*, Science **350**, 182 (2015).

[5] R. Jackiw and C. Rebbi, *Solitons with fermion number* $\frac{1}{2}$, Phys. Rev. D **13**, 3398 (1976).

[6] G. Grüner, *Density Waves in Solids*, Westview Press (2000).

[7] N. D. Mermin and H. Wagner, *Absence of Ferromagnetism or Antiferromagnetism in One- or Two-Dimensional Isotropic Heisenberg Models*, Phys. Rev. Lett. **17**, 1133 (1966).

[8] D. Jerome and L. Caron, *Low-dimensional conductors and superconductors*, Springer Science & Business Media (2013).

[9] C. Schlenker, *Low-dimensional electronic properties of molybdenum bronzes and oxides*, Physics and chemistry of materials with low-dimensional structures, Kluwer Academic Publishers (1989).

[10] P. C. Snijders and H. H. Weitering, *Colloquium : Electronic instabilities in self-assembled atom wires*, Rev. Mod. Phys. **82**, 307 (2010).

[11] C. Blumenstein, J. Schaefer, S. Mietke, S. Meyer, A. Dollinger, M. Lochner, X. Y. Cui, L. Patthey, R. Matzdorf and R. Claessen, *Atomically controlled quantum chains hosting a Tomonaga-Luttinger liquid*, Nat. Phys. **7**, 776 (2011).

[12] J. Park, K. Nakatsuji, T.-H. Kim, S. K. Song, F. Komori and H. W. Yeom, *Absence of Luttinger liquid behavior in Au-Ge wires: A high-resolution scanning tunneling microscopy and spectroscopy study*, Phys. Rev. B **90**, 165410 (2014).

[13] N. de Jong, R. Heimbuch, S. Eliëns, S. Smit, E. Frantzeskakis, J.-S. Caux, H. J. W. Zandvliet and M. S. Golden, *Gold-induced nanowires on the Ge(100) surface yield a 2D and not a 1D electronic structure*, Phys. Rev. B **93**, 235444 (2016).

[14] H. W. Yeom, S. Takeda, E. Rotenberg, I. Matsuda, K. Horikoshi, J. Schaefer, C. M. Lee, S. D. Kevan, T. Ohta, T. Nagao and S. Hasegawa, *Instability and Charge Density Wave of Metallic Quantum Chains on a Silicon Surface*, Phys. Rev. Lett. **82**, 4898 (1999).

[15] T.-H. Kim and H. W. Yeom, *Topological Solitons versus Nonsolitonic Phase Defects in a Quasi-One-Dimensional Charge-Density Wave*, Phys. Rev. Lett. **109**, 246802 (2012).

[16] T.-H. Kim, S. Cheon and H. W. Yeom, *Switching chiral solitons for algebraic operation of topological quaternary digits*, Nat. Phys. pages 1745–2481 (2017).

[17] J. N. Crain, J. L. McChesney, F. Zheng, M. C. Gallagher, P. C. Snijders, M. Bissen, C. Gundelach, S. C. Erwin and F. J. Himpsel, *Chains of gold atoms with tailored electronic states*, Phys. Rev. B **69**, 125401 (2004).

[18] P. Segovia, D. Purdie, M. Hengsberger and Y. Baer, *Observation of spin and charge collective modes in one-dimensional metallic chains*, Nature **402**, 504 (1999).

[19] K. N. Altmann, J. N. Crain, A. Kirakosian, J.-L. Lin, D. Y. Petrovykh, F. J. Himpsel and R. Losio, *Electronic structure of atomic chains on vicinal Si(111)-Au*, Phys. Rev. B **64**, 035406 (2001).

[20] I. Barke, F. Zheng, T. K. Rügheimer and F. J. Himpsel, *Experimental Evidence for Spin-Split Bands in a One-Dimensional Chain Structure*, Phys. Rev. Lett. **97**, 226405 (2006).

[21] T. Okuda, K. Miyamaoto, Y. Takeichi, H. Miyahara, M. Ogawa, A. Harasawa, A. Kimura, I. Matsuda, A. Kakizaki, T. Shishidou and T. Oguchi, *Large out-of-plane spin polarization in a spin-splitting one-dimensional metallic surface state on Si(557)-Au*, Phys. Rev. B **82**, 161410 (2010).

[22] M. Krawiec, *Structural model of the Au-induced Si(553) surface: Double Au rows*, Phys. Rev. B **81**, 115436 (2010).

[23] M. Krawiec, *Spin-orbit splitting in the Si(335)-Au surface*, Surface Science **609**, 44 (2013).

[24] J. R. Ahn, H. W. Yeom, H. S. Yoon and I.-W. Lyo, *Metal-Insulator Transition in Au Atomic Chains on Si with Two Proximal Bands*, Phys. Rev. Lett. **91**, 196403 (2003).

[25] J. R. Ahn, P. G. Kang, K. D. Ryang and H. W. Yeom, *Coexistence of Two Different Peierls Distortions within an Atomic Scale Wire: Si(553)-Au*, Phys. Rev. Lett. **95**, 196402 (2005).

[26] P. C. Snijders, S. Rogge and H. H. Weitering, *Competing Periodicities in Fractionally Filled One-Dimensional Bands*, Phys. Rev. Lett. **96**, 076801 (2006).

[27] J. S. Shin, K.-D. Ryang and H. W. Yeom, *Finite-length charge-density waves on terminated atomic wires*, Phys. Rev. B **85**, 073401 (2012).

[28] W. Voegeli, T. Takayama, T. Shirasawa, M. Abe, K. Kubo, T. Takahashi, K. Akimoto and H. Sugiyama, *Structure of the quasi-one-dimensional Si(553)-Au surface: Gold dimer row and silicon honeycomb chain*, Phys. Rev. B **82**, 075426 (2010).

[29] I. Barke, F. Zheng, S. Bockenhauer, K. Sell, V. v. Oeynhausen, K. H. Meiwes-Broer, S. C. Erwin and F. J. Himpsel, *Coverage-dependent faceting of Au chains on Si(557)*, Phys. Rev. B **79**, 155301 (2009).

[30] S. Ghose, I. Robinson, P. Bennett and F. Himpsel, *Structure of double row quantum wires in Au/Si(553)*, Surface Science **581**, 199 (2005).

[31] I. K. Robinson, P. A. Bennett and F. J. Himpsel, *Structure of quantum wires in* Au/Si(557), Phys. Rev. Lett. **88**, 096104 (2002).

[32] D. Sánchez-Portal, J. D. Gale, A. García and R. M. Martin, *Two distinct metallic bands associated with monatomic Au wires on the Si(557)-Au surface*, Phys. Rev. B **65**, 081401 (2002).

[33] M. Krawiec, T. Kwapiński and M. Jałochowski, *Scanning tunneling microscopy of monoatomic gold chains on vicinal Si(335) surface: experimental and theoretical study*, physica status solidi (b) **242**, 332 (2005).

[34] D. Sánchez-Portal, S. Riikonen and R. M. Martin, *Role of Spin-Orbit Splitting and Dynamical Fluctuations in the Si(557)-Au Surface*, Phys. Rev. Lett. **93**, 146803 (2004).

[35] S. Riikonen and D. Sánchez-Portal, *Interplay between electronic and atomic structures in the Si(557)-Au reconstruction from first principles*, Phys. Rev. B **76**, 035410 (2007).

[36] G. Z. Magda, X. Jin, I. Hagymasi, P. Vancso, Z. Osvath, P. Nemes-Incze, C. Hwang, L. P. Biro and L. Tapaszto, *Room-temperature magnetic order on zigzag edges of narrow graphene nanoribbons*, Nature **514**, 608 (2014).

[37] G. D. Mahan, *Spin Shift Register from a One-Dimensional Atomic Chain*, Phys. Rev. Lett. **102**, 016801 (2009).

[38] S. Brazovskii, C. Brun, Z.-Z. Wang and P. Monceau, *Scanning-Tunneling Microscope Imaging of Single-Electron Solitons in a Material with Incommensurate Charge-Density Waves*, Phys. Rev. Lett. **108**, 096801 (2012).

[39] S. J. Park, H. W. Yeom, S. H. Min, D. H. Park and I. W. Lyo, *Direct Evidence of the Charge Ordered Phase Transition of Indium Nanowires on Si(111)*, Phys. Rev. Lett. **93**, no. r, 106402 (2004).

[40] H. Morikawa, I. Matsuda and S. Hasegawa, *Direct observation of soliton dynamics in charge-density waves on a quasi-one-dimensional metallic surface*, Phys. Rev. B **70**, 085412 (2004).

[41] H. Zhang, J.-H. Choi, Y. Xu, X. Wang, X. Zhai, B. Wang, C. Zeng, J.-H. Cho, Z. Zhang and J. G. Hou, *Atomic Structure, Energetics, and Dynamics of Topological Solitons in Indium Chains on Si(111) Surfaces*, Phys. Rev. Lett. **106**, 026801 (2011).

[42] S. C. Erwin and P. C. Snijders, *Silicon spin chains at finite temperature: Dynamics of Si(553)-Au*, Phys. Rev. B **87**, 235316 (2013).

[43] S. Polei, P. C. Snijders, S. C. Erwin, F. J. Himpsel, K.-H. Meiwes-Broer and I. Barke, *Structural Transition in Atomic Chains Driven by Transient Doping*, Phys. Rev. Lett. **111**, 156801 (2013).

[44] S. Polei, P. C. Snijders, K.-H. Meiwes-Broer and I. Barke, *Current-dependent periodicities of Si(553)-Au*, Phys. Rev. B **89**, 205420 (2014).

[45] T. Dauxois and M. Peyrard, *Physics of Solitons*, Cambridge University Press (2006).

[46] K. Rossnagel, *On the origin of charge-density waves in select layered transition-metal dichalcogenides*, Journal of Physics Condensed Matter **23**, 213001 (2011).

[47] W. Kohn, *Image of the Fermi Surface in the Vibration Spectrum of a Metal*, Phys. Rev. Lett. **2**, 393 (1959).

[48] R. H. Friend and D. Jerome, *Periodic lattice distortions and charge density waves in one- and two-dimensional metals*, Journal of Physics C: Solid State Physics **12**, 1441 (1979).

[49] C. Kittel, *Quantum theory of solids*, 13. Auflage, Second Revised Edition, Wiley (1987).

[50] S. K. Chan and V. Heine, *Spin density wave and soft phonon mode from nesting Fermi surfaces*, Journal of Physics F: Metal Physics **3**, 795 (1973).

[51] T. Aruga, *Charge-density waves on metal surfaces*, Journal of Physics: Condensed Matter **14**, 8393 (2002).

[52] P. A. Lee, T. M. Rice and P. W. Anderson, *Fluctuation Effects at a Peierls Transition*, Phys. Rev. Lett. **31**, 462 (1973).

[53] M. D. Johannes and I. I. Mazin, *Fermi surface nesting and the origin of charge density waves in metals*, Phys. Rev. B **77**, 165135 (2008).

[54] X. Zhu, Y. Cao, J. Zhang, E. W. Plummer and J. Guo, *Classification of charge density waves based on their nature*, Proceedings of the National Academy of Sciences **112**, 2367 (2015).

[55] X. Zhu, J. Guo, J. Zhang and E. W. Plummer, *Misconceptions associated with the origin of charge density waves*, Advances in Physics: X **2**, 622 (2017).

[56] G. Grüner and A. Zettl, *Charge density wave conduction: A novel collective transport phenomenon in solids*, Physics Reports **119**, 117 (1985).

[57] W. Fuller, P. Chaikin and N. Ong, *Effects of radiation damage on the charge density wave transitions in* $NbSe_3$, Solid State Communications **39**, 547 (1981).

[58] W. W. Fuller, G. Grüner, P. M. Chaikin and N. P. Ong, *Effect of radiation damage on the charge-density-wave dynamics in* $Nb\mathrm{Se}_3$, Phys. Rev. B **23**, 6259 (1981).

[59] P.-L. Hsieh, F. de Czito, A. Janossy and G. Grüner, *Effect of Disorder on the Charge Density Wave Transitions and Transport in orthorhombic* TaS_3, J. Phys. Colloques **44**, C3 (1983).

[60] G. Mihaly, N. Housseau, H. Mutka, L. Zuppiroli, J. Pelissier, P. Gressier, A. Meerschaut and J. Rouxel, *Disorder in the quasi-one-dimensional conductor monoclinic tantalum trisulfide* TaS_3, J. Physique Lett. **42**, 263 (1981).

[61] H. H. Weitering, J. M. Carpinelli, A. V. Melechko, J. Zhang, M. Bartkowiak and E. W. Plummer, *Defect-Mediated Condensation of a Charge Density Wave*, Science **285**, 2107 (1999).

[62] A. V. Melechko, J. Braun, H. H. Weitering and E. W. Plummer, *Two-dimensional phase transition mediated by extrinsic defects*, Phys. Rev. Lett. **83**, 999 (1999).

[63] D. F. Urban, C. A. Stafford and H. Grabert, *Scaling theory of the Peierls charge density wave in metal nanowires*, Phys. Rev. B **75**, 205428 (2007).

[64] J. S. Russell, *Report on Waves*, Report of the fourteenth meeting of the British Association for the Advancement of Science pages 311–390 (1844).

[65] A. Filippov, *The Versatile Soliton*, Modern Birkhäuser classics, Springer Science & Business Media (2000).

[66] A. J. Heeger, S. Kivelson, J. R. Schrieffer and W. P. Su, *Solitons in conducting polymers*, Rev. Mod. Phys. **60**, 781 (1988).

[67] W. P. Su, J. R. Schrieffer and A. J. Heeger, *Solitons in polyacetylene*, Phys. Rev. Lett. **42**, 1698 (1979).

[68] W. P. Su, J. R. Schrieffer and A. J. Heeger, *Soliton excitations in polyacetylene*, Phys. Rev. B **22**, 2099 (1980).

[69] C. J. Chen, *Introduction to Scanning Tunneling Microscopy*, Oxford University Press (2008).

[70] *The Nobel Prize in Physics 1986*, `http://www.nobelprize.org/nobel_prizes/physics/laureates/1986/`, retrieved on 25.04.2017.

[71] R. Wiesendanger, *Scanning Probe Microscopy and Spectroscopy: Methods and Applications*, Cambridge University Press (1994).

[72] C. Bai, *Scanning Tunneling Microscopy and Its Applications*, Second Revised Edition, Springer (2000).

[73] O. Fischer, M. Kugler, I. Maggio-Aprile, C. Berthod and C. Renner, *Scanning tunneling spectroscopy of high-temperature superconductors*, Rev. Mod. Phys. **79**, 353 (2007).

[74] G. Binnig, H. Rohrer, C. Gerber and E. Weibel, *Surface Studies by Scanning Tunneling Microscopy*, Phys. Rev. Lett. **49**, 57 (1982).

[75] J. Bardeen, *Tunnelling from a Many-Particle Point of View*, Phys. Rev. Lett. **6**, 57 (1961).

[76] J. Tersoff and D. R. Hamann, *Theory and Application for the Scanning Tunneling Microscope*, Phys. Rev. Lett. **50**, 1998 (1983).

[77] J. Tersoff and D. R. Hamann, *Theory of the scanning tunneling microscope*, Phys. Rev. B **31**, 805 (1985).

[78] J. Kubby and J. Boland, *Scanning tunneling microscopy of semiconductor surfaces*, Surface Science Reports **26**, 61 (1996).

[79] C. J. Chen, *Origin of atomic resolution on metal surfaces in scanning tunneling microscopy*, Phys. Rev. Lett. **65**, 448 (1990).

[80] V. M. Hallmark, S. Chiang, J. F. Rabolt, J. D. Swalen and R. J. Wilson, *Observation of Atomic Corrugation on Au(111) by Scanning Tunneling Microscopy*, Phys. Rev. Lett. **59**, 2879 (1987).

[81] P. H. Lippel, R. J. Wilson, M. D. Miller, C. Wöll and S. Chiang, *High-Resolution Imaging of Copper-Phthalocyanine by Scanning-Tunneling Microscopy*, Phys. Rev. Lett. **62**, 171 (1989).

[82] J. Wintterlin, J. Wiechers, H. Brune, T. Gritsch, H. Höfer and R. J. Behm, *Atomic-Resolution Imaging of Close-Packed Metal Surfaces by Scanning Tunneling Microscopy*, Phys. Rev. Lett. **62**, 59 (1989).

[83] S. Ohnishi and M. Tsukada, *Molecular orbital theory for the scanning tunneling microscopy*, Solid State Communications **71**, 391 (1989).

[84] C. J. Chen, *Microscopic view of scanning tunneling microscopy*, Journal of Vacuum Science & Technology A: Vacuum, Surfaces, and Films **9**, 44 (1991).

[85] R. J. Hamers, *Atomic-Resolution Surface Spectroscopy with the Scanning Tunneling Microscope*, Annual Review of Physical Chemistry **40**, 531 (1989).

[86] S. Crampin, H. Jensen, J. Kröger, L. Limot and R. Berndt, *Resonator design for use in scanning tunneling spectroscopy studies of surface electron lifetimes*, Phys. Rev. B **72**, 035443 (2005).

[87] M. Ternes, *Scanning tunneling spectroscopy at the single atom scale*, Ph.D. thesis, École polytechnique fédérale de Lausanne (2006).

[88] W. Krenner, D. Kühne, F. Klappenberger and J. Barth, *Assessment of Scanning Tunneling Spectroscopy Modes Inspecting Electron Confinement in Surface-Confined Supramolecular Networks*, Scientific Reports **3**, 1454 (2013).

[89] C. Davisson and L. H. Germer, *Diffraction of Electrons by a Crystal of Nickel*, Phys. Rev. **30**, 705 (1927).

[90] M. Horn-von Hoegen, *Growth of semiconductor layers studied by spot profile analysing low energy electron diffraction - Part II*, Zeitschrift für Kristallographie - Crystalline Materials **214**, 1999 (1999).

[91] L. de Broglie, *XXXV. A tentative theory of light quanta*, Philosophical Magazine Series 6 **47**, 446 (1924).

[92] M. P. Seah and W. A. Dench, *Quantitative electron spectroscopy of surfaces: A standard data base for electron inelastic mean free paths in solids*, Surface and Interface Analysis **1**, 2 (1979).

[93] S. Hüfner, *Photoelectron Spectroscopy, Principles and Applications*, Springer Verlag (2003).

[94] G. Ertl and J. Küppers, *Low Energy Electrons and Surface Chemistry*, Wiley-VCH (1985).

[95] M. Henzler and W. Goepel, *Oberflächenphysik des Festkörpers*, Teubner (1994).

[96] M. A. V. Hove, W. H. Einberg and C. M. Chan, *Low-Energy Electron Diffration - Experiment, Theory and Surface Structure Determination*, Springer Verlag (1986).

[97] M. Henzler, *Atomic steps on single crystals: Experimental methods and properties*, Applied physics **9**, 11 (1976).

[98] A. Damascelli, Z. Hussain and Z. X. Shen, *Angle-resolved photoemission studies of the cuprate superconductors*, Reviews of Modern Physics **75**, 473 (2003).

[99] R. Claessen, *Photoelectron spectroscopy: The joys and pitfalls of the photoelectric effect*, Talk given at the School on UV and X-ray spectroscopies of correlated electron systems – SUCCESS-2014 (2014).

[100] F. Reinert and S. Hüfner, *Photoemission spectroscopy – from early days to recent applications*, New Journal of Physics **7**, 97 (2005).

[101] A. Damascelli, *Probing the Electronic Structure of Complex Systems by ARPES*, Physica Scripta **2004**, 61 (2004).

[102] T. Miller, W. E. McMahon and T.-C. Chiang, *Interference between Bulk and Surface Photoemission Transitions in Ag(111)*, Phys. Rev. Lett. **77**, 1167 (1996).

[103] A. Hofmann, X. Y. Cui, J. Schäfer, S. Meyer, P. Höpfner, C. Blumenstein, M. Paul, L. Patthey, E. Rotenberg, J. Bünemann, F. Gebhard, T. Ohm, W. Weber and R. Claessen, *Renormalization of Bulk Magnetic Electron States at High Binding Energies*, Phys. Rev. Lett. **102**, 187204 (2009).

[104] S. Suga and A. Sekiyama, *Photoelectron Spectroscopy – Bulk and Surface Electronic Structures*, Springer (2016).

[105] S. C. Erwin, *Introduction to Density-Functional Theory: From Fundamentals to Applications*, Talk given at the 3rd International Fall School ToCoTronics2016 (2016).

[106] P. Hohenberg and W. Kohn, *Inhomogeneous Electron Gas*, Phys. Rev. **136**, B864 (1964).

[107] W. Kohn, *Nobel lecture: Electronic structure of matter – wave functions and density functionals*, Rev. Mod. Phys. **71**, 1253 (1999).

[108] W. Kohn and L. J. Sham, *Self-Consistent Equations Including Exchange and Correlation Effects*, Phys. Rev. **140**, A1133 (1965).

[109] O. Gunnarsson, M. Jonson and B. I. Lundqvist, *Descriptions of exchange and correlation effects in inhomogeneous electron systems*, Phys. Rev. B **20**, 3136 (1979).

[110] G. Kotliar and D. Vollhardt, *Strongly Correlated Materials: Insights From Dynamical Mean-Field Theory*, Physics Today **57**, 53 (2004).

[111] J. P. Perdew, K. Burke and M. Ernzerhof, *Generalized Gradient Approximation Made Simple*, Phys. Rev. Lett. **77**, 3865 (1996).

[112] J. Heyd, G. E. Scuseria and M. Ernzerhof, *Hybrid functionals based on a screened Coulomb potential*, The Journal of Chemical Physics **118**, 8207 (2003).

[113] K. Lejaeghere *et al.*, *Reproducibility in density functional theory calculations of solids*, Science **351** (2016).

[114] F. Bechstedt, F. Fuchs and G. Kresse, *Ab-initio theory of semiconductor band structures: New developments and progress*, physica status solidi (b) **246**, 1877 (2009).

[115] F. Reis, G. Li, L. Dudy, M. Bauernfeind, S. Glass, W. Hanke, R. Thomale, J. Schäfer and R. Claessen, *Bismuthene on a SiC substrate: A candidate for a high-temperature quantum spin Hall material*, Science (2017).

[116] D. Bruns, S. Gevers and J. Wollschläger, *Formation and morphology of step bunches during B-segregation on vicinal Si(111)*, Surface Science **605**, 861 (2011).

[117] A. Waag, *Wachstum von Gold-induzierten Nanodrähten auf gestuftem Silizium*, Bachelor's thesis, Julius-Maximilians-Universität Würzburg, Lehrstuhl für experimentelle Physik IV (2013).

[118] Y.-N. Yang and E. D. Williams, *The role of carbon in the faceting of silicon surfaces on the (111) to (001) azimuth*, Journal of Vacuum Science & Technology A: Vacuum, Surfaces, and Films **8**, 2481 (1990).

[119] F. Sojka, M. Meissner, C. Zwick, R. Forker and T. Fritz, *Determination and correction of distortions and systematic errors in low-energy electron diffraction*, Review of Scientific Instruments **84**, 015111 (2013).

[120] M. Jałochowski, M. Strȯżak and R. Zdyb, *Gold-induced ordering on vicinal Si(111)*, Surface Science **375**, 203 (1997).

[121] M. Bauernfeind, *Charakterisierung goldinduzierter Nanodrähte auf einem Si(775)-Substrat*, Bachelor's thesis, Julius-Maximilians-Universität Würzburg, Lehrstuhl für experimentelle Physik IV (2014).

[122] M. K. Kim, D.-H. Oh, J. Baik, C. Jeon, I. Song, J. H. Nam, S. H. Woo, C.-Y. Park and J. R. Ahn, *Control of a quasi-one-dimensional phase of a Si nanostructure: Vicinal Si(557) surfaces*, Phys. Rev. B **81**, 085312 (2010).

[123] H. E. Bishop and J. C. Rivière, *Segregation of gold to the silicon (111) surface observed by Auger emission spectroscopy and by LEED*, Journal of Physics D: Applied Physics **2**, 1635 (1969).

[124] H. Lipson and K. E. Singer, *Disorder in a film of gold deposited on silicon: investigation by low-energy electron diffraction*, Journal of Physics C: Solid State Physics **7**, 12 (1974).

[125] W. H. Choi, P. G. Kang, K. D. Ryang and H. W. Yeom, *Band-structure engineering of gold atomic wires on silicon by controlled doping*, Phys. Rev. Lett. **100**, 126801 (2008).

[126] S. C. Erwin, I. Barke and F. J. Himpsel, *Structure and energetics of* $Si(111)-(5\times2)$-*Au*, Phys. Rev. B **80**, 155409 (2009).

[127] S. G. Kwon and M. H. Kang, *Identification of the Au Coverage and Structure of the* Au/Si(111)$-(5 \times 2)$ *Surface*, Phys. Rev. Lett. **113**, 086101 (2014).

[128] T. Abukawa and Y. Nishigaya, *Structure of the Si(111)-(*5×2*)-Au Surface*, Phys. Rev. Lett. **110**, 036102 (2013).

[129] C. Hogan, E. Ferraro, N. McAlinden and J. F. McGilp, *Optical Fingerprints of Si Honeycomb Chains and Atomic Gold Wires on the Si(111)-(*$5{\times}2$*)-Au Surface*, Phys. Rev. Lett. **111**, 087401 (2013).

[130] T. Shirasawa, W. Voegeli, T. Nojima, Y. Iwasawa, Y. Yamaguchi and T. Takahashi, *Identification of the structure model of the* Si(111)$-(5 \times 2)-$Au *surface*, Phys. Rev. Lett. **113**, 165501 (2014).

[131] K. Seino and F. Bechstedt, *First-principles calculations of energetics and electronic structure for reconstructed* Si(111) $-$ $(5 \times n)$ $-$ Au *surfaces*, Phys. Rev. B **90**, 165407 (2014).

[132] P. Bayersdorfer, L. Dudy, J. Aulbach, J. Schaefer and R. Claessen, unpublished.

[133] F. Hötzel, K. Seino, C. Huck, O. Skibbe, F. Bechstedt and A. Pucci, *Metallic Properties of the Si(111)- 5×2 - Au Surface from Infrared Plasmon Polaritons and Ab Initio Theory*, Nano Letters **15**, 4155 (2015).

[134] I. Barke, S. Polei, V. v. Oeynhausen and K.-H. Meiwes-Broer, *Confined Doping on a Metallic Atomic Chain Structure*, Phys. Rev. Lett. **109**, 066801 (2012).

[135] J. Schäfer, S. C. Erwin, M. Hansmann, Z. Song, E. Rotenberg, S. D. Kevan, C. S. Hellberg and K. Horn, *Random registry shifts in quasi-one-dimensional adsorbate systems*, Phys. Rev. B **67**, 085411 (2003).

[136] U. Krieg, Y. Zhang, C. Tegenkamp and H. Pfnür, *Tuning of one-dimensional plasmons by Ag-Doping in Ag-*$\sqrt{3}$*-ordered atomic wires*, New Journal of Physics **16**, 043007 (2014).

[137] J. N. Crain, A. Kirakosian, K. N. Altmann, C. Bromberger, S. C. Erwin, J. L. McChesney, J.-L. Lin and F. J. Himpsel, *Fractional Band Filling in an Atomic Chain Structure*, Phys. Rev. Lett. **90**, 176805 (2003).

[138] K.-D. Ryang, P. G. Kang, H. W. Yeom and S. Jeong, *Structures and defects of atomic wires on Si(553)-Au: An STM and theoretical study*, Phys. Rev. B **76**, 205325 (2007).

[139] D. Armour, *Vacuum aspects of modern surface treatment in analysis*, Vacuum **43**, 117 (1992).

[140] J. Coad, H. Bishop and J. Rivière, *Electron-beam assisted adsorption on the Si(111) surface*, Surface Science **21**, 253 (1970).

[141] S. Riikonen and D. Sánchez-Portal, *Structural models for Si(553)-Au atomic chain reconstruction*, Nanotechnology **16**, S218 (2005).

[142] S. Riikonen and D. Sánchez-Portal, *Systematic investigation of the structure of the Si(553)-Au surface from first principles*, Phys. Rev. B **77**, 165418 (2008).

[143] T. Takayama, W. Voegeli, T. Shirasawa, K. Kubo, M. Abe, T. Takahashi, K. Akimoto and H. Sugiyama, *Structural Study of the Si(553)-Au Surface*, e-Journal of Surface Science and Nanotechnology **7**, 533 (2009).

[144] K. Biedermann, S. Regensburger, T. Fauster, F. J. Himpsel and S. C. Erwin, *Spin-split silicon states at step edges of Si(553)-Au*, Phys. Rev. B **85**, 245413 (2012).

[145] P. C. Snijders, P. S. Johnson, N. P. Guisinger, S. C. Erwin and F. J. Himpsel, *Spectroscopic evidence for spin-polarized edge states in graphitic Si nanowires*, New Journal of Physics **14**, 103004 (2012).

[146] I. Song, J. S. Goh, S.-H. Lee, S. W. Jung, J. S. Shin, H. Yamane, N. Kosugi and H. W. Yeom, *Realization of a Strained Atomic Wire Superlattice*, ACS Nano **9**, 10621 (2015).

[147] M. Bode, *Spin-polarized scanning tunnelling microscopy*, Reports on Progress in Physics **66**, 523 (2003).

[148] M. Bode, M. Heide, K. von Bergmann, P. Ferriani, S. Heinze, G. Bihlmayer, A. Kubetzka, O. Pietzsch, S. Blugel and R. Wiesendanger, *Chiral magnetic order at surfaces driven by inversion asymmetry*, Nature **447**, 190 (2007).

[149] P.-G. Kang, J. S. Shin and H. W. Yeom, *Point defects along metallic atomic wires on vicinal Si surfaces: Si(5 5 7)-Au and Si(5 5 3)-Au*, Surface Science **603**, 2588 (2009).

[150] M. Sauter, R. Hoffmann, C. Sürgers and H. v. Löhneysen, *Temperature-dependent scanning tunneling spectroscopy on the Si(557)-Au surface*, Phys. Rev. B **89**, 075406 (2014).

[151] J.-H. Han, H. S. Kim, H. N. Hwang, B. Kim, S. Chung, J. W. Chung and C. C. Hwang, *Direct evidence of the step-edge buckling at the* $Au/Si(557)\text{-}1\times 2$ *surface*, Phys. Rev. B **80**, 241401 (2009).

[152] L. Pedri, L. Toppozini and M. Gallagher, *Au-induced nanofaceting and the stoichiometry of the Si(775)-Au surface*, Surface Science **601**, 924 (2007).

[153] S. C. Erwin and H. H. Weitering, *Theory of the “honeycomb chain-channel” reconstruction of* $M/\mathrm{Si}(111)\text{-}\ (3\times 1)$, Phys. Rev. Lett. **81**, 2296 (1998).

[154] J. A. Stroscio and D. M. Eigler, *Atomic and Molecular Manipulation with the Scanning Tunneling Microscope*, Science **254**, 1319 (1991).

[155] B. Lalmi, H. Oughaddou, H. Enriquez, A. Kara, S. Vizzini, B. Ealet and B. Aufray, *Epitaxial growth of a silicene sheet*, Applied Physics Letters **97**, 223109 (2010).

[156] A. Fleurence, R. Friedlein, T. Ozaki, H. Kawai, Y. Wang and Y. Yamada-Takamura, *Experimental Evidence for Epitaxial Silicene on Diboride Thin Films*, Phys. Rev. Lett. **108**, 245501 (2012).

[157] B. Feng, Z. Ding, S. Meng, Y. Yao, X. He, P. Cheng, L. Chen and K. Wu, *Evidence of Silicene in Honeycomb Structures of Silicon on Ag(111)*, Nano Letters **12**, 3507 (2012).

[158] L. Li, S.-z. Lu, J. Pan, Z. Qin, Y.-q. Wang, Y. Wang, G.-y. Cao, S. Du and H.-J. Gao, *Buckled germanene formation on pt(111)*, Advanced Materials **26**, 4820 (2014).

[159] M. E. Dávila, L. Xian, S. Cahangirov, A. Rubio and G. L. Lay, *Germanene: a novel two-dimensional germanium allotrope akin to graphene and silicene*, New Journal of Physics **16**, 095002 (2014).

[160] A. Acun, L. Zhang, P. Bampoulis, M. Farmanbar, A. van Houselt, A. N. Rudenko, M. Lingenfelder, G. Brocks, B. Poelsema, M. I. Katsnelson and H. J. W. Zandvliet, *Germanene: the germanium analogue of graphene*, Journal of Physics: Condensed Matter **27**, 443002 (2015).

[161] L. Zhang, P. Bampoulis, A. N. Rudenko, Q. Yao, A. van Houselt, B. Poelsema, M. I. Katsnelson and H. J. W. Zandvliet, *Structural and Electronic Properties of Germanene on* MoS_2, Phys. Rev. Lett. **116**, 256804 (2016).

[162] Y. Xu, B. Yan, H.-J. Zhang, J. Wang, G. Xu, P. Tang, W. Duan and S.-C. Zhang, *Large-Gap Quantum Spin Hall Insulators in Tin Films*, Phys. Rev. Lett. **111**, 136804 (2013).

[163] F.-f. Zhu, W.-j. Chen, Y. Xu, C.-l. Gao, D.-d. Guan, C.-h. Liu, D. Qian, S.-C. Zhang and J.-f. Jia, *Epitaxial growth of two-dimensional stanene*, Nat. Mater. **14**, 1020 (2015).

[164] J. J. Palacios, J. Fernández-Rossier and L. Brey, *Vacancy-induced magnetism in graphene and graphene ribbons*, Phys. Rev. B **77**, 195428 (2008).

[165] H. González-Herrero, J. M. Gómez-Rodríguez, P. Mallet, M. Moaied, J. J. Palacios, C. Salgado, M. M. Ugeda, J.-Y. Veuillen, F. Yndurain and I. Brihuega, *Atomic-scale control of graphene magnetism by using hydrogen atoms*, Science **352**, 437 (2016).

[166] L. Bergmann and C. Schaefer, *Lehrbuch für Experimentalphysik Band 6 Festkörper*, Rainer Kassing (2005).

[167] S. Yunoki and S. Sorella, *Two spin liquid phases in the spatially anisotropic triangular Heisenberg model*, Phys. Rev. B **74**, 014408 (2006).

[168] D. Heidarian, S. Sorella and F. Becca, *Spin-*$\frac{1}{2}$ *heisenberg model on the anisotropic triangular lattice: From magnetism to a one-dimensional spin liquid*, Phys. Rev. B **80**, 012404 (2009).

[169] P. Anderson, *Resonating valence bonds: A new kind of insulator?*, Materials Research Bulletin **8**, 153 (1973).

[170] L. Balents, *Spin liquids in frustrated magnets*, Nature **464**, 199 (2010).

[171] Y. Shimizu, K. Miyagawa, K. Kanoda, M. Maesato and G. Saito, *Spin Liquid State in an Organic Mott Insulator with a Triangular Lattice*, Phys. Rev. Lett. **91**, 107001 (2003).

[172] R. Coldea, D. A. Tennant, A. M. Tsvelik and Z. Tylczynski, *Experimental Realization of a 2D Fractional Quantum Spin Liquid*, Phys. Rev. Lett. **86**, 1335 (2001).

[173] M. Kohno, O. A. Starykh and L. Balents, *Spinons and triplons in spatially anisotropic frustrated antiferromagnets*, Nat. Phys. **3**, 790 (2007).

[174] C. Antoniak, H. C. Herper, Y. N. Zhang, A. Warland, T. Kachel, F. Stromberg, B. Krumme, C. Weis, K. Fauth, W. Keune, P. Entel, R. Q. Wu, J. Lindner and H. Wende, *Induced magnetism on silicon in* Fe_3Si *quasi-Heusler compound*, Phys. Rev. B **85**, 214432 (2012).

[175] S. C. Erwin, unpublished.

[176] K.-D. Ryang, P. G. Kang, H. W. Yeom and S. Jeong, *Structures and defects of atomic wires on si(553)-au: An stm and theoretical study*, Phys. Rev. B **76**, 205325 (2007).

[177] I. Song, D.-H. Oh, H.-C. Shin, S.-J. Ahn, Y. Moon, S.-H. Woo, H. J. Choi, C.-Y. Park and J. R. Ahn, *Direct Momentum-Resolved Observation of One-Dimensional Confinement of Externally Doped Electrons within a Single Subnanometer-Scale Wire*, Nano Letters **15**, 281 (2015).

[178] M. Krawiec, M. Kopciuszyński and R. Zdyb, *Different spin textures in one-dimensional electronic bands on Si(553)-Au surface*, Applied Surface Science **373**, 26 (2016).

[179] H. W. Yeom, S. W. Jung, J. S. Shin, J. Kim, K. S. Kim, K. Miyamoto, T. Okuda, H. Namatame, A. Kimura and M. Taniguchi, *Direct observation of the spin polarization in Au atomic wires on Si(553)*, New Journal of Physics **16**, 093030 (2014).

[180] H. Claus, A. Buessenschuett and M. Henzler, *Low-energy electron diffraction with energy resolution*, Review of Scientific Instruments **63**, 2195 (1992).

[181] D. A. Shirley, *High-Resolution X-Ray Photoemission Spectrum of the Valence Bands of Gold*, Phys. Rev. B **5**, 4709 (1972).

[182] H. W. Yeom, D. M. Oh, S. Wippermann and W. G. Schmidt, *Impurity-Mediated Early Condensation of a Charge Density Wave in an Atomic Wire Array*, ACS Nano **10**, 810 (2016), pMID: 26634634.

[183] A. Grüneis, C. Attaccalite, A. Rubio, S. L. Molodtsov, D. V. Vyalikh, J. Fink, R. Follath and T. Pichler, *Preparation and electronic properties of potassium doped graphite single crystals*, physica status solidi (b) **245**, no. 10, 2072 (2008).

[184] M. A. Hossain, J. D. F. Mottershead, D. Fournier, A. Bostwick, J. L. McChesney, E. Rotenberg, R. Liang, W. N. Hardy, G. A. Sawatzky, I. S. Elfimov, D. A. Bonn and A. Damascelli, *In situ doping control of the surface of high-temperature superconductors*, Nat. Phys. **4**, 527 (2008).

[185] Y. K. Kim, N. H. Sung, J. D. Denlinger and B. J. Kim, *Observation of a d-wave gap in electron-doped* sr_2iro_4, Nat. Phys. **12**, 37 (2015).

[186] P. Nita, M. Jałochowski, M. Krawiec and A. Stępniak, *One-Dimensional Diffusion of Pb Atoms on the Si(553)-Au Surface*, Phys. Rev. Lett. **107**, 026101 (2011).

[187] P. Nita, G. Zawadzki, M. Krawiec and M. Jałochowski, *Structural and electronic properties of double Pb chains on the Si(553)-Au surface*, Phys. Rev. B **84**, 085453 (2011).

[188] S. Meyer, *Model System for Correlation Phenomena in Reduced Dimensions-Gold-induced Atomic Chains on Germanium*, Ph.D. thesis, University of Würzburg (2013).

[189] Y. Zhou, K. Kanoda and T.-K. Ng, *Quantum spin liquid states*, Rev. Mod. Phys. **89**, 025003 (2017).

[190] T. Frigge, B. Hafke, T. Witte, B. Krenzer, C. Streubühr, A. Samad Syed, V. Mikšió Trontl, I. Avigo, P. Zhou, M. Ligges, D. von der Linde, U. Bovensiepen, M. Horn-von Hoegen, S. Wippermann, A. Lücke, S. Sanna, U. Gerstmann and W. G. Schmidt, *Optically excited structural transition in atomic wires on surfaces at the quantum limit*, Nature **544**, 207 (2017).

[191] C. Blumenstein, S. Meyer, A. Ruff, B. Schmid, J. Schäfer and R. Claessen, *High purity chemical etching and thermal passivation process for Ge(001) as nanostructure template*, The Journal of Chemical Physics **135**, 064201 (2011).

[192] T. Wagner, *Charakterisierung Gold-induzierter Nanodrähte auf Germanium-Oberflächen*, Master's thesis, Julius-Maximilians-Universität Würzburg, Lehrstuhl für experimentelle Physik IV (2016).

[193] S. I. Bozhko, A. M. Ionov and A. N. Chaika, *Si(hhm) surfaces: Templates for developing nanostructures*, Semiconductors **49**, 753 (2015).

[194] A. N. Chaika, D. A. Fokin, S. I. Bozhko, A. M. Ionov, F. Debontridder, V. Dubost, T. Cren and D. Roditchev, *Regular stepped structures on clean Si(hhm)7×7 surfaces*, Journal of Applied Physics **105**, 034304 (2009).

[195] F. Bechstedt, A. A. Stekolnikov, J. Furthmüller and P. Käckell, *Origin of the Different Reconstructions of Diamond, Si, and Ge(111) Surfaces*, Phys. Rev. Lett. **87**, 016103 (2001).

[196] P. Palmberg and W. Peria, *Low energy electron diffraction studies on Ge and Na-covered Ge*, Surface Science **6**, 57 (1967).

[197] R. Schlier and H. Farnsworth, *Structure and adsorption characteristics of clean surfaces of germanium and silicon*, The Journal of Chemical Physics **30**, 917 (1959).

Acknowledgements

At this point I would like to thank the people who contribute to the successful accomplishment of this thesis. I am very grateful to the following persons:

- First and foremost I thank Prof. Dr. Ralph Claessen for giving me the opportunity to do my Ph.D. at his Chair, the Experimentelle Physik IV. His comprehensive knowledge of solid state physics and critical proof of paper manuscripts continuously improved the quality of my research. Moreover, he initiated the Sonderforschungsbereich SFB 1170, which enabled access to interesting soft-skill courses and set the stage for inspiring and successful collaborations with other physics groups in Würzburg.
- Special thanks go to my supervisor Priv.-Doz. Dr. Jörg Schäfer for his steady interest on the latest experimental data. His inspiring, forward-looking, and motivating manner to discuss new results, complicated interpretations, and complex issues did not only encourage my studies but also taught me for the upcoming stages of my career. Further, he initiated and continuously pushed forward the close collaborations with Dr. S.C. Erwin, Prof. Dr. Herbert Pfnür, Prof. Dr. Michael Horn-von Hoegen, Prof. Dr. Matthias Bode and their groups.
- I am deeply indebted to Dr. S.C. Erwin for the very fruitful collaborations on nearly all issues discussed in this thesis. Without his enlightening calculations and the intensive discussions (more than 1500 emails!) on how to interpret various experimental and theoretical results, this thesis could not have been realized in its present form.
- Further, I would like to thank Prof. Dr. Herbert Pfnür and Prof. Dr. Christoph Tegenkamp for initiating the Forschergruppe FOR 1700. Being part of this delocalized research unit gave me the opportunity to visit various different labs all around Germany, to meet and work together with many excellent scientists, and to gain unique experiences in the review process of a research unit.
- Prof. Dr. Matthias Bode, Dr. Jeanette Kemmer, Prof. Dr. Ronny Thomale and Dr. Martin Greiter for successful and uncomplicated collaboration as well as inspiring discussions.
- Dr. Lenart Dudy for performing and evaluating the ARPES experiments presented. Without his photoemission and automatization expertise such comprehensive data sets could not have been obtained. It was a pleasure to perform experiments with him.
- The Bacholor- and Masterstudents Anna Waag, Maximilian Bauernfeind, Stefan Glass, and Tim Wagner, who contributed to the results of this thesis by both jointly performed experiments and keeping the laboratory running.
- Florian Adler and Felix Reis for the collegial lab work and many hours of proofreading.

- Moni Seifer for her uncomplicated and warm manner to help me with any kind of things other than physics.
- All other members of the EP IV for an enjoyable and convenient working atmosphere.

Aside this great support at the university, I would like to thank my family and friends, who had strong impact on the success of this work.

- My parents, for constant and unrestricted support during my education.
- My friends and especially my brother Philipp for distracting me from work and physics.
- My wonderful wife Isabel for constant support and encouragement and for showing understanding for long days at the desk and weekends in the lab. Thank you taking care of so many things while I was working for and on this thesis!
- My little ones Niels and Marie for brightening up my life.